Université Paris Diderot (Paris 7)
École Doctorale 517 : Particules, Noyaux et Cosmos

## Thèse de Doctorat

Spécialité : Physique des Particules

présentée par

**Vincent DURAND**

pour l'obtention du titre de

Docteur de l'Université Paris Diderot (Paris 7)

# Mesure du paramètre de mélange leptonique $\theta_{13}$ auprès de l'expérience d'antineutrinos de réacteur Double Chooz

Thèse dirigée par M. Thierry LASSERRE

soutenue le 20 septembre 2012 devant le jury composé de :

| | | | |
|---|---|---|---|
| M. | Hervé | DE KERRET | Examinateur |
| M. | Dominique | DUCHESNEAU | Rapporteur |
| M. | Thierry | LASSERRE | Directeur de thèse |
| M. | Guillaume | MENTION | Co-directeur de thèse |
| M. | Serguey | PETCOV | Examinateur |
| M. | Fabrice | PIQUEMAL | Rapporteur |

*À mes parents,*
*ma sœur Cécile,*
*y mi Sandrita.*

# Acknowledgements

Bien que ce manuscrit de thèse soit rédigé en anglais, je me permets ici d'utiliser le français afin de pouvoir pleinement remercier les nombreuses personnes qui ont contribué, de près ou de loin, à cette aventure. Je suis conscient que ces quelques lignes de remerciements désordonnés ne sont que peu de choses devant l'ampleur de ce que vous avez tous fait pour moi, que ce soit au cours de ma thèse ou avant. Je tiens néanmoins à afficher ma profonde gratitude par ces mots.

Tout d'abord, je souhaite remercier Philippe Chomaz, directeur de l'Institut de Recherche sur les lois Fondamentales de l'Univers du CEA Saclay, et Ursula Bassler, chef du Service de Physique des Particules de cet institut, ainsi que Pierre Binétruy, directeur du laboratoire AstroParticule et Cosmologie, pour m'avoir accepté au sein de leurs établissements respectifs. Ce fût un réel plaisir d'effectuer ma thèse dans de tels lieux, tant les conditions de travail ont été idéales.

Je remercie également Dominique Duchesneau et Fabrice Piquemal pour avoir accepté sans hésitation de faire partie de mon jury de thèse, et plus particulièrement d'être rapporteurs de mon manuscrit, malgré la charge de travail supplémentaire que cela implique. Je remercie de même Serguey Petcov qui m'a fait l'honneur de bien vouloir faire le déplacement de Trieste, malgré les kilomètres. Je n'oublie pas Hervé de Kerret qui m'a fait le grand plaisir d'accepter de participer aussi à mon jury.

Je tiens à remercier Thierry Lasserre et Guillaume Mention, mes directeurs de thèse, pour leur encadrement de tous les jours. Je remercie particulièrement Thierry pour la confiance qu'il m'a accordée en me permettant de faire pleinement partie du groupe Double Chooz du Service de Physique des Particules. Un grand merci à Guillaume pour tous ses conseils. Je n'oublierai pas qu'il faut toujours entamer la résolution d'un problème par l'ordre le plus bas, ou que les statistiques ne sont que de simples outils pour le physicien et n'ont donc pas à faire peur ! Merci également de m'avoir encouragé à présenter mon travail dès que l'occasion se présentait, me forçant à prendre régulièrement du recul.

Je ne peux oublier Maximilien Fechner, qui m'a énormément appris, que ce soit en programmation ou en physique. J'ai passé de très bons moments avec lui, à travailler et/ou à chanter *Final Countdown* à chaque fois qu'un code compilait, et ai été sincèrement désolé de le voir partir. Bien qu'il fût un excellent physicien, je suis persuadé qu'il doit s'éclater dans ce qu'il fait à présent ! Aussi, en lui souhaitant la bienvenue au sein du groupe Double Chooz de Saclay, je remercie Matthieu Vivier, pour ses scrupuleuses relectures et ses questions soit-disant naïves.

Bien entendu je n'oublie pas le reste des membres des groupes Double Chooz et Nucifer du CEA et de l'APC. Je pense notamment à Michel Cribier, David Lhuillier et Alain Letourneau, ainsi qu'aux nombreux thésards (pour certains déjà sensei) et stagiaires qui ont croisé ma route : Rachel Quéval, Thomas Mueller, Tarek Akiri, Antoine Collin, Jonathan Gaffiot, ou encore Romain Roncin. Je remercie d'ailleurs grandement les trois premiers pour leurs thèses de doctorat si bien écrites qui m'ont beaucoup aidé lors de la rédaction de ce manuscrit. Je remercie aussi en particulier Antoine, qui m'a supporté lors de trop nombreuses semaines de shift à Chooz et dans de très nombreux pays à travers le monde, que ce soit pour des École d'Été ou réunions de

collaboration. Je lui souhaite bon courage pour la suite tout en sachant pertinemment que sa thèse sera d'excellente qualité.

J'en profite pour remercier les organisateurs de l'École d'Été ISAPP et des Journées des Jeunes Chercheurs, ainsi que les thésards rencontrés là-bas. J'ai une pensée particulière pour les fougueux et téméraires co-inventeurs de la Pyramide Belge Inversée.

Je remercie également l'ensemble des collaborateurs de Double Chooz qui m'ont permis de travailler dans des conditions optimales. Je pense notamment à Kazuhiro Terao qui a toujours répondu présent lorsque j'avais besoin de lui.

Je remercie aussi tous les membres, permanents et non-permanents, des laboratoires SPP et APC, ainsi que le personnel d'entretien, notamment Fouzia Ben Mesbah qui avait chaque matin un mot d'encouragement et un sourire. Je n'oublie pas Philippe Schune, mon parrain de thèse, qui a su être là lorsque j'en avais besoin.

Je souhaite aussi exprimer ma sincère gratitude envers les personnes qui tout au long de ma scolarité, m'ont permis d'en arriver à une thèse en physique des neutrinos. Je pense bien entendu à de nombreux professeurs, que je ne peux citer un à un au risque de voir ces quelques lignes remplir de trop nombreuses pages. Je veux néanmoins remercier deux enseignants de l'Université de Cergy-Pontoise, Lars Egstrøm Kristensen pour les nombreux cafés que nous avons bus en discutant des étoiles, pour m'avoir offert la chance d'effectuer un stage au Danemark et pour m'avoir motivé à m'orienter vers la recherche, et Gérard Gouédard qui a été un professeur passionnant et le meilleur interlocuteur que je pouvais trouver à un moment où j'hésitais beaucoup pour mon avenir. De l'Université Paris 7, je tiens à remercier Éric Huguet pour ses cours mémorables de relativité générale, Dominique Lecourt pour les nombreuses discussions que nous avons eues, souvent autour d'un très bon whisky, François Vannucci pour sa passion des neutrinos et ses histoires fascinantes, Alessandra Tonazzo pour m'avoir fait découvrir l'expérience Double Chooz et m'avoir permis de participer au Summer School Program de DESY (qui m'a apporté bien plus que des connaissances en physique !), Luc Valentin pour avoir créé le Master NPAC et m'avoir recommandé à y entrer, et enfin Achille Stocchi pour m'y avoir accepté.

Je me dois aussi de remercier, dans une liste clairement non-exhaustive, ces nombreuses personnes, le plus souvent non physiciennes ni même scientifiques, qui m'ont tant apporté ces dernières années. Je pense bien évidemment à Michael Scott, the world's best boss, qu'il soit anglais ou américain, à Dwight Schrute et Andy Bernard, mais aussi à Jon Stewart, Stephen Colbert et John Oliver, à Stan, Cartman, Kyle et Kenny, à Homer Simpson et sa petite famille, mais également à Ross Geller et Chandler Bing, à Marshall Eriksen et Barney Stinson, à Sheldon Cooper et Howard Wolowitz, et enfin à Troy and Abed. J'aurais aimé avoir suffisamment de chapitres pour tous vous citer afin de partager votre sagesse avec les lecteurs de ce document.

Je souhaite continuer ces lignes en remerciant le café, sans qui tout ceci n'aurait jamais pu être possible (du moins dans les temps), ainsi que mon partenaire de café de toujours, Fabien Déchery. Si j'ai eu la chance de profiter de notre association magique en TP de Physique de L3, au cours desquels nous avons réinventé le concept de travail en binôme, en Travaux de Laboratoire du NPAC, ou pour la rédaction du rapport de stage de détection terminée easy en une semaine de fonctionnaire, je le dois à sa mère en sumo, que je remercie donc grossement. Je remercie aussi Michaël Macaire, partenaire de semi-marathons, de triathlons et autres défis sportifs fous. Je ne sais d'ailleurs toujours pas comment nous avons réussi à engrener Fabien dans tout ça ! Quoiqu'il en soit, un grand merci à Fabien et Michaël pour ces très bons moments, qui m'ont permis de régulièrement me changer les idées au cours de la thèse. D'ailleurs les mecs, je me permets de vous faire remarquer, au cas où vous n'auriez pas vu, que les notes d'onde sont disponibles.

Je remercie également Nayanka Bolnet pour avoir eu la force de nous supporter et pour ses super-pouvoirs de ROOTGirl. Je lui souhaite bon courage pour la fin de sa thèse. Je veux qu'elle

sache que j'ai hâte d'assister à sa soutenance et de me goinfrer à son pot de thèse ! Je n'oublie bien entendu pas Corinne Louchart-Henning, qui finit la thèse de Corinne Louchart, ainsi que Léa Gauthier. Je vous souhaite à toutes les trois le meilleur pour la suite.

Je remercie les membres du Patrick Celtick Big Band Orchestra & Friends featuring Rothie pour les très bons moments que nous avons passés ensemble, pour m'avoir offert l'unique exemplaire de votre album d'anthologie et pour m'avoir laissé gagner quelques matchs de Konami Küp, parce que de toute façon le Grønk il marque pas et que je méritais de marquer. Je remercie aussi Nicolas Harvey pour ces quelques années partagées entre la physique et la chimie à l'Université de Cergy-Pontoise, à manger des Big Kahuna Burgers, aller au cinéma pendant les amphis de chimie et jouer à Mario Tennis. Je pense bien évidemment à quelqu'un à qui je tiens beaucoup, Rabia Mazmouz, sans qui ma scolarité n'aurait clairement pas été la même. J'en profite aussi pour la féliciter pour sa thèse ! Je pense à Florent Vidalenche, avec qui j'ai failli mourir une nuit de février dans la forêt de Rambouillet, et qui a accepté de venir me supporter le jour de ma soutenance, bien que ses derniers souvenirs de physique remontent à l'époque où il incarnait Gordon Freeman dans le centre de recherche de Black Mesa.

Je remercie bien évidemment Sylvain So, mon mari Facebook et ex-colocataire rue Barrault. Ce lieu a vu la remise au goût du jour de l'art ancestral du Krav-ball, ce qui n'est pas rien. J'ai bien évidemment une pensée particulière pour le Master. Sylvain, je te remercie vraiment pour tout, pour les cafés à 3 heures du matin lors de mes interminables révisions, pour ces heures de CS et de perfectionnement du Kopo, pour ces nombreux schémas que tu me faisais à toute heure n'oubliant jamais d'y ajouter ta touche personnelle (...), et pour ce régime alimentaire si particulier que nous avons suivi pendant trop longtemps, basé sur les pâtes au pistou et le saucisson. Sache que je suis sincèrement désolé que tu n'aies jamais eu l'occasion de finir ta thèse en ENS sur la probabilité que les étoiles tombent sur la Lune. Aussi, je ne peux bien entendu pas remercier Sylvain sans avoir une pensée pour l'ensemble de la Triade.

Doy las gracias igualmente a Chago, Manoli y Dani, y a toda la familia, por recibirme siempre con la más grande amabilidad, ¡y mostrarme las habitudes de estos españoles tan raros! Es siempre un verdadero placer venir a veros a vuestro bello pais. Os prometo que la próxima vez que me veáis, ¡notareis la diferencia en mi español!

Je souhaite terminer ces remerciements en exprimant, dans un premier temps, ma plus grande gratitude envers ma famille, et en particulier envers mes parents et ma sœur Cécile, qui ont toujours été là pour moi. Bien qu'il leur était impossible de me relire ou de m'aider au jour le jour dans mon travail, leur soutien indéfectible a été des plus importants. Ils m'ont donné les moyens de choisir ce que je voulais faire de ma vie et m'ont toujours soutenu. Ils supportent depuis des années mes "cours" quasi-quotidien de physique et s'intéressent réellement à ce que je fais. J'ai une pensée particulière pour ma sœur dont je suis très fier, pour ce qu'elle est et pour la voie professionnelle qu'elle a choisie, qui ne pouvait être plus éloignée de la mienne ! Notre relation de frère et sœur, si forte, et notre famille soudée ont été indéniablement l'un des moteurs qui m'ont poussé à entreprendre et finir cette thèse. Je tiens donc à les remercier grandement pour tout ça. Et si je devais avoir un dernier mot, en particulier pour ma mère et ma sœur, j'aimerais leur dire "téléphone recette" (et oui, là, j'ai marqué un point !).

Finalement, je termine ces lignes en remerciant Alexandra Martín Sánchez, aussi connue sous le nom de Sandrita, que je n'ai plus quittée depuis cette belle soirée au bord du lac de Zeuthen. Je pourrais écrire des pages et ne jamais pleinement exprimer ce que je ressens pour toi, à quel point je souhaite te remercier de tout mon cœur pour ces quatre années géniales passées à tes côtés, pour ces attentions et petits riens de tous les jours. Tu as été mon meilleur soutien et je sais à quel point tu as pris énormément sur toi à la fin de ma thèse. Tu as toujours trouvé les mots pour me réconforter ou me remotiver lorsque j'en avais besoin, tu t'es occupée de moi et je te promets de tout faire pour te rendre la pareille. Merci ma belle.

# Contents

# Introduction

*Liebe Radioaktive Damen und Herren,*
*ich bin auf einen verzweifelten Ausweg verfallen um den Energiesatz zu retten* [1].

Wolfgang Pauli,
Austrian physicist, Physics Nobel Prize in 1945.

From 1930 and the first postulate of a light neutral particle that would solve a missing energy issue more than thirty years old, to the end of the twentieth century with the definitive proof of flavor mixing and oscillation, via the first detection of this mysterious particle in 1956, the history of the neutrino has been a marvelous journey. The discoveries of its astonishing properties are however still underway. Many deficits from expectations have allowed to understand and formalize one of these properties, the neutrino oscillations, as a result of a quantum fact: neutrino interaction eigenstates are different than neutrino propagation eigenstates. The experimental evidences are now explained by a flavor mixing parametrized by three angles, one phase, and two differences of masses squarred.

Although the neutrino may be the most abundant known particle in the Universe, it is certainly the less understood one and many of its fundamental properties are yet to be measured. Indeed, the neutrino mass eigenstates spectrum is not known, and neither are the neutrinos absolute masses. The nature itself of this particle is still a mystery. This sector could also imply a CP symmetry violation, which is of a great importance in many baryogenesis models at the Big Bang. Moreover, some experimental results obtained from accelerators, nuclear reactors, and radioactive sources cannot be explained by the current picture of neutrino oscillation.

Until really recently, one of the unknowns of this sector was $\theta_{13}$, a mixing angle found from previous experiments to be way tinier than the other two. Non-zero, it was just waiting to be discovered. The Double Chooz experiment has been conceived for such a measurement.

The first chapter of this thesis exposes the theoritical bases behind the flavor oscillation, after a quick historical introduction. It explains how such a phenomenon can be considered as beyond the minimal Standard Model of particle physics, since it involves non-zero neutrino masses. The second chapter completes the general introduction by presenting the current experimental status on neutrino masses and flavor oscillation parameters. The present values of these parameters are given, along with explanations on the different kinds of experiments which measured them. The special case of $\theta_{13}$ is particularly highlighted.

In a third chapter, the Double Chooz experiment, built for the measurement of the leptonic parameter $\theta_{13}$, is presented. Once the site of this reactor electron antineutrino experiment is

[1] "Dear radioactive Ladies and Gentlemen, I have hit upon a desperate remedy to save the law of conservation of energy.", from the now famous "Liebe Radioaktive Damen und Herren" letter. A translation from German of the complete letter can be found in [155].

introduced, the source itself is detailed. The $\theta_{13}$ determination concept and the detection method are also both presented, along with the expected signal and backgrounds in the Double Chooz detectors. A careful description of the detector and its peculiar design completes this chapter.

Both the fourth and the fifth chapters introduce the Chapter 6, which is centered on data analysis. Since analysis requires data files of reconstructed physical quantities on which calibration constants have been applied, the Chapter 4 presents the Double Chooz event reconstruction performed within the collaborative software and the calibration of the detector. A calibrated detector is fundamental and this is why I have been involved in the channel time offsets measurement. Moreover, since I was part of the reconstruction software team and was involved in the data files production and monitoring, and since I cocreated a data reducer software that allows fast and efficient analysis, and was responsible for these light trees production and sanity checks, a section dedicated to the data files concludes this chapter.

The Chapter 5 concerns the Monte Carlo simulation generation and tuning. Indeed, with only one detector, the $\theta_{13}$ determination is done by comparing the detector data to high quality non-oscillated simulated data. CocoReco, an energy and vertex reconstruction package, that I cocreated, maintained, and improved, is also presented in this chapter since it has been developed from Monte Carlo simulations studies. The energy reconstruction is indeed fundamental for an experiment as Double Chooz, given the fact that the electron antineutrino events are basically selected as energy depositions.

The next chapter deals with the neutrino selection and the background studies. All the cuts and the selection methods are presented, along with the unexpected background called light-noise that Double Chooz has to cope with. I have been strongly involved in the neutrino candidates selection and its cuts optimization, along with the accidental and correlated cosmogenics backgrounds studies. The related sections are therefore detailed. The next-to-last section of the Chapter 6 presents a cut that I proposed which is now used in the official Double Chooz analysis. Called lithium-free, it allows to reduce the $^9$Li cosmogenic background contamination in the electron antineutrino candidates selection by applying a veto after the high energy depositions. Finally, this chapter ends with the analysis of the data taken when both Chooz reactors were shut down, allowing a study of the total background of the experiment. A background subtraction method that I developed for one day of both reactors OFF data is also presented.

Finally, the Chapter 7 presents the oscillation fit performed for the $\theta_{13}$ determination. The method of comparing data to simulated non-oscillated data, which necessitate a precise flux prediction, is exposed, along with the Bugey 4 anchor point method applied to drastically lower the systematics. After a reminder of the uncertainties involved, the fitting procedure is defined. Based on a $\chi^2$ approach, it uses covariance matrices or pull terms. The final fit results are then presented, with a rate only analysis and a rate and shape analysis. Diagnostic plots obtained from a fitting software developed at Saclay and discussions of these results conclude this chapter.

# Chapter 1

# Neutrinos within and beyond the Standard Model

*Who knows how things are invented?*
*Isaac Newton invented gravity because some [guy] hit him with an apple!* [1]

Christopher Moltisanti,
Capo in the Soprano family, Newark, NJ.

The Standard Model of particle physics gives a coherent framework to account for the elementary particles composing matter and their interactions. Both descriptive and predictive, this theory is a magnificent scientific construction based on theoretical considerations, all verified by experimental results, from the proof of the existence of the neutral weak currents in the early seventies to the discovery of the tau neutrino at the beginning of the twenty-first century. In order to account for the mass of the particles in the theory, the Higgs mechanism extends the Standard Model. After a brief review of the neutrino history, the second section of this chapter consists of a brief presentation of the fermion masses in the Standard Model, while the last part highlights the neutrino properties, especially its mixing and thus flavor oscillation. These latter specificities are due to a neutrino non-zero mass, even if the absence of right-handed neutrinos and left-handed antineutrinos in the Standard Model makes the Higgs mechanism inapplicable to this sector. Mechanisms developed to give the neutrino a mass, linked to its nature, are then presented. Finally, the standard neutrino oscillation probability is derived, as well as the special case of the two flavors oscillation in vacuum.

## 1.1 A little bit of history

The neutrino history begins with a textbook example of a serendipity. In 1896, while he is studying the phosphorescence of uranium salt, H. Becquerel discovers an unknown and penetrating radiation coming from it, without any external excitation, called radioactivity [41]. There followed a period of intense research and, for several years, the discoveries in this new field followed one another, improving the understanding of the three $\alpha$, $\beta$, and $\gamma$ radiations. The key-discovery though, regarding the neutrino, comes from J. Chadwick. Since at that time the

[1] From the HBO "The Sopranos" television series created by David Chase. Season 6, episode 14.

electron is expected to be the only particle emitted during a $\beta$ decay, understood as a simple two body decay, its energy should therefore be fixed. The English physicist shows in 1914 that the electron actually fills a continuous spectrum [51]. This $\beta$ radioactivity problem will rack many physicists's brain for more than two decades. Numerous hypotheses are then proposed, from the more pragmatic one to the more fanciful. Some of them venture the hypotheses that $\gamma$ rays or even several electrons are emitted, while others say that secondary diffusions inside the nucleus are transforming this initially discrete $\beta$ decay spectrum into a continuous spectrum. In 1924, N. Bohr himself even postulates that the energy might be conserved only statistically [44]!

At the end of the year 1930, W. Pauli proposes for the first time, in a famous open letter addressed to L. Meitner and H. Geiger [155], a revolutionnary solution to this issue. In order to save the energy conservation principle jeopardized by N. Bohr, the Austrian physicist develops what he calls himself *einen verzweifelten Ausweg*. This "desperate remedy" consists of postulating the existence of a 1/2 spin really light neutral particle, to which he gives the name "neutron". In 1932, J. Chadwick discovers a neutral particle, unfortunately way to heavy to satisfy Pauli's prescriptions. A year after, the hypothetical particle introduced by W. Pauli is incorporated within the theory developed by E. Fermi, that he baptizes *neutrino*, for "small neutral one" [86]. This theory of the radioactive decays is a great success in the sense that it explains many experimentally observed phenomena. This is truly the beginning of the Standard Model of particle physics.

One needs to wait 1956, that is to say twenty-six years after W. Pauli's letter, for the first electron antineutrinos to be detected by a team of physicists led by F. Reines and C. Cowan [59]. In order to do so, they placed a tank surrounded by photomultipliers, filled with a few tons of hydrogenous liquid scintillator doped with cadmium chloride, in the vicinity of the Savanah River nuclear reactor. The detection principle, although improved since then, is basically the same used in experiments such as KamLAND, Chooz, or Double Chooz: two events correlated in time signing the inverse $\beta$ decay interaction of an electron antineutrino on a proton.

In the meantime, T. D. Lee and C. N. Yang expose a fundamental particularity of the weak interaction, known to be responsible for the $\beta$ decay of radioactive nuclei [132]. Indeed, the two American physicists come to the conclusion that the weak interaction violates the discrete symmetry called parity. The next year, this property is experimentally verified by C. S. Wu [192]. Her conclusion is uniquevocal: the particle emitted but not detected during a $\beta$ decay, the antineutrino, only exists in a state of right helicity, while its antiparticle only has a left helicity. From the current scheme of giving masses to the Standard Model particles, via the Higgs mechanism, the neutrinos are then massless. The discovery of parity violation was a major contribution to high energy physics and the development of the Standard Model.

In 1963, the particle content expands with the discovery at Brookhaven of a second neutrino, the muon neutrino, from pions decays [64]. In 1991, Z gauge boson studies at LEP allows an important fact to be stated: there are only three families of light neutrinos as measured in the Breit-Wigner Z boson width, from the visible lepton and quark decay channels [181]. Nine years later, the third neutrino, produced along with a tau lepton, is indeed measured by the DONUT experiment [126].

In parallel, the mechanism of energy creation within the Sun is being studied and many theoretical processes imply neutrino creation [38]. The efforts to detect electron neutrinos coming from the Sun begin with the Homestake mine experiment, lead by R. Davis Jr. and J. N. Bahcall [65]. It is the first experiment to detect, in the late sixties, a deficit of electron flavored neutrinos with respect to most of the theoretical models. Dedicated experiments like Gallex/GNO,

SuperKamiokande, and SNO then follow: they all show the same deficit [24, 91, 108]. This means either that the energy production processes within the Sun are not quite understood and the theory needs to be modified, or that an unexpected neutrino property plays a role. Indeed, it will later be explained by flavor oscillations of massive neutrinos.

Meanwhile, another problem is highlighted by atmospheric neutrino experiments. In the 1980's, Kamiokande and IMB both study the neutrinos coming from interactions of primary cosmic rays with the upper layers of the atmosphere [40, 92]. The number of upward and downward neutrinos are found different from expectations. In 1998, the Superkamiokande experiment gives the proof of the flavor atmospheric neutrino oscillation [93]. Four years later, R. David (Homestake) and M. Koshiba (Kamiokande) receive the Physics Nobel Prize for their contributions in the discovery of the neutrino oscillation. The same year, the SNO experiment measures all the flavors of solar neutrinos and confirms the mixing. Indeed, the total flux, composed of all flavors, is found to be consistent with solar models. This property is finally independently confirmed by beam experiments, like K2K [28], and by the KamLAND experiment, which shows that the neutrinos from nuclear reactors oscillate as well [7].

The picture of flavor neutrino oscillations was incomplete until really recently. This phenomenon is first theoretically introduced by B. Pontecorvo in 1957 [156, 157], in analogy with the $K^0-\overline{K}^0$ mesons oscillations, but it is fully developed by Z. Maki, M. Nakagawa, and S. Sakata in 1962 [135]. The three Japanese physicists theory is later confirmed by many experiments using different neutrino sources.

The oscillations are now understood as the result of three massive neutrinos, whose propagation eigenstates are different than their interaction eigenstates. To go from one base to the other, the $U_{PMNS}$ matrix (named after Pontecorvo, Maki, Nakagawa, and Sakata) is used, parametrized with three angles $\theta_{ij}$ and a CP-violating phase $\delta_{CP}$. Three massive neutrinos imply two independent differences of squarred masses, $\Delta m^2_{sol}$ and $\Delta m^2_{atm}$. This picture is composed of two distincts oscillation regimes. The $\Delta m^2_{sol}$ parameter is actually $\Delta m^2_{21}$ and is measured along with $\theta_{12}$ in solar experiments and KamLAND. Concerning $\Delta m^2_{atm}$, it basically corresponds to $\Delta m^2_{32}$ or $\Delta m^2_{31}$ and is measured by atmospheric neutrino detectors and the K2K-like experiments, along with the mixing parameter $\theta_{23}$.

The last mixing parameter $\theta_{13}$ is really small with respect to the two others. The CHOOZ and the Palo Verde experiments gave for a long time the best constrain on it, from reactor electron antineutrino flux measurements, a kilometer away from the nuclear cores [30, 43]. Measuring $\theta_{13}$ with great precision is important as it is the condition for the study of the CP violation in the neutrino sector. The violation of this symmetry plays a key role in many leptogenesis models [94]. The $\theta_{13}$ parameter is therefore linked to very profound questions about the Universe, with significant phenomenological consequences. Measuring this parameter is the goal of the Double Chooz experiment. This will be developed from Chapter 3.

Since the neutrinos interact really weakly, although they may be the most abundant known particle in the Universe, most of their basic properties are still unknown. This is especially the case of their absolute masses and the mass hierarchy. The nature itself of the neutrinos is also still unknown: it could be a Dirac particle, like any other fermions, or a Majorana particle, making then neutrinos really different from all the other Standard Model components. Furthermore, several problems, called "anomalies", need to be added to this picture. The LSND and the MiniBooNE experiments, the reactor antineutrinos experiments located at short distances from the core, and the source calibration of the gallium experiments all seem to indicate that the current picture of neutrinos and their oscillations is far from being completed.

## 1.2 Fermions masses in the Standard Model framework

### 1.2.1 Standard Model of particle physics

The Standard Model of particle physics (SM) is a quantum field theory which unifies both the quantum mechanics and the special relativity, and is derived from the Fermi theory [86] and the Glashow-Weinberg-Salam model [101, 164, 186]. The SM describes in a consistent framework the elementary particles constituting matter, called fermions, as well as three of their known interactions, corresponding each time to the exchange of a mediator particle: the strong with the gluons, the weak with the gauge bosons $W^{\pm}$ and $Z^0$, and the electromagnetic with the photon; despite huge work on conciliating them with gravitation, the latter is being considered, for now, in a separated theory called general relativity. Among the 36 particles forming the Standard Model, 24 are fermions, divided in three quark and three lepton families, and 12 are bosons. The SM is made of two distincts sectors: the gauge sector and the Higgs one. The Higgs mechanism, which in a way extends the minimal Standard Model, is presented in the next section. The gauge sector represents the interactions of the quarks and leptons with the gauge bosons.

The particles of the SM are divided in two main categories, whether they follow the Fermi-Dirac statistics or the Bose-Einstein one. Matter is composed of fermions, that own a 1/2 spin, and therefore obey the Fermi-Dirac statistics and follow the Pauli exclusion principle [56]. They are of two types: six quarks and six leptons, plus their antiparticles. The quarks are sensitive to all the interactions and form the hadrons and mesons. The leptons on the other hand do not have a strong charge, *i.e* a color. The three electromagnetic charged leptons (the electron, the muon, and the tau) will then be sensitive to the electroweak interaction while their partners, the neutrinos, will only interact via weak interaction. In this theory the forces are mediated by a boson, of integer spin. The weak interaction is the force associated to the radioactivity, while the strong one ensures the cohesion of the nucleus via the gluons.

Based on a local symmetry group that corresponds to the direct product of three subgroups, $SU(3)_C \otimes SU(2)_L \otimes U(1)_Y$, the Standard Model is a gauge theory [186]. $SU(3)_C$ is the color group of quantum chromodynamics (QCD), $SU(2)_L$ the weak isospin group, and $U(1)_Y$ the hypercharge one. The fermions are different representations of the SM group, while its generators induce the bosons. There are eight massless gluons, corresponding to the eight generators of $SU(3)_C$, and four gauge bosons, of which three are massive ($W^{\pm}$ and $Z^0$) and one is massless (the photon $\gamma$), corresponding to the three generators of $SU(2)_L$ and the one of $U(1)_Y$. As the electromagnetic and the weak interactions are unified, the $W^{\pm}$, the $Z^0$, and the $\gamma$ are actually mixtures of the gauge boson fields of the electroweak sector, $W^{\mu} = (W_1^{\mu}, W_2^{\mu}, W_3^{\mu}, B^{\mu})$. $W_i^{\mu}$ are the three bosons of weak isospin SU(2) and $B^{\mu}$ the boson of the weak hypercharge from U(1). They are all massless. The $W^{\pm}$ and $Z^0$ bosons, and the photon, are produced by the spontaneous symmetry breaking of the electroweak symmetry, caused by the Higgs mechanism (*cf.* Section 1.2.2). During this process, the $W^{\pm}$ and $Z^0$ bosons acquire their important masses, which explain the short range of the weak interaction.

In the electroweak $SU(2)_L \otimes U(1)_Y$ sector, the elementary particles are arranged as doublets for left-handed fields and singlets for right-handed ones, in order to take into account the V-A structure of the electroweak interactions, according to the Fermi theory in which the right-handed components do not interact with gauge bosons (Table 1.1) [87].

The Lagrangian of the electroweak part of the Standard Model $\mathcal{L}_{EW}$ is basically the sum of two contributions. One contains the kinetic terms and self-couplings of the four gauge bosons and one expresses the interactions between the fermions and these gauge bosons, done through the covariant derivative. $\mathcal{L}_{EW}$ is then written as follows:

| | 1st family | 2nd family | 3rd family |
|---|---|---|---|
| Quarks | $\begin{pmatrix} u \\ d' \end{pmatrix}_L$ | $\begin{pmatrix} c \\ s' \end{pmatrix}_L$ | $\begin{pmatrix} t \\ b' \end{pmatrix}_L$ |
| | $u_R$, $d_R$ | $c_R$, $s_R$ | $t_R$, $b_R$ |
| Leptons | $\begin{pmatrix} e \\ \nu_e \end{pmatrix}_L$ | $\begin{pmatrix} \mu \\ \nu_\mu \end{pmatrix}_L$ | $\begin{pmatrix} \tau \\ \nu_\tau \end{pmatrix}_L$ |
| | $e_R$ | $\mu_R$ | $\tau_R$ |

Table 1.1: *Summary of the elementary particles of the Standard Model composing matter, called fermions. They are divided in three families and in two types, quarks and leptons. The left-handed doublets and the right-handed singlets are a consequence of the V-A structure of the electroweak sector [87]. There are no right-handed neutrinos in the SM. The $d'$, $s'$, and $b'$ quarks are interaction eigenstates, mixtures of the mass eigenstates (from flavor-changing weak decays, expressed in the CKM matrix [125]).*

$$\mathcal{L}_{\mathrm{EW}} = -\frac{1}{4}F^a_{\mu\nu}F^{\mu\nu}_a - \frac{1}{4}G_{\mu\nu}G^{\mu\nu} + i\overline{\ell}^a_L\gamma_\mu D^\mu \ell_{aL} + i\overline{q}^a_L\gamma_\mu D^\mu q_{aL} + i\sum_{f=e,u,d}\overline{f}^a_R\gamma_\mu D^\mu f_{aR}, \tag{1.1}$$

where the sum is performed over $a$, the three families (Table 1.1). The $f_R$ fields represent the right components of the charged leptons (electron, muon, and tau), whereas the doublets $\ell_L$ and $q_L$, representations of $\mathrm{SU(2)_L}\times\mathrm{U(1)_Y}$, are respectively the left-handed lepton and the left-handed quark fields arranged as:

$$\begin{pmatrix} \nu_{eL} \\ e_L \end{pmatrix}, \quad \begin{pmatrix} u_L \\ d_L \end{pmatrix}, \tag{1.2}$$

The gauge field tensors $F^{\mu\nu}$ and $G^{\mu\nu}$ are defined as:

$$F^{\mu\nu}_a = \partial^\mu W^\nu_a - \partial^\nu W^\mu_a + g\epsilon_{abc}W^\mu_b W^\nu_c \quad \text{and} \quad G^{\mu\nu} = \partial^\mu B^\nu - \partial^\nu B^\mu, \tag{1.3}$$

where $W^\mu$ and $B^\mu$ are the generators of the electroweak sector and $\epsilon_{abc}$ is the structure constant of the gauge group.

The covariant derivative, which replaces the standard derivative in a gauge theory, is defined as:

$$D^\mu = \partial^\mu - ig\mathrm{T}_\nu W^{\mu\nu} - ig'\frac{\mathrm{Y}}{2}B^\mu, \tag{1.4}$$

with $g$ and $g'$ the gauge coupling constants of $\mathrm{SU(2)_L}$ and $\mathrm{U(1)_Y}$, respectively. T and $\frac{\mathrm{Y}}{2}$ are the representations of the $\mathrm{SU(2)_L}$ and $\mathrm{U(1)_Y}$ groups, and $\gamma_\mu$ are the Dirac matrices.

The Lagrangian of the Standard Model of particles physics depends on 17 parameters that are not constrained by the theory. Indeed, no fundamental principle allows to determine them. They need to be measured via experimental observations. The boson sector is responsible for four of them: the three independent coupling constants of SU(3), SU(2), and U(1), and the vacuum angle of QCD for chiral symmetry breaking. The fermion sector implies thirteen independent

parameters, among which six are the quark masses, three the charged lepton masses, and four the quark mixing parameters (three angles and a CP violating phase) [125]. Two other parameters can be added for the Higgs sector: its quadratic coupling constant and its self-coupling strength; they will be presented in the next section.

In the electroweak Lagrangian $\mathcal{L}_{\mathrm{EW}}$, there is no mass term for fermion nor boson, with the form $\mathrm{m}\overline{\phi}\phi$, where $\phi$ is a field. This kind of terms would violate the required $\mathrm{SU(2)_L}$ gauge invariance. However, these massless fields in the theory are not in agreement with experimental evidences acquired over the years. This is why the Higgs mechanism, or any mechanism confering a mass to the Standard Model particles, is needed.

### 1.2.2 Higgs mechanism

The masses of the Standard Model fermions, as well as the $\mathrm{W}^{\pm}$ and $\mathrm{Z}^0$ ones, are generated through the spontaneous breaking of the $\mathrm{SU(2)_L} \otimes \mathrm{U(1)_Y}$ symmetry. A spontaneous symmetry breaking results in the fundamental state of a system that does not have the full symmetries corresponding to the underlying Lagrangian. The Nature therefore chooses between all the possible symmetric configurations: the breaking occurs at the solution level, but not for the equations themselves. The one explained hereafter is called the Higgs mechanism [81, 110]. The resulting Higgs field can be understood as an inertial force, which fills the vacuum and constrains the particles movements. The results is then an apparent mass.

The symmetry breaking is done by adding a new field to the theory, such as a complex doublet of SU(2) of scalar fields with spin 0 and hypercharge 1, called the Higgs doublet:

$$\Phi(x) = \begin{pmatrix} \Phi^+(x) \\ \Phi^0(x) \end{pmatrix}, \tag{1.5}$$

where $\Phi^+(x)$ and $\Phi^0(x)$ are a charged scalar field and a neutral field, respectively.

This new field implies to add a new term $\mathcal{L}_{\mathrm{Higgs}}$ to the electroweak Lagrangian presented in equation (1.1):

$$\mathcal{L}_{\mathrm{Higgs}} = (\mathrm{D}^{\mu}\Phi)^{\dagger}\,(\mathrm{D}_{\mu}\Phi) - \mathrm{V}(\Phi). \tag{1.6}$$

The most general form of the potential used for the symmetry breaking is:

$$\mathrm{V}(\Phi) = -\mu^2\Phi^{\dagger}\Phi + \lambda(\Phi^{\dagger}\Phi)^2, \tag{1.7}$$

where $\lambda$ is the Higgs self-coupling strength that has to be positive in order to have a potential bounded from below and $\mu$ the Higgs quadratic coupling, a parameter related to the Higgs boson mass $\mathrm{m_{Higgs}} = \sqrt{-2\mu^2}$, if $\mu^2 < 0$, necessary for the spontaneous symmetry breaking. In this case, the minimum potential corresponds to the vacuum expectation values of the field and is $v = \sqrt{-\mu^2/\lambda}$. This ground state is degenerated. The spontaneous symmetry breaking lies in the choice of a particular field configuration, which is no longer invariant under $\mathrm{SU(2)_L}$ and $\mathrm{U(1)_Y}$ transformations, and is defined as:

$$\Phi_0 = \frac{1}{\sqrt{2}}\sqrt{-\mu^2/\lambda}. \tag{1.8}$$

Indeed, if the physical Higgs boson is represented by the $H(x)$ field, the Higgs doublet is now written as:

$$\Phi(x) = \frac{1}{\sqrt{2}} \begin{pmatrix} 0 \\ v + H(x) \end{pmatrix}. \tag{1.9}$$

The masses of the fermions come from a Yukawa coupling between the fermions fields and the vacuum expectation value of the Higgs doublet. The Higgs-fermion Yukawa Lagrangian is written as follows:

$$\mathcal{L}_{\text{Higgs}-\text{fermion}} = -\sum_{\alpha} \frac{y_{\alpha}^{\ell} v}{\sqrt{2}} \overline{\ell}_{\alpha} \ell_{\alpha} - \sum_{\alpha} \frac{y_{\alpha}^{\ell}}{\sqrt{2}} \overline{\ell}_{\alpha} \ell_{\alpha} H, \tag{1.10}$$

where the sum is performed over $\alpha$, the three charged leptons $e$, $\mu$, and $\tau$. The $v$ parameter is the Higgs vacuum expectation value, $H$ is the Higgs boson field, the $\ell_{\alpha}$ are the charged leptons with $\ell_{\alpha} = \ell_{\alpha L} + \ell_{\alpha R}$ , and the $y_{\alpha}^{\ell}$ are elements of the charged leptons Yukawa coupling matrices. The second term corresponds to the lepton coupling to the Higgs boson while the first one is a mass term with $\mathrm{m}_{\alpha} = y_{\alpha}^{\ell} v/\sqrt{2}$.

As predictive and descriptive the Standard Model is, two points have to be made. The first thing is that the Higgs boson has not yet been discovered, altough recent results from LHC experiments seem to show an excess of events around 126 GeV for several channels [35, 36, 55]. More precisely, the two experiments presented the discovery of a new particle in most of the standard Higgs boson expected decay channels. It is very probable that this new particle is indeed the Higgs boson, or one of its more exotic versions (from SuperSymmetry models for instance [148]).

The second point is that the neutrinos remain massless with this current scheme of giving mass to the fermions because of the absence of right-handed $\nu_R$ states. The discovery of neutrino flavor oscillations is an indirect evidence for massive neutrinos (*cf.* Section 1.4). It forces us to find another way to generate their masses, such as using a Higgs triplet or adding right-handed neutrino singlets in the theory, which have not been observed yet. In that sense, the evidence of neutrino flavor oscillations [2] and especially the non-zero neutrino masses are a clear hint of physics beyond the Standard Model.

## 1.3 Neutrinos masses: beyond the Standard Model

### 1.3.1 Dirac mass term

Neutrino masses can be generated by the Higgs mechanism via Yukawa couplings. The Lagrangian of equation (1.10) can therefore be modified to account for neutrino to Higgs couplings. Analogous couplings and mass terms to the Standard Model quarks and charged leptons are introduced:

$$\mathcal{L}_{\text{Higgs}-\text{neutrino}} = -\sum_{\mathrm{k}} \frac{y_{\mathrm{k}}^{\nu} v}{\sqrt{2}} \overline{\nu_{\mathrm{k}}} \nu_{\mathrm{k}} - \sum_{\mathrm{k}} \frac{y_{\mathrm{k}}^{\nu}}{\sqrt{2}} \overline{\nu_{\mathrm{k}}} \nu_{\mathrm{k}} H, \tag{1.11}$$

[2] Neutrino masses have to be accounted for, as the multiple deficits observed while studying these particles is nowadays explained by flavor oscillations arising from a non-correspondance of the neutrino propagation eigenstates and the interaction eigenstates.

where $k = 1, 2, 3$. The $\nu_k$ are neutrinos with $\nu_k = \nu_{kL} + \nu_{kR}$ and the $y_k^\nu$ are elements of the neutrinos Yukawa coupling matrices. The first term is a mass term with $m_k = y_k^\nu v/\sqrt{2}$. The $\nu_k$ are fields of well defined masses $m_k$ and are therefore physical particles.

Dirac neutrino mass terms are really similar to charged leptons ones, since the same Higgs mechanism is used. The only extension to the Standard Model is the addition of a right-handed neutrino. Indeed, as explained in Section 1.2.1, the neutrinos are only represented as left-handed fields in doublets with their respective charged leptons, while all the other fermions exist as right and left chiral projections. With the addition of a right-handed component to the theory, the asymmetry between leptons and quarks is eliminated. The $\nu_L$ and $\nu_R$ fields are independent and can pair through the Higgs mechanism. The resulting mass Lagrangian can be formulated as:

$$\mathcal{L}^D_{\text{mass}} = -m_\nu^D \left(\overline{\nu_R}\nu_L + \overline{\nu_L}\nu_R\right). \tag{1.12}$$

However, an issue arises when the neutrinos are considered as Dirac particles: new free paramaters of the Standard Model, their Yukawa couplings, have to be chosen accordingly to the observations and need therefore to be several orders of magnitude smaller than the charged leptons Yukawa couplings to explain the smallness of the neutrinos masses.

These three new neutrino fields, called right-handed Dirac neutrino fields, correspond each of them to a right-handed charged lepton $\ell_R$. They are assumed to be singlets of $SU(3)_C \otimes SU(2)_L$, with null hypercharge. They do not participate to any SM interaction presented before and are thus called sterile. Fundamentally different from the other Standard Model particles, they would only interact via gravitation because of their mass. The presence of these new fields do not explain the light masses of the neutrinos with respect to the other fermions.

### 1.3.2 Majorana mass term

In the previous section, the Dirac nature of the neutrinos is postulated. This implies that they are like any other Standard Model particles, with their left-handed and right-handed chiral projection, $\nu_L$ and $\nu_R$, considered independent. However, the neutrinos are quite different from the other Standard Model particles: they do not carry any electric charge. This leads to the theoretical possibility that neutrinos are actually Majorana particles.

Usually it is simply stated that a Majorana particle is identical to its antiparticle. More precisely, this means that neutrinos and antineutrinos would be the opposite chiral states of the same particle, which are CPT conjugates of each other. Therefore, mass terms can be built using the left-handed and the right-handed fields along with their conjugates. This is strictly impossible for other Standard Model particles, since this kind of process would violate the electric charge conservation. In that sense, Majorana masses would make the neutrinos very distinctive with respect to all the other fermions.

The Majorana mass terms mix the neutrinos and the antineutrinos. Therefore, these terms cannot come from Higgs couplings. Neutrino Majorana masses must have a different origin than the masses of quarks and charged leptons. The resulting mass Lagrangian, which can be compared to the Dirac mass Lagrangian presented in equation (1.12), is:

$$\mathcal{L}^M_{\text{mass}} = -\frac{1}{2} m_\nu^M \left(\overline{\nu_L^C}\nu_L + \overline{\nu_L}\nu_L^C\right), \tag{1.13}$$

where $\nu_L^C$ is the charge conjugate of the left-handed neutrino, therefore the right-handed field. The 1/2 factor is explained by the new neutrino-antineutrino symmetry which implies to divide all the degrees of freedom by 2.

One of the most promising way of determining whether neutrinos are Majorana particles, is to seek for neutrinoless double $\beta$ decays (*cf.* Section 2.1.4). Whatever diagram causes such a process, whatever the parent nuclei, its observation would imply the existence of a Majorana mass term. Indeed, the process leads to the violation by two units of the global lepton number L [3], while the Standard Model weak interactions conserve this quantity. In the absence of other non-SM L-violating interactions, $\Delta \mathrm{L} = 2$ of a neutrinoless double $\beta$ decay can only come from Majorana neutrino masses. The violation of the global leptonic number in case of Majorana neutrino masses is however weak, as the neutrino masses are actually really small.

Finally, from a standard weak interaction point of view, the Dirac and the Majorana descriptions are equivalent since only the left-handed neutrino field and the right-handed antineutrino contribute anyway. The oscillation experiments, whose principles will be presented in Section 1.4, despite the fact that they are sensitive to neutrino masses, cannot distringuish between these two possible descriptions.

### 1.3.3 See-saw mechanism

The previous sections propose two ways of creating neutrino mass terms. The first description needs an extension of the Standard Model with a right-handed neutrino to allow neutrino-Higgs Yukawa couplings, whereas the second one needs neutrino to be Majorana particles. If the neutrino is only left-handed, it would be a pure Majorana particle. However, if a right-handed component does exist, a Dirac mass term can be considered, making then the neutrino a Dirac particle, but the right Majorana mass term can also be added. Therefore, it is possible to write a general mass Lagrangian by mixing the two descriptions with a mass matrix:

$$\mathcal{L}_{\mathrm{mass}}^{D+M} = -\frac{1}{2}\left(\overline{\nu_L^C}\ ,\ \overline{\nu_R}\right)\begin{pmatrix} M_L & \mathrm{m}_D \\ \mathrm{m}_D & M_R \end{pmatrix}\begin{pmatrix} \nu_L \\ \nu_R^C \end{pmatrix}, \tag{1.14}$$

where $\mathrm{m}_D$ is the Dirac neutrino mass, and $M_L$ and $M_R$ are the left and right-handed Majorana neutrino masses, respectively. The two fields, $\nu_L$ and $\nu_R$, are Majorana spinors [99].

The diagonalization of the mass matrix can be done with an orthogonal rotation matrix of parameter $\theta$. The corresponding mass eigenvalues are extracted for $\tan 2\theta = 2\mathrm{m}_D/(M_R - M_L)$:

$$\mathrm{m}_{1,2} = \frac{1}{2}\left(M_L + M_R \pm \sqrt{(M_L - M_R)^2 + 4\mathrm{m}_D^2}\right). \tag{1.15}$$

Different cases can therefore be considered as neither the absolute values nor the hierarchy of the masses are known. In the See-saw picture, the Majorana mass is much larger than the Dirac one, $M_R \gg \mathrm{m}_D$, and $M_L$ is 0. The right-handed sterile neutrino $\nu_R$ is therefore very heavy with respect to the Standard Model neutrinos. The See-saw mechanism provides then:

$$\mathrm{m}_1 \simeq M_R \quad \text{and} \quad \mathrm{m}_2 \simeq \frac{\mathrm{m}_D}{M_R}. \tag{1.16}$$

[3] The global lepton number is defined as: $\mathrm{L}_\nu = \mathrm{L}_\ell = -\mathrm{L}_{\overline{\nu}} = -\mathrm{L}_{\overline{\ell}}$. This is the quantum number that distinguishes leptons from antileptons.

The $m_1$ mass corresponds to a neutrino as heavy as $M_R$, whereas $m_2$ corresponds to a light neutrino, which explains the name of this mechanism ("See-saw"). The heavy neutrino can therefore be described as a sterile neutrino $\nu_R$ and the light one as an active neutrino $\nu_L$. The See-saw mechanism allows to explain the smallness of the neutrino mass, while generating the Dirac mass $m_D$ according to the Higgs mechanism as for all the SM fermions. Concerning the heavy sterile neutrino, it could be connected to baryogenesis through leptogenesis processes. A large Majorana mass for right-handed neutrinos is the key ingredient of many baryogenesis-related theory. Indeed, in the early universe, the heavy right-handed neutrino could decay along with lepton number violation. If these decays were accompanied by a new source of CP violation in the leptonic sector (*cf.* Section 1.4.1), then it would have been possible to create a lepton-antilepton asymmetry at the moment the right-handed neutrinos decay. Since the Standard Model interactions preserve baryon and lepton numbers at all orders in the perturbation theory, but violate them at the quantum level, such lepton asymmetry could be converted by these purely quantum effects into a baryon-antibaryon asymmetry [94].

## 1.4 Neutrinos mixing and oscillations

### 1.4.1 Neutrino mixing

As explained in Section 1.1, experiments using different neutrino sources have brought over the last decade compelling evidences of the existence of neutrino flavor oscillations driven by non-zero neutrino masses. A flavor change requires leptonic mixing, and a neutrino of a definite flavor ($\nu_e$, $\nu_\mu$, or $\nu_\tau$) must be therefore a superposition of the mass eigenstates (called $\nu_1$, $\nu_2$, and $\nu_3$), and vice versa. A given physical neutrino can then couple to more than one charged lepton via the charged current.

The neutrino oscillation is a quantum mechanical phenomenon that is first proposed by B. Pontecorvo in 1957, in analogy with the $K^0$–$\overline{K}^0$ mesons oscillations [156, 157]. This phenomenon is then fully developed by Z. Maki, M. Nakagawa, and S. Sakata in 1962 on the quark mixing model [135]. The oscillations are generated by the interferences of different massive neutrinos, which are produced and detected coherently because of their very small mass differences.

The non-correspondance between the flavor eigenstates and the mass eigenstates allows to represent a definite flavor state $\nu_\alpha$ as a linear combination of mass eigenstates $\nu_\mathrm{k}$. Since there are 3 orthogonal neutrinos of a definite flavor $\alpha$, there must be at least 3 mass eigenstates k (k = 1, 2, 3). The mixing matrix $\mathrm{U_{PMNS}}$ (from the names of Pontecorvo, Maki, Nakagawa, and Sakata; sometimes just called U) links the two kinds of eigenstates and allows to go from one base to the other:

$$\begin{pmatrix} \nu_e \\ \nu_\mu \\ \nu_\tau \end{pmatrix} = \mathrm{U_{PMNS}} \begin{pmatrix} \nu_1 \\ \nu_2 \\ \nu_3 \end{pmatrix} \quad \text{or} \quad |\nu_\alpha\rangle = \sum_\mathrm{k} \mathrm{U}^*_{\alpha\mathrm{k}} |\nu_\mathrm{k}\rangle \,. \tag{1.17}$$

This unitary $3 \times 3$ complex matrix is similar to $\mathrm{U_{CKM}}$ from the quark sector [125]. The $\mathrm{U}^*_{\alpha\mathrm{k}}$ represent the proportion of $\nu_\mathrm{k}$ in the flavor state $\nu_\alpha$. The mixing matrix $\mathrm{U_{PMNS}}$ describes the transitions between the neutrino flavors:

$$\mathrm{U_{PMNS}} = \begin{pmatrix} \mathrm{U}_{e1} & \mathrm{U}_{e2} & \mathrm{U}_{e3} \\ \mathrm{U}_{\mu 1} & \mathrm{U}_{\mu 2} & \mathrm{U}_{\mu 3} \\ \mathrm{U}_{\tau 1} & \mathrm{U}_{\tau 2} & \mathrm{U}_{\tau 3} \end{pmatrix}. \tag{1.18}$$

According to [99], $\mathrm{U_{PMNS}}$ can be parametrized with 3 mixing angles $\theta_{\mathrm{ij}}$ and one CP-violating phase $\delta_{\mathrm{CP}}$. A standard parametrization of this matrix consists in factorizing it as independent matrices, each of them corresponding to one mixing parameter $\theta_{\mathrm{ij}}$: one "atmospheric" contribution, one linked to $\theta_{13}$, and one "solar" (*cf.* Section 1.1). If simplified notations are used ($c_{\mathrm{ij}} = \cos\theta_{\mathrm{ij}}$ and $s_{\mathrm{ij}} = \sin\theta_{\mathrm{ij}}$) this matrix becomes:

$$\mathrm{U_{PMNS}} = \begin{pmatrix} 1 & 0 & 0 \\ 0 & c_{23} & s_{23} \\ 0 & -s_{23} & c_{23} \end{pmatrix} \begin{pmatrix} c_{13} & 0 & s_{13}\mathrm{e}^{-i\delta} \\ 0 & 1 & 0 \\ -s_{13}\mathrm{e}^{i\delta} & 0 & c_{13} \end{pmatrix} \begin{pmatrix} c_{12} & s_{12} & 0 \\ -s_{12} & c_{12} & 0 \\ 0 & 0 & 1 \end{pmatrix}, \tag{1.19}$$

where its general developed form is:

$$\mathrm{U_{PMNS}} = \begin{pmatrix} c_{12}c_{13} & s_{12}c_{13} & s_{13}\mathrm{e}^{-i\delta} \\ -s_{12}c_{23} - c_{12}s_{23}s_{13}\mathrm{e}^{i\delta} & c_{12}c_{23} - s_{12}s_{23}s_{13}\mathrm{e}^{i\delta} & s_{23}c_{13} \\ s_{12}s_{23} - c_{12}c_{23}s_{13}\mathrm{e}^{i\delta} & -c_{12}s_{23} - s_{12}c_{23}s_{13}\mathrm{e}^{i\delta} & c_{23}c_{13} \end{pmatrix}. \tag{1.20}$$

It is interesting to notice that if the neutrinos are Majorana particles (*cf.* Section 1.3.2), another contribution with two additional phases $\alpha$ and $\beta$ can be considered:

$$\mathrm{U_{PMNS}^{Majorana}} = \mathrm{U_{PMNS}} \times \mathrm{diag}\left(1, \mathrm{e}^{i\alpha}, \mathrm{e}^{i\beta}\right). \tag{1.21}$$

However, since the flavor oscillation experiments are not sensitive to these phases, they will not appear from now on in any of the following calculations.

The first row of the $\mathrm{U_{PMNS}}$ matrix corresponds to the linear combination of neutrino mass eigenstates which couple to an electron. Concerning the first column $\nu_1$, it is the linear combination of charged lepton mass eigenstates which couple to $\nu_1$.

Altough the developed form of the $\mathrm{U_{PMNS}}$ mixing matrix does not allow to see it easily, there is a direct relation between the mixing angles $\theta_{\mathrm{ij}}$ and the matrix elements:

$$\begin{aligned} \tan\theta_{12} &= |\mathrm{U_{e2}}/\mathrm{U_{e1}}|, \\ \tan\theta_{23} &= |\mathrm{U}_{\mu 3}/\mathrm{U}_{\tau 3}|, \\ \text{and} \quad \sin\theta_{13} &= |\mathrm{U_{e3}}|. \end{aligned} \tag{1.22}$$

The mixing parameter $\tan\theta_{12}$ corresponds therefore to the ratio between the $\nu_1$ and $\nu_2$ composition of the electron neutrino $\nu_e$. Moreover, $\tan\theta_{23}$ expresses the $\nu_\mu$ and $\nu_\tau$ composition of a $\nu_3$, whereas $\sin\theta_{13}$ represents the coupling between these two transition regimes [140].

### 1.4.2 Standard derivation of the neutrino oscillation probability

The theory of neutrino flavor oscillations has been developed for the first time in 1976. The following derivation of the standard neutrino oscillation probability is however more recent and based on [98].

As already presented in Section 1.4.1, the non-correspondance between the neutrino flavor and mass eigenstates allows to represent a definite flavor state $\nu_\alpha$ as a superposition of mass eigenstates $\nu_\mathrm{k}$, with k = 1, 2, 3:

$$|\nu_\alpha\rangle \;=\; \sum_\mathrm{k} \mathrm{U}^*_{\alpha\mathrm{k}} \,|\nu_\mathrm{k}\rangle \,. \tag{1.23}$$

Neutrinos can be considered as plane waves when propagating in vacuum. In quantum mechanics, the evolution of any state is determined by the Schrödinger equation:

$$i\frac{\mathrm{d}}{\mathrm{d}t}\,|\psi(t)\rangle \;=\; \hat{H}(t)\,|\psi(t)\rangle \,, \tag{1.24}$$

where $\hat{H}$ is a Hamiltonian operator which is in general time-dependent, and $|\psi(t)\rangle$ is an arbitrary state vector.

The time evolution of a neutrino $\nu_\mathrm{k}$, with $E_\mathrm{k}$ its energy eigenvalues and $p_\mathrm{k}$ its momentum eigenvalues is then:

$$|\nu_\mathrm{k}(x,t)\rangle \;=\; \mathrm{e}^{-i(E_\mathrm{k}t - p_\mathrm{k}x)}\,|\nu_\mathrm{k}\rangle \,. \tag{1.25}$$

We consider a neutrino created in the flavor state $\nu_\alpha$ at the time $t = 0$ and at the position $x = 0$. The evolution of this state is found by using both previous equations. After a time $t$ and therefore a travelled distance $x$, the leptonic flavor state of the neutrino is given by:

$$|\nu_\alpha(x,t)\rangle \;=\; \sum_\mathrm{k} \mathrm{U}^*_{\alpha\mathrm{k}} \mathrm{e}^{-i(E_\mathrm{k}t - p_\mathrm{k}x)}\,|\nu_\mathrm{k}\rangle \,. \tag{1.26}$$

By inverting equation (1.23), using the unitarity property of $\mathrm{U}_\mathrm{PMNS}$, the relation showing that after its production a neutrino is a linear superposition of the existing leptonic states is found to be:

$$|\nu_\alpha(x,t)\rangle \;=\; \sum_\beta \left( \sum_\mathrm{k} \mathrm{U}^*_{\alpha\mathrm{k}} \mathrm{e}^{-i(E_\mathrm{k}t - p_\mathrm{k}x)} \mathrm{U}_{\beta\mathrm{k}} \right) |\nu_\mathrm{k}\rangle \,, \tag{1.27}$$

where the $\beta$ are the three flavor states $e$, $\mu$, and $\tau$.

In quantum mechanics, the probability of a process is its squarred amplitude. Therefore, the probability to find neutrinos produced as a $\nu_\alpha$ in a flavor state $\nu_\beta$ after a time $t$ and a distance $x$ is the amplitude of the transition $\nu_\alpha$ to $\nu_\beta$ squarred:

$$\mathrm{P}_{\nu_\alpha \to \nu_\beta}(x,t) \;=\; |\langle \nu_\beta | \nu_\alpha(x,t)\rangle|^2 \;=\; \left| \sum_\mathrm{k} \mathrm{U}^*_{\alpha\mathrm{k}} \mathrm{e}^{-i(E_\mathrm{k}t - p_\mathrm{k}x)} \mathrm{U}_{\beta\mathrm{k}} \right|^2 . \tag{1.28}$$

Since the neutrinos propagate almost at the speed of light, they can be considered as ultrarelativistic particles and the approximation $x = t = L$, with $L$ is the distance travelled by

the neutrinos between their production and detection locations, can be done. The phase in equation (1.28) becomes therefore:

$$E_{\mathrm{k}}t - p_{\mathrm{k}}x \;=\; (E_{\mathrm{k}} - p_{\mathrm{k}})\,L \;=\; \frac{E_{\mathrm{k}}^2 - p_{\mathrm{k}}^2}{E_{\mathrm{k}} + p_{\mathrm{k}}}L \;=\; \frac{\mathrm{m}_{\mathrm{k}}^2}{E_{\mathrm{k}} + p_{\mathrm{k}}}L \;\simeq\; \frac{\mathrm{m}_{\mathrm{k}}^2}{2E}L, \tag{1.29}$$

where $E = p$ is the energy of the neutrino if $\mathrm{m} \ll E$.

Using the approximation of equation (1.29), the $\nu_\alpha \to \nu_\beta$ transition of equation (1.28) can be rewritten as:

$$\mathrm{P}_{\nu_\alpha \to \nu_\beta}(L, E) \;=\; \sum_{\mathrm{k,j}} \mathrm{U}_{\alpha\mathrm{k}}^* \mathrm{U}_{\beta\mathrm{k}} \mathrm{U}_{\alpha\mathrm{j}} \mathrm{U}_{\beta\mathrm{j}}^* \exp\left(-i\frac{\Delta\mathrm{m}_{\mathrm{kj}}^2 L}{2E}\right), \tag{1.30}$$

where $\Delta\mathrm{m}_{\mathrm{kj}}^2$ is the differences of squarred masses defined as $\mathrm{m}_{\mathrm{k}}^2 - \mathrm{m}_{\mathrm{j}}^2$.

The equation (1.30) is more conveniently written as a sum of the real and the imaginary parts of the oscillation probability $\mathrm{P}_{\nu_\alpha \to \nu_\beta}(L, E)$:

$$\begin{aligned} \mathrm{P}_{\nu_\alpha \to \nu_\beta}(L, E) \;=\; \delta_{\alpha\beta} \;&-\; 4\sum_{\mathrm{k>j}} \Re\mathrm{e}\left(\mathrm{U}_{\alpha\mathrm{k}}^* \mathrm{U}_{\beta\mathrm{k}} \mathrm{U}_{\alpha\mathrm{j}} \mathrm{U}_{\beta\mathrm{j}}^*\right) \sin^2\left(\frac{\Delta\mathrm{m}_{\mathrm{kj}}^2 L}{4E}\right) \\ &-\; 2\sum_{\mathrm{k>j}} \Im\mathrm{m}\left(\mathrm{U}_{\alpha\mathrm{k}}^* \mathrm{U}_{\beta\mathrm{k}} \mathrm{U}_{\alpha\mathrm{j}} \mathrm{U}_{\beta\mathrm{j}}^*\right) \sin\left(\frac{\Delta\mathrm{m}_{\mathrm{kj}}^2 L}{2E}\right), \end{aligned} \tag{1.31}$$

where the opposite of the imaginary term is considered in the case of antineutrinos oscillations $\overline{\nu}_\alpha \to \overline{\nu}_\beta$.

The probability presented in equation (1.30) and (1.31) shows an oscillatory behavior. It is called the probability of oscillation of the neutrino flavor state $\nu_\alpha$ into a $\nu_\beta$ state and is directly related to the neutrino masses. Its phase corresponds to the frequency of the oscillations and is linked to the squarred masses differences, the distance source-detector, and the neutrino energy. The discovery of such flavor changing processes (*cf.* Section 1.1) implies that the neutrinos actually have a mass, even though they are massless particles in the minimum Standard Model extended by the Higgs mechanism (*cf.* Section 1.2.2). The amplitude of this flavor change probability is described by the $\mathrm{U}_{\mathrm{PMNS}}$ matrix elements and therefore the mixing parameters $\theta_{\mathrm{ij}}$.

The derivation of the probability oscillation has been here performed assuming that the neutrinos travelled in vacuum. The probability is modified when taking into account matter effects [191]. While passing through matter, neutrinos can be affected by interactions with the medium by coherently scattering on electrons and nucleons composing the medium. All neutrino flavors interact in matter through neutral current whereas only the electron neutrino interacts through charged current. Therefore, they are not affected the same way and a new potential, function of the electron density of the medium, is added to the interaction Hamiltonian. A relative phase between the different components of the propagation eigenstate is created, resulting in an effective mass splitting and mixing. The mixing angles and the differences of squarred masses are then modified: $\theta \to \theta_{\mathrm{M}}$ and $\Delta\mathrm{m}^2 \to \Delta\mathrm{m}_{\mathrm{M}}^2$, where M stands for matter. This is called the MSW effect, from S. Mikheyev, A. Smirnov, and L. Wolfenstein. For the Double Chooz experiment, subject of this thesis, the matter does affect the studied electron antineutrinos only marginally and will therefore not be taken into account.

### 1.4.3 Two flavors oscillation in vacuum

For many experiments, a two flavors oscillation model is a really good approximation. The mixing matrix can be therefore parametrized with only one angle $\theta$.

$$\begin{pmatrix} \nu_e \\ \nu_\mu \end{pmatrix} = \begin{pmatrix} \cos\theta & \sin\theta \\ -\sin\theta & \cos\theta \end{pmatrix} \begin{pmatrix} \nu_\mathrm{i} \\ \nu_\mathrm{j} \end{pmatrix}. \tag{1.32}$$

The probability of equation (1.30) is simplified in the case of two flavors oscillations and can be written as follows:

$$\mathrm{P}_{\nu_\alpha \to \nu_\beta}(L,E) = \sin^2 2\theta \, \sin^2\left(\frac{\Delta \mathrm{m}^2 L}{4E}\right), \tag{1.33}$$

where $\Delta \mathrm{m}^2$ is the squarred masses difference between the $\nu_\mathrm{i}$ and the $\nu_\mathrm{j}$ states, $E$ is the neutrino energy, and $L$ is the distance between the source of neutrinos and the detector.

Using units suitable to oscillation experiments, the apparation probability of a flavor $\beta$ when the neutrino was created as a $\nu_\alpha$ is:

$$\mathrm{P}_{\nu_\alpha \to \nu_\beta}(L,E) = \sin^2 2\theta \, \sin^2\left(1.27 \, \frac{\Delta \mathrm{m}^2[\mathrm{eV}^2] \times L[\mathrm{km}]}{E[\mathrm{GeV}]}\right). \tag{1.34}$$

In a two flavors scheme, a neutrino created as a $\nu_\alpha$ is expected either to survive and be detected as a $\nu_\alpha$ or to oscillate into a $\nu_\beta$. The following relation is then always verified in this case: $\mathrm{P}_{\nu_\alpha \to \nu_\beta} + \mathrm{P}_{\nu_\alpha \to \nu_\alpha} = 1$.

The survival probability of a $\nu_\alpha$, studied in disappearance experiments like Double Chooz (*cf.* Chapter 3), is then:

$$\mathrm{P}_{\nu_\alpha \to \nu_\alpha}(L,E) = 1 - \sin^2 2\theta \, \sin^2\left(\frac{\Delta \mathrm{m}^2 L}{4E}\right). \tag{1.35}$$

If the two flavors approximation is not used, additional terms appear in equation (1.35). For disappearance experiments like Double Chooz, the electron antineutrino survival probability is studied for the $\theta_{13}$ parameter measurement.

$$\begin{aligned} \mathrm{P}_{\overline{\nu}_e \to \overline{\nu}_e}(L,E) = 1 &- \sin^2 2\theta_{13} \, \sin^2\left(1.27 \, \frac{\Delta \mathrm{m}^2_{31} L}{E}\right) \\ &- \cos^4\theta_{13} \, \sin^2 2\theta_{12} \, \sin^2\left(1.27 \, \frac{\Delta \mathrm{m}^2_{21} L}{E}\right) \\ &+ \frac{1}{2} \sin^2 2\theta_{12} \, \sin^2 2\theta_{13} \, \sin\left(1.27 \, \frac{\Delta \mathrm{m}^2_{31} L}{E}\right) \sin\left(1.27 \, \frac{\Delta \mathrm{m}^2_{21} L}{E}\right) \\ &- \sin^2 2\theta_{12} \, \sin^2 2\theta_{13} \, \cos\left(1.27 \, \frac{\Delta \mathrm{m}^2_{31} L}{E}\right) \sin^2\left(1.27 \, \frac{\Delta \mathrm{m}^2_{21} L}{E}\right). \end{aligned} \tag{1.36}$$

The first two terms are atmospheric ($\Delta \mathrm{m}^2_{31}$) and solar ($\Delta \mathrm{m}^2_{21}$) driven, respectively. The last two terms are interferences between both contributions. Given the energy regime (few MeV) and the distance ($\sim 1$ km) between the source and the detector in this kind of electron antineutrino disappearance experiment, the extra terms are actually found to be negligeable.

# Chapter 2

# Experimental status on $\nu$ masses and mixing parameters

*Pour le savant, croire la science achevée est toujours une illusion aussi complète que le serait pour l'historien de croire l'histoire terminée.* [1]

Louis de Broglie,
French physicist, Physics Nobel Prize in 1929.

Although the neutrino flavor oscillation theory is now backed up by many experimental evidences, mostly brought over the past fifteen years, the neutrino sector is still filled with unknowns. Due to their really weak interactions and despite that neutrinos may be the most abundant Standard Model particle in the Universe, many years have been necessary to establish clear phenomenological bases for $\nu$ flavor oscillations. The questions of their absolute mass scale, and even of their nature, are still unanswered. However, strong link between particle physics and cosmology, nuclear physics and astrophysics, the neutrino is a fundamental messenger for the search of non-standard processes. From the late sixties and the Homestake experiment discovery of a solar $\nu$ deficit, experiments followed one another to measure the neutrino mixing parameters and better define and constrain the theory of flavor oscillation. Without a clear definition of this process, many experiments had to grope their way around and some of them were unlucky enough to scan the wrong part of the parameter space. The confirmation of the three flavor scheme of $\nu$ oscillation came thirty years after the first anomaly in neutrino measurements. The key of the oscillations is now understood as $\nu$ non-zero masses, which is already beyond the minimal Standard Model of particle physics. The central question of the $\nu$ mass is addressed by many experiments, using direct measurement methods, like $\beta$ decay studies and spectral distortion, or more indirect approach, from the study of the flavor oscillation parameters.

This chapter presents the current experimental status on neutrino masses in a first section and on the mixing parameters in a second one. Among the mixing parameters, the special case of $\theta_{13}$ is developed, as it was the last unknown mixing parameter until really recently and is the subject of this thesis, via the Double Chooz experiment. Its precise measurement is needed to fully characterize the flavor oscillation picture. It is important to notice that its search seems to be now over thanks to the reactor $\overline{\nu}_e$ and accelerator experiments observations. Results on $\theta_{13}$ are therefore reported, but are discussed in more details in the last chapter of this document. Finally, the current anomalies with respect to the theory, all linked to hypothetical sterile neutrino states, all obtained at beam, reactor $\overline{\nu}_e$, and gallium experiments, are presented.

[1] From the "Physique et microphysique" book of Louis de Broglie (1956) [45].

## 2.1 Absolute neutrinos masses

The neutrino flavor oscillations brought indirect proof of non-zero neutrinos masses. However two major points are still unknown about these latter. Indeed, their hierarchy and even their absolute values have not yet been measured. This section briefly presents the current knowledge on these important parameters of neutrino physics, obtained mostly from direct measurements, along with the experiments developed in that purpose.

### 2.1.1 Mass hierarchy

Except for differences of squarred masses, coming from oscillation experiments (*cf.* Section 2.2), not much is known about the neutrino mass eigenstates spectrum. The flavor changing processes observed from many sources allow to state that at least two of the mass eigenstates have a non-zero mass. However, the absolute scale is unknown: as far as we know, the lighter neutrino could be massless. There are two possible ordering for the neutrino masses $m_k$. Either the lighter particle is the $m_1$ state and the hierarchy is called "normal", or it is $m_3$ and this corresponds to the "inverted" case. These appellations are only conventions. The Figure 2.1 displays a scheme of the two hierarchies along with the flavor composition of the mass eigenstates. These proportions depend on the flavor mixing parameters (*cf.* Section 1.4.1).

The matter effect, briefly presented in Section 1.4.2, can be exploited in neutrino beam experiments to discriminate from the normal to the inverted hierarchy. Since this effect raises the effective electron neutrino mass, but lowers that of its antiparticle, the neutrino and antineutrino oscillations are differently affected. This could lead to a fake CP violation as the $\nu_\alpha$ and the $\overline{\nu}_\alpha$ disappearance probabilities would differ: a ratio of these probabilities $P(\nu_\alpha \to \nu_\beta)/P(\overline{\nu}_\alpha \to \overline{\nu}_\beta)$ would then be different from 1. This ratio would be therefore higher than 1 in the case of the normal hierarchy, but lower than 1 for the inverted hierarchy.

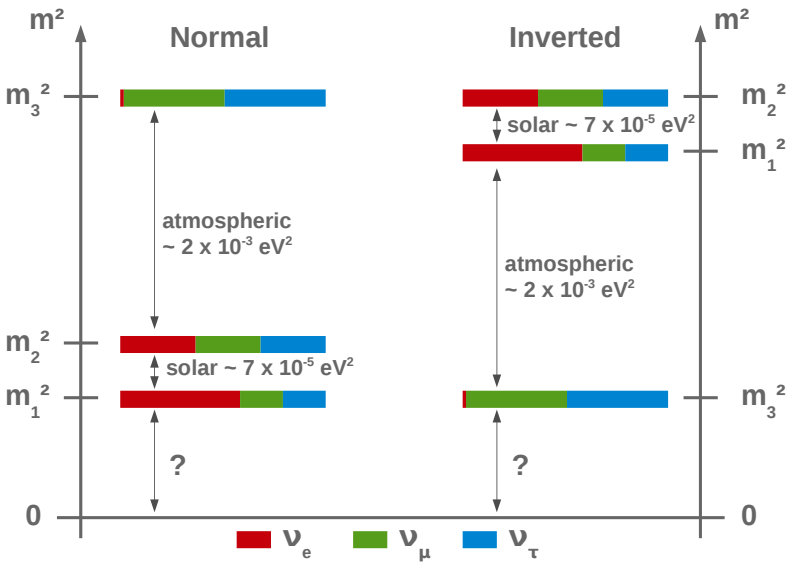


Figure 2.1: *Neutrino mass eigenstates spectra in the case of a normal and an inverted hierarchy, and composition in terms of $\nu_e$, $\nu_\mu$, and $\nu_\tau$. Neither the absolute scale, nor the masses values, nor the hierarchy arrangement are known so far.*

### 2.1.2 Tritium $\beta$ decay

The study of the tritium ($^3$H) $\beta$ decay allows to directly measure the electron antineutrino mass. The method is based on kinematic considerations and energy conservation. Indeed, the total energy of a nucleus $\beta$ decay, the $Q_\beta$ of the reaction, is shared between the electron and the antineutrino. In the case of $^3$H, the $Q_\beta$ is 18.6 keV and the decay:

$$^3\mathrm{H} \;\rightarrow\; ^3\mathrm{He} + e^- + \overline{\nu}_e. \tag{2.1}$$

If the neutrino has a finite mass, the maximum electron energy gets lowered by the amount of the neutrino mass. Therefore, the endpoint of the $\beta^-$ spectrum would be $Q_\beta - m^2_{\overline{\nu}_e}$. Very small with respect to the $Q_\beta$, the neutrino mass is easier to measure as the considered nucleus is lighter.

Since the neutrino flavor eigenstates are different from the mass eigenstates (*cf.* Section 1.4.1), what is measured is actually an effective mass coming from neutrino mixing:

$$m^2_{\overline{\nu}_e} \;=\; \sum_k |U_{ek}|\, {m_k}^2 \;=\; c^2_{12}c^2_{13}m^2_1 + s^2_{12}c^2_{13}m^2_2 + s^2_{13}m^2_3. \tag{2.2}$$

where the sum is performed over the mass eigenstates, k = 1, 2, 3, whose masses are $m_1$, $m_2$, and $m_3$, respectively. The $U_{ek}$ are elements of the $U_{PMNS}$ mixing matrix, and the $c_{ij}$ and $s_{ij}$ parameters are the cosinus and sinus of the $\theta_{ij}$ mixing angle, respectively.

Using spectrometers, the former Mainz and Troitzk experiments measured electron antineutrino mass upper values with 95 % CL: $m_{\overline{\nu}_e} < 2.3$ eV and $m_{\overline{\nu}_e} < 2.5$ eV, respectively [129, 133]. Since the experimental uncertainty was mainly caused by the backgrounds and the energy resolution, the huge $\beta$ spectrometer of the KATRIN experiment (Karlsruhe Tritium Neutrino) has been built. Providing a really good $\beta$ energy resolution, its expected sensitivity is as good as 0.2 eV [187].

Concerning the $\nu_\mu$ and $\nu_\tau$ effective masses, the muon momentum in charged pions decay, $\pi^+ \rightarrow \mu^+ + \nu_\mu$, and the shape of decay products spectra from the $\tau$ lepton give the following upper limits $m_{\nu_\mu} < 170$ keV and $m_{\nu_\tau} < 15.5$ MeV [34, 39].

### 2.1.3 Cosmological observations

The total neutrino mass can also be measured from cosmological studies as the massive neutrinos contribute to the matter density of the Universe. This quantity can be extracted from the survey of angular matter power spectrum and particularly from large scale structures like galaxy distributions. Indeed, the neutrino masses affect the shape of the matter power spectrum and suppress fluctuations in the cosmic microwave background (CMB). The contribution of neutrinos to the energy density of the Universe depends therefore on the sum of neutrino masses [1].

Many observables can be used and many cosmological parameters can be fix in the analysis: primordial cosmic microwave background, galaxy distribution, baryon acoustic oscillation, lensing effect, Lyman $\alpha$, supernovae observation, etc. The limit from cosmology is then complicated to obtain since there is a large number of correlated parameters. The boundary on the total neutrino mass highly depends on them. For instance, if only the CMB surveys of WMAP and Planck are used [104]:

$$\sum_{\mathrm{k}} \mathrm{m_k} \; < \; 0.36 \text{ eV}, \quad \text{at } 95 \text{ \% CL}, \tag{2.3}$$

where the sum is performed over the three neutrino mass eigenstates. A combination between these results and other effects like baryon acoustic oscillations and high redshift type-I supernovae observations tend to increase the limit up to 1.5 eV.

### 2.1.4 Neutrinoless double $\beta$ decay

The double $\beta$ decay is a nuclear transition in which an initial nucleus $\mathrm{X(Z, A)}$, with Z protons and A nucleons, decays into $\mathrm{Y(Z + 2, A)}$ by emitting two electrons and two antineutrinos in the process. This has been observed in many experiments from different nuclei. They are typically even-even nucleus (Z, A), like $^{82}$Se, $^{100}$Mo, or $^{136}$Xe, which pairing forces make more bound than its (Z + 1, A) neighbour, but less than the (Z + 2, A) nuclide.

The neutrinoless double $\beta$ decay corresponds to the decay of a nucleus with the combined emission of two electrons, and nothing more: $\mathrm{X(Z, A)} \rightarrow \mathrm{Y(Z + 2, A)} \; + \; 2e^-$. This process cannot occur in the minimal Standard Model, since it would violate the global lepton number. It implies that neutrinos have Majorana masses (*cf.* Section 1.3.2), and that they basically are their own antiparticles. The same neutrino would therefore be emitted and absorbed within the nucleus (left panel of Figure 2.2).

Given the fundamental contribution that the discovery of neutrinoless double $\beta$ decays can give to neutrino physics, many experiments are nowadays looking for this peculiar process. The idea is to measure the energy of the two electrons with a very good resolution and reject the backgrounds with a very good efficiency. With only the two electrons in the final state, the total kinetic energy of the two charged particles would correspond to the $\mathrm{Q}_\beta$ of the reaction. In order to do so, several experimental techniques have been developed: pure calorimeters like germanium crystals and bolometers (Heidelberg-Moscow and Cuoricino experiments for instance [50, 122]) or both tracker and calorimeter. This latter approach is the only technology that provides access to all the final state parameters (energies and angular distributions of the electrons), allowing its complete determination. This was the path followed by the NEMO-3 experiment [32]. The source was separated from the detector and therefore several isotopes could be studied. SuperNEMO, the next generation of NEMOs experiment, should achieve a sensitivity on the Majorana neutrino mass of about 50 meV in few years [33].

The neutrinoless double $\beta$ decay is dominated by a neutrino exchange mechanism, so its rate is proportional to $\mathrm{m}^2_{\beta\beta}$, the effective Majorana mass. The half-life of a nucleus which encounters that process is therefore:

$$\left(T^{0\nu}_{1/2}\right)^{-1} \; = \; G^{0\nu}\left(\mathrm{Q}_\beta, \mathrm{Z}\right) \left|M^{0\nu}\right|^2 \mathrm{m}^2_{\beta\beta} \tag{2.4}$$

where $G^{0\nu}(E_0, Z)$ is a phase-space factor and $M^{0\nu}$ the nuclear matrix element [96].

The effective Majorana mass involved in the neutrinoless double $\beta$ decay can be expressed as a combination of the neutrino mixing parameters:

$$\mathrm{m}^2_{\beta\beta} \; = \; \left|\sum_{\mathrm{k}} \mathrm{U}^2_{\mathrm{ek}}\right| {\mathrm{m_k}}^2 \; = \; c^2_{12}c^2_{13}\mathrm{m}^2_1 + \mathrm{e}^{i\beta}s^2_{12}c^2_{13}\mathrm{m}^2_2 + \mathrm{e}^{i\alpha}s^2_{13}\mathrm{m}^2_3. \tag{2.5}$$

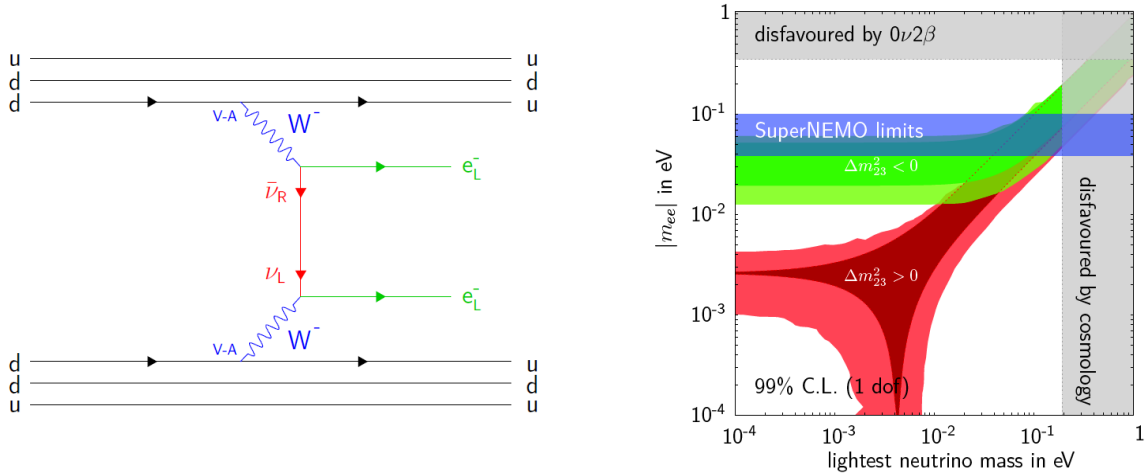


Figure 2.2: *(left) Neutrinoless double $\beta$ decay process, with neutrino exchange. (right) Effective Majorana mass as a function of the mass of the lightest neutrino. Illustration of the power of neutrinoless double $\beta$ decay experiment to test the two mass hierarchy hypotheses: normal hierarchy in red and inverted hierarchy in green [96].*

No signal of neutrinoless double $\beta$ decay has been observed yet, except for the Heidelberg-Moscow experiment, based on the study of the $^{76}$Ge isotope. Some members of this collaboration claimed they found $m_{\beta\beta} = (0.2 - 0.60)$ eV at 99.73 % CL [122]. However, these results seem to be disfavored by [121]. Nonetheless, many projects are ongoing in order to check them. The new generation of experiments will increase the considered isotope mass and try to reach a sensitivity one order of magnitude better than the current limits: $m_{\beta\beta} = (20 - 100)$ meV.

Finally, it is interesting to notice that the neutrinoless double $\beta$ decay observation would indeed imply that the neutrinos are Majorana particles and would allow a measurement of its effective mass, but could also allow to probe the mass hierarchy if the lightest neutrino is light enough (right panel of Figure 2.2).

## 2.2 Flavor oscillations parameters

### 2.2.1 Measurement principles

The neutrino flavor oscillations can be studied with two kinds of experiments. The first ones are called disappearance experiments. They consist in the study of the survival probability $P(\nu_\alpha \to \nu_\alpha)$ of an initial beam of known flavor $\nu_\alpha$, with a mean energy $E$, over the distance $L$. The goal is to dertermine the number of $\nu_\alpha$ which disappeared, *i.e.* oscillated, at a given distance from the source. The second kind looks for the appearance of $\nu_\beta$ states in an initial beam of $\nu_\alpha$ with energy $E$ at a distance $L$ from the source. The transition probability $P(\nu_\alpha \to \nu_\beta)$ is therefore studied.

These two types of experiments allow to determine the oscillation parameters $\theta_{ij}$ and $\Delta m^2_{ji}$. The mixing angles $\theta_{ij}$ are linked to the amplitude of the oscillation, while the difference of squarred masses, defined as ${m_j}^2 - {m_i}^2$ are basically its frequency (*cf.* equation (1.31)). To constrain the right $\theta$ or $\Delta m^2$, the physicists have to chose wisely the $L$ and $E$ parameters (*cf.* Section 1.4.3), *i.e.*

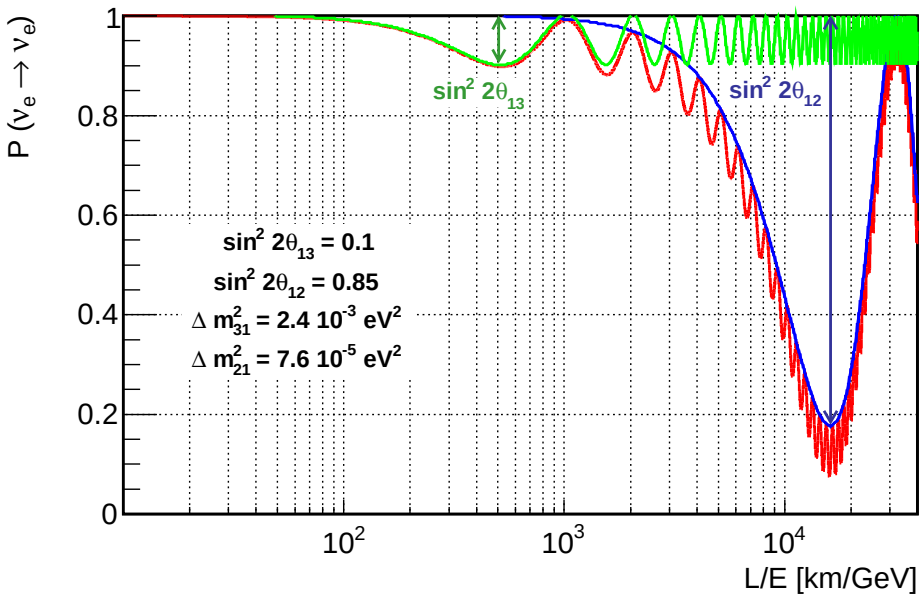


Figure 2.3: *Electron neutrino survival probability (red) as a function of $L/E$, for fixed values of $sin^2\theta_{12}$, $sin^2\theta_{13}$, $\Delta m^2_{21}$, and $\Delta m^2_{31}$. The $\theta_{12} = 0$ and $\theta_{13} = 0$ hypotheses are drawn in green and blue, respectively.*

the distance between the source and the detector, and the neutrino beam energy. If $E/L \gg \Delta m^2$, the oscillation did not occur yet when the neutrinos are detected. Neutrino flavor transitions can be observed only if the travelled distance is longer than one period of oscillation.

With beam energies of the order of the GeV, the accelerator experiments usually place their detector few hundred of kilometers away from the source, while reactor experiments, which measure MeV antineutrinos, are located one kilometer away from the cores or few hundred of kilometers away, depending on the studied parameters (*cf.* Sections 2.2.2 and 2.2.4).

The Figure 2.3 displays the survival probability of an electron neutrino as a function of $L/E$, for fixed values of oscillation parameters. The $\theta_{13}$ and $\theta_{12}$ dominated parts are made visible by drawing the probability in the case of a null $\theta_{12}$ and a null $\theta_{13}$, respectively. The two regimes, solar driven $\Delta m^2_{\text{sol}}$ (small squarred masses difference) and atmospheric driven $\Delta m^2_{\text{atm}}$ (large squarred masses difference) are also clearly visible.

### 2.2.2 Solar neutrino sector

The current knowledge on solar neutrinos and their related mixing parameters $\Delta m^2_{21}$ and $\theta_{12}$ come from various experiments, which studied for several tens of years the neutrinos emitted by our star. More recently, the reactor neutrino long baseline experiment KamLAND increased the constraints on these parameters.

The solar neutrino experiments used in the first place a radiochemical method to detect the neutrino interactions. The electron neutrinos were captured on target nuclei and counting the number of reaction products gave information on the initial neutrino flux. The first team to detect a deficit of electron neutrinos coming from the Sun was the one led by R. Davis Jr. and J. N. Bahcall, with 390 $m^3$ of tetrachloroethylene ($C_2Cl_4$) as neutrino target [65]:

$$^{37}\mathrm{Cl} \; + \; \nu_e \; \rightarrow \; ^{37}\mathrm{Ar} \; + \; e^{-}. \tag{2.6}$$

The unstable argon 37 was regularly extracted by chemical methods and its decay counted in order to estimate the number of neutrino interactions. The Gallex/GNO (Gallium Experiment/Gallium Neutrino Observatory) and the SAGE (Soviet American Gallium Experiment) followed few years later using a gallium isotope: $^{71}\mathrm{Ga} + \nu_e \rightarrow ^{71}\mathrm{Ge} + e^{-}$. The same extraction method than Homestake experiment was used [3, 108].

All these experiments found a deficit of solar neutrinos. This phenomenon has been later explained as a flavor conversion of the $\nu_e$ into $\nu_\mu$ or $\nu_\tau$, and fits really well with the three flavor oscillation phenomenology, together with matter effect inside the Sun (*cf.* Section 1.4.2). However, only the SNO (Sudbury Neutrino Observatory) experiment allowed to verify the flavor oscillation hypothesis [24]. This experiment consists in a heavy water Čerenkov detector of 1 kiloton, located in a Canadian mine at a depth corresponding to 6,000 meters-water-equivalent (mwe). It measured the whole neutrino flux coming from the Sun and allowed to solve the solar neutrino problem in 2001.

KamLAND (Kamioka Liquid Scintillator Antineutrino Detector), located near Toyama in Japan, is a reactor antineutrino long baseline detector [7]. It benefits from the 2,700 mwe overburden of the Kamioka mine. The electron antineutrinos from all the surrounding reactors, with an average distance to the detector of 180 km, are detected. The solar neutrinos experiments dominant dependence is $\theta_{12}$, while KamLAND's is $\Delta\mathrm{m}^2_{21}$. This experiment is also dependent on the $\theta_{12}$ and $\theta_{13}$ parameters, which allows it to constrain them.

The current values of the solar parameters are obtained by combining the KamLAND and the solar experiments results in a three neutrino flavors basis [95]. The solar squarred masses difference and its related mixing angle are:

$$\begin{aligned} \Delta\mathrm{m}^2_{21} &= (7.50 \; \pm \; 0.20) \times 10^{-5} \; \mathrm{eV}^2, \\ \sin^2 2\theta_{12} &= 0.857 \; \pm \; 0.024. \end{aligned} \tag{2.7}$$

### 2.2.3 Atmospheric neutrino sector

The current knowledge on the mixing parameters $\Delta\mathrm{m}^2_{31}$ and $\theta_{23}$ mostly come from studies of $\nu_\mu$ transition into $\nu_\tau$ in atmospheric neutrinos and long baseline experiments. Given the low value of $\Delta\mathrm{m}^2_{21}$ with respect to $\Delta\mathrm{m}^2_{32}$, both $\Delta\mathrm{m}^2_{32}$ and $\Delta\mathrm{m}^2_{31}$ squarred masses differences are extremely close.

The $\nu_\mu$ disappearance was first observed in atmospheric neutrinos experiment. The neutrinos were resulting from interactions of cosmic rays with the upper layers of the atmosphere. The SuperKamiokande detector performed many measurements over the years of atmospheric and solar neutrinos. It is a gigantic 50 kilotons water Čerenkov detector located at the Kamioka mine, in Japan. It was originally designed for the search of the proton decay, but was the one which really brought the proof of the flavor atmospheric neutrino oscillation.

Using the measurements of the atmospheric parameters performed by SuperKamiokande, the K2K experiment (KEK to Kamioka) looked for and found $\nu_\mu \rightarrow \nu_\tau$ oscillations. It consisted in a $\nu_\mu$ beam originated from the KEK accelerator facility and detected in the SuperKamiokande

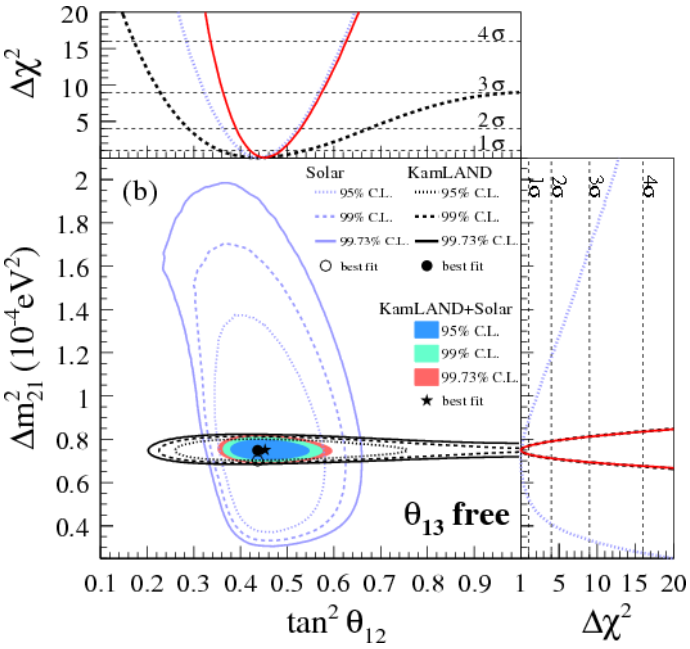


Figure 2.4: *Allowed regions projected in the $(tan^2\theta_{12}, \Delta m^2_{21})$ plane, for solar data (blue) and KamLAND (black) data from a three flavors oscillation analysis, where $\theta_{13}$ is a free parameter. The color filled regions are from the combined analysis. The side panels show the $\Delta\chi^2$ profiles projected onto the $tan^2\theta_{12}$ and $\Delta m^2_{21}$ axes [95].*

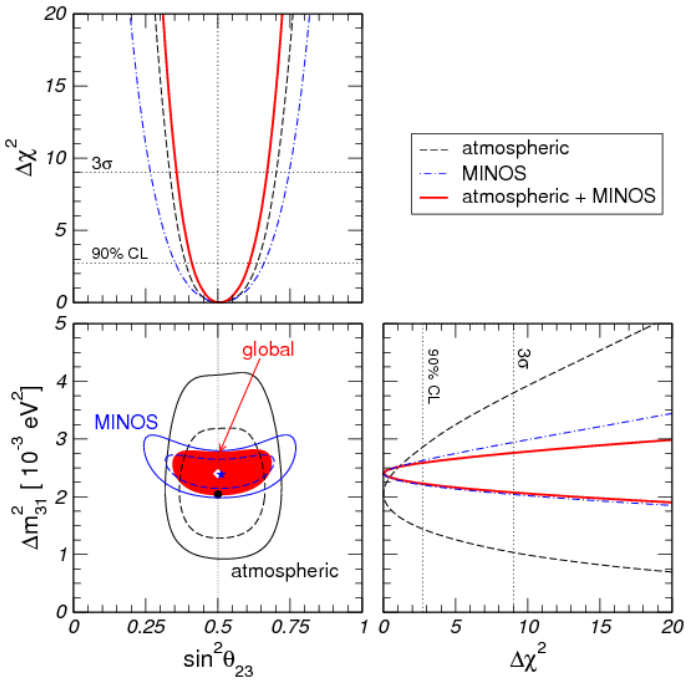


Figure 2.5: *Allowed regions projected in the $(sin^2\theta_{23}, \Delta m^2_{31})$ plane, for atmospheric data (black lines) and MINOS (blue lines) data from a three flavors oscillation analysis, where $\theta_{13}$ is a free parameter. The red filled region shows the combined analysis, including K2K results. The side panels show the $\Delta\chi^2$ profiles projected onto the $sin^2\theta_{23}$ and $\Delta m^2_{31}$ axes [166].*

detector, 250 km away. By measuring the atmospheric mixing parameters and thus prove the neutrino flavor oscillations, this experiment gave the first evidence for massive neutrino. MINOS, a long baseline $\nu_\mu$ disappearance experiment dominated by the atmospheric $\Delta m^2_{\text{atm}}$, gave later a really precise measurement of it. It used the NuMI beam line (Neutrinos at the Main Injector), a facility at Fermilab which uses protons from the Main Injector accelerator to produce an intense beam of muon neutrinos. This experiment was also strongly dependent of $\theta_{23}$, along with $\theta_{13}$ and the CP violating phase $\delta_{\text{CP}}$ (*cf.* Section 2.2.4.2).

The current values of $|\Delta m^2_{31}|$ and $\sin^2 2\theta_{23}$, with their error bars, are given in [5, 19]. They are strongly constrained by the SuperKamiokande results on atmospheric neutrinos and by the MINOS measurements. However, the sign of $\Delta m^2_{31}$ is still unknown (*cf.* Section 2.1.1). Although a recent global analysis has been performed, mostly driven by the SuperKamiokande results on atmostpheric neutrinos, the hierarchy problem is still not constrain [103]. Also, despite the fact that $\theta_{23}$ seems to be maximal, recent global fits tend to disfavor this hypothesis at 2 $\sigma$ [103].

$$\begin{aligned} |\Delta m^2_{31}| &= 2.32^{+0.12}_{-0.08} \times 10^{-3}\text{eV}^2, \\ \sin^2 2\theta_{23} &> 0.95. \end{aligned} \tag{2.8}$$

It has been showed previously with K2K and MINOS how important are man-made neutrino sources for neutrino oscillations studies. Two other important oscillation experiments use themselves the CNGS $\nu_\mu$ beam (CERN neutrino to Gran Sasso) for $\nu_\tau$ and $\nu_e$ appearance studies. It is a 10 to 30 GeV beam created from 400 GeV proton interactions coming from the CERN SPS (Super Proton Synchroton).

The OPERA experiment, located in the Gran Sasso laboratory, is 732 km away from CERN. This experiment is mostly designed to investigate $\nu_\mu \to \nu_\tau$ oscillations in the atmospheric neutrino sector. The detection principle is based on 150,000 emulsion blocks interleaved with lead sheets. The $\tau$ particle is identified by its typical decay topology. It indeed involves a kink, *i.e.* an angle, indicating the decay of the $\tau$ particle shortly after its creation. The OPERA experiment began in 2008 and accumulated by 2011 a statistics of $1.4\times10^{20}$ POT [2]. By the end of June 2012, the appearance of two $\nu_\tau$ candidates have been discovered when 2.1 were expected, including 0.2 background events [20].

The OPERA physicists also reported a neutrino speed slightly higher than the speed of light in September 2011 [18], but eventually updated their analysis and finally found no deviation. This is consistent with results of many other Gran Sasso based detectors.

The ICARUS experiment, which started data taking in October 2010, also studies the neutrinos coming from the CNGS facility [163]. It is made of 600 tons of liquid argon TPC (Time Projection Chambers) and is the first large scale experiment to exploit this detection technique. So far, $5.8 \times 10^{19}$ POT have been accumulated by the experiment.

[2] POT stands for "protons on target", a typical unit for accelerator physics. It corresponds to the number of protons from the primary accelerator hitting the target for the mesons creation, and therefore the neutrino beam creation.

### 2.2.4 The $\theta_{13}$ sector

Both CP violation search in the neutrino sector and our ability to tell whether the neutrino spectrum is normal or inverted depend on $\theta_{13}$. The violation of the CP symmetry in the neutrino sector plays a key role in many leptogenesis models (*cf.* Section 1.3.3). Determining $\theta_{13}$ is therefore an important step for the neutrino physics understanding.

It has however to be noticed that there is a priori nothing special about this mixing angle. Although this parameter has to be non-zero and big enough to look for CP violation, this is actually the case for the other mixing angles. The $\theta_{13}$ parameter was just until really recently the last unknown, the final piece, of the minimal three flavors mixing model. In the current parametrization of the flavor mixing (*cf.* Section 1.4.1), the CP violating phase is scaled by $\sin^2 2\theta_{13}$, but this is only a convention.

#### 2.2.4.1 Previous reactor experiments

Two experiments already looked for an oscillation linked to the large $\Delta m^2$ and the $\theta_{13}$ mixing angle. CHOOZ and Palo Verde both studied electron antineutrinos coming from nuclear reactor cores. They are an important neurino source: intense ($\sim 10^{21}$ $\overline{\nu}_e$/s) and pure (only $\overline{\nu}_e$ are emitted from $\beta$ decays of fission products of the nuclear fuel). The detectors were located roughly one kilometer away from the reactors. This distance corresponds to the baseline at which the first oscillation maximum can be observed, if $\theta_{13}$ is not zero (Figure 2.3). However, these two experiments did not find any oscillation at this distance. Their results were later backed up by KamLAND [95].

**CHOOZ**

The CHOOZ experiment single detector was located in a hill (300 mwe) in the vicinity of the Chooz B1 and B2 reactors and acquired data from April 1997 to July 1998 [30]. The experiment total live time amounted for more than 300 days but 40 % corresponded to both reactors OFF data, since the two 4.25 $GW_{th}$ reactors encountered issues during their commissioning. The search of electron antineutrino disappearance, emitted by the nuclear cores, was done through inverse $\beta$ decay reaction, $\overline{\nu}_e + p \rightarrow e^+ + n$ (*cf.* Section 3.3.1). The detector was basically composed of three regions. The innermost volume played the role of neutrino target and consisted in 5 tons of liquid scintillator doped with gadolium to reduce the natural experiment background and clearly sign the neutron capture by emitting 8 MeV $\gamma$ particles, correlated in time with the positron annihilation with $\tau \sim 30$ µs (*cf.* Section 3.3.2). This volume was surrounded by a hundred tons of undoped scintillator, whose goal was to fully contain the escaping energy. The scintillation liquid was seen by 192 photomultiplier tubes (PMTs). Finally, a last region played the role of a veto. Equiped with 48 PMTs and filled with scintillator liquid, it allowed to reject cosmic muon related backgrounds and shield the target against incoming radioactivity. The whole detector was also surrounded by a 14 cm thick steel vessel and 75 cm of low-radioactivity sand.

Unfortunately, the CHOOZ experiment got limited by the degradation of its liquid scintillator. Indeed, the attenuation length decreased faster than expected and the transparency got impaired. The CHOOZ physicists were compelled to intensively and frequently calibrate their detector.

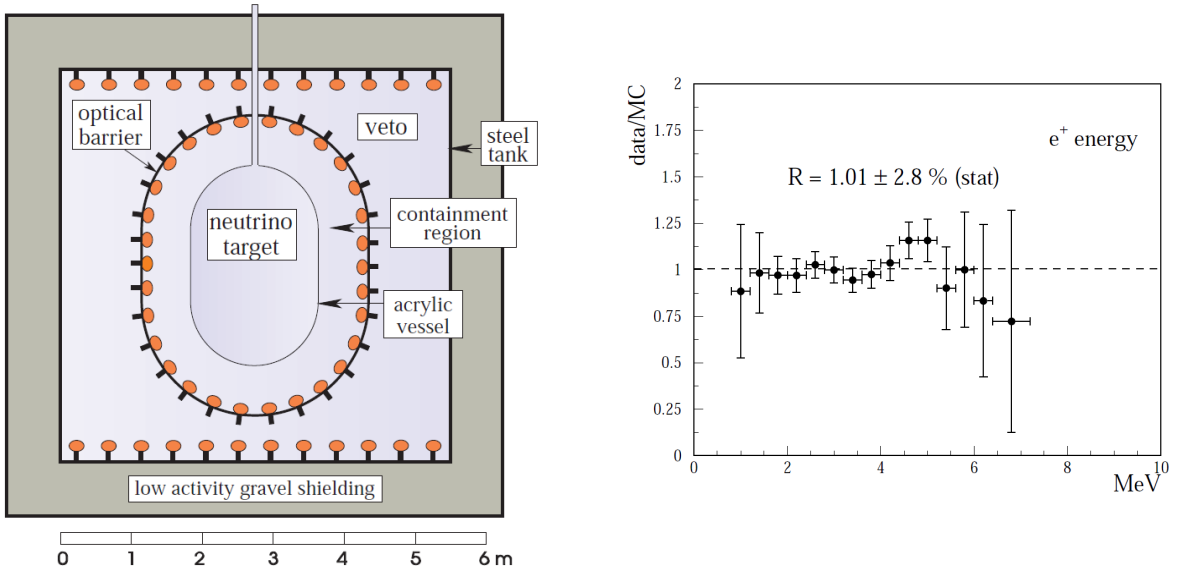


Figure 2.6: *(left) The CHOOZ detector with all its different volumes represented. (right) Detected number of events over expected number of events ratio per positron energy bin. The errors shown are only statistical. It is consistent with 1.*

CHOOZ finally observed 2,991 antineutrino candidate events one kilometer away from the cores. To reduce the uncertainty on the neutrino flux, the Bugey 4 reactor flux measurement was used as a "CHOOZ near detector" (*cf.* Section 7.1). Finally, the result of the CHOOZ experiment was presented as a ratio of detected events to expected events without $\theta_{13}$ oscillation. They found R $=$ 1.01 $\pm$ 2.8 % (stat) $\pm$ 2.7 % (syst), which allowed to state an upper limit on $\theta_{13}$: $\sin^2 2\theta_{13} < 0.14$ at 90 % CL with $\Delta m^2_{31} = 2.5 \times 10^{-3}$ eV$^2$, since R was compatible with 1 within the error bars.

### Palo Verde

The Palo Verde experiment also studied electron antineutrino froms reactors [43]. The single detector was located 890 m away from two of the three Palo Verde Nuclear Generating Station of 11.6 GW total power, and 750 m away from the third, in Arizona, with an overburden of 32 mwe. It took 352 days of data, between July 1998 and July 2000. Its design was different from the CHOOZ detector as it was composed of segmented detection cells. The innermost region was made up of 66 cells. Each of them were filled with liquid scintillator doped with gadolinium and were surrounding on two of their sides by mineral oil buffer cells. Each buffer cell was linked to a PMT for readout of the scintillation light. The whole detector amounted for 11 tons of liquid scintillator and was surrounded by 105 tons of water for incoming background reduction. Finally, a muon veto completed the design.

The Palo Verde experiment applied the same technique as shown before for the reduction of the systematic uncertainty on the neutrino flux and the Bugey 4 measurement was used as an anchor point. The ratio of detected number of events to expected number of events without oscillation was measured to be R $=$ 0.982 $\pm$ 2.3 % (stat) $\pm$ 5.3 % (syst). With a ratio consistent with 1, the Palo Verde experiment confirmed the CHOOZ results, but set an upper limit on $\theta_{13}$ a little higher because of its large systematic error.

**Multiple detectors concept**

The CHOOZ experiment was limited by both its statistic and systematic uncertainties, which were respectively 2.8 and 2.7 %. The statistics issue can be taken care of by building bigger target volumes, taking data for a longer time (and therefore improve the liquid scintillator stability over time), or even use more powerfull nuclear reactors.

One of the dominant systematic uncertainty was the knowledge on the reactor $\nu$ flux. The abandonned Kr2Det project proposed for the first time to build two identical detectors for the $\theta_{13}$ search [136]. Indeed, the far detector would measure the possibly oscillated neutrino flux, while the near detector would measure the flux normalization before oscillation. This concept of two identical detectors has been followed since in several collaborations, like Double Chooz.

#### 2.2.4.2 Long baseline experiments

Long baseline beam experiments are able to measure the $\theta_{13}$ parameter from the study of the appearance of $\nu_e$ neutrinos in a $\nu_\mu$ beam. However, $\theta_{13}$ is entwined with other parameters: the probability of this transition depends on the CP-violating phase $\delta_{\rm CP}$ and on matter effects. Such experiments are also able to probe whether the mass spectrum is normal or inverted (*cf.* Section 2.1.1). Another important dependence of these measurements is the mixing angle $\theta_{23}$.

$$\begin{aligned} \mathrm{P}_{\nu_\mu \to \nu_e}(L,E) \;&=\; \sin^2 2\theta_{13} \sin^2\theta_{23} \sin^2\left(\frac{\Delta \mathrm{m}^2_{31} L}{4E}\right) \\ &+ \text{ CP violating term } + \text{ Matter effect term} + ... \end{aligned} \tag{2.9}$$

The $\nu_\mu$ beam is usually of the order of a few tens of GeV and arises from pion decays, created by the collision of accelerated protons on a fixed target. The principal challenge a long baseline beam experiment has to cope with is the understanding of the beam itself: the hadrons production from protons (momentum and angle distribution) and the beam line geometry. The baseline of such experiment is basically few hundred of kilometers.

The T2K and the MINOS experiments were the first to measure an electron neutrino appearance in their far detector, favoring a non-zero $\theta_{13}$. These two experiments and their recent results are presented in this section, along with the upcoming NO$\nu$A.

**T2K**

The T2K experiment is a long baseline experiment designed to study neutrino oscillations in the atmospheric neutrino regime, *i.e.* large $\Delta \mathrm{m}^2$ [6]. It has been mainly designed for both the determination of $\theta_{13}$ from the $\nu_\mu \to \nu_e$ transition, and precision measurements of the $\nu_\mu$ disappearance.

T2K uses a 2.5 degrees off-axis neutrino beam created at the J-PARC (Japan Proton Accelerator Research Complex) accelerator facility in Tokai, Japan. The beam is comes from focused pions decays in a hundred meters tunnel, which are the results of the 30 GeV proton beam interaction with a graphite target. The off-axis concept allows to narrow the energy of the neutrino beam and peak it at 600 MeV, which corresponds to the maximum for the $\nu_\mu \to \nu_e$ appearance probability in the far detector. The neutrinos are detected in the water Čerenkov SuperKamiokande detector, 295 km away, where $\nu_e$ charged current interactions, $\nu_e + n \to p + e^-$,

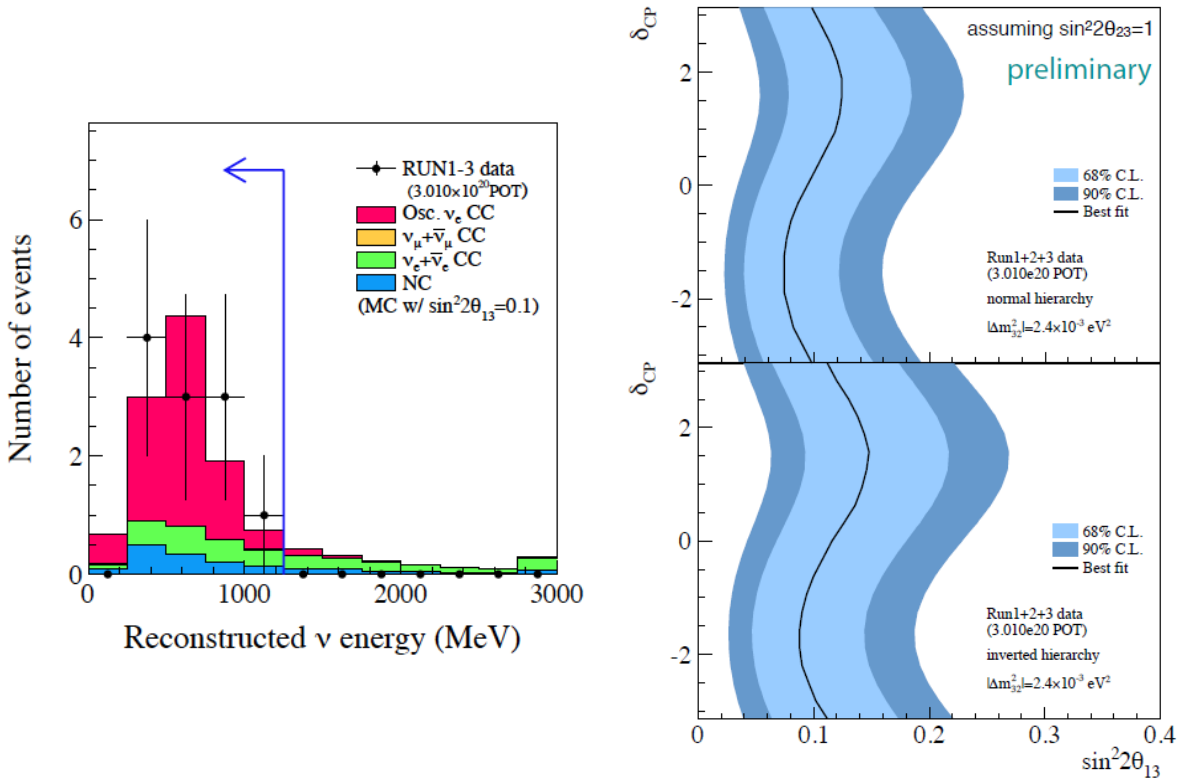


Figure 2.7: *(left) T2K electron neutrino appearance spectrum for $3.01 \times 10^{20}$ POT. Eleven candidates are selected. (right) Allowed region of $sin^2 2\theta_{13}$ for each value of $\delta_{CP}$, for both hierarchy hypotheses: normal (top) and inverted (bottom) [162].*

are looked for by selecting the single ring created by the electron. Two near detectors complete the experimental setup, 280 m from the source. INGRID (Interactive Neutrino Grid), an on-axis iron-scintillator detector, monitors the neutrino beam, while ND280 measures its intrinsic $\nu_e$ contamination. This is a primordial step before the analysis of the SuperKamiokande data, as the seeked signal for the $\theta_{13}$ measurement is actually an appearance of $\nu_e$ [134]. It provides consistency checks of the background predictions.

The data taking started in January 2010 and the first physics results were released, with the full data available before the April 2011 earthquake, in June 2011 [4]. These data indicated for the first time an appearance of $\nu_e$ in the initial $\nu_\mu$ beam. The new results, with data until June 9$^{\text{th}}$ 2012, correspond to a statistics of $3.01 \times 10^{20}$ POT. Eleven electron neutrino candidates have been detected whereas the expected background was $3.22 \pm 0.43$ for $\sin^2 2\theta_{13} = 0$. The probability to observe 11 events with $\theta_{13} = 0$ was estimated to be 0.08 % (3.2 $\sigma$). So far, the T2K experiment cannot distinguish between the normal and the inverted hierarchy. The best fit values, with 68 % CL errors and $\delta_{\text{CP}} = 0$, for both cases are therefore quoted:

$$\begin{aligned} \sin^2 2\theta_{13} &= 0.094^{+0.053}_{-0.040} \quad \text{(Normal hierarchy)}, \\ \sin^2 2\theta_{13} &= 0.116^{+0.063}_{-0.049} \quad \text{(Inverted hierarchy)}. \end{aligned} \tag{2.10}$$

#### MINOS

The long baseline experiment MINOS (Main Injector Neutrino Oscillation Search) has been designed for detailed studies of the $\nu_\mu$ survival probability and therefore the measurements of the atmospheric mixing parameters [142]. It provides nowadays the most precise value of the atmospheric difference of squarred masses (*cf.* Section 2.2.3) and its results are consistent with SuperKamiokande and T2K measurements. This experiment can also look for $\nu_e$, like T2K, and provide a good insight on $\theta_{13}$ value.

MINOS uses two detectors to measure a beam of initially $\nu_\mu$ at two different locations. The neutrino beam is peaked around 3 GeV and is produced in the Fermilab NuMI (Neutrinos at the Main Injector) facility from pions decays coming from roughly 20 GeV protons interacting on a graphite target. The MINOS near detector measures the beam spectrum and composition close to the production point of the neutrinos. It allows an absolute flux study and cross section measurements. The far detector is installed in the Soudan mine, 735 km away. Both detectors are trackers and consist of magnetized alterning sheets of steel and scintillator of 980 tons (near) and 5,400 kilotons (far). The scintillator readout is performed by photomultiplier tubes and optical fibers.

The MINOS experiment finished data taking in April 2012 after having accumulated $10.7 \times 10^{20}$ POT $\nu_\mu$ and $3.4 \times 10^{20}$ POT $\overline{\nu}_\mu$. For the $\theta_{13}$ determination, MINOS looked for an excess of $\nu_e$ in its far detector: 62 candidates have been selected, whereas only 50 were expected for $\theta_{13} = 0$ [19]. Although not highly significant, this result is consistent with the T2K first publication.

#### NO$\nu$A

The NO$\nu$A experiment is a future second-generation experiment using the Fermilab NuMI beam line [37]. It is expected to start data taking in the second half of 2013. This project is optimized for the detection of $\nu_\mu \rightarrow \nu_e$ oscillations and seeks to improve the sensitivity for the study of this reaction by approximately an order of magnitude from that of the MINOS experiment. The characteristic of NO$\nu$A is its really long baseline, which also allows it to access to matter effects that can be used to determine the ordering of the neutrino mass states. It consists of two detectors, off-axis with respect to the NuMI beam line. The near detector is located on the Fermilab site, approximately 1 km from the NuMI target. The far detector is located 810 km from the neutrino production point and is a 14 kilotons liquid scintillator fine grained detector. The NO$\nu$A project also includes a power upgrade of the NuMI line, from 320 kW to 700 kW.

### 2.2.4.3 Short baseline experiments

As explained in Section 2.2.4.1, the search of $\theta_{13}$ can be done in the atmospheric neutrino regime using electron antineutrinos emitted by nuclear reactors. According to the Figure 2.3, the $\theta_{13}$ is indeed accessible for a $L/E$ of the order of 500 km/GeV. Since the reactor neutrino energy is comprised between 2 and 8 MeV (*cf.* Section 3.2.2), the distance between the source and the detector should be of the order of 1 km. This is the path already followed by CHOOZ and Palo Verde, which got limited by statistical and systematic uncertainties, leaving us in 2003 with an upper limit on $\theta_{13}$: $\sin^2 2\theta_{13} < 0.14$, at 90 % CL with $\Delta m^2_{31} = 2.5 \times 10^{-3}$ eV$^2$.

The Double Chooz experiment has been therefore created with the goal of improving the sensitivity to $\theta_{13}$, by improving CHOOZ concept. Few years later, the two collaborations Daya Bay and RENO decided to use the Double Chooz detector concept in order to carry out independent measurements.

### Double Chooz

The Double Chooz experiment pioneered the current concept used to study $\theta_{13}$ with electron antineutrinos. A more complete presentation of the Double Chooz experiment with its detector, detection method, and its expected backgrounds and signal is available in Chapter 3. Double Chooz is located at the same site of the previous CHOOZ experiment.

The changes brought by Double Chooz with respect to CHOOZ aim at improving the statistical and systematic uncertainties of the latter. In order to reduce the systematics, a relative measurement by two identical detectors is done. The near detector, whose goal is the reactor antineutrino flux normalization and a measurement without the $\theta_{13}$ oscillation effect, is under construction 400 m from the cores and is expected to be delivered in 2013. The far detector is the one sensitive to the flavor oscillation and is already acquiring data since April 2011 1,050 m from the Chooz reactors. It benefits from an overburden of 300 mwe. A comparison between the two allows the extraction of the parameter $\sin^2 2\theta_{13}$. The detection method is the same than the one followed by CHOOZ: inverse $\beta$ decay in a gadolium-doped liquid scintillator. The novelty with respect to CHOOZ is the addition of a non-scintillating oil layer called buffer, which plays the role of shielding against radioactivity and incoming particles. It surrounds the whole inner detector, composed by the neutrino target and a $\gamma$-catcher volume, whose goal is to contain most of the scintillation photons. The signal is seen by 390 10 inches PMTs per detector. Finally, two muons detectors surround the whole detector.

The major backgrounds Double Chooz has to cope with are of two types: correlated and accidental. The accidental events background consist in fortuitous coincidences due to radioactivity $\gamma$ and neutrons, while the correlated events are physically related events mimicking the electron antineutrino signal, mostly cosmogenics isotopes, fast-neutrons, and stopping muons (*cf.* Section 6.3).

The first Double Chooz analysis has been performed on 102 days and found an indication for the disappearance of reactor electron neutrinos a kilometer away from the source [12]. This deficit was understood as resulting for a flavor oscillation linked to the mixing parameter $\theta_{13}$, and a rate and shape analysis implied $\sin^2 2\theta_{13} = 0.086 \pm 0.041\ (\text{stat}) \pm 0.030\ (\text{syst})$, or, at 90 % CL, $0.015 < \sin^2 2\theta_{13} < 0.16$. A second analysis on twice the statistics and with improved energy scale and background subtractions, released during the summer 2012, reported:

$$\sin^2 2\theta_{13} = 0.109 \pm 0.030\ (\text{stat}) \pm 0.025\ (\text{syst}), \tag{2.11}$$

for $\Delta m^2_{31} = 2.32 \times 10^{-3}$ eV$^2$ [11]. The data excluded the no-oscillation hypothesis at 99.8 % CL (2.9 $\sigma$) (*cf.* Chapters 6 and 7).

It is interesting to notice that Double Chooz is the only reactor antineutrino experiment which performed a rate and shape analysis. In that kind of analysis, both the deficit and the spectral distortion of neutrinos are considered. Moreover, rate only analysis on one hand, and rate and shape analysis on the other hand, give consistent results.

### Daya Bay

The Daya Bay experiment distances itself from Double Chooz by its size. It is located close to the two reactors of Daya Bay and four reactors of the LingAo nuclear power plants. The two plants are 1 km away from each other. The six cores amounts for 17.4 $GW_{th}$. Daya Bay uses the Double Chooz detection concept, first proposed for the Kr2Det project [136]. The detectors are placed on three separated sites: one near the LingAo reactors (480 m, 290 mwe), one near the Daya Bay reactors (360 m, 255 mwe), and one more far away, 1.6 km from the LingAo plant and almost 2 km from the Daya Bay one (left panel of Figure 2.8). Each near experimental hall is composed of two 20 tons identical detectors, while the far one have four of these detectors, benefiting from an overburden of more than 900 mwe. These multiple detectors at each site allows redundancy in the measurements. Although the design of the Daya Bay detectors is similar to the Double Chooz ones, the photomultipliers coverage is different: the top and bottom PMTs are replaced by reflective panels. Thus, each detector owns 192 8 inches PMTs.

With the high statistics that can provide six powerful nuclear reactors and the huge detection volumes, the Daya Bay experiment was design to probe really small values of $\theta_{13}$. Its expected sensitivity was of the order of 0.008 at 90 % CL after three years of data taking with all the detectors.

With only six detectors running (three at the far site) and 55 days of data, Daya Bay published in March 2012 the first measurement of $\theta_{13}$ following the T2K, MINOS, and Double Chooz observations at the end of 2011: $\sin^2 2\theta_{13} = 0.092 \pm 0.016$ (stat) $\pm$ 0.005 (syst), and $\theta_{13} = 0$ hypothesis was found to be disfavored at 5.2 $\sigma$ [29]. In June 4$^{\text{th}}$ 2012, with 139 days of data, the Daya Bay collaboration released a new measurement, disfavoring the no-oscillation hypothesis at 7.7 $\sigma$:

$$\sin^2 2\theta_{13} = 0.089 \pm 0.010 \text{ (stat)} \pm 0.005 \text{ (syst)}. \tag{2.12}$$

The installation of the remaing two detectors is expected to be completed during the summer 2012 and the data taking to begin with the full Daya Bay configuration in the fall.

### RENO

RENO is an experiment which uses the Double Chooz concept and is installed at the Yonggwang nuclear power station. It is composed of six cores with a total thermal power of 16.4 GW. The six reactors are lined up over 1.5 km (left panel of Figures 2.9). This experiment consists in two 15 tons detectors, one near at an average distance of the core of 290 m and one far at 1,380 m, with on overburden of 120 mwe and 450 mwe, respectively. This peculiar arrangement implies that the fraction of neutrino flux coming from each reactor is quite different in the near and far detectors. It leads to only a partial systematic cancellation (*cf.* Section 3.4). The expected sensitivity for $\sin^2 2\theta_{13}$ without oscillation was 0.02 at 90 % CL after three years of data taking with two detectors.

The data taking started on August 2011. The first physics results based on 228 days of data (up to March 25$^{\text{th}}$, 2012) was released on April 3$^{\text{rd}}$ 2012, and few days later revised on April 8$^{\text{th}}$ 2012 [25]. The no-oscillation hypothesis was disfavored at 4.9 $\sigma$ and their measurement is:

$$\sin^2 2\theta_{13} = 0.113 \pm 0.013 \text{ (stat)} \pm 0.019 \text{ (syst)}. \tag{2.13}$$

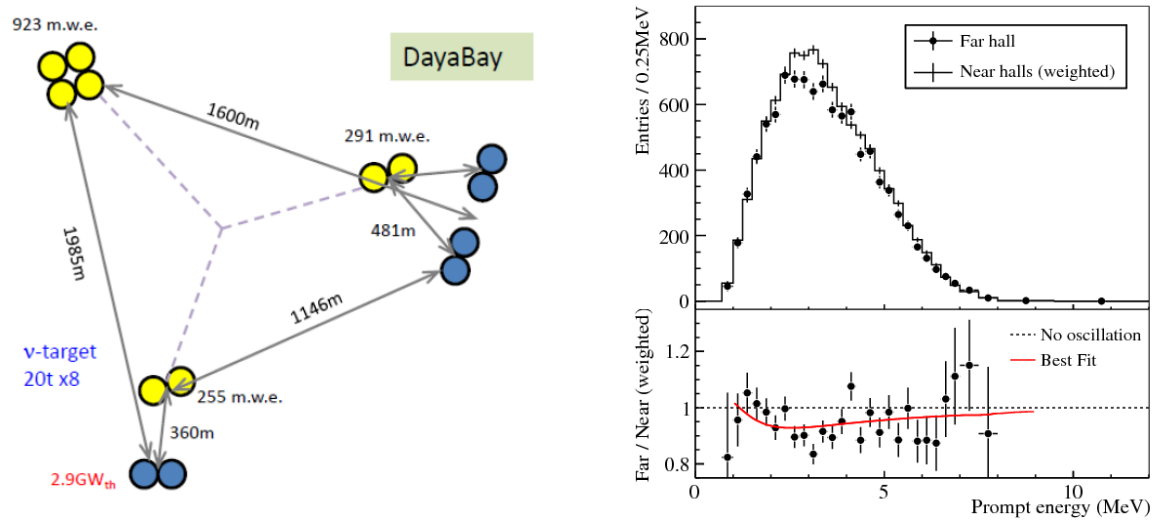


Figure 2.8: *(left) Scheme of the Daya Bay experiment arrangement. The yellow points are detectors, while the blue ones are reactors [127]. (top right) Measured prompt energy spectrum at the far detectors site compared with the no-oscillation prediction from the measurements of the near detectors. (bottom right) Ratio of measured and predicted no-oscillation spectra. The red curve is the best fit solution with* $\sin^2 2\theta_{13} = 0.092$ *obtained from the rate-only analysis. The dashed line is the no-oscillation prediction [29].*

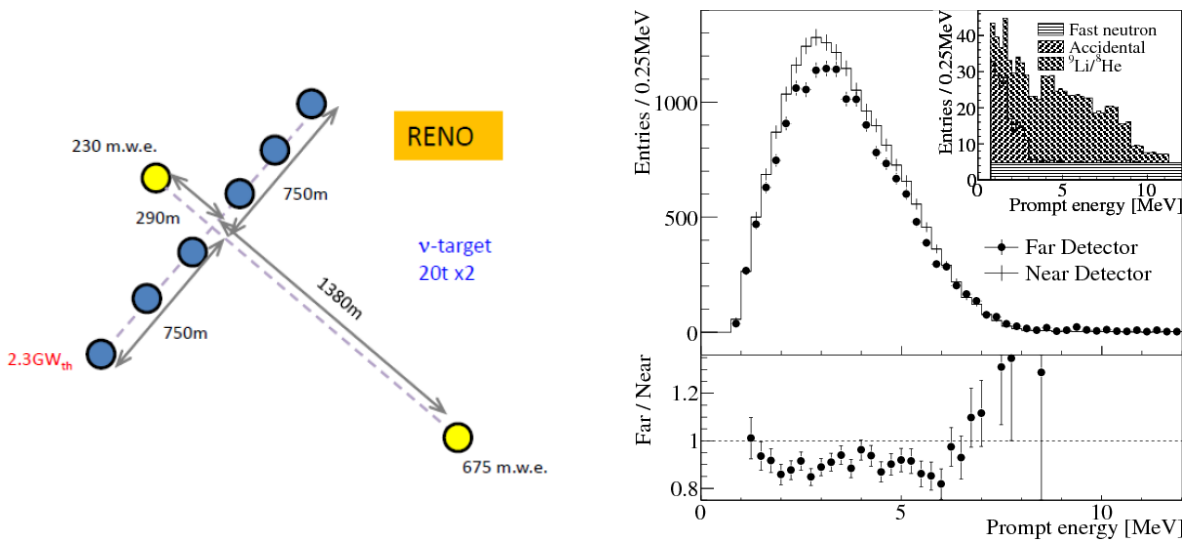


Figure 2.9: *(left) Scheme of the RENO experiment arrangement. The yellow points are detectors, while the blue ones are reactors [127]. (top right) Measured prompt energy spectrum at the far detector compared with the no-oscillation prediction from the measurements of the near detectors. (bottom right) Ratio of measured and predicted no-oscillation spectra [25].*

## 2.3 Anomalies

Even though the three neutrino flavors picture seems to perfectly embrace all the experimental evidences acquired so far, some of them has been deliberately put aside in the previous sections. Indeed, three so-called "anomalies" are clearly not compatible with the current phenomenological framework. The explanations require usually more than three neutrino mass eigenstates and are related to hypothetical sterile neutrinos.

#### Reactor antineutrino experiments anomaly

In order to predict the electron antineutrino flux emitted by a nuclear core, the measured electron spectra from the $\beta$ decays of fissile isotopes $^{235}$U, $^{239}$Pu, and $^{241}$Pu have to be converted using the energy conservation principle (*cf.* Section 3.2.3). The electron reference spectra have been measured at the ILL reactor (*Institut Laue-Langevin*, France). Recent improved calculations performed at Saclay showed that the previous flux determination was underestimated [147]. The new $\overline{\nu}_e$ fluxes are roughly 3 % more important. Other effects were found to increase this shift, like the new neutron lifetime measured value. The overall deficit finally amounted for 6-7 %.

This reevaluation had to be applied to all reactor neutrino experiments and a new analysis of their data was performed [141]. The mean ratio of observed event rate to predicted rate for all the reactor experiments located less than 100 m from the nuclear core was $0.976 \pm 0.024$ (Figure 2.10). With the new flux evaluation, this ratio shifts to

$$\mathrm{R} = \frac{\mathrm{N_{obs}}}{\mathrm{N_{th}}} = 0.943 \pm 0.023, \tag{2.14}$$

leading to a deviation from unity at 98.6 % CL, if only the short baseline reactors rate measurements are used. This was called the reactor antineutrino anomaly. These results can be well fitted as $\nu_e$ disappearance into a sterile neutrino state, with $\left|\Delta \mathrm{m}^2_{\mathrm{new}}\right| > 1.5$ eV$^2$ and $\sin^2 2\theta_{\mathrm{new}} = 0.14 \pm 0.08$ at 95 % CL.

This reactor anomaly affects all the reactor experiments without near detector for near/far comparisons, as they are highly sensitive to flux assumptions. The Bugey 4 anchor point method, presented in Sections 2.2.4.1 and 7.1, was used to fix the global normalization to the most precise reactor $\overline{\nu}_e$ flux measurement.

#### Gallium experiments source calibration anomaly

As explained in Section 2.2.2, the Gallex and SAGE experiments studied the solar neutrinos using gallium based detectors. The calibration of their detectors was performed using intense artificial radioactive sources of electron neutrinos, such as $^{51}$Cr (for Gallex and SAGE) and $^{37}$Ar (for SAGE only). As short baseline electron neutrino experiments, their data were analyzed again using the new spectra prediction [100, 141]. Both Gallex and SAGE observed an average deficit of events, that can be explained as a $\nu_e$ disappearance into a sterile neutrino state. The ratio of observed number of events over the expectation without oscillation is:

$$\mathrm{R} = \frac{\mathrm{N_{obs}}}{\mathrm{N_{th}}} = 0.86 \pm 0.06. \tag{2.15}$$

When combining both reactor neutrinos and gallium experiments, the no-oscillation hypothesis is disfavored at 99.8% CL (Figure 2.11).

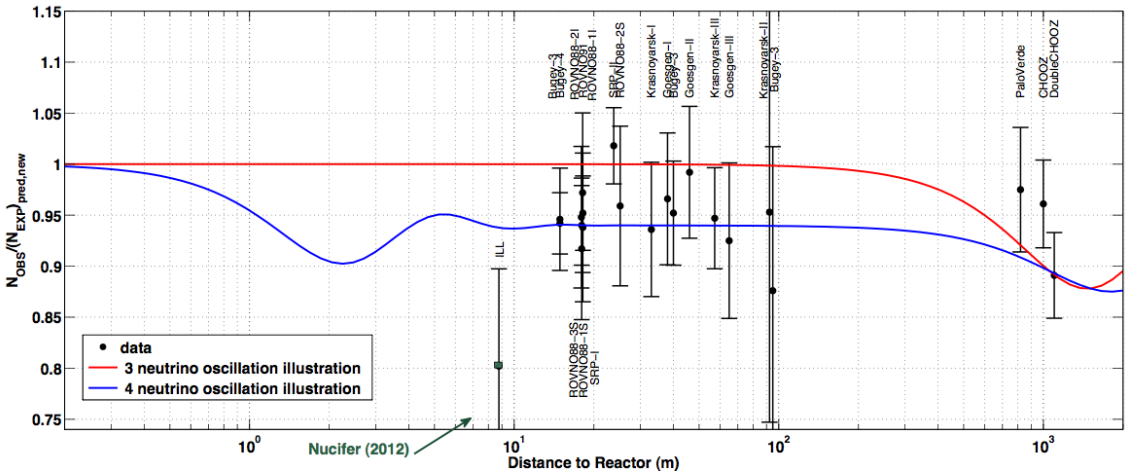


Figure 2.10: *Illustration of the short baseline reactor antineutrino anomaly: comparison of the experimental results and the prediction without oscillation, taking into account the new $\overline{\nu}_e$ spectra. The red line shows a possible 3 active neutrino mixing solution with $sin^2 2\theta_{13} = 0.06$ and the blue line displays a solution including a new mass state [141].*

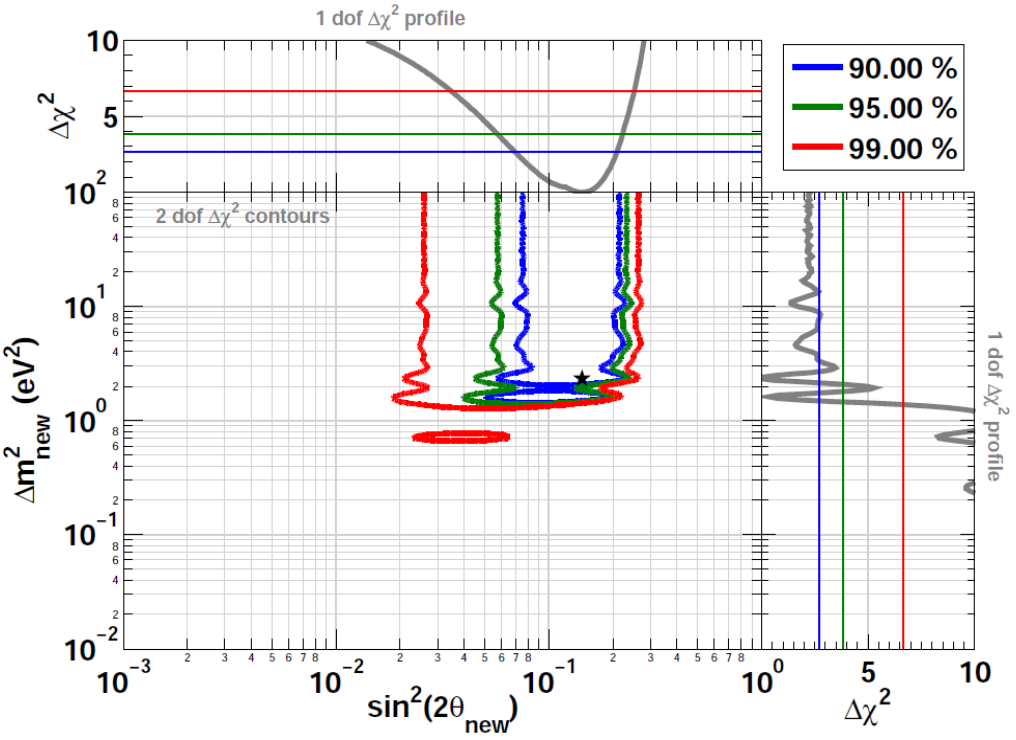


Figure 2.11: *Allowed regions projected in the $(sin^2 2\theta_{new}, \Delta m^2_{new})$ plane from the combination of reactor neutrino experiment, Gallex and SAGE calibration source experiments, MiniBooNE reanalysis of [100], and ILL-energy spectrum distortion [141].*

### LSND and MiniBooNE anomalies

The LSND (Liquid Scintillator Neutrino Detector) experiment started in 1993 and ended in 1998. The 167 tons detector filled with liquid scintillator was located in the Los Alamos Neutron Science Center. Using a 800 MeV proton beam accelerator, the experiment studied neutrinos coming from the decay of muons $\mu^+ \rightarrow e^+ + \nu_e + \overline{\nu}_\mu$ at rest and from the decay of pions $\pi^+ \rightarrow \mu^+ + \nu_\mu$ in flight. The $\overline{\nu}_\mu \rightarrow \overline{\nu}_e$ flavor oscillation was investigated.

In 2001, LSND showed that an excess of events was observed in the $\overline{\nu}_\mu \rightarrow \overline{\nu}_e$ transition search [21]. This excess may be interpreted as due to $\overline{\nu}_\mu$ disappearance into $\overline{\nu}_e$ flavor state. However, the fitted difference of squarred masses was found to be much larger than the solar $\Delta m^2_{\text{sol}} \simeq 7 \times 10^{-5}$ eV$^2$ and the atmospheric ones $\Delta m^2_{\text{atm}} \simeq 2 \times 10^{-3}$ eV$^2$, as it was: $\Delta m^2_{\text{LSND}} > 0.1$ eV$^2$. Such a value means rapid oscillations and cannot be explained with only three massive neutrinos.

The MiniBooNE (Mini Booster Neutrino Experiment) was built to test the evidence of neutrino oscillations from the LSND experiment. It did this by searching for $\nu_e$ appearance in a $\nu_\mu$ beam, with a distance source-detector $L$ and an average neutrino energy $E$ both 17 times larger than LSND. This led to a comparable $L/E$ parameter. Also, the same search as LSND was performed: $\overline{\nu}_\mu \rightarrow \overline{\nu}_e$. Although the results for antineutrinos are fairly in agreement betweeen the two experiments, the neutrino chanel is inconsistent with them [22, 23]. Moreover, this anomaly seems to come from the low energy part of the MiniBooNE spectrum, which is why the future MicroBooNE detector will investigate this observed low energy excess events [115].

### Sterile neutrino search

Even though they are only indications, these anomalies are intriguing and require new experiments. The reactor antineutrino anomaly could be tested with new detectors located at a very short distance of a reactor (typically a few meters), or using a very active neutrino or antineutrino source really close or even inside an existent neutrino detector (like KamLAND for instance). Several projects are ongoing, but three of them will be briefly presentend.

A detector which could probe the reactor antineutrino anomaly is Nucifer [63]. This compact, miniature Double Chooz (1 m$^3$ Gd loaded scintillator), was built for non-proliferation purpose and aims at controlling the operation of nuclear reactors via the detection of their neutrino flux (Figure 2.12). It is now running at the Osiris nuclear reactor, in Saclay, and being calibrated. Although it is not optimized for the reactor antineutrino anomaly, Nucifer can bring extra information as it is the closest experiment from a compact nuclear core ($\sim$ 7 m) ever built. The Figure 2.13 displays the results of a simulation for $\sin^2 2\theta_{\text{new}} = 0.15$ and $\Delta m^2_{\text{new}} = 2.4$ eV$^2$, indicating the discovery potential of Nucifer.

The STEREO project aims at observing an unambiguous signal of a new neutrino as it must show an oscillation pattern related to the large $\Delta m^2_{\text{new}}$ [2]. It would consist of a liquid scintillator detector with a 1 m$^2$ section and a length of 2.5 m, oriented toward a compact nuclear reactor core (typically the ILL one). With emitted electron antineutrinos of a few MeV, the expected oscillation length is of the order of 1 m. It could therefore resolve oscillation paterns if its resolution is well below 1 m. This seems to be feasible considering the results of the ongoing Nucifer calibration campaign and the fact that these two detectors are quite similar.

CeLAND is a source experiment which proposed to search for a fourth neutrino with a PBq antineutrino source ideally placed inside an existing neutrino detector, like KamLAND or SNO, or very close to it [61, 130].

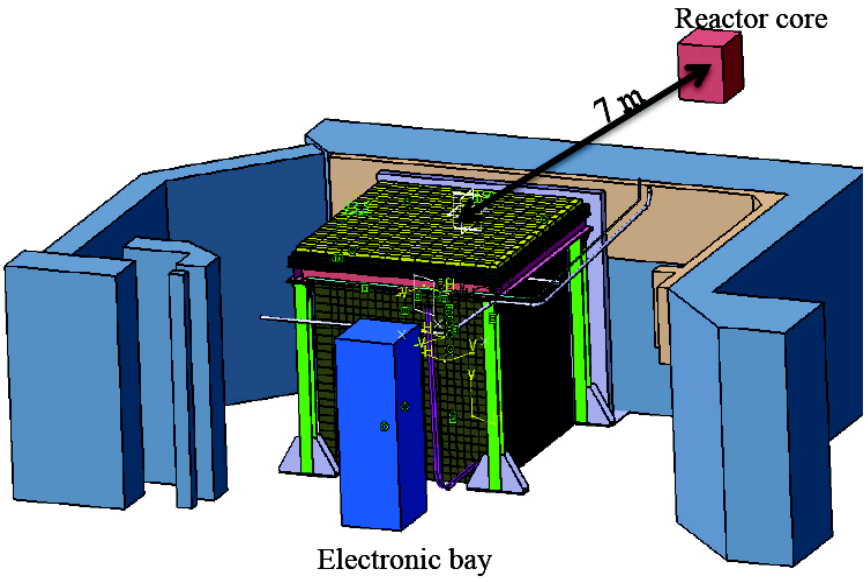


Figure 2.12: *Technical drawing of the Nucifer detector and the experimental hall at the Osiris reactor [63].*

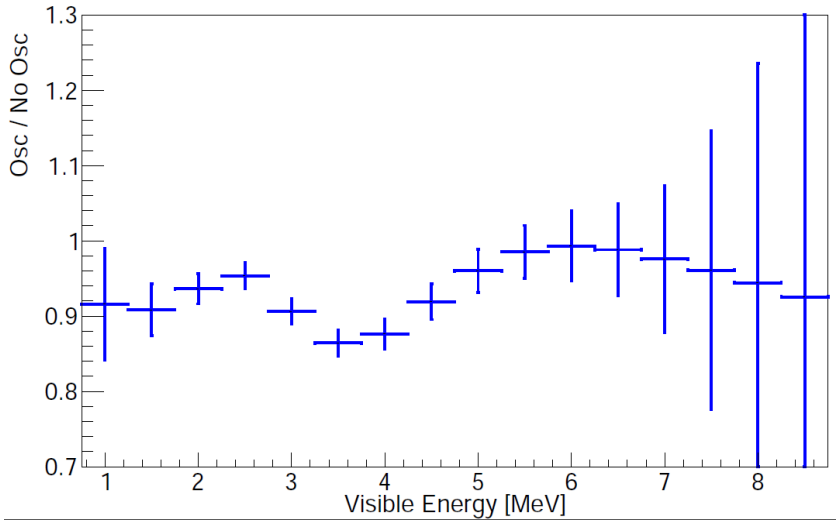


Figure 2.13: *Ratio of the expected number of events with oscillation over the expected number of events without oscillations, per visible energy bins, from preliminary simulations, with* $sin^2 2\theta_{new} = 0.15$ *and* $\Delta m^2_{new} = 2.4\ eV^2$.

# Chapter 3

# $\theta_{13}$ at Double Chooz

*A neutrino walks into a bar.*
*The bartender says: "We don't serve neutrinos in here."*
*And the neutrino answers: "Hey, I was just passing through!"*

Brian Malow,
Earth's Premier Science Comedian.

The Double Chooz experiment consists of two identical detectors measuring the flux of electron antineutrinos coming from the Chooz B nuclear reactors in the French Ardennes. It aims at measuring the unknown leptonic parameter $\theta_{13}$. The farthest detector from the source of electron antineutrinos, which is sensitive to $\theta_{13}$, is already taking data since April 2011. The near detector, whose goal is the reactor antineutrino flux normalization and a measurement without the $\theta_{13}$ oscillation effect, is under construction and is expected to be delivered in 2013.

This chapter presents the Double Chooz concept adopted to improve the former limit on $\theta_{13}$. The antineutrino source is described as well as the chosen detection method, which lead to specific expected signal and backgrounds. The Double Chooz detector itself is also presented. It has been designed to improve the signal over background ratio and to lower the systematic uncertainties associated to our signal.

## 3.1 Experimental site and laboratories

Between 1967 and 1991, the French Electricity Company EDF (*Électricité de France*) ran the first Pressurized Water Reactor (PWR) ever built in France. Called Chooz A it was located one kilometer away from the actual Chooz B site under the hill boarding the Meuse river. The decommissioning of this reactor began in 2007 and should be conducted until 2020-2025. However, some galleries were already available in 1996 when the former CHOOZ experiment decided to build its detector and hence benefit from the local overburden, a natural way to reduce cosmic muon-related backgrounds [30].

The Double Chooz experiment consists of two identical detectors studying the flux of electron antineutrinos coming from the two nuclear reactors of Chooz B (Figure 3.1). Called reactor B1 and reactor B2, they are 165 m away from each other. The far detector is located at the exact place where the CHOOZ experiment built its single detector, *i.e.* 1,115 and 998 m away from reactor B1 and reactor B2, respectively. The near detector, which aims at monitoring the reactor antineutrino flux before oscillation, will be 466 and 351 m away from the cores. The respective

weighted distances of the far and near Double Chooz detectors are then of the order of 1,050 and 400 m with respect to the nuclear reactors.

At the end of a 200 m tunnel, the far neutrino laboratory is located in a 20 m long, 7 m large, and 3.5 m high (at most) cave (Figure 3.2). The existing room, with a useful overburden of 300 meters-water-equivalent (mwe) of 2.8 g/cm$^3$ rock, allowed the collaboration to save money and time on excavation and civil engineering. However, the narrow available space turned out to be a limiting factor for the detector integration speed. The near laboratory, built from scratch, was designed larger to facilitate and fasten the near detector integration. It has an overburden of 150 mwe. The digging of the tunnel began in April 2011 and the laboratory excavation should be finished in November 2012. The near detector construction will be completed in 2013.

## 3.2 Source of electron antineutrinos

### 3.2.1 Chooz power plant and PWR principles

Double Chooz is located near the Chooz B nuclear plant on the Meuse river's edge, in the Champagne-Ardennes French region close to the Belgium border (Figure 3.1). The two reactors of Chooz B are among the most recent and the most powerful French N4 PWRs [1] delivering a maximum total thermal power of $2 \times 4.25$ GW$_{\text{th}}$. The power plant is operated by the electricity company EDF. Reactors B1 and B2 construction began in 1984 and 1985, and they both started operation between 1996 and 1997 [114].

In a PWR, the nuclear fuel is made of pellets of weakly enriched uranium 235 ($^{235}$U) in the form of uranium dioxide ($UO_2$). The natural isotopic composition of uranium is 99.28 % of $^{238}$U, 0.71 % of $^{235}$U, and less than 0.01 % of $^{234}$U, while the enriched fuel contains 3.45 % of $^{235}$U. The cylindrical pellets are stacked inside corrosion-resistant zirconium tubes which are backfilled with helium to improve the heat conduction and detect possible leakages. These fuel rods are grouped into fuel assemblies, called fuel bundles, and are used to build the core of the reactor. The Chooz B N4 reactor core is made of 205 fuel bundles, each of them containing 264 rods. This is where the nuclear chain reaction occurs: under the action of thermal neutrons (whose energy is roughly a few tens of meV), fissile isotopes such as $^{235}$U are broken into unstable lighter nuclei, releasing energy, electron antineutrinos from $\beta$ decays of these latter, and neutrons that will sustain the reaction (*cf.* Section 3.2.2 and Figure 3.3).

The chain reaction brings the fuel assemblies to very high temperature. The goal of the reactor primary circuit is to recover the heat produced using a coolant. It is made of pressurized water (155 bars, to prevent water from boiling) that flows among the rods. This water plays also the role of moderator, as it slows down the neutrons. The hot primary coolant is then pumped into a heat exchanger called the steam generator, where heat is transferred to the lower pressure secondary coolant, which evaporates. This is thus accomplished without mixing the two fluids. It is important since the pressurized water in contact with the assemblies might be activated even though the reaction products should stay confined into the zirconium tubes.

The pressurized steam of the secondary circuit is fed into a turbine which drives an electrical generator connected to the electric grid for distribution. After passing through the turbine, the secondary coolant is cooled down and condensed into water before being fed back into the steam generator to start a new cycle.

For a more detailed explanation of a PWR functioning, see [188].

[1] N4 corresponds nowadays to the latest commercial reactor design that should soon be overtaken by the forthcoming Evolutionary Power Reactors (EPR).

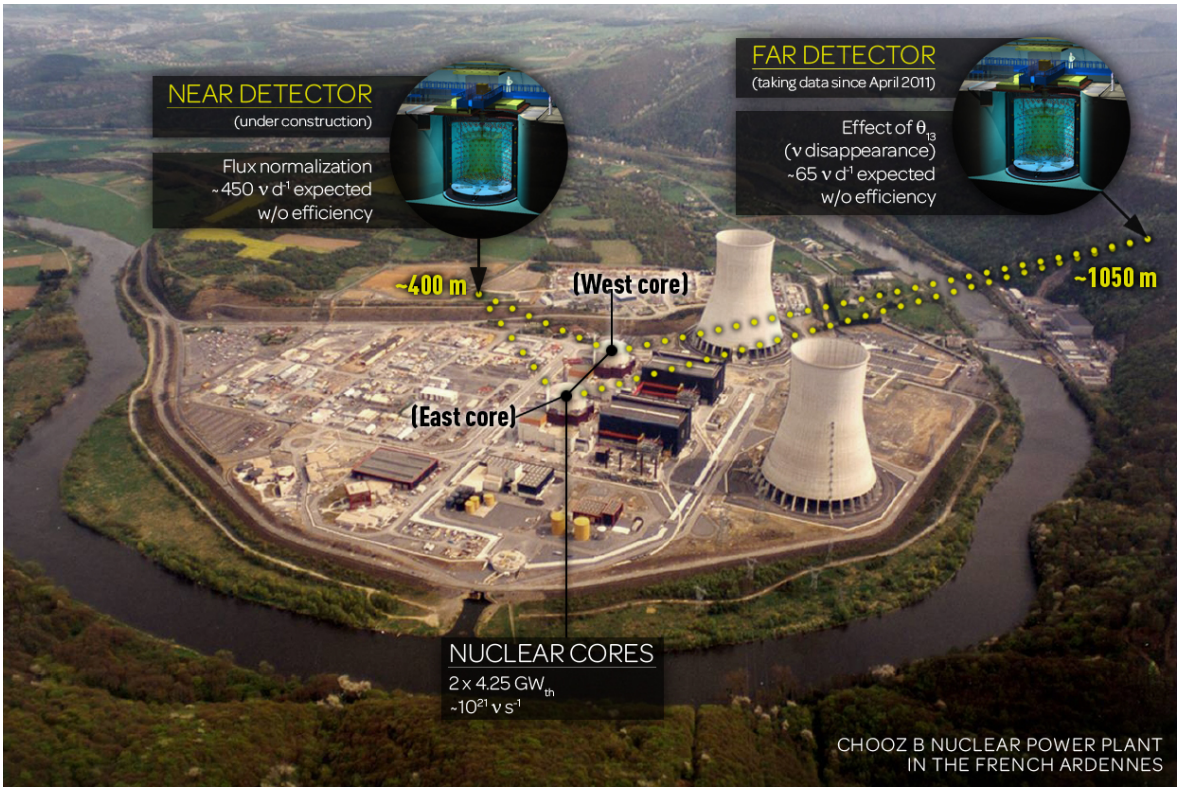


Figure 3.1: *The Double Chooz experimental site. The two N4 Chooz B reactors, the Meuse river, and the location of both near and far detectors are displayed.*


Figure 3.2: *Picture of the tunnel underneath the hill (left) leading to the Double Chooz far laboratory (right). The installation was almost completed when the picture was taken.*

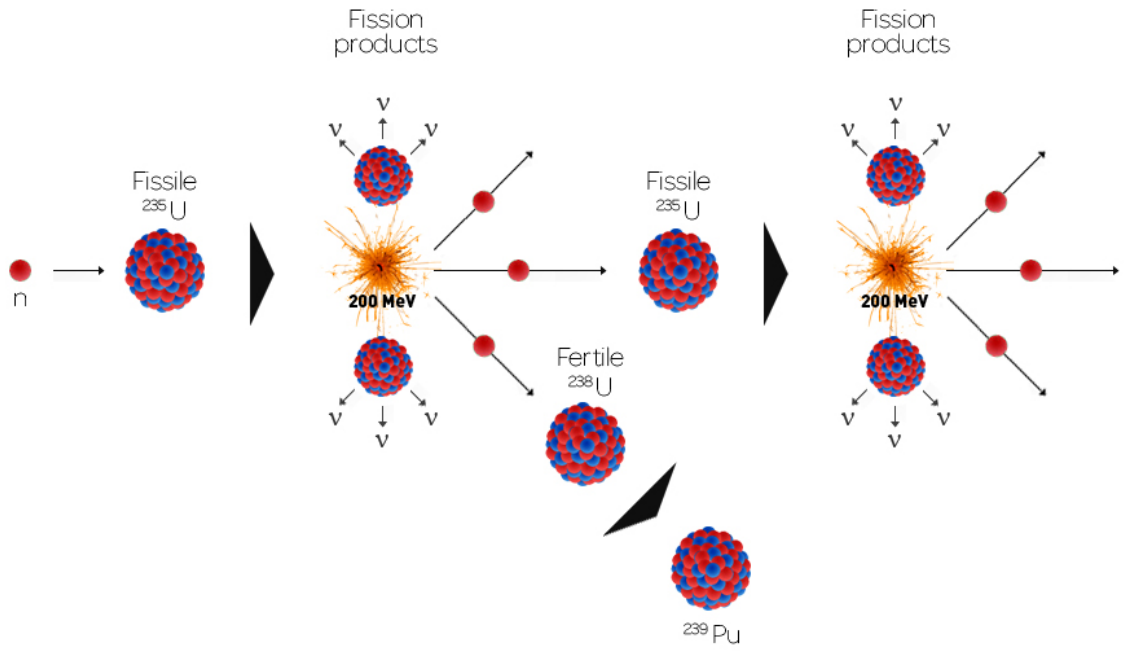


Figure 3.3: *Chain reaction of $^{235}U$ fission self-sustained by the emission of neutrons.*

### 3.2.2 Electron antineutrino production

Nuclear power plants produce energy by chain reactions of fission of the enriched $^{235}$U contained in the $UO_2$ fuel (Figure 3.3). $^{235}$U is a fissile isotope. It will transform into a short unstable state $^{236}U^*$ under the action of thermal neutrons, and split into two neutron-rich lighter nuclei, called fission products. This reaction implies an energy release of 200 MeV and the emission of two or three neutrons which sustain the chain reaction by breaking other $^{235}$U nuclei after being thermalized in water. The majority of the fission products are unstable. On average, they will undergo three $\beta$ decays before getting to a stable nucleus and therefore produce a total mean number of six electron antineutrinos.

The $^{235}$U isotope is not the only fuel component producing electron antineutrinos. Three other elements contribute notably: $^{238}$U, $^{239}$Pu, and $^{241}$Pu. $^{238}$U is a fertile nucleus and transforms, by capture of a fast-neutron (whose energy is above 1 MeV) into an unstable isotope $^{239}$U, which decays into $^{239}$Pu after two successive $\beta$ decays:

$$\mathrm{n} + {}^{238}\mathrm{U} \rightarrow {}^{239}\mathrm{U} \rightarrow {}^{239}\mathrm{Np} \rightarrow {}^{239}\mathrm{Pu}. \tag{3.1}$$

$^{241}$Pu is produced by two successive neutron captures on $^{239}$Pu:

$$\mathrm{n} + {}^{239}\mathrm{Pu} \rightarrow {}^{240}\mathrm{Pu} + \mathrm{n} \rightarrow {}^{241}\mathrm{Pu}. \tag{3.2}$$

These different reactions explain why the fuel composition evolves through time: as shown on Figure 3.4, the fission rates of $^{239}$Pu and $^{241}$Pu increase while the $^{235}$U one decreases. The rate and the spectrum shape of the emitted $\overline{\nu}_e$ differ significantly between the different nuclei,

| Isotope | Number of $\overline{\nu}_e$ per fission | Energy released per fission (MeV) |
|---|---|---|
| $^{235}$U | 1.92 ± 0.036 | 201.7 ± 0.6 |
| $^{238}$U | 2.38 ± 0.048 | 205.0 ± 0.9 |
| $^{239}$Pu | 1.45 ± 0.030 | 210.0 ± 0.9 |
| $^{241}$Pu | 1.83 ± 0.035 | 212.4 ± 1.0 |

Table 3.1: *Total number of electron antineutrinos produced and energy released by fission above the detection energy threshold of 1.8 MeV, for the four main isotopes in a PWR [113].*

especially for the two major fissile isotopes, $^{235}$U and $^{239}$Pu. Table 3.1 shows the total number of electron antineutrinos produced per fission for the four main isotopes of a PWR above the detection energy threshold of 1.8 MeV [2], as well as the released energy per fission. Taking into account the change in the fission rate as a function of time (Figure 3.4) and considering that the reactor runs at constant power, the number of emitted electron antineutrinos is then expected to decrease with time until the reactor is refueled. This is known as the burnup effect.

As explained in the previous paragraphs, the Chooz B reactors produce a maximum thermal power of $2 \times 4.25$ GW$_{\text{th}}$. Each fission reaction releases on average 6 $\overline{\nu}_e$ and an energy of 200 MeV. The nuclear power plant of Chooz B is a pure and intense source of electron antineutrinos with no other flavor component, allowing a direct measurement of $\theta_{13}$ (*cf.* Section 2.2.4). The total number of emitted electron antineutrinos per second is then expected to be, in a $4\pi$ solid angle:

$$\mathrm{N}_{\overline{\nu}_e}^{\text{emit}} \simeq \frac{6 \times 2 \times 4,250}{200 \times 1.6\ 10^{-19}} \sim 10^{21}\ \mathrm{s}^{-1}. \tag{3.3}$$

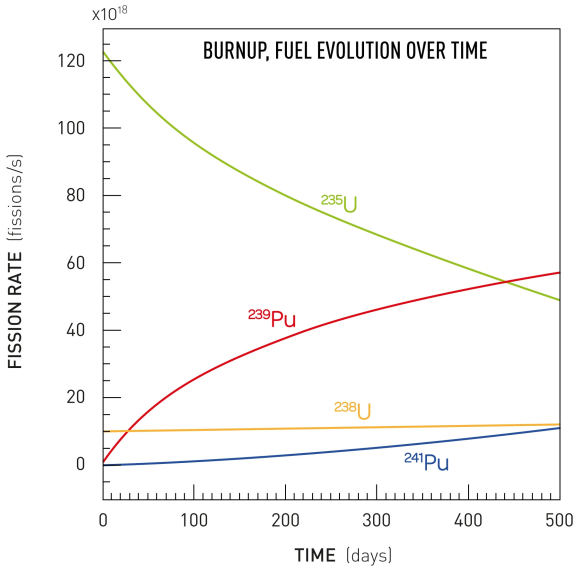


Figure 3.4: *Simulated fission rates as a function of time for the four main isotopes in a PWR running at constant power [144].*

[2] This threshold corresponds to the reaction of inverse $\beta$ decay on free proton (*cf.* Section 3.3.1).

### 3.2.3 Electron antineutrino spectrum

In order to compute an expected antineutrino spectrum, the energy conservation principle for a $\beta$ decay is used. Indeed, this process is understood as a two body decay, where the total energy is conserved and carried along by the electron and the antineutrino. The spectra of the emitted electrons and the electron antineutrinos are expected to be both continuous, from zero to the endpoint, the $Q_\beta$-value of the reaction. Therefore, by measuring the energy of one particle, say the electron one E, and by knowing the decay $Q_\beta$-value, the energy of the antineutrino $E_{\nu_e}$ can be easily computed with $Q_\beta = E + E_{\nu_e}$. Additionnal corrections, as radiative corrections, are however required to strictly respect the energy conservation.

A tremendous work had been performed at the ILL reactor (*Institut Laue-Langevin*, France) in order to measure the $\beta$ spectra of $^{235}$U, $^{239}$Pu, and $^{241}$Pu isotopes [107, 165]. The idea was to use thermal neutrons emitted by the nuclear core to induce fissions of these latter isotopes within a high resolution spectrometer. Thin foils cointaining the fissile isotopes were exposed to a thermal neutron flux placed 80 cm away from the core. Part of the electrons produced by $\beta$ decay were then detected a few meters away in the spectrometer, which provided an uncertainty lower than a percent on the electrons spectra measurement. The statistical error could also be kept below the percent level for the whole energy range except in the high energy region (Figure 3.5, right). The main contribution to the error is the absolute normalization of the flux, inducing an uncertainty of roughly 3 % on the total number of $\overline{\nu}_e$. The $^{238}$U spectrum had not been measured at ILL because this isotope is not fissile under the action of thermal neutrons. $^{238}$U is indeed a fertile nucleus, whose fission is triggered by fast-neutrons.

Two approaches have been developed in order to predict the electron antineutrino spectrum emitted by a nuclear reactor from $\beta$ spectra measurements. The historical way, from Schreckenbach *et al.*, is based on an effective method [165]. Their predictions have been used in every past reactor antineutrino experiments to compute the $\overline{\nu}_e$ flux normalization since they were the most accurate at that time: the uncertainty on the neutrino rate was around 3 %. The conversion procedure used by Schreckenbach *et al.* was based on fitting the total ILL measured electron spectra by 30 "virtual" $\beta$-branches (*i.e.* not associated to any real $\beta$ decay) and using the energy conservation to recover the $\overline{\nu}_e$ energy distributions. To each $\beta$-branch corresponds an electron spectrum and hence an antineutrino one, with a $Q_\beta$. The 30 $Q_\beta$ values were chosen according to the shape of the total $\beta$ spectrum obtained from $^{235}$U, $^{239}$Pu, and $^{241}$Pu.

However another approach exists and is called *ab initio*, or microscopic. It makes uttermost use of nuclear database. This approach together with theoretical predictions for missing information yielded a 30 to 50 % uncertainty on the $\overline{\nu}_e$ spectra prediction in the eighties. A new approach developed at Saclay mixes both *ab initio* and effective methods [147].

The *ab initio* approach is based on a microscopic description of all the real $\beta$-branches involved. In this framework, the total spectrum $S_{tot}(E)$ emitted by a reactor, where E is the electron kinetic energy, is the sum of the four $^{235}$U, $^{238}$U, $^{239}$Pu, and $^{241}$Pu nuclei contributions, and can be expressed as follows:

$$S_{tot}(E) = \sum_{k=1}^{4} \alpha_k(t) \times S_k(E), \tag{3.4}$$

where the sum is performed on k, the four fissioning isotopes, $\alpha_k(t)$ is the number of fissions of the $k^{th}$ isotope at a time t, and $S_k(E)$ its corresponding $\beta$ spectrum normalized to one fission.

Getting $S_k(E)$ is far from being simple: to compute this spectrum, all the fission products contributions have to be taken into account. The $\beta$ spectrum of an isotope is then usually expressed as the following sum:

$$S_k(E) = \sum_{p=1}^{N_p} \mathcal{A}_p(t) \times S_p(E), \tag{3.5}$$

where the index p runs over all the fissions products of the $k^{th}$ isotope, $\mathcal{A}_p(t)$ is the activity of the $p^{th}$ fission product at the time t normalized to one fission of the $k^{th}$ isotope, and $S_p(E)$ is the $\beta$ spectrum of the $p^{th}$ fission product, which is itself a sum of the $N_b$ $\beta$-branches involved:

$$S_p(E) = \sum_{b=1}^{N_b} BR_p^b \times S_p^b \left(Z_p, A_p, E_{0p}^b, E\right), \tag{3.6}$$

where $BR_p^b$ and $E_{0p}^b$ are respectively the branching ratio and the endpoint energy of the $b^{th}$ branch of the $p^{th}$ fission product ($E_0$=$E_{\nu_e}$ + E). $Z_p$ and $A_p$ are the charge and atomic number of the nucleus undergoing the $\beta$ decay. The spectrum $S_p^b$ of the $b^{th}$ branch can be expressed as:

$$S_p^b = K_p^b \times \mathcal{F}(Z_p, A_p, E) \times pE(E - E_{0p}^b)^2 \times C_p^b(E) \times \left(1 + \delta_p^b(Z_p, A_p, E)\right), \tag{3.7}$$

where $K_p^b$ is a normalization factor, $\mathcal{F}$ the Fermi function that corrects for the deceleration of the electron in the Coulomb field created by the $Z_p$ positive charges, $pE(E - E_{0p}^b)^2$ the phase space factor, $C_p^b$ a shape factor that brings extra energy dependence due to the nuclear matrix element connecting the two nuclear levels of the $\beta$ decay, and the last one is a correction factor,

$$\delta_p^b(Z_p, A_p, E) = \delta_{QED}(E) + A_C(Z_p, A_p) \times E + A_W \times E, \tag{3.8}$$

where $\delta_{QED}$ corrects for real and virtual photons radiations by the charged fermion lines of the $\beta$ decay vertex (that basically implies: $E_0$=$E + E_{\nu_e} + E_\gamma$, the $A_C$ term is a Coulomb correction induced by the finite size of the decaying nucleus, and $A_W$ is the weak magnetism correction [147, 184]. All these theoretical basis can be found in greater detail in [144].

The *ab initio* approach was first used in [147] to lower the systematic uncertainties of the effective method conversion procedure. These new calculations used all the $\beta$-branches measurements available in the ENSDF nuclear [83] to reconstruct the $S_k$ spectra. The 30 virtual $\beta$-branches of the effective method were replaced by 10,000 measured $\beta$-branches, which represent 95 % of the total measured electron spectrum from the ILL measurements. The remaining 5 % were then fitted with 5 virtual branches using an effective model as for Schreckenbach's original prediction.

This new technique induced a mean systematic normalization of +3 % with respect to the previous estimation of [165] (Figure 3.5, left). This shift is understood as arising from the old conversion method itself. Indeed, the use of virtual $\beta$-branches induces non-physical corrective terms, such as a wrong $Z_p$ distribution or an energy dependent effective linear correction of the ILL data, while the new calculations use corrections at the $\beta$-branch level.

The increase of the mean flux by 3 % made it necessary to reevaluate all reactor antineutrino experiments for the past 25 years. The Saclay group did so and found out a significant decrease of the normalized ratio of observed to expected event rates in all previous reactor experiments performed below 100 m from the cores [141], leading to the so-called reactor antineutrino anomaly. Although this deficit might be explained by our lack of understanding of reactor physics, it can also be interpreted as a suppression of the electron antineutrino rate at short distance, a consequence of standard neutrino to sterile neutrino oscillation, with $|\Delta m^2_{new}| \gg \Delta m^2_{31}$.

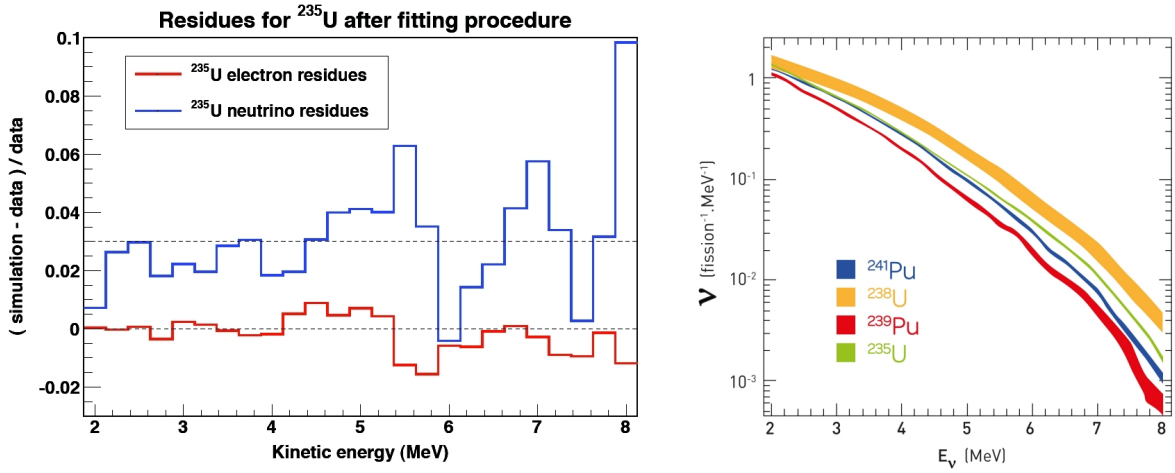


Figure 3.5: *(left)* $^{235}U$ *residuals between the total electron and* $\overline{\nu}_e$ *spectra as computed by the ILL group [165] and by the Saclay group [147]. The residuals are below 1 % for electrons (red), while they show a mean shift of +3 % for antineutrinos (blue) [144]. (right) Estimated emitted* $\overline{\nu}_e$ *spectra for the four main isotopes in a PWR taken from [112, 147]. Thickness of the lines corresponds to uncertainties.*

## 3.3 Detection of $\overline{\nu}_e$

### 3.3.1 Inverse $\beta$ decay reaction

In the Standard Model of particle physics, neutrinos only interact by electroweak processes, via the exchange of charged or neutral gauge bosons (*cf.* Section 1.2.1). Electron antineutrinos can then interact through elastic scattering on electrons, with a $W^-$ or a $Z^0$ boson production for the charged and the neutral current component, respectively. Electron antineutrino can also scatter on a nucleon within a nucleus. Depending on the neutrino incident energy, the process can be elastic, quasi-elastic, or deep-inelastic, and implies the nucleon to be ejected from its nucleus or even broken apart in a spray of light hadrons. The scattering on a nucleon with the exchange of a Z boson is called neutral current (NC), while the interaction on a proton, called charged current reaction (CC), happens with the exchange of a W boson (Figure 3.6).

The elastic scattering on electron has a small cross-section and no real discriminating signature, making it hard to detect. The NC scattering on a nucleon is even more tricky to detect since it consists in studying the nucleus recoil, of the order of the keV. However, the CC interaction on proton, also called inverse $\beta$ decay (Figure 3.7), gives a clear signature of an $\overline{\nu}_e$ interaction:

$$\overline{\nu}_e \; + \; p \; \rightarrow \; e^+ \; + \; n. \tag{3.9}$$

The threshold of this reaction depends on the nucleus whose the proton belongs to. On a free proton of mass $m_p$, assumed at rest, if one neglects the $\overline{\nu}_e$ mass, the center-of-mass energy of the reaction is:

$$s = 2E_{\overline{\nu}_e} m_p + m_p^2, \tag{3.10}$$

The energy threshold becomes then:

$$E_{\overline{\nu}_e}^{thres} = \frac{(m_e + m_n)^2 - m_p^2}{2m_p} \simeq 1.806 \text{ MeV}, \tag{3.11}$$

where $m_e$ and $m_n$ are respectively the positron and neutron masses. The threshold is 14 MeV in the case of an interaction on $^{12}C$, 11.4 MeV on $^{16}O$, and 4 MeV on deuterium. The hydrogen is the only conceivable target for Double Chooz, since $\overline{\nu}_e$ oscillations due to $\theta_{13}$ mostly happen below 6 MeV for a detector placed one kilometer away from the source. Indeed, the reactor antineutrinos spectrum typically goes up to roughly 8 MeV and its product with the inverse $\beta$ decay cross-section peaks around 4 MeV (*cf.* Section 3.2.3 and Figure 3.8).

Using simple kinematics, the relation between the positron energy $E_{e^+}$ and the antineutrino energy $E_{\overline{\nu}_e}$ in an inverse $\beta$ decay is:

$$E_{\overline{\nu}_e} = \frac{2m_p E_{e^+} + m_n^2 - m_p^2 - m_e^2}{2\left(m_p - E_{e^+} + \sqrt{E_{e^+}^2 - m_e^2}\cos\theta\right)}, \tag{3.12}$$

where $\cos\theta$ is the angle between the $\overline{\nu}_e$ and the positron directions. Since $E_{e^+}/m_n \ll 1$ is always true, the equation (3.12) is well approximated by

$$E_{\overline{\nu}_e} = E_{e^+} + \Delta + \mathcal{O}(E_{e^+}/m_n), \tag{3.13}$$

where $\Delta$ is the difference between the neutron and the proton masses, therefore

$$\Delta = m_n - m_p \simeq 1.293 \text{ MeV}. \tag{3.14}$$

In a liquid scintillator detector, the positron annihilation with an electron of the medium is observed at the same time as its kinetic energy loss. Hence the visible energy $E_{vis}$ in the detector is the sum of the positron energy and the electron rest mass, and is related to the $\overline{\nu}_e$ energy through:

$$E_{vis} = E_{e^+} + m_e \simeq E_{\overline{\nu}_e} - \Delta + m_e \simeq E_{\overline{\nu}_e} - 0.782\ MeV. \tag{3.15}$$

The threshold of the inverse $\beta$ decay reaction $E_{\overline{\nu}_e}^{thres}$= 1.806 MeV corresponds to a threshold in visible energy of $E_{vis}^{thres} = 2m_e = 1.022$ MeV.

### 3.3.2 Expected signal and backgrounds

#### Electron antineutrino rate

In Double Chooz, the reactor electron antineutrinos are detected through inverse $\beta$ decay in a liquid scintillator, where the proton targets come from hydrogen atoms of alkane hydrocarbons.

The cross-section of the interaction of a $\overline{\nu}_e$ on a free proton [185] as a function of the positron energy $E_{e^+}$ can be expressed by the following formula:

$$\sigma(E_{e^+}) = \frac{2\pi^2\hbar^3}{m_e^5 f \tau_n} p_{e^+} E_{e^+} (1 + \delta_{rad} + \delta_{WM}), \tag{3.16}$$

where the terms $\delta_{rad}$ and $\delta_{WM}$ are respectively the radiative and weak magnetism corrections (of the order of a few percents), $f$ the phase factor of the free neutron decay, and $\tau_n$ the neutron lifetime [3]. To the first order, this cross-section can then be expressed as a function of the $\overline{\nu}_e$ energy:

[3] The most up-to-date value is used: $\tau_n = 881.5 \pm 1.5$ s, from [149].

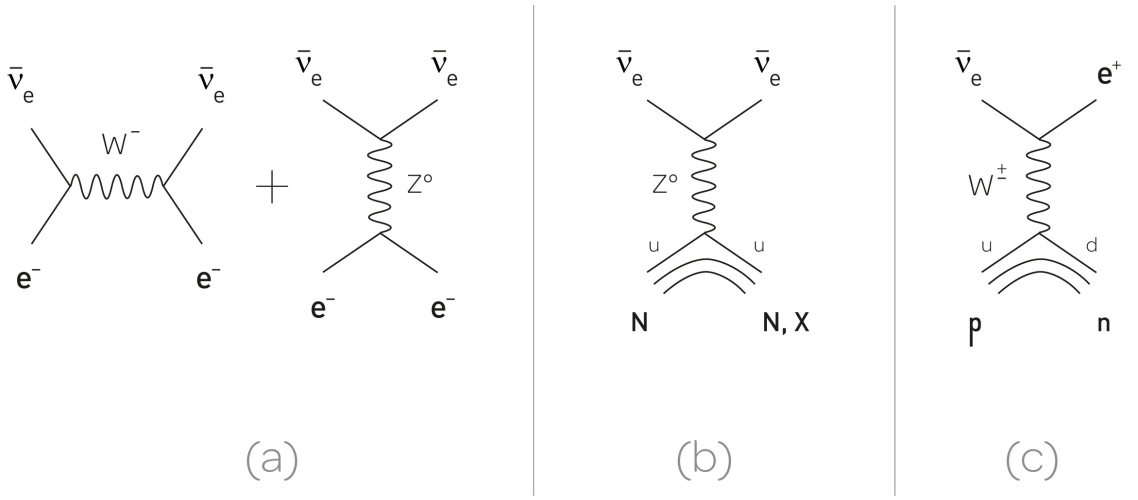


Figure 3.6: *Feynman diagrams of electron antineutrino interactions through (a) elastic scattering on electron (neutral and charged components), (b) neutral current on a nucleon, and (c) charged current on a proton of a nucleus (inverse $\beta$ decay).*

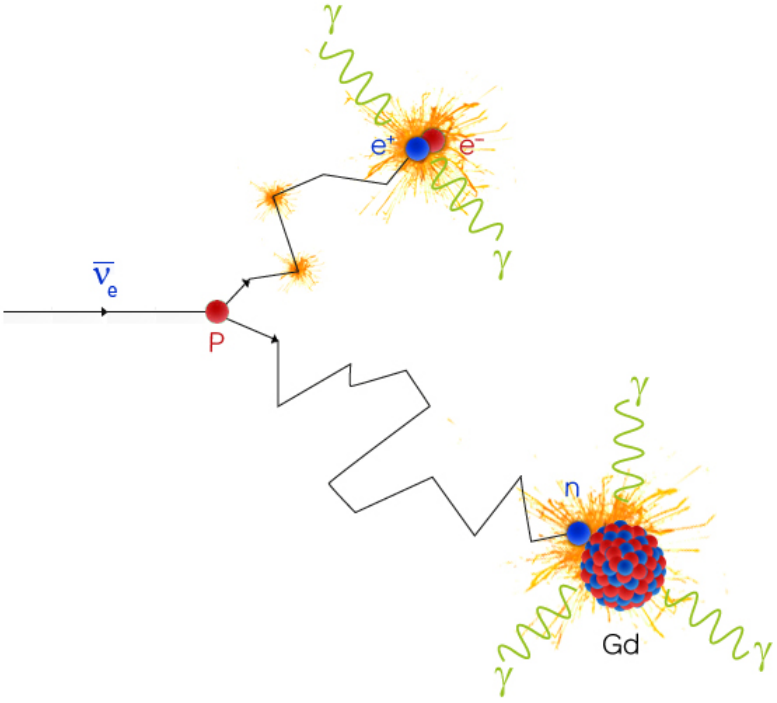


Figure 3.7: *Illustration of the inverse $\beta$ decay: interaction between an electron antineutrino and a proton, creating a positron and a neutron. It is followed by the prompt annihilation of the positron with an electron of the medium and the delayed capture of the neutron on a Gd nucleus, which deexcites by emitting three $\gamma$ on average.*

$$\sigma(\mathrm{E}_{\overline{\nu}_e}) = \mathrm{K} \times (\mathrm{E}_{\overline{\nu}_e} - \Delta)\sqrt{(\mathrm{E}_{\overline{\nu}_e} - \Delta)^2 - \mathrm{m_e}^2}, \tag{3.17}$$

where the prefactor K is directly related to the neutron lifetime,

$$\mathrm{K} = 9.61 \times 10^{-44}\ \mathrm{cm}^2\ \mathrm{MeV}^{-2}. \tag{3.18}$$

The $\overline{\nu}_e$ spectrum observed in a liquid scintillator detector is proportional to the product of the electron antineutrino flux emitted by the reactors and the inverse $\beta$ decay cross-section (Figure 3.8). The expected number of $\overline{\nu}_e$ observed for a data taking period $\mathcal{T}$ in the $\mathrm{i}^{\mathrm{th}}$ antineutrino energy bin $[\mathrm{E_i}\,;\,\mathrm{E_{i+1}}]$ is:

$$\mathrm{N_i} = \frac{\mathcal{T}\,\mathcal{F}}{4\pi \mathrm{L}^2} \sum_{\ell} \frac{f_\ell}{\mathrm{E}_\ell} \int_{\mathrm{E_i}}^{\mathrm{E_{i+1}}} \sigma(\mathrm{E}_{\overline{\nu}_e})\, \phi_\ell(\mathrm{E}_{\overline{\nu}_e})\, \mathcal{R}_\mathrm{i}(\mathrm{E}_{\overline{\nu}_e})\, \mathrm{P_{ee}}(\mathrm{E}_{\overline{\nu}_e}, \mathrm{L}, \Delta \mathrm{m}^2_{31}, \theta_{13})\, \mathrm{dE}_{\overline{\nu}_e}, \tag{3.19}$$

where the sum is performed over the four isotopes $^{235}$U, $^{238}$U, $^{239}$Pu, and $^{241}$Pu, $\mathcal{F}$ is the product of the load factor and the total thermal power of the reactors, L the reactor-detector distance, $\phi_\ell(\mathrm{E}_{\overline{\nu}_e})$ the emitted flux of the $\ell^{\mathrm{th}}$ isotope, $\mathcal{R}_\mathrm{i}(\mathrm{E}_{\overline{\nu}_e})$ the detector response in the $\mathrm{i}^{\mathrm{th}}$ energy bin, $\mathrm{P_{ee}}$ the electron antineutrino survival probability (*cf.* Section 1.4.2). Finally, $f_\ell$ is the ratio:

$$f_\ell = \frac{\mathrm{N}_\ell^{\mathrm{fis}} \mathrm{E}_\ell}{\mathcal{P}}, \tag{3.20}$$

where $\mathrm{N}_\ell^{\mathrm{fis}}$ is the number of fissions for $\ell^{\mathrm{th}}$ isotope and $\mathcal{P}$ is the total thermal power,

$$\mathcal{P} = \sum_{\mathrm{m}} \mathrm{N}_\mathrm{m}^{\mathrm{fis}} \mathrm{E}_\mathrm{m}. \tag{3.21}$$

The detector response $\mathcal{R}_\mathrm{i}(\mathrm{E}_{\overline{\nu}_e})$ particularly takes into account the detector energy resolution and the $\overline{\nu}_e$ detection efficiency,

$$\mathcal{R}_\mathrm{i}(\mathrm{E}_{\overline{\nu}_e}) = \mathcal{V} \int_0^\infty \mathrm{S}(\mathrm{E}_{\overline{\nu}_e}, \mathrm{E}'_{\overline{\nu}_e})\, \varepsilon(\mathrm{E}'_{\overline{\nu}_e})\, \mathrm{dE}'_{\overline{\nu}_e}, \tag{3.22}$$

where the effect on energy resolution is modelled by a gaussian probability density function S centered on $\mathrm{E}'_{\overline{\nu}_e}$ with a $7\ \%/\sqrt{\mathrm{E}_{\overline{\nu}_e}}$ spread, $\varepsilon$ is the detection efficiency, and the normalization factor $\mathcal{V}$ is basically the product of the target volume and the experiment live time (*i.e.* the run time minus the $\mu$-veto time, sometimes called dead time, *cf.* Section 6.1). The expected response of the detector is estimated via Monte Carlo studies.

The emitted flux of electron antineutrino for the isotope $\ell$ can be parametrized using the exponential of a polynomial, as explained in [147]:

$$\phi_\ell(\mathrm{E}_{\overline{\nu}_e}) = \exp\left(\sum_{\mathrm{k}=1}^{6} \mathrm{a}_{\mathrm{k}\ell}\, \mathrm{E}_{\overline{\nu}_e}^{\mathrm{k}-1}\right), \tag{3.23}$$

where the $\mathrm{a_k}$ coefficients are determined by a fit to the data for the four isotopes, following the new method presented in Section 3.2.3. The $\mathrm{a}_{\mathrm{k}\ell}$ coefficients can be found in [147].

The antineutrino rates expected without oscillation for the Double Chooz near and far detectors are given in Table 3.2.

| | Near detector | Far detector |
|---|---|---|
| Distance from reactor 1 | 465 | 1,115 |
| Distance from reactor 2 | 351 | 998 |
| Expected detector efficiency | 80 % | 80 % |
| Expected reactor efficiency | 78 % | 78 % |
| Experiment dead time | 10 % | 3 % |
| $\overline{\nu}_e$ rate without efficiency ($d^{-1}$) | 485 | 68.8 |
| $\overline{\nu}_e$ rate with efficiencies ($d^{-1}$) | 348 | 53.4 |
| $\overline{\nu}_e$ integrated rate ($y^{-1}$) | 99,343 | 15,200 |

Table 3.2: *Expected antineutrino rates at both detectors with and without detector efficiency and dead time [31]. The dead time expectation differs for the far and near detector because of different overburdens, which then lead to different cosmic muon background, and therefore different cumulated veto times.*

**Electron antineutrino signal in the detector**

The detection principle is based on a correlated signature in time and space of the positron annihilation and the neutron capture on a nucleus. Both energy depositions are expected in a definite energy range.

The positron looses quickly its energy in the liquid scintillator by ionizing and exciting the electrons of the molecules, before it annihilates with an electron of the medium. This energy deposition is called the "prompt" event. The corresponding spectrum is directly related to the antineutrino and the positron energies, and is called the visible energy (*cf.* Section 3.3.1). Equation (3.15) is a definition of $E_{vis}$.

In the meanwhile, the neutron, which carries a small kinetic energy ($E_n \lesssim 100$ keV), thermalizes by making collisions mainly on protons, until its energy drops to the ambiant temperature. After a certain amount of time that depends on the liquid contents, the neutron is captured on a nucleus, which afterwards deexcites by emitting $\gamma$ rays, leading to the so-called "delayed" event. The capture time and the energy of the emitted $\gamma$ are optimized by adding Gd in the liquid. The mean capture time in the Double Chooz liquid scintillator is 30 µs on Gd [4], while it is typically of the order of 200 µs on an hydrogen nucleus. The deexcitation of the Gd emits a cascade of an average of three $\gamma$ carrying in total 8 MeV. A hydrogen capture implies a 2.2 MeV peak. From the analysis point of view, a 100 µs time window is used to select the typical prompt-delayed coincidence of an electron antineutrino interaction. Indeed, the neutron capture follows an exponential law $e^{-t/\tau}$, with $\tau \simeq 30$ µs. A 100 µs time coincidence window corresponds then to roughly $3\tau$ and selects more than 96 % of the captures with a low level of uncorrelated physics events contamination.

Even if other energy depositions, which are unrelated to an electron antineutrino interaction, may still mimic the prompt-delayed signal, this correlated signature, with a high energy delayed signal around 8 MeV close to the prompt signal in time and space, is a rare and characteristic event in our detector.

[4] The neutron capture time is strongly related to the Gd concentration in the liquid, which will be identical in both Double Chooz detectors (single batch, see Section 3.5), and can be measured at a level of 0.3 % by studying $\Delta T_{prompt-delayed}$ distributions for near and far detectors or by analyzing the neutron multiplicity from a $^{252}Cf$ radioactive source.

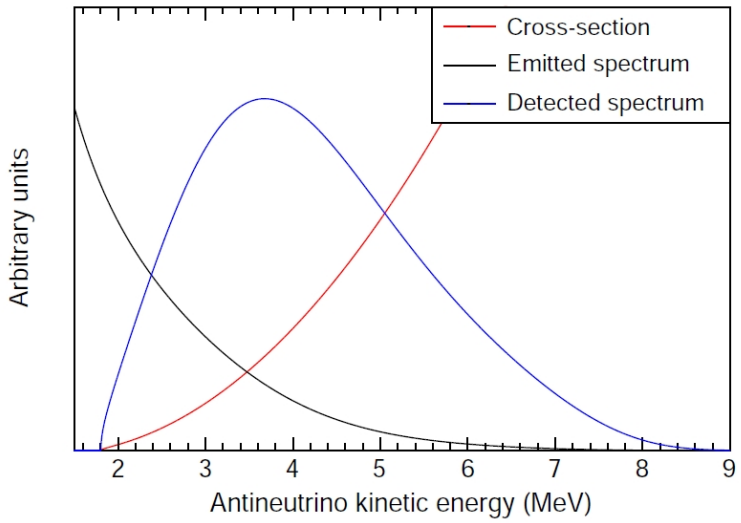


Figure 3.8: *Expected $\overline{\nu}_e$ spectrum in a detector (blue), which is the product of the $\overline{\nu}_e$ spectrum emitted by the reactor (black) and the inverse $\beta$ decay cross-section on free protons (red) [147].*

### Double Chooz backgrounds

Two kinds of backgrounds can mimic the characteristic electron antineutrino signal: the accidental and the correlated.

The correlated background consists of two events within the analysis coincidence window of 100 µs physically correlated to each other. These events are all caused by cosmic muons interactions in the detector and its surroundings. The overburden and the detector shielding stop most of the cosmic particles. Nevertheless, a muon may still enter the detector and create $\beta$-n decaying cosmogenic isotopes such as $^{9}$Li and $^{8}$He by spallation processes on $^{12}$C. With a half-life of 178 ms (that prevents veto considering the 45 Hz of muons expected in the Double Chooz detector), $^{9}$Li beta decays into excited states of $^{9}$Be with a branching ratio of roughly 50 %, which deexcite into two $\alpha$ particles via neutron emission. Knowing as well that the $\beta^-$ decay spectrum of this isotope goes up to 13.6 MeV, those electrons and neutrons can mimic electron antineutrino signals.

The other type of correlated background that Double Chooz has to cope with is the fast-neutron one. Cosmic muons may interact with the surrounding rock of the detector and create high energy neutrons called "fast-neutrons". Such neutrons could then enter the detector and loose energy by collisions on protons which would excite the scintillator leading to a fake prompt event. After thermalization, the fast-neutron would then be captured on a Gd nucleus, emitting thereby the characteristic 8 MeV signal of a delayed event. The energy of these fast-neutrons can go up to 100 MeV, whereas neutrons with higher energy tend to cross the detector without being stopped (a bigger detector volume would make fast-neutrons with higher energies completely lose their energy and then get captured).

The accidental background corresponds to a fortuitous coincidence of two events which are not related by any physics process. For instance, a fast-neutron capture and a radioactivity $\gamma$ emitted by the $^{40}$K of a photomultiplier glass can be accidentally selected as a delayed event and a prompt event in the 100 µs time coincidence window. This pair of energy depositions would then incorrectly sign an electron antineutrino interaction.

In the Double Chooz experiment proposal, the contributions of the different types of back-

ground for the far detector were estimated to be 1.4 ± 0.5 $d^{-1}$ of cosmogenics $^9$Li, 0.2 ± 0.2 $d^{-1}$ of fast-neutron, and 2.0 ± 0.9 $d^{-1}$ of accidentals [31]. These estimations were mostly done by scaling the CHOOZ experiment backgrounds to the Double Chooz detectors.

## 3.4 Double Chooz concept

When the Double Chooz experiment was being designed, the best upper limit on $\theta_{13}$ was given by CHOOZ. This experiment was limited by its statistical and systematic uncertainties, which were respectively 2.8 and 2.7 % [5] [30]. The concept of Double Chooz is mainly based on lowering these uncertainties with a new detector design [31].

### Improving CHOOZ statistical uncertainty

The CHOOZ detector installation started before the Chooz B reactors commissioning, which allowed them to benefit from long both reactors OFF data taking periods, and thus to study the experiment total background in great detail. However, some problems with the reactor cooling systems during the commissioning prevented to run at full power. This made the physics runs data taking non-optimal from the $\overline{\nu}_e$ statistics point of view. The other issue that CHOOZ suffered from was the stability of the detector, and especially a change of the liquid scintillator performance with time. Within a few months the liquid transparency got impaired, reducing the light yield [6] consequently. CHOOZ physicists were then compelled to calibrate their detector more and more frequently. All of these issues led to a full data set for analysis of 340 days, with 40 % with both reactors OFF.

Unless a serious issue happens with the Chooz B reactors, Double Chooz should not need to deal with such exterior problems. The only limitations of a longer data taking are then the stability of the liquids and the material compatibility over time. A tremendous effort has been made on the choices of liquids and materials to make sure the experiment will be able to run optimally during at least five years. In order to increase even more the statistics, the target volume of Double Chooz has been built bigger than the one used for the CHOOZ experiment: the number of protons in the Double Chooz target is 1.8 times higher than in CHOOZ's. Since Double Chooz far detector and CHOOZ detector share the same location, they have to deal with the same muon-related backgrounds in the same available confined space. The bigger target of Double Chooz makes the choice of an appropriate shielding against external backgrounds a challenge (*cf.* Section 3.5.2).

### Improving CHOOZ systematic uncertainty

The two main novelties in comparison to CHOOZ are the new detector design, with a buffer vessel (*cf.* Section 3.5), idea that originally comes from the Borexino experiment [27], and the building of two identical detectors at different distances from the reactors, one near, one far.

Knowing the flux normalization at short distance, given by an identical near detector, allows to cancel the systematic uncertainty on the antineutrinos flux and the dependence on model

[5] These are uncertainties on the ratio of the number of observed $\overline{\nu}_e$ over the number of expected $\overline{\nu}_e$ without oscillation. This ratio is expected to deviate from 1 in case of $\overline{\nu}_e$ oscillation, *i.e.* if $\theta_{13}$ is non-zero.

[6] The light yield is a quantity that characterizes the amount of light, or the number of scintillation photons, a liquid scintillator emits per unit of deposited energy.

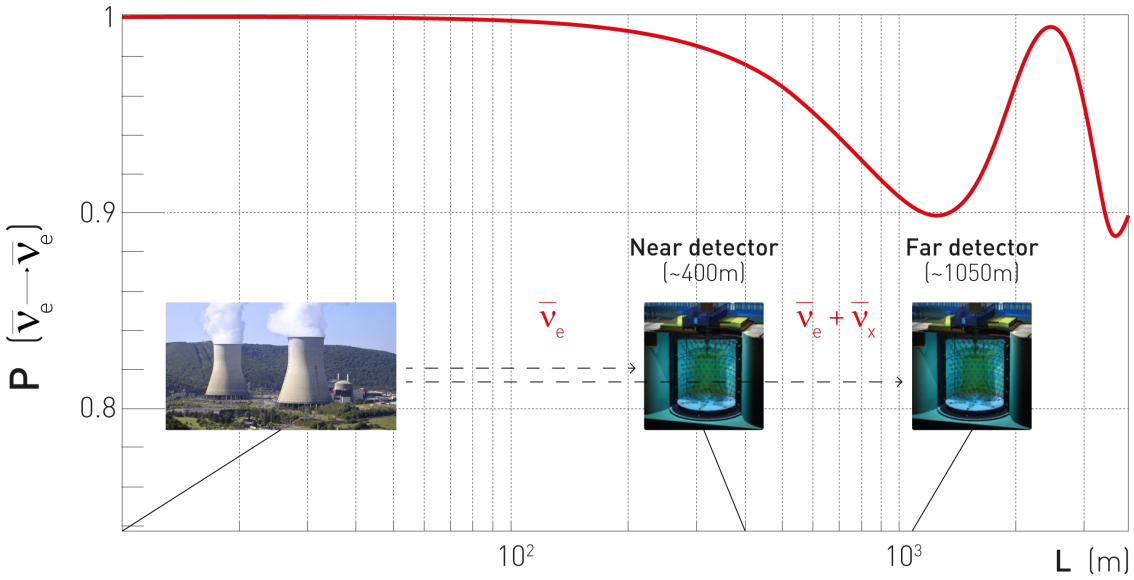


Figure 3.9: *Survival probability of an electron antineutrino, as a function of the source-detector distance L, in meters. The energy is fixed at 3 MeV, $sin^2\ 2\theta_{13} = 0.1$, and $\Delta m^2_{31} = 2.5{\times}10^{-3}\ eV^2$. The Double Chooz principle is reminded with the positions of the near and the far detectors at respectively 400 and 1,050 m from the reactors.*

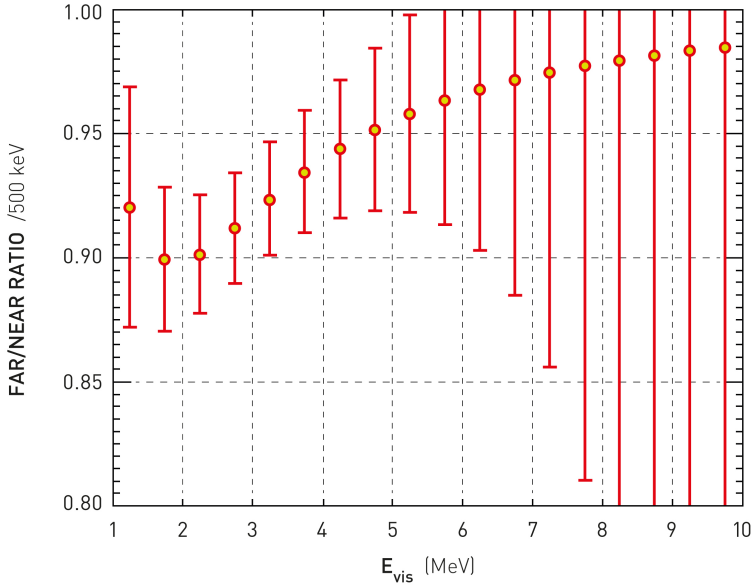


Figure 3.10: *Expected far to near spectrum ratio after three years of data taking with both detectors, assuming $sin^2\ 2\theta_{13} = 0.1$ and $\Delta m^2_{31} = 2.5{\times}10^{-3}\ eV^2$ [31].*

prediction of the reactor $\overline{\nu}_e$ spectrum, and therefore on associated systematics, while it was a limiting factor for the CHOOZ experiment. Indeed, the normalization of the neutrino flux was based on Bugey-4 and ILL measurements and then extrapolated [67, 165], making then the Bugey-4 detector the near detector of CHOOZ, although it was not identical nor placed close to the same reactors. This led to a 2 % systematic uncertainty on the antineutrino rate. The concept of two identical target volumes (*cf.* Section 3.5.1) allows a good relative normalization of the near and far detectors, with a systematic uncertainty of 0.4 to 0.6 %. The absolute knowledge on both detectors proton content is difficult to improve and should be of the order of 0.8 % as for CHOOZ, but the use of liquids from the same batch in the same target volumes will allow to rely only on relative proton content, lowering the uncertainty to 0.2 %. Furthermore, the Double Chooz detector design with a new buffer vessel and two concentric vessels filled with scintillator, one loaded with Gd and the other not, creates a physical fiducial volume that reduces the number of necessary analysis cuts and removes potential associated systematic uncertainties. The buffer volume also aims at lowering the accidental background (*cf.* Sections 3.3.2 and 3.5), allowing a signal over background ratio higher than 100 for the far detector, while it was of the order of 25 for CHOOZ. The specific protections against backgrounds at the near site have been chosen to induce a signal over background ratio above 100 for the near detector as well.

If the statistics is high enough and the systematic uncertainties low as expected, the comparison of the near and far detectors signals reveals the $\theta_{13}$ effect, *i.e* the disappearance of electron antineutrinos one kilometer away for the nuclear reactors (Figures 3.9 and 3.10). For the first phase of Double Chooz, with the far detector only, the near detector data are replaced by Monte Carlo $\overline{\nu}_e$ based on EDF data, predicted spectra, and full core simulations. The normalization of the experiment is done using the predicted cross-section from Bugey-4, called our "anchor point", as CHOOZ did (*cf.* Section 7.1). Double Chooz aims at obtaining a statistical error of 0.4 % and a systematic uncertainty of 0.6 % after three years of data taking with both detectors. Its expected sensitivity is $\sin^2 2\theta_{13} \leqslant 0.03$ at 90 % CL and its discovery potential $\sin^2 2\theta_{13} \geqslant 0.05$ at $3\sigma$ [140].

## 3.5 Detector design

Not only Double Chooz has been the first neutrino experiment proposing to build two identical detectors [7], but also the detector design itself shows innovation, in comparison to and with the intention of improving the former CHOOZ experiment. Both detectors consist of four layers of concentric vessels in a $7 \times 7$ m cylindrical pit, each layer filled with a different liquid to fulfill its own purpose. In order to ensure a low level of accidental background (desired radioactivity $< 10$ Bq in the detection volumes), the radioactivity of each component has been cautiously counted. Furthermore, the design and the liquids properties were chosen to maximize the number of detected neutrinos: number of target protons (*cf.* Section 3.3.1), attenuation lengths, light yields, acrylic transparency, number and orientation of the photomultipliers (PMTs), etc. In order to guarantee a relative normalization systematic error of 0.6 %, the liquids of the two detectors come from the same batch and the inner detectors vessels were built at the same time. However, due to the different overburdens and thus the different cosmic muon rates, part of the muon background-related detectors and the external shielding are not identical: the idea is to keep anyway a good and similar signal over background ratio for both detectors.

[7] However, Double Chooz is not the first experiment using a two detectors concept. Indeed, Bugey-3 built two detectors for the electron antineutrinos from reactor oscillation measurement [17] and the abandonned Kr2Det project proposed for the first time to build two identical detectors for the $\theta_{13}$ search [136].

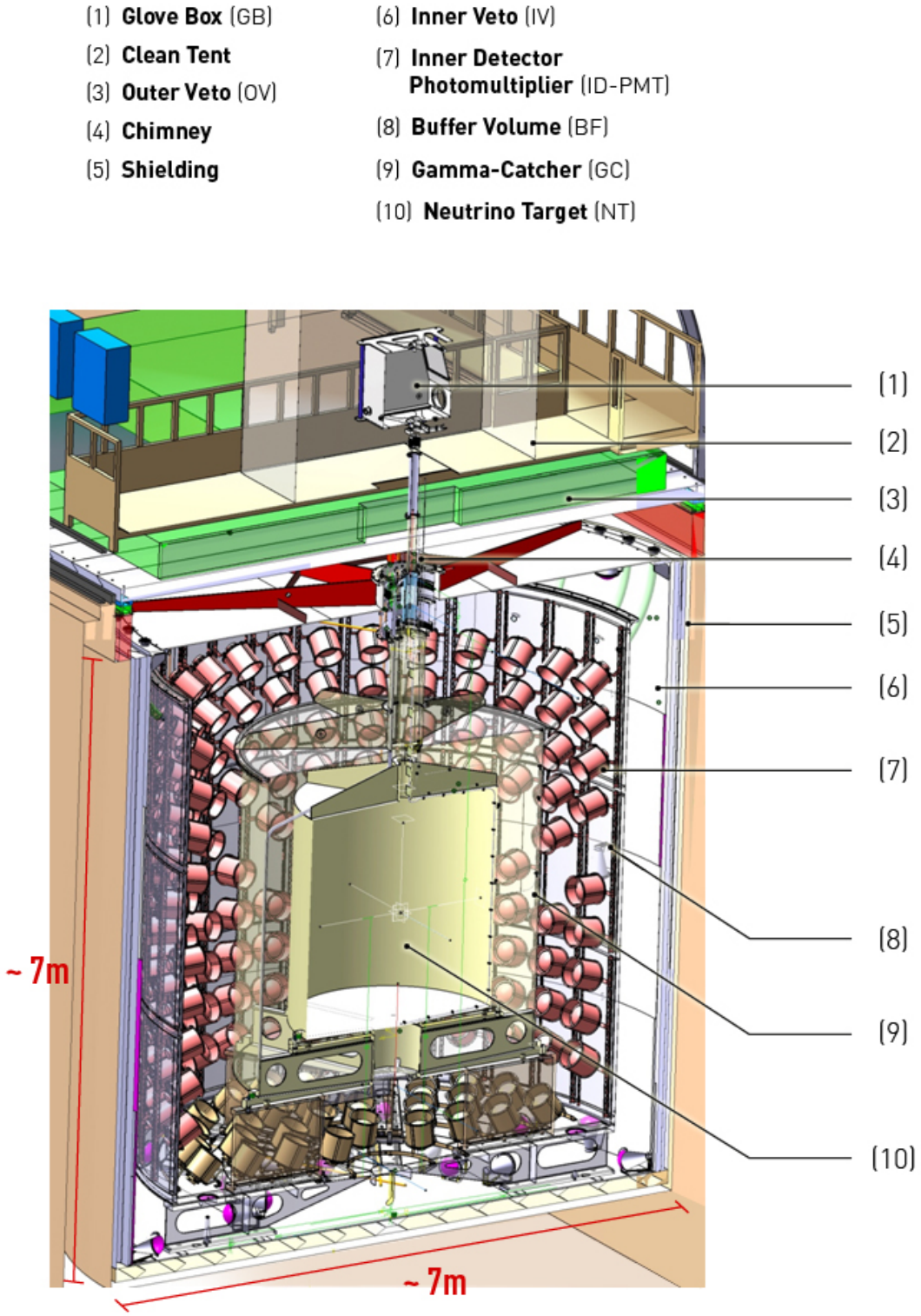


Figure 3.11: *Full detector schematic with the $\nu$-target (NT), the $\gamma$-catcher (GC), the buffer vessel (BF) and the inner detector PMTs, the inner veto (IV) and its PMTs, the outer veto (OV), the deck, and the glove box (GB).*

### 3.5.1 From the interaction point to the detection

The main purpose of the Double Chooz detector is to bring out the electron antineutrino signature. This is the goal of the inner detector (ID). It consists of three cylindrical, concentric vessels. The two innermost ones are made of acrylic. Since none of the commercial acrylics were adapted to the optical and practical constraints of Double Chooz, a new acrylic was developed to match our expected performances. Among them one can highlight low radioactivity, long-term tightness (which means barely reactive with the liquids, especially by the glue, to avoid leakages for at least five years), good robustness in order not to get out of shape by the liquid or its own weight (as a good knowledge of the actual volume is important for the analysis), and transparency to UV and visible light with wavelength higher than 400 nm [158].

The smaller vessel, an 8 mm thick cylinder-shaped container of 10.3 $m^3$ capacity, is the neutrino target (NT). Filled with a Gd-doped scintillator liquid of density 0.8035, it has an average internal radius of 1,150 mm and a height of 2,459 mm for a loaded mass of 8.23 tons. Efforts have been made on the scintillator composition and compatibility with its container to ensure stability over a long data taking period [16]. Durable transparency and good optical properties are another key point. The liquid, doped with 1 g/L of Gd to signal neutron capture more clearly (*cf.* Section 3.3), is composed of 80 % of n-dodecane [8], in order to provide a large amount of target protons, and 20 % of PXE [9], an aromatic molecule that gets easily excited or ionized by energy deposition. The scintillation occurs when a charged particle travels through matter (here through a liquid scintillator), losing its energy by inelastic collisions with electrons of the medium. The deposited energy induces PXE molecules excitation and, if it is large enough, ionization, thus freeing secondary electrons that themselves ionize other molecules until their thermalization. The deexcitation of the molecules can be radiative or non-radiative. The latter is the case in the Double Chooz scintillator. The energy is transferred from the solvent excited molecules to the solute molecules, called wavelength shifters, with a high fluorescent quantic yield in UV and visible. Two wavelength shifters are added in our liquid scintillator: 7 g/L of the primary fluor PPO [10] and 20 mg/L of the secondary fluor bis-MSB [11]. PPO absorbs the scintillation light and reemits it with higher wavelengths; these gamma rays are then reabsorbed by bis-MSB molecules and drifted again towards blue and UV wavelengths, where the PMTs are more sensitive and the liquids more transparent. The light yield of the $\nu$-target has been estimated to be around 200 photons/MeV (*cf.* Section 4.2.4). The target integration occurred in September-October 2009.

The second acrylic vessel is called the $\gamma$-catcher (GC). It surrounds the NT and has a volume of 22.6 $m^3$ filled with unloaded scintillator. It is 12 mm thick, with an internal radius of 1,708 mm and a height of 3,572 mm. The liquid composition has been chosen to ensure the same density and optical properties than the NT liquid, and is the following: 30 % n-dodecane, 66 % ondina 909 mineral oil, and 4 % PXE, with 2 g/L of PPO and 20 mg/L of bis-MSB. The purpose of such a volume is to increase the detection efficiency by collecting most of the energy released by the positron and the neutron capture occurring in the NT. Completely containing the energy deposition of the $\gamma$ rays allows to have a fully efficient target volume. However, non-trivial spill-in and spill-out effects have to be quantified. The spill-out happens when the interaction occurs in the $\nu$-target volume, close to the wall, and the neutron is captured outside, in the $\gamma$-catcher. The spill-in is the opposite: the positron deposits its energy in the GC when the interaction occurs

[8] Linear alkane hydrocarbon, $C_{12}H_{26}$.
[9] 1,2-dimethyl-4-(1-phenyl-ethyl)-benzene.
[10] 2,5-diphenyloxazole.
[11] 1,4-bis(2-methylstyryl)benzene.

| Vessel | Volume ($m^3$) | Radius (mm) | Height (mm) | Liquid composition |
|---|---|---|---|---|
| $\nu$-target (NT) | 10.3 | 1,150 | 2,459 | 80 % n-dodecane + 20 % PXE + Gd + wavelength shifters |
| $\gamma$-catcher (GC) | 22.6 | 1,708 | 3,572 | 30 % n-dodecane + 4 % PXE + 66 % mineral oil + wavelength shifters |
| Buffer (BF) | 114.2 | 2,760 | 5,680 | 43 % n-dodecane + 57 % mineral oil |

Table 3.3: *Summary table of inner detector vessels dimensions and liquid composition.*

close to the separation between the NT and the GC, but the neutron leaks inside and is then captured on a NT nucleus. The two effects do not exactly compensate and have to be taken into account for the Double Chooz first phase, but can be neglected if the two detectors are running and identical (a few millimeters geometrical difference between both detectors has a negligible effect on the results though). The $\gamma$-catcher integration happened in August-September 2009. It was a delicate operation on site due to the narrow tunnel and laboratory (Figure 3.12).

The buffer (BF) is the biggest vessel of the Double Chooz inner detector. It is a 10 tons, 5,680 mm high, 3 mm thick stainless steel cylindrical vessel of radius 2,760 mm. Its main goals are to provide an optical decoupling with the inner veto vessel and to support the 390 10 inches Hamamatsu PMTs that will collect light, by turning scintillation photons into photoelectrons (PEs) on their photocathode [137]. These PEs will then be multiplied by a system of dynodes inside the PMT to form an electrical signal sent to the acquisition system via the anode. All of the PMTs are encapsulated inside a $\mu$-metal shielding in order to disable the Earth electromagnetic field which might disturb the light collection. The PMTs are spread on the buffer wall, top, and bottom, and are all oriented towards the center of the detector in order to increase the detection sensitivity and the light collection uniformity. The total equivalent coverage of the ID PMTs is 13.5 %. Furthermore, the vessel is coated and has a reflection coefficient of 40 %. The buffer tank was integrated in March-April 2009 and the PMTs were installed in May-June 2009.

### 3.5.2 Reducing the internal and external backgrounds

The buffer volume has another purpose in Double Chooz: it helps to fight against backgrounds. One of the most important backgrounds in this experiment is accidental coincidences of single events, in which radioactivity $\gamma$ are majority. $^{40}$K in the PMTs glass is the main source of radioactivity in the detector. The 114.2 $m^3$ of non-scintillating liquid[12] surrounding the GC play then their role as buffer (over 950 mm separate the GC from the BF wall). This liquid has been chosen for its good transparency to the scintillation photons wavelengths. In order to avoid any buoyancy force on the acrylic vessels and have optimal optical transmission, its density matches NT and GC's ones. Like in any other part of the detector, the material-liquid compatibility over time is requested. A summary of the liquids and vessels of the ID can be found in Table 3.3.

The external backgrounds are mainly muon-induced. The main purpose of the next volume, called inner veto (IV), optically separated from the ID, is to detect and track cosmic muons.

[12] 43 % of n-dodecane and 57 % of the mineral oil ondina 917.

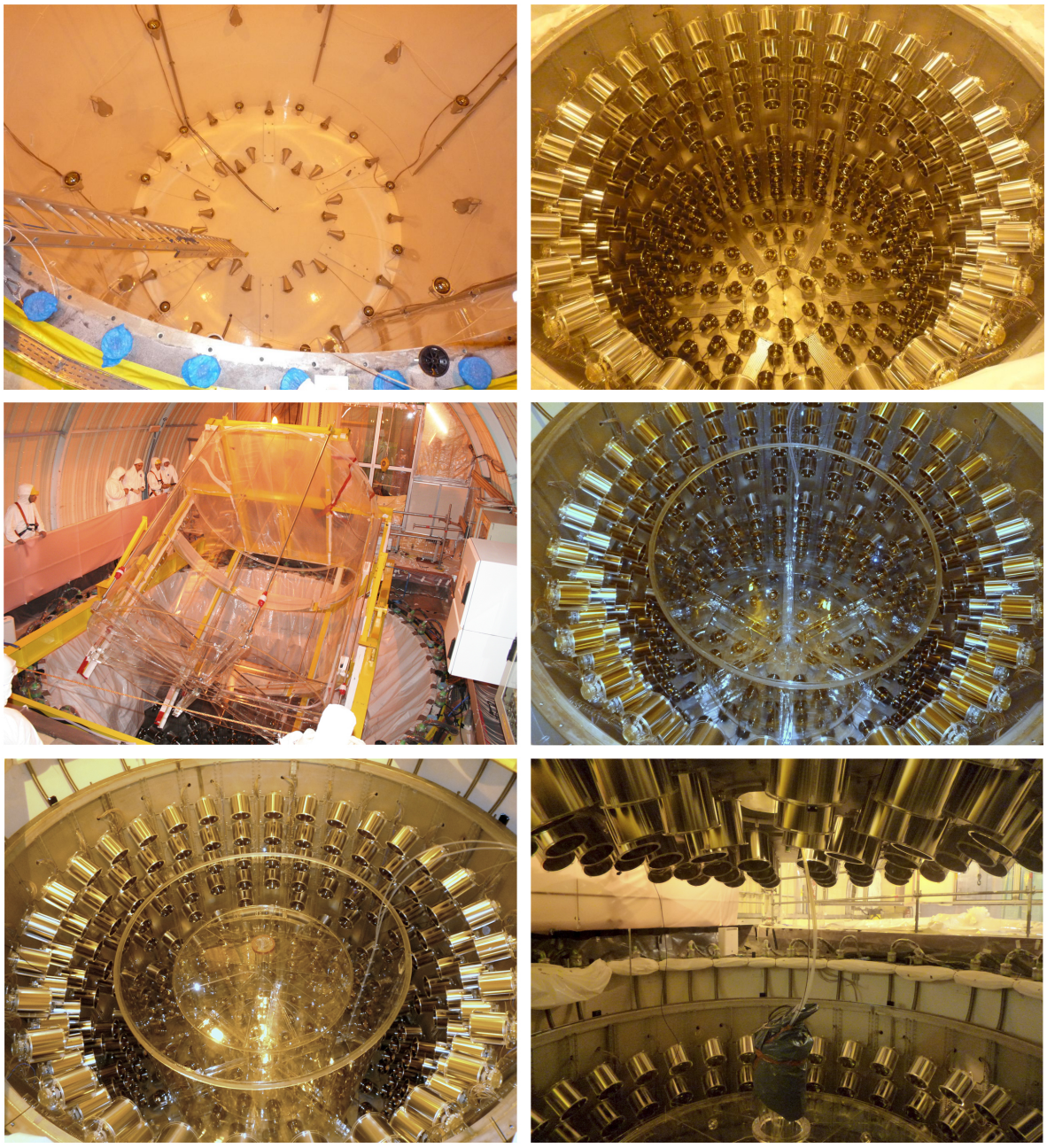

Figure 3.12: *Double Chooz detector pictures, taken at different stages of the integration. (top left) Inner veto vessel wired with its 8 inches PMTs. (top right) Buffer vessel with all the wall and bottom PMTs mounted. (middle left) $\gamma$-catcher tricky and risky integration. (middle right) $\gamma$-catcher integrated within the buffer volume (filling tubes going down the detector are visible). (bottom left) $\nu$-target integrated within the $\gamma$-catcher volume with its top glued. (bottom right) End of inner detector integration with the PMT-wired buffer lid closing.*

Figure 3.13: *(top) Inside of the inner veto volume. IV PMTs with their peculiar orientation and the reflective foils and white paint on the IV wall are visible. (bottom) Outer veto fully mounted above the detector, at the ground level.*

This is why the 90 $m^3$ of liquid scintillator (half n-dodecane, half LAB scintillator [13], with 2 g/L of PPO and 20 mg/L of bis-MSB) in a tank of 3,250 mm of internal radius and 6,830 mm in height, are watched by 78 8 inches Hamamatsu PMTs fixed on the top, bottom, and lateral surfaces of the 10 mm thick IV tank. In order to optimize the light collection in such a confined space (roughly 500 mm between the IV and BF walls) the PMTs are parallel to the surface they are fixed to, looking in different directions, and the tank wall is covered with reflective foils (VM2000) and white paint (Figure 3.13). The inner veto integration happened at the end of 2008 and its PMTs were installed in May 2010.

Because of the enlargement of the $\nu$-target and the adding of the buffer volume in comparison to the previous CHOOZ experiment, the space for the shielding against external radioactivity $\gamma$ was strongly reduced. It was therefore decided to enclose the detector in a 150 mm thick stainless steel volume. This protection is made of 66 V-shaped bars individually demagnetized in order to reduced PMT signal disturbances, 42 for the lateral part and 12 for the upper and lower lids. The inner radius of the shielding is 3,300 mm and its height is 7,150 mm. It was assembled in the pit during the summer 2008.

The outer veto (OV) is an additional rejection tool against muons with respect to CHOOZ. It is made of 82 $m^2$ of plastic scintillator strips coupled to wavelength-shifting fibers placed on the ground level, on top of the detector, and extended over its diameter. Above the chimney and glove box (*cf.* Section 3.5.4) are mounted another 42 $m^2$ of scintillator called the upper outer veto, in order to avoid dead zone. The purpose of the OV is to detect the entry point of muons with a better precision than with the IV only. Furthermore, the extension beyond the detector diameter allows to observe near-miss muons and thus give the opportunity to reject muon-induced fast-neutron background more efficiently. The outer veto was installed in April 2011, while its upper part was set up during the summer 2012.

### 3.5.3 Data acquisition

#### Readout system

The scintillation light seen by the PMTs creates a signal carried together with the 1.5 kV high voltage (HV) required to supply the photomultipliers. In order to isolate the few mV of signal from the high voltage one, a custom HV splitter is used. The signal is then sent to the front end electronic (FEE) boards, that amplify it to match the dynamic range of the FADCs [14].

Two sets of FADCs are used: the neutrino FADC system ($\nu$FADC) and the muon FADC system ($\mu$FADC). The Double Chooz $\nu$FADCs are 8-bit 500 MHz cards (digitization every 2 ns) with 2 MB of internal memory per channel split into 1,024 buffers of 4,096 ns. As long as the $\nu$FADC does not receive any external trigger signal, the digitization process is continuous inside a buffer. In case of arrival of such a signal, the $\nu$FADC moves to the next buffer. The $\nu$FADC can keep up to 1,024 events in memory. Since the trigger rate, of the order of 130 Hz, remains lower than the readout speed, there is no dead time induced by the acquisition. As for the $\mu$FADCs, although they are not yet installed, they will sample at 125 MHz. These $\nu$FADCs and $\mu$FADCs cards are distributed by groups of 16 on VME [15] crates. The data acquisition (DAQ) software was written in the Ada language; for an exhaustive description of the DAQ, one may refer to [26]. A scheme of the Double Chooz readout system can be found in Figure 3.14.

[13] Linear alkylbenzene.
[14] Flash-Analog to Digital Converter
[15] VERSAmodule Eurocard, or Versa Module Europa.

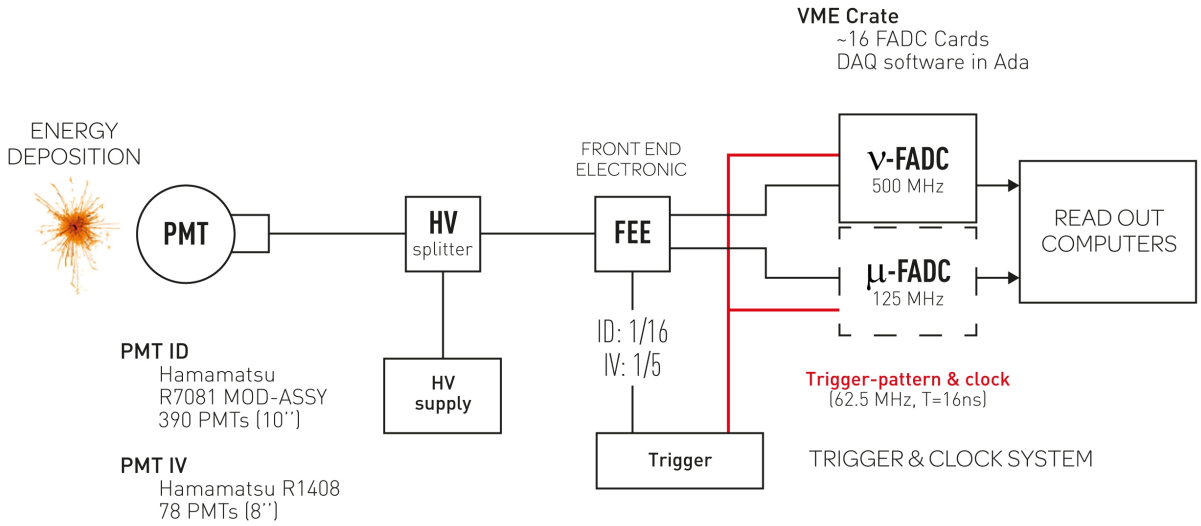


Figure 3.14: *Scheme of the Double Chooz readout system.*

### Trigger system

While the PMTs signal is sent to the FADCs, it is also directed to the trigger system [174]. The trigger system consists of three trigger boards (TB) and one trigger master board (TMB). The so-called TB V is for the IV PMTs, while the TMB provides a system clock for the whole DAQ. The TB A and the TB B correspond to each half of the ID PMTs (uniformly distributed throughout the volume). The ID PMTs are divided into 12 sectors, each one of them containing 32 PMTs. Six sectors are for the upper part of the inner detector while the other six are for the bottom part. Basically half of the PMTs from a given sector is connected to the first trigger board TB A while the other half is connected to the TB B. The FEE sums the signals from a sector by groups of 16 PMTs, and sends it to the trigger boards. The choice of the PMTs grouping in a sector is done in order to always have a PMT connected to a certain trigger board only surrounded by PMTs connected to the other one. Each board makes a trigger decision based on the analog sum on half of the ID PMTs. This technique implies that both trigger boards look at the same volume and thus that their trigger decision should be the same apart from statistical fluctuations. Four trigger conditions based on energy deposition can be set, that are enabled only if the multiplicity is higher than two, *i.e.* if at least two sectors are hit. If any of the analog sums is above a set energy threshold, a NIM [16] trigger signal is sent to the FADCs for storage of the information in their internal memory. The waveforms of both ID and IV signals are then recorded in a 256 ns time window. In addition, an external trigger may also be injected into the system for calibration. The trigger system decision is recorded within a 32-bit triggerword used for analysis (*cf.* Chapter 6). Regarding the inner veto trigger board, it works a bit differently than the ID TB A and B: the trigger condition is mainly based on the hit pattern.

The ID readout threshold has been set at 350 keV, well below the 1.022 MeV minimum visible energy of an inverse $\beta$ decay positron (*cf.* Section 3.3.1), greatly reducing the threshold systematics. The trigger rate is thus increased, but anyway still rather low with an average value of 130 Hz.

[16] Nuclear Instrumentation Module.

The OV works as a different detector in the sense that the ID or IV do not need it to function. It is meant to give complementary information on the muon rate. The OV system is however synchronized with the main readout system via the TMB clock signal. An energy deposition by a cosmic muon in the OV scintillator strips creates light that is shifted and transported to its PMTs, which are connected to custom boards for acquisition.

#### Online system

The FADCs and the trigger system are VME devices and are the core of the readout system. They are plugged in groups of 21 into a VME crate where one card, called the readout processor (ROP), is used for the readout through the VMEbus. Six ROPs are needed for one detector: four for the $\nu$FADCs, one for the $\mu$FADCs, and one for the trigger system. The main data acquisition system collects the data from these six ROPs. Afterwards, the data streams from the main DAQ and the outer veto data acquisition system (OVDAQ) are merged and converted into ROOT format [17]. These data files are then converted into the Double Chooz offline analysis software (called DOGS for "Double Chooz Offline Group Software", *cf.* Chapter 4) format before being sent to the CCIN2P3 Computing Center at Lyon for data storage. The data taking is monitored at different stages, from the low level monitoring of the DAQ to the offline data quality checks performed on the final data files.

### 3.5.4 Calibration devices

In a detector such as Double Chooz, it is important to determine as accurately as possible the scintillator response to the different particles involved in the physics processes of the experiment ($\alpha$, $\beta^{\pm}$, $\gamma$, protons, and neutrons), the light transport properties of the liquid (such as the speed of light in it and the attenuation lengths), and the fundamental PMTs properties (electronic time offsets, gains, and quantum efficiencies). The goal is to have an absolute uncertainty on the detector efficiency of about 1.5 % and a precise knowledge of the detector response through its energy scale. In order to do so, several calibration devices are installed in the detector.

#### Radioactive sources

A part of the Double Chooz detector calibration is based on radioactive sources deployment in the vessels. These are useful to better understand the detector response (for instance the neutron capture detection efficiency) and its energy scale. Four devices are used: the Z-axis system, the articulated arm (AA), the guide tube (GT), and the buffer tube (BT). They all are operated from above the detector, in a clean tent.

The deployment of sources with the Z-axis and the AA is performed using a glove box (GB) under nitrogen atmosphere at the detector pressure. Connected to the chimney and its ball valve, it allows us to insert calibration sources in the inner detector avoiding unwanted extra-dust in the liquids. These devices allow the deployment of sources directly in the $\nu$-target. While the Z-axis system is indeed restricted to the vertical symmetry axis of the detector and is in fact a simple fishing line, the AA makes deployment in every point of the $\nu$-target feasible. The articulated arm is expected to be operated in the fall of 2012.

[17] Object-oriented program and library developed by CERN (European Organization for Nuclear Research) for data analysis [161].

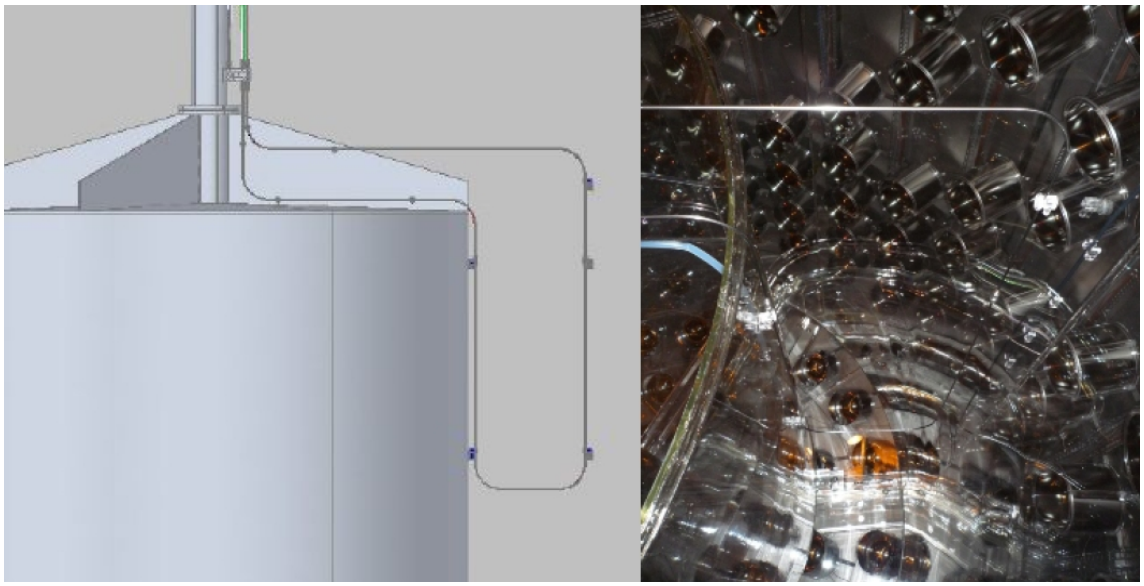

Figure 3.15: *Calibration device guide tube (GT) in the GC vessel, attached to both the $\gamma$-catcher and buffer walls. Computer-aided design model (left) and actual photo (right).*

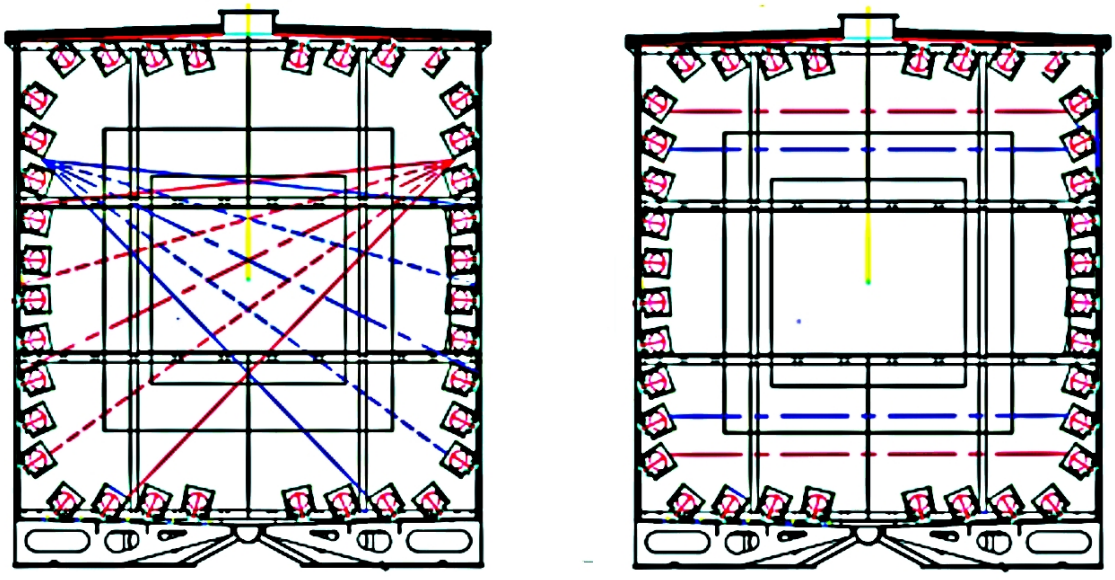

Figure 3.16: *Two Double Chooz detector schematics, with typical position of LEDs for calibration. The light injection systems may be used either in diffuse mode (left) or in pencil beam mode (right).*

| Radioactive sources | | Activities (kBq) | Energy (MeV) |
|---|---|---|---|
| $\gamma$ | $^{60}$Co | 0.2 | 1.173 and 1.333 |
| | $^{68}$Ge | 0.2 | $2 \times 0.511$ |
| | $^{137}$Cs | 0.2 | 0.667 |
| neutron | $^{252}$Cf | 1 | 2.2 (on H) or 8 (on Gd) |
| | Am-Be | 3.7 | 2.2 (on H) or 8 (on Gd) |

Table 3.4: *Summary table of neutron and $\gamma$ radioactive sources used for the Double Chooz far detector calibration.*

The guide tube is used for deployment of radioactive sources inside the $\gamma$-catcher. The GT layout in the detector is illustrated on Figure 3.15. The tube is permanently fixed inside the $\gamma$-catcher. During calibrations, sources are pushed inside by a wire. The size of the tube has been minimized in order to reduce absorption of radiation and shadowing of scintillation light, imposing strict dimensional constraints on the sources. Their design provides two levels of encapsulation and they are 6.5 mm long for 1.6 mm of diameter. The Table 3.4 gives a summary of the neutron and $\gamma$ sources that have been used. The $^{68}$Ge source emits a positron, after a decay through electron capture. This positron will annihilate with an electron of the medium, creating then two gammas that carry a total energy of 1.022 MeV. According to equation (3.15), this is the minimal energy of an inverse $\beta$ decay on proton that the Double Chooz detector has to cope with. This source is thus useful to calibrate our trigger efficiency, while the neutron efficiency is studied with $^{252}$Cf sources, that emit several neutrons with an average multiplicity of 3.7 (*cf.* Section 6.2.4).

Regarding the buffer tube, it is a similar device that makes possible the deployment of sources inside the buffer vessel along the $\gamma$-catcher wall.

For the first and second Double Chooz publications, only the Z-axis and the guide tube deployment systems were used [47].

### Light sources

Embedded light injection systems emit LED light guided via optical fibers fixed on the edge of some PMTs in the inner detector (IDLI) and inner veto (IVLI). The wavelength of such light can be set at 385 nm, 425 nm, or 475 nm for the IDLI system, and 365 nm or 475 nm for the IVLI, allowing to probe the detector response to specific excitations. Either diffuse or pencil beam mode is available (Figure 3.16). For the IDLI, the injection of diffuse light can be done from 32 points of the inner detector: 20 on the wall, 6 on the top, and 6 others on the bottom. There are 14 injection points for pencil beam LED.

While the 385 nm wavelength should be totally absorbed and reemitted, the 425 nm is only partially absorbed by the scintillator liquid and will then reach the PMTs on the opposite side of the detector, thus allowing to monitor the absorption of the $\nu$-target and $\gamma$-catcher as well as to calibrate the PMTs characteristics. At 475 nm the light should not excite the liquid scintillator, which makes LED at this wavelength a direct light source to the PMTs.

The advantage of using light sources is that they provide signals of precisely known timing and amplitudes. All independent and remotely controlled, they can be run alone or in a multi-LED mode, while the light intensity is monitored by photodiodes. A control board provides an external trigger to the data acquisition system for each light injection.

Light diffusers can also be deployed in the Double Chooz detector through its chimney, allowing for instance a calibration of the PMT time offsets (*cf.* Section 4.2.2). For that purpose, a LED flasher has been developed. This device is a 5 cm Teflon [18] diffuser ball coupled to a blue LED which flashes at 10 Hz, looping over eight different light intensities [120]. Moreover, in order to study the PMTs response and the optical properties of the liquid scintillator, a laser diffuser ball is under development. It will be a 80 mm acrylic ball coupled to a 470 nm (blue) and a 375 nm (UV) laser, that would be placed at the center of the Double Chooz $\nu$-target through the chimney, along its vertical symmetry axis, aiming at a maximum 5 % light anisotropy [106].

### Natural sources

The Double Chooz detector calibration is also performed through the use of "natural calibration sources", with neutron capture peaks, on hydrogen or gadolinium. These events are selected few tens of milliseconds after a muon, very likely to induce neutrons in the detector via spallation reactions on carbon atoms for instance. The H peak mean energy is 2.2 MeV while the Gd one, a combination of several lines, is around 8 MeV. Natural radioactivity peaks or Michel electrons may also be used for calibration or energy scale cross-checks.

Since this section aimed only to present the calibration devices of the Double Chooz detector, more details will be given in the next chapter, treating the event reconstruction and detector calibration.

[18] Or PTFE (polytetrafluoroethylene); material non-reactive, hydrophobic, with a low coefficient of friction against solids, that has been used to make the filling and calibration tubes of the Double Chooz detector.

# Chapter 4

# Event reconstruction and detector calibration

*I am fast. To give you a reference point I am somewhere between a snake and a mongoose... and a panther.* [1]

Dwight Schrute,
Assistant (to the) Regional Manager, Dunder Mifflin Inc., Paper Company, Scranton, PA.

This chapter presents the Double Chooz event reconstruction and detector calibration. The data acquisition system saves the waveforms delivered by the PMTs for each energy deposition that triggers the detector. After the calibration of the PMT gains and time offsets, the charge and the time of the pulses are used to reconstruct the vertex position, which is then saved in data files among other event information. The last section describes the architecture of the data files required for the offline analysis, and especially introduces the software Cheetah, that I codeveloped with the Saclay group, which aims at simplifying the Double Chooz data format for easier and faster analyses.

Once the DAQ [2] binary files are converted into ROOT [3] data files, the last steps of the event reconstruction procedure are usually performed with the Double Chooz Offline Group Software, or DOGS. This software is being developed and maintained by the collaboration through the use of the SVN tool [4] and depends on two external softwares, ROOT and GEANT4 [5]. DOGS is composed of several packages for offline analysis, data production, and Monte Carlo generation purposes. The Monte Carlo related packages are presented in Chapter 5. One of the DOGS packages is the Double Chooz Common Trunk (DCCT, or just CT). The Common Trunk is a set of reconstruction algorithms which are applied on RAW data [6] prior to any other calculations. Its output files can be used by any of the Double Chooz collaborators for their own analyses. It uses a Processor class concept for applying several algorithms to each event of the Double Chooz data. These events are called EnDep, which stands for energy deposition. The algorithms of the CT are basically reconstruction, as well as monitoring units. I have been strongly involved in the Common Trunk development and the data quality checks.

[1] From the NBC "The Office" television series created by Ricky Gervais. Season 3, episode 8.
[2] For data acquisition. Most of the detector related acronyms used hereafter are defined in Chapter 3.
[3] Object-oriented program and library developed by CERN for data analysis [161].
[4] Or Subversion, a software versioning and a revision control system [179].
[5] A toolkit for the simulation of the passage of particles through matter [97].
[6] RAW data are binary files converted into ROOT files on which no reconstruction has been performed yet.

Inside the Common Trunk, the RAW data processing first starts with the reconstruction of each PMT pulse. The event reconstructed charge and pulse time per PMT, crucial information for analysis, are extracted. The second step is then to apply calibration constants, such as PMT gains and channel time offsets, to the reconstructed PMT pulses. These calibration constants are obtained through light injection calibration campaigns within the detector (*cf.* Section 3.5.4 and 4.2). Once this step is finalized, a set of algorithms is applied in order to reconstruct the vertex position and energy of a "neutrino-like" event, while other algorithms are run over "muon-like" events in order to reconstruct their entry and exit points from the detector.

All the reconstruction algorithms developed within the Double Chooz collaboration are not part of the official data release because of limited computing time and disk space considerations. A compromise had to be found and the most reliable and fastest algorithms were run, even if a careful comparison of all available algorithms on data would have been appreciated, since they usually rely on different reconstruction methods or input information (charge on PMTs, timing information, fit techniques, etc.). This is the case of the energy reconstruction tool CocoReco that I developed with the Saclay group. It is presented in the Double Chooz Monte Carlo chapter, in Section 5.2.

## 4.1 Pulse reconstruction

The Double Chooz PMT pulse reconstruction and pedestal analysis are performed within the DOGS framework by the DCRecoPulse package, which comprises different algorithms and tools. The main goal of DCRecoPulse is to provide the charge collected in any readout channel, along with some characteristic times of the pulse. This package is the first step of the Common Trunk and can be applied on RAW data or on Monte Carlo (after the readout simulation RoSS, *cf.* Section 5.1.3). The authors of the DCRecoPulse package documented it with several Double Chooz internal notes [150, 151].

The DCRecoPulse package contains three basic pieces: a pedestal analyzer which computes channel pedestal mean and variance, a charge analyzer which computes the charge of a pulse in a given readout window, and a time analyzer which computes several characteristic pulse times.

### Pedestal analysis

In order to obtain the actual charge, one needs to subtract the pedestal [7] of the pulse. There are several ways to do so. A first method, called "offset time measurement", offers the possibility to take advantage of the electronics capabilities [8]. It consists in setting a time offset previous to the pulse arrival and measuring the pedestal within the first time samples of the channel readout. However, this approach suffers from the smallness of the size of the integration window, which could then not be wide enough to estimate the pedestal with a good accuracy. Also, if any signal such as dark noise [9] or light-noise (*cf.* Section 6.2.1) arises within this window, the pedestal mean would be incorrectly computed and its RMS would be too large, impacting then the energy resolution and linearity. Another idea is to use the full readout window for the

[7] A channel always measures a certain amount of signal, even though it does not necessarily comes from a photon. This small quantity of charge on the ADC is called the pedestal.

[8] For a presentation of the Double Chooz readout system, see Section 3.5.3.

[9] Small electric current that flows through a photomultiplier tube even when no photons hit the photocathode.

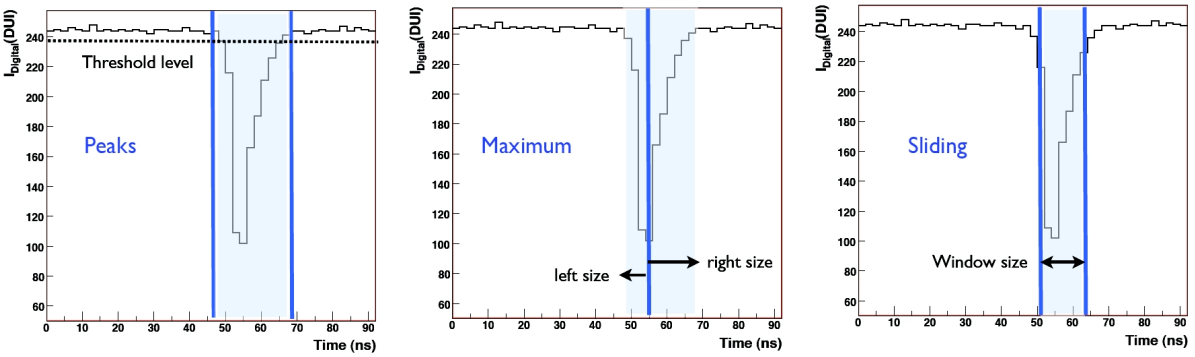


Figure 4.1: *Illustration of the reconstruction time window for the various algorithms [151]. The y-axis is in DUI, an arbitrary unit that stands for digital unit of current.*

pedestal mean and variance estimation. The mean of the ADC count distribution is computed and the bin with the largest deviation from the mean is removed, making the mean of the remaining ADC value distribution closer to the mean of an ADC value distribution without pulse. This process is iterated until the largest and lowest ADC values have the same deviation, within a tolerance of 1 ADC count. The drawback of this method is that is does not work for very large pulses which do not return to the pedestal level by the end of the readout time window. The third approach consists in using external triggers. At a rate of 1 Hz, the Double Chooz detector triggers even if the energy threshold has not been exceeded. The corresponding waveform in the 256 ns readout window should then be "pedestal only". A fit of the ADC count distribution would thus give the mean and RMS of the pedestal. This method is however not always appropriate: the computation of the pedestal using the external triggers is not possible because of large baseline fluctuations within a time window of several hundreds of microseconds after a muon passes through the detector and triggers it.

The default pedestal analysis method used in DCRecoPulse consists of a hybrid solution. It uses by default the pedestal computation of the offset time method with a window of 20 ns, or the 1 Hz external trigger method if the results of the offset window method are not reliable. By reliable one means that the computed offset time method RMS is away from the external triggers method RMS by 0.5 ADC counts.

### Charge analysis

Three algorithms are implemented in DCRecoPulse for the charge reconstruction: the peak window, maximum window, and sliding window methods. They all search for an arbitrary number of peaks in the full readout window and reconstruct their charge and times. The difference between these algorithms is the method used to find the peaks and consequently the way in which the analysis time window is built (Figure 4.1).

The peak window algorithm is the fastest among the three algorithms, but it is the less accurate. It searches for continuous regions (at least three 2 ns time samples) with absolute amplitudes above a threshold. In this case, the size of the integration window depends on the shape of the pulse. The maximum window algorithm searches for the absolute maximum amplitude of the pulse and opens an asymmetric window around it, where the charge reconstruction is applied. Then, the algorithm searches for the subsequent relative maxima and repeat the procedure, until the charge reconstructed in the current window is below a threshold. With this algorithm, the size of the window is fixed by the user. The sliding window algorithm is the slowest, but most precise. It searches for the maximum integral among all the possible windows

of a fixed size within the full readout. After reconstructing the peak of the window with the maximum integral, it iterates the procedure over the rest of the unanalyzed readout window until the integral over the time window is below a threshold. Once again, the size of the integration window is fixed by the user.

When estimating the pedestal mean and variance, a compromise has to be found when choosing the size of the integration window. A larger window will give a worse energy resolution, but will induce less loss of charge in the tail of the pulse and will give a better energy linearity.

In order to quickly monitor the data quality, the peak window algorithm is applied on the RAW data. However, the default within the Common Trunk is the sliding window algorithm with an integration gate of 112 ns, allowing to integrate most of the charge in the readout window. A threshold on the pulse maximum amplitude is set to 1 DUI [10] to select good pulses: if too high, low charge pulses will not be reconstructed, whereas if it is too low, the pedestal fluctuations could bias the reconstructed charge. An additional charge threshold can be applied, which gives fairly similar results, although some recent studies seem to show that it yields to non-linearity in the detector energy response. On the opposite, the single photoelectron (SPE) reconstruction efficiency and the energy resolution of the n-capture on hydrogen improve by 4 % if the charge threshold is not applied [60].

#### Time analysis

The DCRecoPulse output also gives several characteristic pulse times such as the maximum amplitude time, which corresponds to the time where the pulse amplitude is maximal. The start time of a pulse can be computed in two different ways. It can either be defined as the time where the pulse reaches 30 % of its maximum, or the time when the pulse passes a fixed threshold. DCRecoPulse also provides a value for the end time of the pulse, defined as the time after which it drops to 20 % of its maximum amplitude.

Other important pulse time related variables are computed within this package. They are for instance the rise time $T_{rise}$ and the start time spread $RMS(T_{start})$, and are very useful to suppress the so-called light-noise background (*cf.* Section 6.2.1).

## 4.2 Calibration

### 4.2.1 Photomultiplier gain

The photomultiplier gain calibration is one of the most important things to do prior to any analyses of the Double Chooz data. It gives the number of electrons deposited on the PMT anode per photoelectron (PE) ejected of the PMT photocathode after an incident photon hits it. It is calculated in DUQ per PE [11]. The PMT gain is expected to drift and fluctuate over time [12], and then needs to be regularly monitored with the different devices available (*cf.* Section 3.5.4).

The gain can be estimated by several techniques. The Double Chooz official method consists in fitting the distribution of the single photoelectron charge on each channel using data from the

[10] DUI is an arbitrary unit that stands for digital unit of current.
[11] DUQ is an arbitrary unit that stands for digital unit of charge.
[12] Power glitches induce baseline shifts for the channels. PMT aging needs to be taken into account as well.

inner detector light injection system [13], assuming that the SPE distribution is Gaussian [116]. With a very low light level, only the first PE peak is revealed (Figure 4.2, left). The low intensity multi-LED mode of the IDLI system is used as a faint photon source to collect single photoelectron events on the PMTs. The fit function is basically the product of a Poisson component which models the PMT behavior with a Gaussian component which corresponds to the SPE peak and comes from the resolution of the PMT:

$$\mathcal{G}(\mathrm{x};\mu,\sigma_1,g) = \sum_{\mathrm{n}=1}^{2} \frac{\mathrm{N}\mathrm{e}^{-\mu}\mu^{\mathrm{n}}}{\sqrt{2\pi}(\sigma_1\sqrt{\mathrm{n}})\mathrm{n}!} \mathrm{e}^{-\frac{1}{2}\left(\frac{\mathrm{x}-\mathrm{n}g}{\sigma_1\sqrt{\mathrm{n}}}\right)^2}, \tag{4.1}$$

where the sum is done over the first and second PE peaks, $\mu$ is the mean number of PEs collected by the PMT, $\sigma_1$ the SPE distribution RMS, N the constant average number of PEs injected into the detector per flash of LED, and $g$ the fitted SPE gain of the considered PMT.

The Double Chooz inner detector PMT gains resulting from the SPE fit are of the order of 70 DUQ/PE (Figure 4.2). Once each PMT gain is estimated, the mean of all channels over five days of IDLI runs is computed. The SPE gain variation over the second publication period is available on the right panel of Figure 4.2. The abrupt changes are explained by baseline shifts induced by power glitches. The SPE gain calibration is therefore needed at least after each power cut.

Unfortunately, the PMT gain is not a linear function of the charge (Figure 4.3) and it varies from one channel to another. Therefore, applying the mean SPE gain on each PMT cannot be done. The SPE gain is valid for low charge but incorrect otherwise. This non-linearity can be corrected by parametrizing the curve of Figure 4.3 with three parameters: a slope at low charge, a constant at higher charge, and the value of the intersection between the two regimes [10].

The method used to compute the PMT gains for high charge is called multiple PE (mPE) [10, 66]. The gain G is estimated by using the relation between the mean $\mu$ and the width $\sigma$ of the charge distribution for a constant average number of photoelectrons N per flash of IDLI. The mean charge is $\mathrm{G}\times\mathrm{N}$ and the width is basically the sum of two effects: a Poisson component $\sigma_{\mathrm{poisson}} \simeq \mathrm{G}^2\times\mathrm{N}$ which can be approximated by a Gaussian if the mean charge is large enough, and a Gaussian component $\sigma_{\mathrm{spe}} = \alpha^2\times\mathrm{G}^2\times\mathrm{N}$ coming from the resolution of the PMT. The constant $\alpha$ is defined as the standard deviation of the entire single photoelectron distribution, which is not a perfect Gaussian as shown on the left panel of Figure 4.2 (its value is chosen to be 0.4 to match the SPE gain). The mPE gain is thus defined as:

$$\mathrm{G} = \frac{\sigma^2}{\mu}\frac{1}{1+\alpha^2}. \tag{4.2}$$

This gain G is estimated from different IDLI middle and high intensities, and coupled to measurements obtained from the single photoelectron method. The Figure 4.3 is thus a gain curve which allows to take into account gain non-linearity (*cf.* Section 4.2.4), when the single photoelectron gain and the multiple photoelectron gain are combined together. The calibrated number of photoelectrons for a certain measured charge on a PMT is therefore calculated and saved at the Common Trunk level.

[13] The inner detector light injection (IDLI) calibration system is presented in Section 3.5.4.

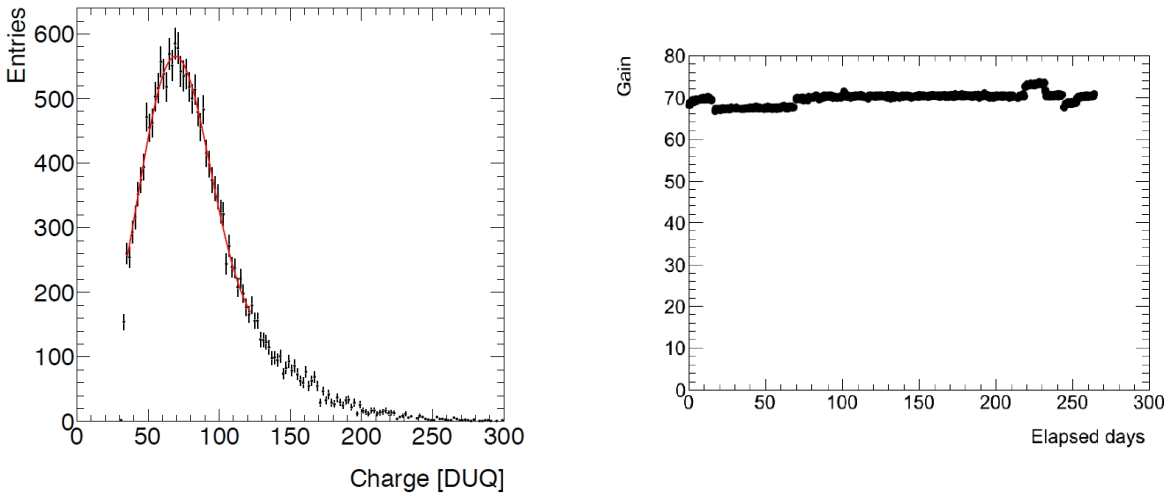


Figure 4.2: *(left) Charge distribution obtained with very low intensity IDLI (here, only the first PE peak is visible). The fitted SPE gain is roughly 70 DUQ/PE [116]. The red curve is a fit to the distribution with equation (4.1). The SPE gain is defined as the position of the fit maximum. (right) Mean PMTs gains per day. The steps are due to power glitches [116].*

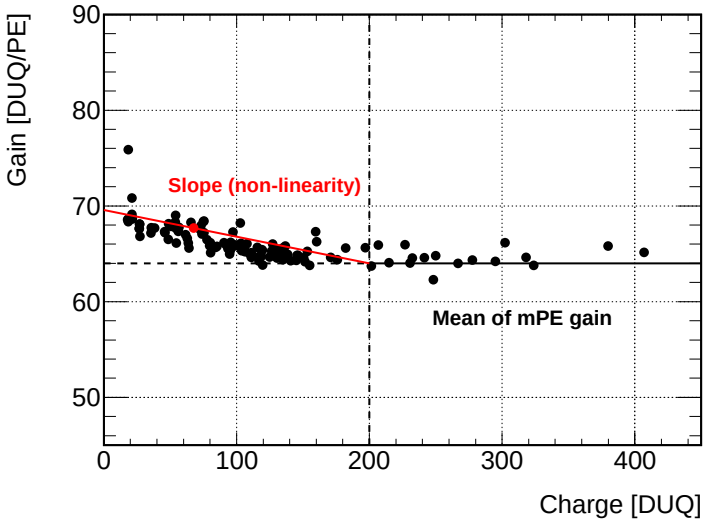


Figure 4.3: *Gain non-linearity calibration. The gains at low intensity are fitted with a linear function while the region above 200 DUQ is fitted with a constant [10].*

### 4.2.2 Channel time offset

Another important quantity to know prior to data analysis is the relative time differences between each PMT response, called the channel time offsets. The timing information is fundamental in Double Chooz since it is used in the event reconstruction algorithms and especially for the vertex position reconstruction (*cf.* Section 4.3). The time offsets between the channels (and thus the corresponding PMTs) are mainly caused by the acquisition system, such as the slightly different lengths of the signal cables connecting the photomultipliers bases to the FADC boards (*cf.* Section 3.5.3). By applying time offset corrections, called hereafter $T_0$, the hit time of the PMT can be estimated more precisely.

A way of measuring the time offsets is to deploy within the $\nu$-target volume a special LED flasher device. I was involved since the beginning in the channel time offsets measurement using this method [78]. The device used in Double Chooz is a 5 cm Teflon diffuser ball coupled to a 10 Hz flashing blue LED, which loops over eight different intensities and provides 128 consecutive pulses per light level [120]. The idea behind this is to measure simultaneously each channel's time offset with the same isotropic source (Figure 4.4). The deployment occurred while the detector was still empty. The measured time on the $i^{th}$ PMT $T^i_{PMT}$, which corresponds to the arrival time of the first photons, should be:

$$T^i_{PMT} = T_{event} + T^i_{TOF}, \tag{4.3}$$

where $T_{event}$ is the absolute event time and $T^i_{TOF}$ is the time of flight of the photons from the LED flasher to the $i^{th}$ PMT. However, the detector is such that there are time offsets $T^i_0$ for each channel, changing equation (4.3) into:

$$T^i_{PMT} + T^i_0 = T_{event} + T^i_{TOF}. \tag{4.4}$$

Since the absolute event time is unknown, it is necessary to use a PMT as a reference, thus getting rid of $T_{event}$ when subtracting equation (4.4) for a channel i, by the same equation for a channel j. The time offsets computed using this method are then relative to the PMT which serves as reference.

Unfortunately, a serious issue with the FADC firmware made the data taken during this calibration campaign not usable. It was discovered that the FADC firmware was introducing random 2 to 8 ns time delays for some channels after reinitialization of the electronics. This means that the time offsets measured with the LED flasher are representative to a few nanoseconds at best. Another method had then to be used to extract them, since the detector was already filled when this DAQ issue was discovered [169].

The second idea for measuring and then correcting for the channels time offsets is to use data taken with the IDLI system operated at strong intensities [9] (*cf.* Section 3.5.4). Here, the time offset corrections are the time differences between the estimated and the observed times, where the estimates come from the known distance between the LED and the PMT being calibrated. Eight LEDs are used for this measurement: two placed on top of the detector, four placed on the wall, and two at the bottom. An LED can be used to calibrate a PMT only if it sees its light with an opening angle less than 45 degrees, which means that for wall PMTs the LED should be placed on the opposite side of the detector. Such a measurement is done in three steps. The first one is to obtain the observed time for each PMT. In order to do so, the difference between the pulse maximum and the start time of the IDLI external trigger $T_{max} - T_{start}$ is filled into a histogram for each channel, and the observed time is obtained by fitting it. Then the times of

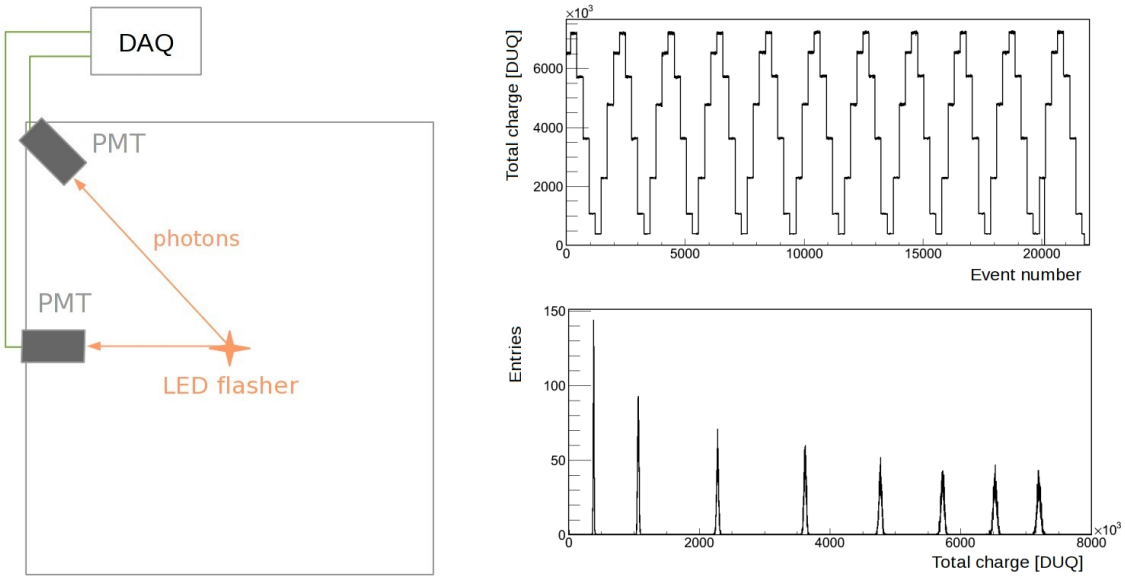


Figure 4.4: *(left) Scheme of the time offsets computation method with the LED flasher. The flasher is placed at the center of the empty detector and emits light detected by the PMTs. Two different LED flasher photons times of flight and the associated PMT cables lengths in the DAQ are represented. (top right) LED flasher looping over eight intensities. (bottom right) Total charge distributions for the eight LED intensities [78].*

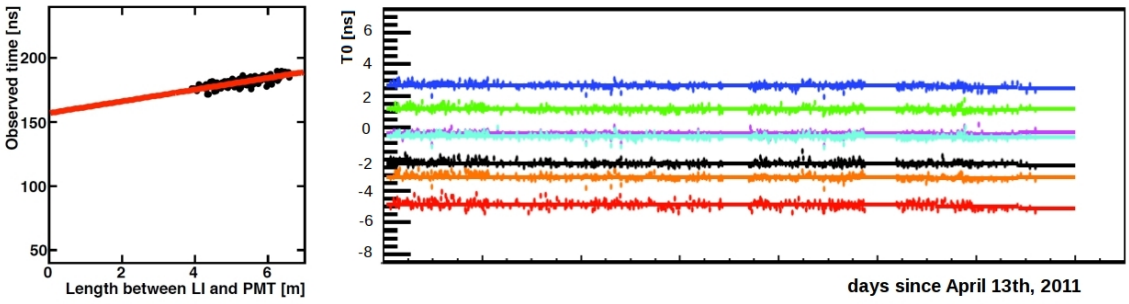


Figure 4.5: *(left) Observed time as a function of the length between an LED and opposite PMTs [9]. (right) Time offsets stability over a hundred days for seven channels [9].*

flight from the LED to the PMT are estimated by fitting by a linear function the observed times versus the distances between the LED and the PMTs (Figure 4.5, left). Finally, the relative time offsets are obtained by subtracting the observed times to the expected times.

The good stability of these offsets, within less than 0.5 ns for the whole Double Chooz first publication data taking period, is presented in the right panel of Figure 4.5.

The $T_0$ calibration constants are finally uploaded to a database allowing a correction of the Common Trunk data. The IDLI runs are taken every 12 hours, allowing a regular monitoring of both the PMT gains and time offsets. The rest of the Common Trunk algorithms is then applied, such as the vertex reconstruction algorithm (*cf.* Section 4.3).

### 4.2.3 Problematic channels

Among the 468 PMTs spread within the buffer and inner veto walls, connected to the front end electronics (*cf.* Section 3.5), some problematic channels inevitably show up in the Double Chooz far detector. For instance, the baselines of a few channels are oscillating or saturating, or a few channels exhibit a pedestal value which is several standard deviations away from the overall mean pedestal value. Most of these online problems have been solved during commissioning, while some others could not. This is especially the case for the light-noise, a background that Double Chooz analyzers had to live with. This new background as well as the offline rejection cuts applied on the data are presented in Section 6.2.1. The light-noise background consists of some PMTs producing light from the circuits integrated in their base, illuminating themselves and the other nearby photomultipliers. This random light emission turned out to depend on the high voltage value and the ambient temperature.

Fifteen inner detector photomultipliers had to be turned off because of their large light production, even if they do not evenly contribute to the light-noise. The accidental background rate was lowered by more than a factor of 10 by switching off these 15 PMTs (*cf.* Section 6.3.1). Turning off less than 4 % of the ID PMTs does not drastically change the photodetection coverage nor the energy response of the detector. A schematic of the ID PMT arrangement with their voltage value given by a data taking monitoring tool (*cf.* Section 4.5) is shown on Figure 4.6. The 15 disabled PMTs have zero voltage and appear in purple.

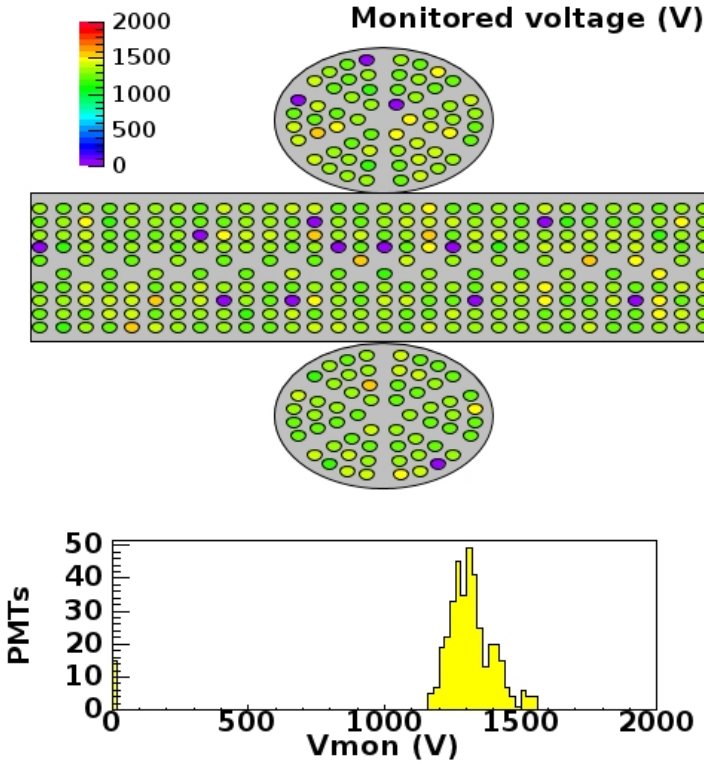


Figure 4.6: *(top) Far detector PMT arrangement from the HV monitoring tool. Each circle represents an ID PMT, and the color scale corresponds to the HV applied to each PMT, in volts. Purple-colored PMTs are turned off due to high light-noise activity. (bottom) Distribution of high voltage values. The first bin corresponds to the 15 disabled PMTs.*

### 4.2.4 Energy scale

The detector energy scale definition changed between the first and the second Double Chooz official analyses, allowing an improvement of more than a factor 4 on the energy scale uncertainty [11, 12]. Both methods compute the photoelectrons (PEs) to energy (MeV) conversion factor using the neutron capture peak on hydrogen within the detector. The following section describes the method used in the second Double Chooz publication, which improved the energy calibration mostly by taking into account spatial uniformity response and time stability considerations. All these information are taken from [49].

The energy scale is evaluated by defining the visible energy $E_{vis}$ in the Double Chooz inner detector. It provides an absolute calorimetric estimation of the energy deposited in the scintillator per trigger and is defined as:

$$E_{vis} \;=\; {}^{k}PE(\rho, z, t) \times {}^{k} f_{uniformity}(\rho, z) \times {}^{data} f_{stability}(t) \times {}^{k} f_{MeV}, \tag{4.5}$$

where k refers to data or Monte Carlo simulations, $PE(\rho, z, t)$ is the sum over the calibrated RAW charge of each channel performed over channels flagged as "goods" (*cf.* Sections 4.1 and 4.5), $f_{uniformity}(\rho, z)$ and $f_{stability}(t)$ are the detector spatial uniformity and time stability response correction functions, respectively, and $f_{MeV}$ provides the absolute PEs to MeV scale factor from neutron capture on hydrogen studies.

The PE function characterizes the response of the detector per trigger and depends on both the vertex position and time. As written in equation (4.5), this function is different for data and MC and the position and time dependencies have to be corrected in order to provide an absolute energy definition, independent from data or Monte Carlo. Uncorrected differences between data and MC would affect the measured neutrino oscillation parameter $\theta_{13}$, as its determination relies on energy selection cuts (*cf.* Section 6.2). The PE function is defined as:

$$PE(\rho, z, t) \;=\; \sum_{i} q_i \;\times\; gain_i(q_i), \tag{4.6}$$

where $q_i$ are the RAW charges per channel i and $gain_i(q_i)$ is a function that corrects for the charge non-linearity arising from biased baseline measurements (*cf.* Section 4.2.1). Since the mean offset of the baseline varies slightly from an electronics power-cycle to another, one calibration curve $gain_i(q_i)$ has to be generated for each electronics power-cycle.

The detector response is intrinsically non-uniform across the detector volume. The PE response is therefore position-dependent, for data and Monte Carlo simulations, and is not the same for both of them. Response maps were generated such that the PE response for any event located at a position $(\rho, z)$ can be converted into an effective $PE_{00}$, *i.e.* the response as if it was measured at the detector center ($\rho = 0$, $z = 0$):

$${}^{k}PE_{00}(t) \;=\; {}^{k}PE(\rho, z, t) \times {}^{k} f_{uniformity}(\rho, z). \tag{4.7}$$

The response maps were computed using the hydrogen capture of neutrons created either by muon spallation or neutrino interaction, for data and Monte Carlo samples respectively, across the full volume of the inner detector.

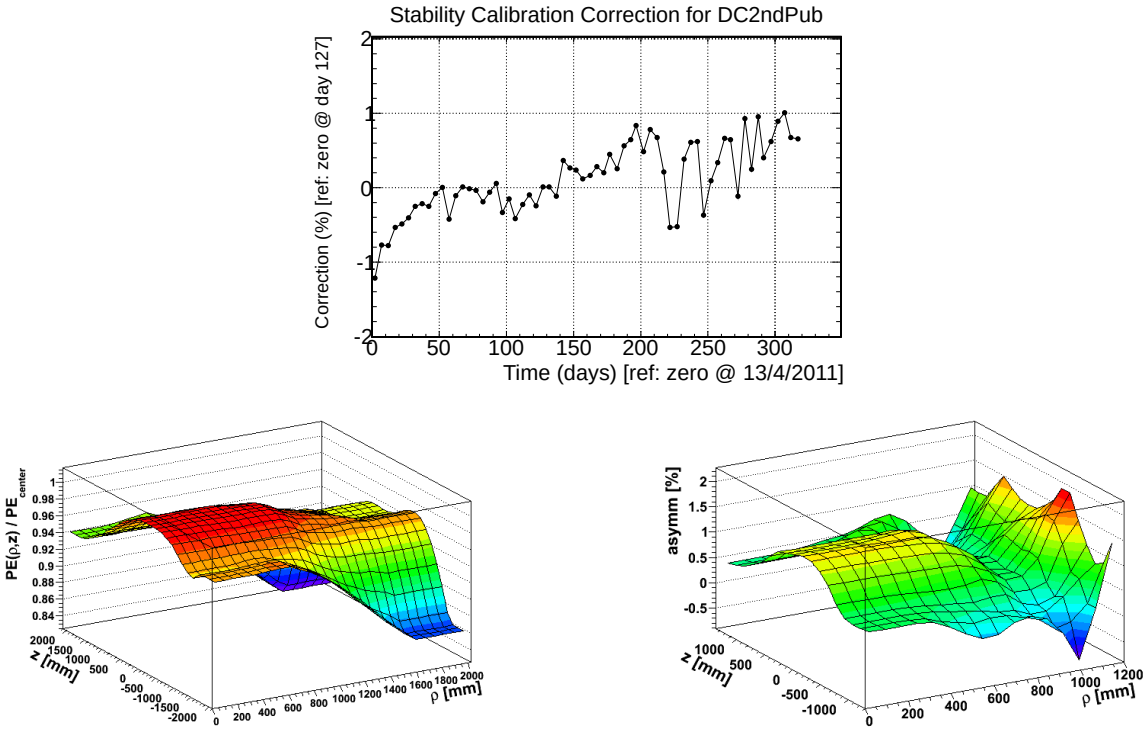


Figure 4.7: *(top) Time stability response correction $f_{stability}(t)$ over the 2nd publication period. (bottom left) Example of detector response map obtained from the selection of spallation neutrons on data. (bottom right) Data/MC asymmetry map for the position correction factor [49].*

The detector time stability function corrects mostly for a detector response drift arising from variations in PMT gain. The ${}^{\text{data}}f_{stability}(t)$ function is applied on both data and MC and corrects the average response time variation with respect to a reference run used for the MeV absolute calibration $f_{MeV}$. The position and time corrected PE, called $\text{PE}_{000}$, is therefore:

$$ {}^{\text{k}}\text{PE}_{000} \;=\; {}^{\text{k}}\text{PE}_{00}(\text{t}) \times {}^{\text{data}}f_{stability}(\text{t}). \tag{4.8} $$

Finally, the absolute MeV calibration is done by studying the neutron capture on hydrogen peak (at 2.2 MeV) arising from a $^{252}$Cf calibration source deployed in the center of the detector. The detector response is measured in $\text{PE}_{000}$ which allows to define the detector MeV scale. The $f_{MeV}$ conversion factors were measured for both data and MC, and found to be 229.9 and 227.7, respectively.

The energy scale systematic errors are evaluated by estimating the remaining differences between data and Monte Carlo. The relative energy response spatial non-uniformity and time instability account for 0.43 % and 0.61 %, respectively. The non-linearity is estimated to account for 0.85 %. The relative non-uniformity response systematic uncertainty affecting neutrinos was estimated by comparing the maps response for data and MC obtained with neutron capture on Gd (within the $\nu$-target volume only). Sampling homogeneously the relative difference MC/data across the volume allows us to characterize the remaining non-uniformity. In addition, the uniformity calibration was further validated with all calibration sources in all deployed positions. Concerning the relative instability systematic uncertainty, it was estimated with the response evolution of spallation neutrons capture on hydrogen. The total energy scale systematic uncertainty is finally estimated to be 1.13 %.

## 4.3 Vertex reconstruction

The energy deposition vertex reconstruction is performed, within the Double Chooz Common Trunk, by the RecoBAMA package. Several algorithms can be run using only the charge or the time information, or both of them. The charge-only version of RecoBAMA relies on a charge likelihood derived from MC simulations, and is therefore different from a reconstruction such as CocoReco which will be presented in the next chapter.

The official RecoBAMA run on physics data is based on charge and time likelihoods. Basically, for each vertex, the light flux is calculated as the total visible charge over the total solid angle. Details on the optical model used in RecoBAMA presented hereafter can be found in a Double Chooz internal note [170]. For a point-like source of isotropic light flux per unit of solid angle $\Phi$ (calculated in photons per steradian), and if the light propagation is expected to only be affected by pure attenuation and not by absorption with reemission, nor scattering, the $i^{th}$ PMT is expected to see a charge:

$$\mu_i = \varepsilon_i \times \Phi \times \Omega_i \times e^{-r_i/\lambda}, \tag{4.9}$$

where $\varepsilon_i$ is its quantum efficiency, $\lambda$ is the characteristic attenuation length, $r_i$ the distance from the source, and $\Omega_i$ is the solid angle subtended by the PMT. Assuming the angular response function of the $i^{th}$ PMT to be $f(\cos\eta_i)$, where $\eta_i$ is the angle of incidence of the light with respect to the $i^{th}$ PMT normal, the solid angle subtended by the $i^{th}$ PMT with radius R can be written, to a good approximation ($R \ll r_i$), as

$$\Omega_i = \pi R^2 \times \frac{f(\cos\eta_i)}{r_i^2}. \tag{4.10}$$

The optical model is used to predict the amount of light the PMTs see. It is fully characterized by the optical parameters $\lambda$ and $f(\cos\eta)$. These allow then to calculate the total amount of light created in an event, which is basically proportional to its total energy. From this, using Monte Carlo simulations, the charge likelihoods are obtained. They are essentially the probability of measuring a certain charge where $\mu_i$ is expected. These functional values are saved in files, fastening the reconstruction.

These charge likelihoods can be used in a tridimensional vertex minimization algorithm by themselves. However, the precision of the reconstruction can be improved by adding timing information of photons hits on PMTs, via time likelihoods. These functions are derived from Monte Carlo simulations and saved in lookup tables as well.

Eventually the time and charge likelihoods will be extracted from UV laser calibration data with multiple intensities, once the system is ready. This new calibration system is under development and will consist of an 80 mm acrylic ball coupled to a 470 nm (blue) and a 375 nm (UV) lasers, that would be placed at the center of the Double Chooz $\nu$-target through the chimney [105, 106]. However, the likelihoods that have been used so far are still estimated via Monte Carlo. A comparison between them and likelihood functions extracted from radioactive sources deployments showed that they are good enough. The precision of the time and charge likelihoods method is of the order of 12 cm for 1 MeV electrons and is very robust with respect to the uncertainties on the channels time offsets [168]. The Figure 4.8 shows RecoBAMA performances on $^{68}$Ge calibration source simulation.

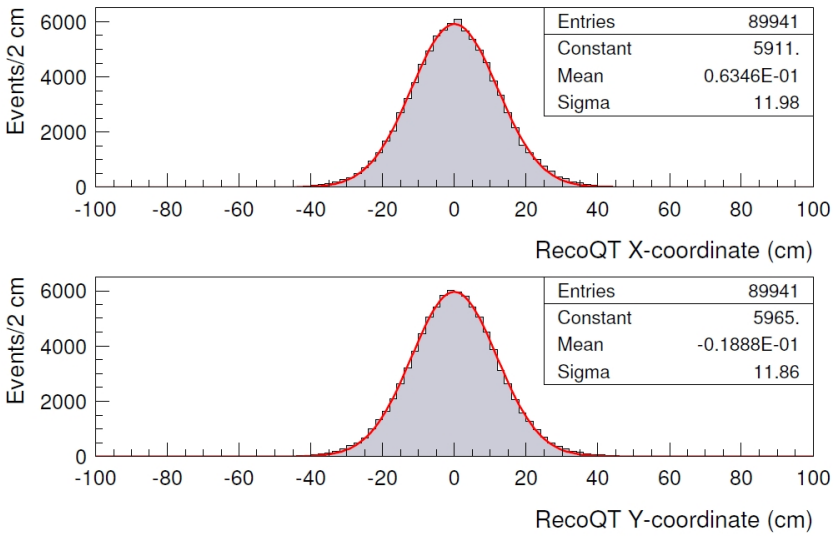


Figure 4.8: *RecoBAMA performances for X and Y coordinates reconstruction from Monte Carlo simulations of a $^{68}Ge$ source at the center of the detector [172].*

## 4.4 Muon reconstruction

In the Common Trunk, the RecoBAMA vertex reconstruction algorithm is run on events corresponding to an energy deposition lower than 30 MeV. Everything higher than 30 MeV deposited in the inner detector is considered as a probable muon, or a Michel electron [14].

Many of the muon reconstruction tools developed within the Double Chooz collaboration are not part of the Common Trunk, essentially due to the goal of minimizing the data processing time and the size of the output files. One may notice that their main difference lies in the information they use: the timing information and the charge information from the inner detector (ID), from the inner veto (IV), from the outer veto (OV), or even from a combination of them are possible [15].

An example of muon reconstruction algorithm is FIDO MUTT, for Fused Inner Detector Outer veto MUon Track reconsTruction, where both information of the ID and the OV are used [173]. The IV information is then ignored. Basically FIDO uses the timing information on the inner detector PMTs to fit the muon track. This is a five parameters fit using the MINUIT package [16] to minimize a $\chi^2$ based on the ID entry time, the entry position (two angles, $\theta_{\text{in}}$ and $\phi_{\text{in}}$), and the exit position ($\theta_{\text{out}}$, $\phi_{\text{out}}$). If an OV entry point is found, the fit is repeated using the position in the OV as constraint, and the five parameters become the ID entry time, the OV position (x,y), and the track angle fitted before ($\theta$, $\phi$).

The RecoMuHamID package, part of the common algorithms applied on physics data, uses a similar approach while RecoMuJP is based on ID information only: the muon track is reconstructed by PMT hit timing assuming a straight trajectory inside the detector, via a maximum likelihood method [180]. This tool can however reconstruct only muons passing through the $\gamma$-catcher, and can therefore not reconstruct muons passing through the IV or in the buffer volume only.

[14] Michel electrons are produced by decay of stopping muons in the detector.
[15] The detector related acronyms used here are defined in Chapter 3 and summarized in Figure 3.11.
[16] MINUIT is a physics analysis tool for function minimization first developed in FORTRAN, then ported in C++ for ROOT [143, 161].

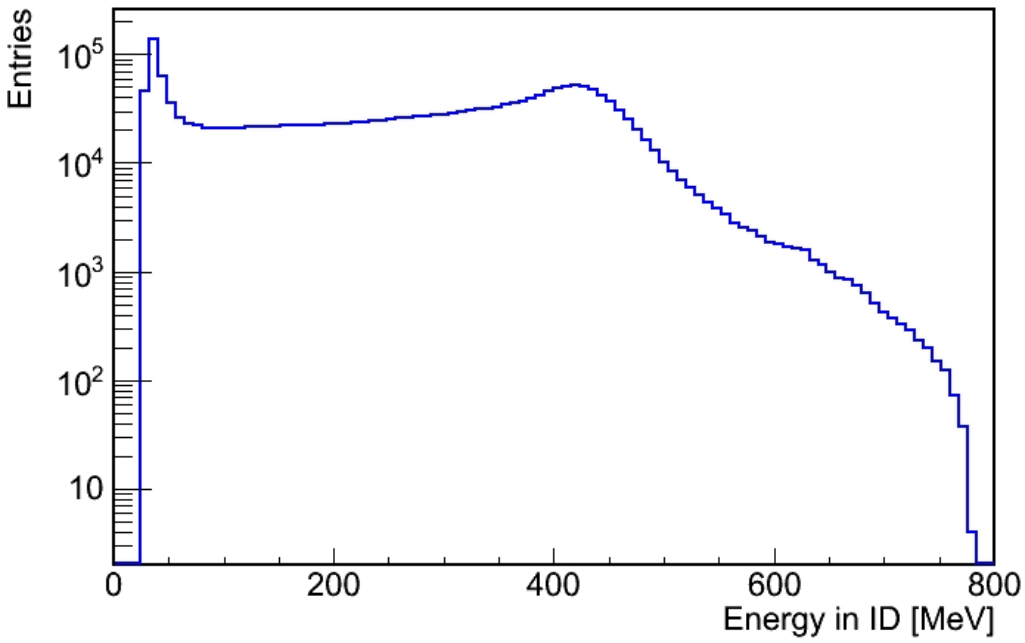


Figure 4.9: *Inner detector deposited energy distribution above 30 MeV. This is the sum of the muons spectrum, the Michel electrons spectrum, and the fast-neutrons spectrum.*

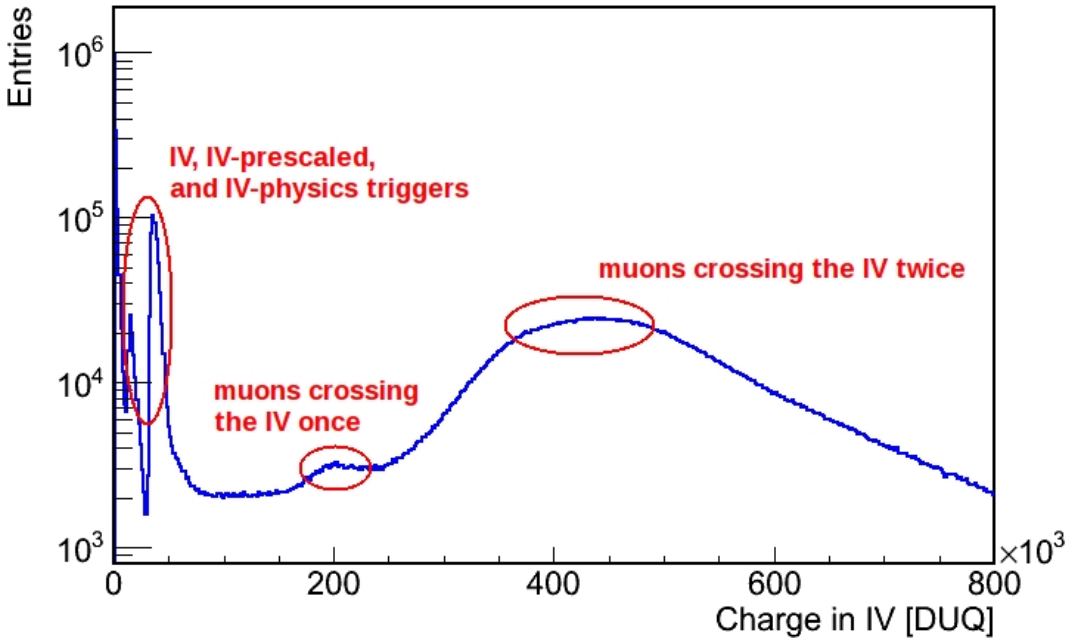


Figure 4.10: *Inner veto charge distribution in DUQ. The bump around 200,000 DUQ was found to be caused by muons crossing once the IV, the one around 400,000 DUQ by muons crossing it twice, and the structure at low energy by the IV, IV-prescaled, and IV-physics triggers [160]. The Double Chooz trigger system is briefly presented in Section 3.5.3.*

None of these tools have been used for the first Double Chooz publication since they were still under development at that time. However, they will definitely be used for future publications to better understand and better tag the muon-related backgrounds. Indeed, the $^9$Li background determination presented in Section 6.3.3 actually uses ID information for $\mu$ tracking.

The Figure 4.9 displays the energy spectrum of muons selected using inner detector energy depositions, while the spectrum of Figure 4.10 corresponds ton inner veto triggers. The energy cuts applied for muon selection are discussed in Section 6.2.2.

## 4.5 Data and reconstruction algorithms monitoring

Data monitoring happens at several steps from the data taking to the final reconstruction. The data taking and the detector are monitored on site and off site by a team of shifters using online and slow control monitoring tools, giving the current and high voltage values of the PMTs, the usage of all readout processors, the trigger rate recorded in real time, the liquid levels in the different vessels, etc. The sanity of the data themselves is checked using basic information, obtained through the application of a fast version of DCRecoPulse, the peak window method (*cf.* Section 4.1).

In order to ensure a good data quality, monitoring tools have been implemented within the Common Trunk. Their goals are to check the good conduct of the data transfer and processing, and the proper application of all the Common Trunk reconstruction algorithms.

Thereby, the monitoring is mainly performed using a simple web interface in order to check easily the ongoing CT production, the disks and buffers capacities, the CCIN2P3 Lyon Computing Center available batch resources, etc. Diagnosis units, basically Common Trunk algorithms using the CT Processor class concept, run after the reconstruction ones, and check specific physical values: the pedestal mean and spread from DCRecoPulse, the minimization function value from RecoBAMA, etc. These units can fill histograms visible on the monitoring website as well as run by run or event by event flags saved in the data files. The purposes of these flags are to spot quickly atypical and regular events during analysis and to be benchmarks for results comparison between the analyzers. Although useful when the detector was still being commissioned, most of theses diagnosis units are now not run in order to minimize the processing time.

## 4.6 Data files

The official data files used for offline analysis are the final outputs of the Common Trunk (Figure 4.11). They all share the Double Chooz software DOGS format. Each EnDep, *i.e.* energy deposition, has been reconstructed, from its charge and timing information, to its vertex position. During my thesis, member of the Common Trunk group involved in the CT data files production and monitoring, I codeveloped in parallel Cheetah with the Saclay group. It is both a data reducer, allowing fast analysis on easy to use ROOT ntuples, and an alternative way to fit our data, using directly RAW or even binary data access.

The DOGS software evolved a lot between the first commissioning data and the first publication. The idea here is not to use this platform to relate the story of developments through time of the collaborative offline software and its data format. However, it is important to notice that

the creation of Cheetah was at a certain time a pressing need for the analyzers. In order to take advantage of the calibration campaigns and thus reprocess the existent data, it was necessary to use a fast offline software, providing the collaboration with small and simple data files. I have been therefore strongly involved in the production of these light data files, and even responsible of the Cheetah outputs sanity checks for several months, during the Double Chooz first publication preparation. These files were used by a large fraction of the collaboration and allowed us to publish as fast as we planed to [12].

The problems of the first versions of the full Common Trunk was that it suffered from a slow processing and that the output data files were way too big to be used efficiently for analysis. An hour of physics data used to result in more than twenty reconstructed files (called CT-ed files), inducing then more than 20 GB of data on disks [80]. Processing such files with usual analysis scripts involved many I/O operations to access tree branches, slowing the analyzers down.

Two versions of Cheetah were developed in parallel. One is basically a format converter, also called "light trees maker", applied on CT or RAW data from DOGS and was called Cheetah-1, while the other one, Cheetah-2, intended to be completely independent from DOGS, taking then its input information directly from the binary files [84].

DOGS I/O objects have many fields and many access functions. Since ROOT, which is the tool that Double Chooz analyzers use, does not know what fields might be used, it has to read all of them for any operation in case a member function is called on the object. Light trees produced from CT outputs, the Cheetah-1 files are essentially "column wise ntuples": they are basic TTrees ROOT objects with simple leaves, like integers, floats, booleans, or arrays of such variables, since ROOT is highly optimized for these [161]. No complicated objects were used, such as C++ vectors, unlike DOGS. The entries of the data files could then be easily and quickly scanned using standard ROOT tools. This is very convenient for analysis and it allows to finally retrieve from data only what is needed. Small event size is a must for coincidence searches since analysis scripts tend to navigate a lot in the data tree. Furthermore, Cheetah-1 can do much more: some additional useful calculations are made within specific algorithms, such as, for an event, the maximum charge divided by its total charge, or other light-noise rejection variables like the rise time [17]. I actually ported the $T_{rise}$ calculation algorithm developed by the Saclay group [57] into the Cheetah framework. Cheetah-1 helped making these variables official and computed within our collaborative SVN maintained software, in Common Trunk algorithms. A Double Chooz one hour physics run of 20 GB was then reduced to a simple ntuple of a few dozen of MB, strongly lowering the risk of disk saturation at Chooz when connection to the CCIN2P3 Computing Center at Lyon is down. I dealt with the production of such files for several months and carefully checked that the Cheetah outputs for each run were identical to the CT outputs.

However Cheetah-1 can do more than just produce light ntuples and calculate few additional variables: as in the Common Trunk, a sequence of algorithms can be applied on each event, such as calibration constant application and reapplication of fitting algorithms (new charge and timing reconstruction strategy for instance). The vertex reconstruction package RecoBAMA has been for example totally ported to Cheetah.

Cheetah-2 code organization is really similar to Cheetah-1 yet with more functionalities. The Cheetah code principles are available in a Double Chooz internal note [84]. However, it can be highlighted that the key to Cheetah efficiency is in the data storage code, written from scratch and separated from the reconstruction algorithms. Cheetah-2 has two purposes. First of all it proposes heavier outputs, of the order of the GB, in which more information are stored, essentially channel-by-channel charge and timing information. Cheetah-2 can also directly read

[17] For details on this so-called light-noise background and the related rejection variables, *cf.* Section 6.2.1.

the binary files from DAQ and induces an overwhelming performance gain compared to DOGS in terms of processing speed (factor $> 10$), allowing a data processing faster than the DAQ.

Cheetah finally triggered improvements of some DOGS packages, such as reducing data access to a minimum, reducing the usage of STL [18] in ROOT (C++ vectors in TTree for instance), etc. The Cheetah-1 storage philosophy is now embedded within the CT, and a production of official light trees along with the classical DOGS files is now standard for data processing.

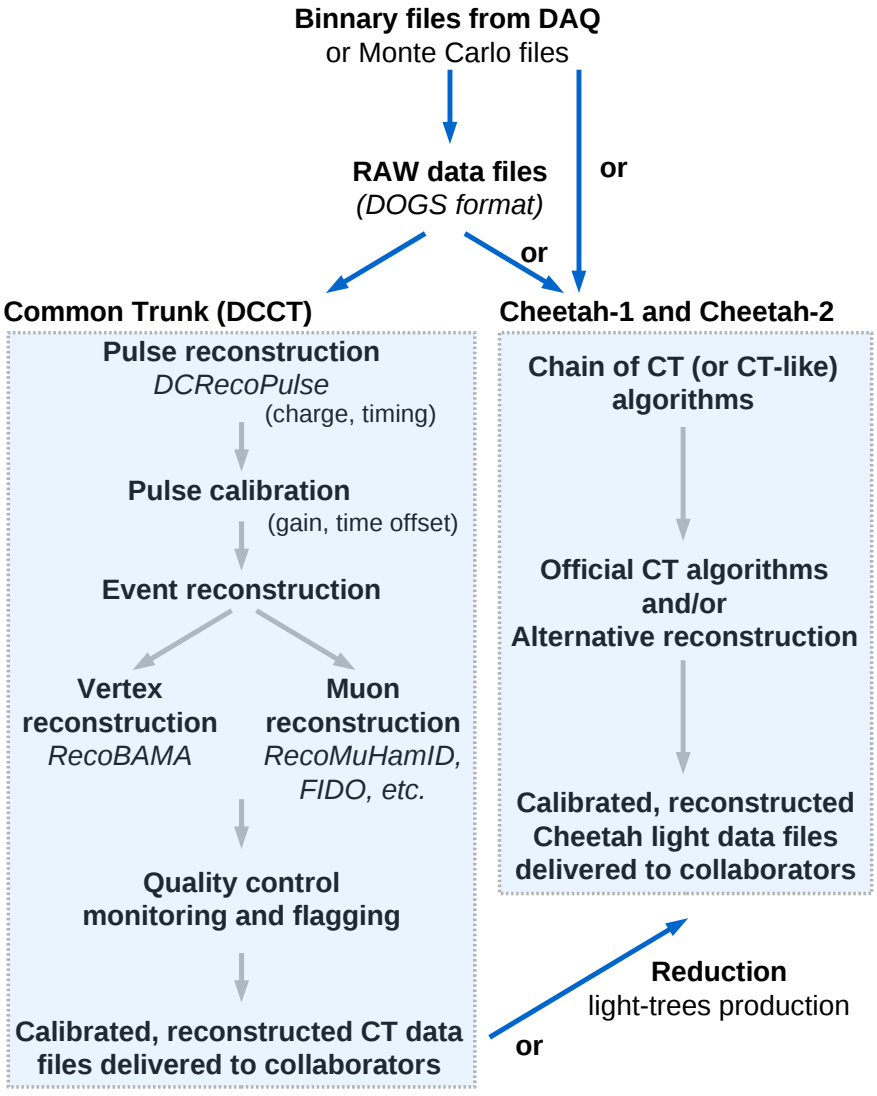


Figure 4.11: *Data files production summary outline: official way through the CT and alternative through the Cheetah framework. The Cheetah softwares can read information from the binary, the RAW, or the CT files. This schematic is incomplete since the CT produces now official light trees based on Cheetah data structure.*

[18] Standard Template Library, C++ software library.

# Chapter 5

# The Double Chooz Monte Carlo

*Monte Carlo is simply Monte Carlo.*

Sébastien Loeb, six times winner of the WRC Monte Carlo Rally.

In order to compute the neutrino selection cut efficiencies and compare the far detector outputs with non-oscillated data, a complete and precise simulation from the reactor cores to the Double Chooz detector output is necessary since the near detector is not yet installed. For that purpose, the Double Chooz Monte Carlo is embedded within the collaborative offline software DOGS. It is composed of four steps: the neutrino generation, the simulation of all physics processes occurring in the detector liquids, the readout simulation, and the reconstruction. This chapter presents the Monte Carlo generation chain as well as the energy reconstruction algorithm "CocoReco" that I developed with the Saclay group. The tuning of Monte Carlo parameters from calibration and comparison to real physics data is presented in a last section.

## 5.1 Monte Carlo generation

### 5.1.1 Electron antineutrino generation

The electron antineutrino generation is performed within the DOGS framework by a package called DCRxtrTools [90]. This package simulates the neutrino interactions in the Double Chooz liquids using information on the reactor cores power, the fuel compositions, the locations with respect to the detector, the Double Chooz detector specific geometry, and the proton content of the liquids. Monte Carlo (MC) files with different values of $\sin^2 2\theta_{13}$ can then be produced, thus leading to more or less electron antineutrino disappearance at short distance (Figure 5.1). The output of such a package is basically a list of events with all the relevant true information, like the neutrino energies and directions, the position of the interaction vertices, the basic properties of the positrons and neutrons created after each $\overline{\nu}_e$ interaction, etc. This list is then fed into the Double Chooz detector simulation package DCGLG4sim.

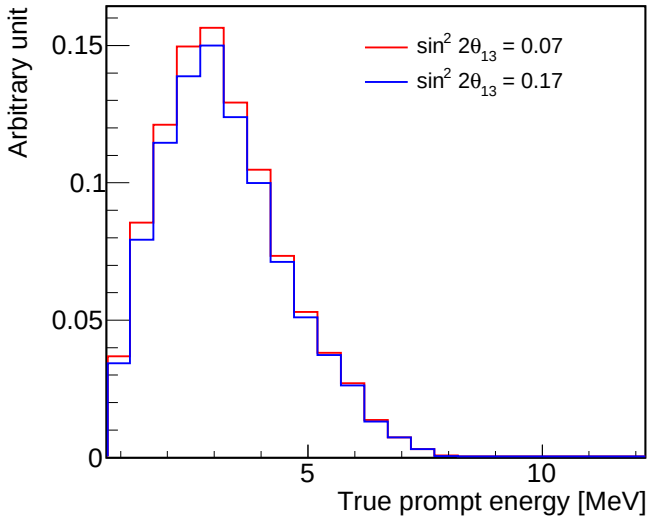


Figure 5.1: *Prompt spectra created with the Double Chooz electron antineutrino Monte Carlo generation package, with* $sin^2\ 2\theta_{13} = 0.07$ *(red) and* $sin^2\ 2\theta_{13} = 0.17$ *(blue).*

### 5.1.2 Liquid scintillator physics simulation

The DCGLG4sim package aims at simulating all the physics processes occurring in the Double Chooz liquids [14, 13]. It is based on the KamLAND GEANT4 [97, 123] (a toolkit for the simulation of the passage of particles through matter) and it is specifically adapted to the Double Chooz geometry and technological choices [1]. All the detector related properties (such as its exact dimensions, the liquid compositions and optical properties, the reflectivity of the vessels, etc.) are taken into account via datacards. The GEANT4 geometry is particularly detailed in the central part of detector. These properties values are mainly based on laboratory measurements, and sometimes on estimations or manufacturers specifications, to make the simulation of the expected physics as close as what one gets with the actual data. As good as the MC package is, it is anyway tuned using calibration data to correct possible discrepancies with real data. This is for example the case of the light yield (*cf.* Section 5.3). For that matter, the calibration devices such as the guide tube (*cf.* Section 3.5.4) are also modeled in the Double Chooz GEANT4.

The secondary particles created by the electron antineutrino and the target proton are propagated from the interaction vertex to the photomultipliers by GEANT4. Activation or deactivation of the Čerenkov radiation or the wavelength shifters reemission processes in order to study the detector response is possible within the MC simulations (*cf.* Section 5.2). Although the standard GEANT4 physics processes are used, the scintillation process, the photocathode optical surface model (absorption and refraction), and the thermal neutron model are customized. For instance, the neutron physics implemented in GEANT4 is known to present limitations for sub-MeV neutrons, mainly due to the absence of atomic liaisons considerations, and needs to be improved. This is done by using a new tool, NeutronTH [2].

[1] The GEANT4 version used in the DCGLG4sim package is 9.2-p02 [97].

[2] NeutronTH differs from the standard neutron generator of GEANT4 as it gives a precise description of slow neutrons moderation and radiative capture [82, 111].

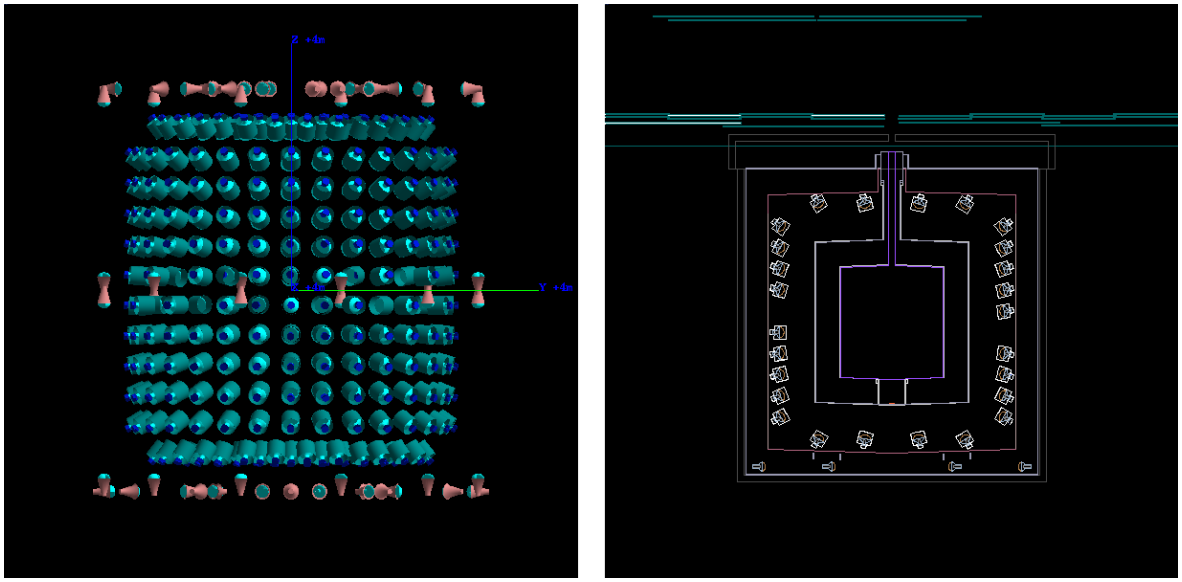

Figure 5.2: *Visualizations of the Double Chooz detector from GEANT4 macros [13]. (left) Inner detector and inner veto PMTs arrangement. (right) Double Chooz geometry simulation.*

Once the photons reach the PMT [3] photocathode, the production of a photoelectron (PE) depends on the quantum efficiency of each PMT, along with the collection efficiency, accounting for the homogeneity of the response on the photocathode surface. The relevant information of each PE are then fed into the readout simulation package called DCRoSS.

Physics events other than inverse $\beta$ decay interactions can be simulated within the Double Chooz detector. Indeed, radioactive sources like $^{60}$Co and $^{252}$Cf are simulated using standalone generators, and $^{252}$Cf source is modeled according to published data [183]. Cosmogenic isotopes such as $^{9}$Li are also simulated using detailed models of its nuclear levels, taking into account their various branching ratios and the corresponding transition spectra [182, 189].

### 5.1.3 Readout simulation

The whole readout system, from the electron multiplication through the PMT dynodes to the trigger decision, is simulated in the DCRoSS package [48]. The true deposited energy is converted into true charge in each channel by simulating the whole frond end electronics, the FADCs, the whole trigger system and various PMT related effects such as pedestal fluctuations or dark noise (around 10 kHz, according to measurements), quantum and collection efficiencies profiles (from measurements), single photoelectron shape as well as PMT to PMT fluctuations. Channel time offsets and PMT gains are also taken into account (*cf.* Section 4.2).

The output of this package shares the same format as the detector data, *i.e.* DOGS format, for convenience. The same event reconstruction algorithms than those used by the Common Trunk can then be applied (such as the vertex reconstruction algorithm, presented in Section 4.3). As for the far detector configuration, 15 PMTs are disabled in the Double Chooz simulation because of unexpected light-noise emission (*cf.* Section 4.2.3).

[3] PMT stands for photomultiplier tube. All the detector-related acronyms used in this chapter are defined in Section 3.5 and can be found in the detector schematic of Figure 3.11.

### 5.1.4 Event reconstruction

Once the simulated data shares the same architecture than the detector data format, one can apply the generic reconstruction algorithms of the Common Trunk presented in Chapter 4. The first step of this set of packages is the charge and time reconstructions of each pulse on each channel. Then, once the calibration constants are applied, the vertex reconstruction algorithm can be run.

For real data, the event energy reconstruction is done through the fit of the 2.2 MeV neutron capture peak on hydrogen, in the center of the detector from $^{252}$Cf calibration source data, corrected from gain non-linearity and detector response non-uniformity and unstability (*cf.* Section 4.2.4). However, an energy reconstruction tool may be applied, and some have been developed with Monte Carlo studies, allowing to convert the true charge into a reconstructed energy in MeV, through the reconstructed photoelectrons. This is the case of CocoReco, which is presented in the next section.

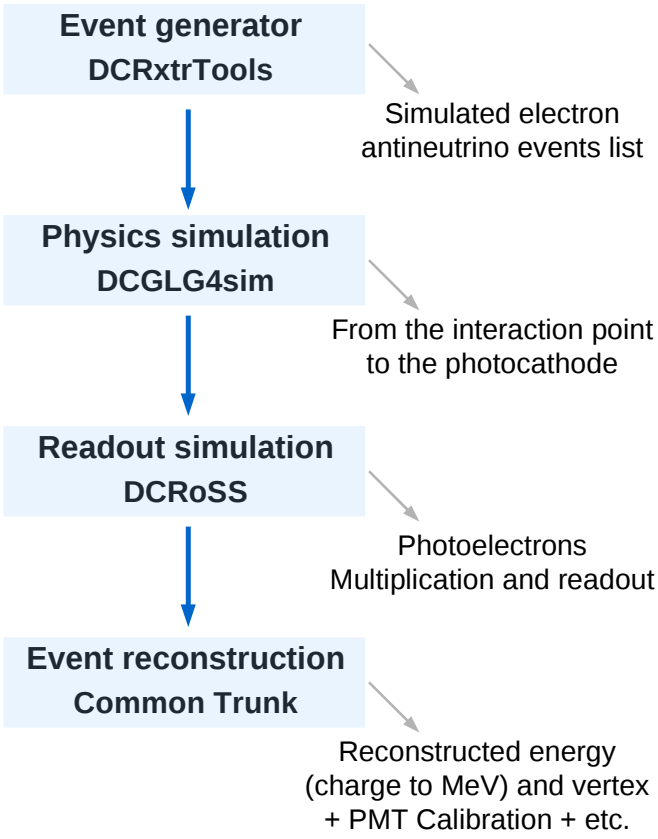


Figure 5.3: *Schematic of the Monte Carlo production chain. The four steps are summarized: the electron antineutrino generation, the liquid scintillator physics, the electrons multiplication within the photomultiplier tubes, and the reconstruction algorithms (cf. Chapter 4).*

## 5.2 CocoReco, an energy reconstruction tool

For the Double Chooz analysis, a corrected number of photoelectrons is used as an energy estimator (*cf.* Section 4.2.4) in spite of the fact that several energy reconstruction algorithms have been developed. CocoReco, which is presented below, is one of them. However, it has been decided not to use it for the first Double Chooz publications because it needs a lot of computing ressources. Its principle based on the understanding of liquid scintillator physics and its results on Monte Carlo are presented in this section. RecoEJP, developed later by another group, uses the same kind of technique as the one detailed below, and is also not part of the common reconstruction tools.

CocoReco [4] is an alternative energy and vertex position reconstruction tool developed at Saclay, that I helped to create, improved, and tested [71, 79]. As explained in Section 4.1, the RecoPulse package reconstructs the pulse and provides notably the charge collected on each photomultiplier tube. However, a critical information is still missing: how much energy was then deposited by an event in the detector? Since energy selection cuts are applied (*cf.* Section 6.2.2), a robust and reliable energy reconstruction tool is necessary. For CocoReco, the choice that had been made was to compare the observed charge of the PMTs with respect to an expected charge, estimated by modeling the physics taking place in our liquid scintillator, without the use of any timing information. Non-linear physics effects had also to be studied and taken into account in our model, such as Čerenkov radiation.

### 5.2.1 Method

#### Expected number of photoelectrons

The CocoReco estimate of the expected charge on the PMTs relies on three physical processes: the scintillation, the Čerenkov radiation, and the quenching. A detailed explanation of the scintillation process taking place in the Double Chooz liquid scintillator can be found in Section 3.5.1.

The Čerenkov radiation is an electromagnetic radiation emitted when a charged particle passes through matter with a velocity greater than the speed of light in that medium. The molecules of the medium are polarized by the charged particle, and deexcite themselves by emitting photons along the travelling path. These photons constructively interfere, intensifying the observed radiation, to create a photonic shock wave [5]. The geometry of Čerenkov radiation is peculiar: the emitted light forms a cone, whose angle is directly related to the velocity of the charged particle, therefore creating characteristic rings in water Čerenkov detectors [118, 124]. Even though Double Chooz is not expected to resolve these rings, some fraction of the visible energy should come from the Čerenkov radiation [6].

The quenching is a phenomenon typically occurring in liquid scintillators. In a nutshell, the idea is that the heavier the particle loosing its energy in the scintillator is, the less linear the relation between the deposited energy and the energy of the scintillation signal is. This is particularly true for protons or $\alpha$ particles. The effect is then, unlike Čerenkov radiation, a

[4] *Cocorico* is the way the French people hear the sound emitted by fowls, and especially roosters ("cock-a-doodle-doo", in English).

[5] An analogy can be made with the sonic boom of a supersonic aircraft for instance.

[6] More precisely, the Čerenkov radiation is not expected to produce rings in the Double Chooz detector because this radiation is absorded and isotropically reemitted by the bis-MSB and PPO compounds (*cf.* Section 3.5.1).

reduction of the light output. The quenching is described by the Birk's law and its constant $k_B$, which depends on the particle type [42, 124].

If quenching and Čerenkov radiation are neglected at the first order, the visible energy $E_{vis}$ is expected to be directly proportional to the number of photoelectrons generated by scintillation photons hitting the photomultipliers. $E_{vis}$ is the sum of the positron energy and the electron rest mass and is related to the $\overline{\nu}_e$ energy as explained in Section 3.3.1 (*cf.* equation (3.15)). In order to obtain the number of expected photoelectrons for a given PMT, one needs at first to multiply the visible energy by the light yield and the PMT quantum efficiency. The light yield is a quantity that characterizes the liquid scintillation power and is measured in number of scintillation photons produced per unit of deposited energy, while the quantum efficiency is the number of PEs produced per incident photons on the PMT glass and is different for each PMT. Two correction factors are then added to the model: one taking into account the light attenuation along the path of the scintillation photons in the liquid, and another one correcting for the PMT geometric acceptance. The expected number of photoelectrons for the $i^{th}$ PMT is written as follows:

$$N_i^{exp} = E_{vis} \times Y \times \eta_i \times e^{-\sum_j \frac{\ell_{ji}}{L_j}} \times \frac{\Omega_i}{4\pi} \tag{5.1}$$

where $E_{vis}$ is the visible quenched energy (MeV), Y the light yield of the liquid scintillator (photons/MeV), $\eta_i$ the quantum efficiency of the $i^{th}$ PMT (PEs/photons), $\ell_{ji}$ the length from the vertex to the $i^{th}$ PMT in the $j^{th}$ volume (j = 1, 2, 3, for $\nu$-target, $\gamma$-catcher, and buffer volume), $L_j$ the effective attenuation length in the $j^{th}$ volume, and $\Omega_i$ the solid angle of the $i^{th}$ PMT.

This simple model can then be modified as we go along in order to take into account other effects than scintillation.

Two important points should be highlighted though. First, the output of CocoReco is a visible quenched energy. A quenching correction has to be applied after CocoReco if the true deposited energy is wanted. Finally, all the Monte Carlos simulation studies reported here consist of a comparison between the reconstructed visible quenched energy and the true quenched energy, which is lower than the true simulated energy. As already pointed out before, the visible energy $E_{vis}$ that one expects to measure in our detector is anyway a quenched energy.

The second remark is that CocoReco strongly depends on four input parameters: the light yield Y and three effective attenuation lengths, each one corresponding to the three inner detector volumes ($\nu$-target, $\gamma$-catcher, and buffer). Those inputs can be tuned using calibration data (*cf.* Section 4.2.4). As opposed to RecoBAMA, the Double Chooz official vertex fitter, which uses only one effective attenuation length for the whole inner detector (*cf.* Section 4.3), CocoReco uses three different attenuation lengths and provides in this way a more realistic modeling of the inner detector physics.

### Likelihood model

Using a likelihood model with the expected number of photoelectrons, one can reconstruct the visible energy $E_{vis}$ from the observed charge pattern on the PMTs $N^{obs}$ in the data. This basic idea was used in other experiments, such as CHOOZ or KamLAND [30, 190].

The expected number of PEs for the $i^{th}$ PMT $N_i^{exp}$ is calculated using equation (5.1). A Poisson likelihood ratio is then built where $N_i^{obs}$ is the observed number of PEs on the $i^{th}$ PMT and $N_{PMT}$ is the total number of PMTs in the inner detector of Double Chooz, which amounts to 390 if none of them is turned off:

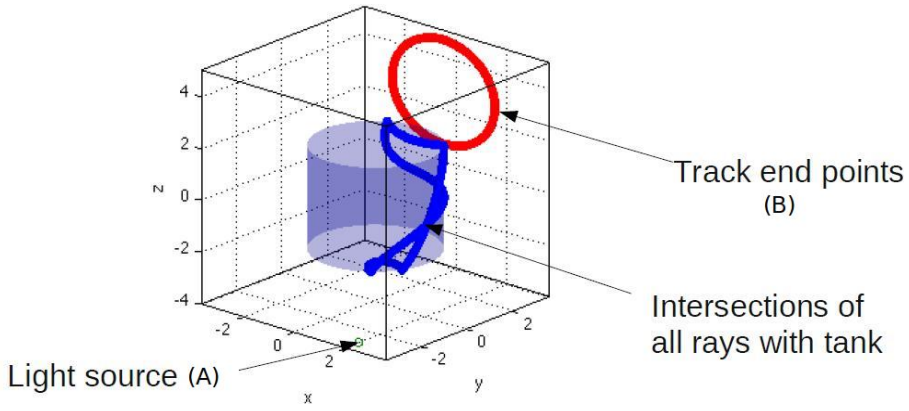


Figure 5.4: *Showcase used to check intersections. The blue twisted line shows all intersection points between photon rays, emitted from a light source A (green), and a cylinder (light blue). The track end points are the B points, represented by the red circle.*

$$-2\log\mathcal{L} = 2\sum_{i=1}^{N_{PMT}}\left[N_i^{exp} - N_i^{obs} + N_i^{obs}\log\frac{N_i^{obs}}{N_i^{exp}}\right] \tag{5.2}$$

This log-likelihood function is adjusted using the TMinuit Class from ROOT [161] in order to find the reconstructed visible energy $E_{vis}$ assuming that the vertex position is correctly reconstructed. A first iteration of CocoReco can be used with initial vertex position being the barycenter of the charge distribution and with the total expected charge fixed to the total observed charge. Another vertex reconstruction tool output, such as RecoBAMA (*cf.* Section 4.3), can also be used to set the log-likelihood function vertex position parameters. Therefore the energy determination is done through the adjustement of the log-likelihood function of equation (5.2) with only one free parameter: the visible energy, expressed in equation (5.1).

However, CocoReco is not only an energy reconstruction tool. The vertex position can be fitted using the same idea, since the charge pattern on the PMTs is directly related to the event position in the detector. In that case, the visible energy is fixed and the likelihood function is adjusted with three free parameters, the X, Y, and Z coordinates of the event position. One needs to remember from equation (5.1) that the expected vertex coordinates are used to compute $\ell_{ji}$, the length from the vertex to the $i^{th}$ PMT in the $j^{th}$ volume.

Fixing the vertex coordinates or the visible energy is only done to improve the algorithm speed. Indeed, if $E_{vis}$ and (X,Y,Z) are free in the fit, the results are actually similar in terms of energy or vertex reconstruction.

### Special features

One of the specificities of CocoReco is that one effective attenuation length is implemented for each volume ($L_{NT}$ for the $\nu$-target, $L_{GC}$ for the $\gamma$-catcher, and $L_{BF}$ for the buffer). From an energy deposition vertex, the path lengths of the photons traveled through each volume are calculated, in order to properly describe the light attenuation along their path. It consists on computing the intersection of each photon path with different cylinder volumes. The drawback is that these non-trivial ray tracing with cylinder computations tend to slow down the algorithm. An important effort was done to check the results in intersections calculations. A showcase can be found in Figure 5.4.

An advantage of this feature is that each effective attenuation length can be tuned independently. A change in one of the liquid attenuation properties is then easier to take into account without introducing unwanted biases in the reconstruction.

### 5.2.2 First results on Monte Carlo

CocoReco was first tested simulating 10,000 electrons in the $\nu$-target, at the center of the inner detector, for ten true energies ranging from 1 to 10 MeV [79]. The whole GEANT4-based Double Chooz Monte Carlo software was used is used (*cf.* Section 5.1). As explained earlier, the electrons simulated with the DCGLG4sim package were fed into the readout simulation DCRoSS before being reconstructed by the Common Trunk algorithms. Since CocoReco is an independent energy and vertex reconstruction algorithm, I had to hack the CT algorithms to run it within the event loop (*cf.* Section 4) and run Monte Carlo productions myself.

The physics modelling in equation (5.1) introduced a positive bias that went up to 13 % for a 10 MeV simulated electron (Figure 5.5). The right panel of Figure 5.5 represents the residuals as a function of the true quenched energy. The residuals are defined as the relative difference between the reconstructed and the true quenched energy, in percents. This is a way to determine the goodness of the reconstruction algorithm. The left panel of Figure 5.5 represents the reconstructed and the true quenched energy distributions for simulated 10 MeV electrons. The true quenched energy (in blue) is not a perfect Dirac distribution since it includes quenching and is then centered around 9.7 MeV instead of 10 MeV. The relative difference between the mean values of the true quenched and the reconstructed energy distributions amounts to 13 %.

The discrepancy between the simulated and the reconstructed energies shows that the model described by equation (5.1), developed in order to cover the scintillation process occurring in the detector liquid, is imperfect and that other physics processes need to be taken into account, such as those introduced at the beginning of this section.

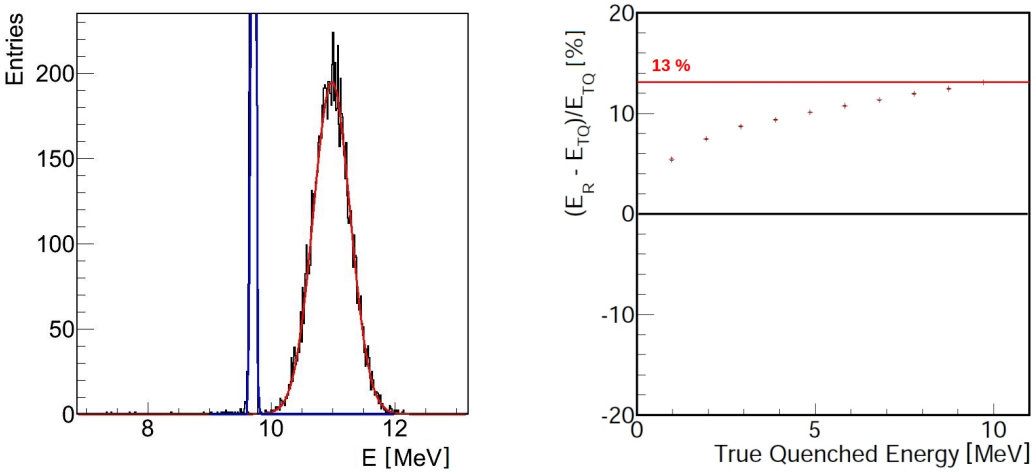


Figure 5.5: *(left) Energy distributions for 10,000 electrons simulated with an energy of 10 MeV at the center of the $\nu$-target. The blue Gaussian is the true quenched energy and the red one the reconstructed energy, in MeV. (right) Residuals for electrons simulated between 1 and 10 MeV. The red horizontal line shows the 13 % bias at 10 MeV.*

### 5.2.3 Čerenkov radiation in CocoReco

#### Improving the model

The observed positive bias in the reconstruction is explained by the fact that the model used to compute the expected number of PEs on a PMT is not complete. A Čerenkov radiation component is in particular absent [7]. In order to check whether or not this affects our results, the same GEANT4 simulation was performed without the Čerenkov radiation process activated. By looking at the residuals between the true and the reconstructed energies, one can see that the bias is strongly reduced and is lower than 4 % at 10 MeV (Figure 5.6). This means that the Čerenkov radiation is not negligible and has to be taken into account in CocoReco. This is thus done by modifying the physical model of equation (5.1).

CocoReco is modified by adding a corrective term: a function called $\mathcal{C}(\mathrm{E_{vis}})$ times a geometrical factor. This function was obtained by first simulating electrons at the center of the inner detector with the GEANT4 Čerenkov radiation process only (which means no scintillation). The total charge delivered by the PMTs for each simulated energy is then drawn. The mean value is each time extracted and divided by the total number of PMTs. Those points, which are pairs of energy value and related mean charge, are linearly interpolated to give the $\mathcal{C}(\mathrm{E_{vis}})$ correction function (Figure 5.6, left). $\mathcal{C}(\mathrm{E_{vis}})$ provides then the amount of charge per PMT per event only caused by Čerenkov light hitting the PMT, that is absent in the previous expected number of photoelectrons formula. The geometrical factor deals with the fact that $\mathcal{C}(\mathrm{E_{vis}})$ is calculated for particles simulated at the center of the $\nu$-target.

The new CocoReco modelling of the expected number of PEs in the $\mathrm{i^{th}}$ PMT, taking into account a Čerenkov radiation component, is as follows:

$$\mathrm{N_i^{exp}} = \mathrm{E_{vis}} \times \mathrm{Y} \times \eta_\mathrm{i} \times \mathrm{e}^{-\sum_\mathrm{j} \frac{\ell_\mathrm{ji}}{\mathrm{L_j}}} \times \frac{\Omega_\mathrm{i}}{4\pi} + \mathcal{C}(\mathrm{E_{vis}}) \times \frac{\mathrm{e}^{-\sum_\mathrm{j} \frac{\ell_\mathrm{ji}}{\mathrm{L_j}}} \times \frac{\Omega_\mathrm{i}}{4\pi}}{\mathrm{e}^{-\sum_\mathrm{j} \frac{\ell_{\mathrm{ji_{center}}}}{\mathrm{L_j}}} \times \frac{\Omega_{\mathrm{i_{center}}}}{4\pi}} \tag{5.3}$$

#### Results with new model

The new CocoReco model was once again used on 10,000 electrons, simulated at the center of the inner detector for ten true energies ranging from 1 to 10 MeV [79]. All the Double Chooz Monte Carlo packages were applied and both scintillation and Čerenkov processes are activated. As expected, the 13 % positive bias at high energy is strongly reduced. As shown by the right panel of Figure 5.7, the bias is lowered to 4 % at 10 MeV, pointing out the importance of the Čerenkov correction function $\mathcal{C}(\mathrm{E_{vis}})$ implemented in our model. The right panel of Figure 5.7 and the Figure 5.6 are indeed similar.

It can be emphasized that the reconstruction improves toward low energies, reaching 2 % at 6 MeV and 1 % for energies smaller than 4 MeV. Achieving a very good energy reconstruction in the 1 to 6 MeV energy region is very important. Indeed, an energy reconstruction bias in this energy region could be problematic since $\theta_{13}$ is expected to affect the low energy part of the $\mathrm{E_{vis}}$ spectrum, by altering its initial shape (*cf.* Figure 3.10).

[7] The Čerenkov radiation principle is reminded in Section 5.2.1 and details can be found in [118, 124].

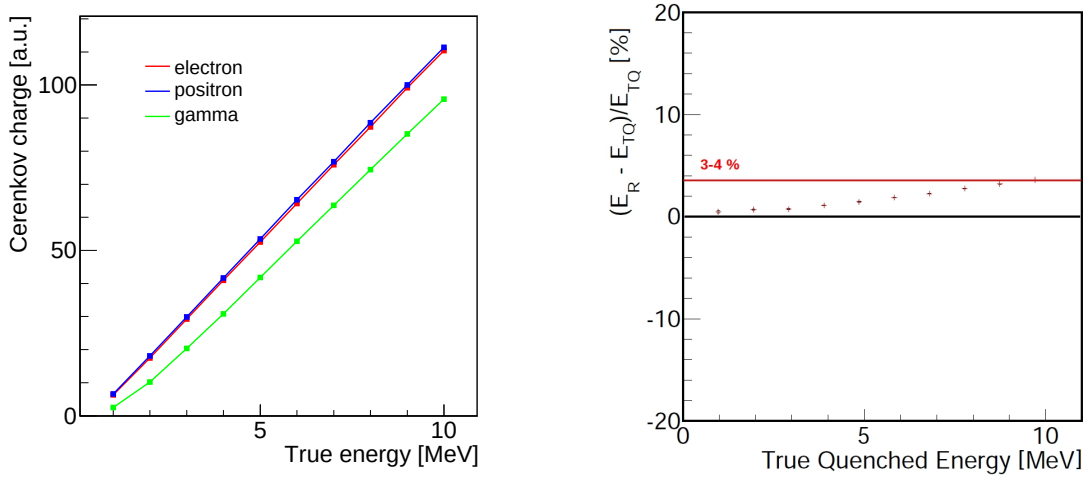


Figure 5.6: *(left) $\mathcal{C}(E_{vis})$ correction function generated for electron, positron, and gamma. (right) Residuals for electrons simulated between 1 and 10 MeV, with the Čerenkov process inactivated in GEANT4. The red line shows the highest level of bias, reached at 10 MeV.*

### Performances

The performance of CocoReco can be estimated by computing the energy resolution, $\sigma_{\mathrm{E_R}}/\mathrm{E_R}$, in percent, as a function of the true quenched energy (Figure 5.8). The CocoReco energy resolution is of the order of 8 % at 1 MeV and goes down to less than 3 % at 10 MeV. According to the Double Chooz proposal, the energy resolution was expected to be between 7 and 8 % for 1 MeV electrons [31].

Similar energy resolutions and slightly higher biases are found if one tries to reconstruct the energy, up to 10 MeV, of simulated positrons or gammas at the center of the inner detector. These differences are mainly explained by the fact that the Čerenkov correction function $\mathcal{C}(\mathrm{E_{vis}})$ has been estimated for electron and that the positron and $\gamma$ physics slightly differ (left panel of Figure 5.6). Indeed, the biases are reduced for each particle type if the corresponding Čerenkov correction function is used ($\mathcal{C}^{\gamma}(\mathrm{E_{vis}})$ for $\gamma$, etc.). However, particle type is not an available information in Double Chooz, therefore we used the generic $\mathcal{C}(\mathrm{E_{vis}})$ obtained with electrons.

### Position dependance

CocoReco has also been tested at different positions within the $\nu$-target and the $\gamma$-catcher. The performances presented above are mainly unchanged for electrons simulated at the top, at the bottom of the $\nu$-target, near the NT-GC wall, or even at random positions within the NT, making then CocoReco a robust and reliable energy reconstruction tool for neutrino events. However, they tend to worsen for particles simulated within the $\gamma$-catcher volume.

As shows in Figure 5.9, this is particularly true for energy deposition close to the $\nu$-target corner, within the $\gamma$-catcher volume, where the reconstructed energy is always underestimated. Indeed, what happens as one looks at the reconstruction outputs close to the GC boundaries or within its volume, is that the CocoReco optical model of equation (5.3) may be no longer valid. An explanation would be that in the $\gamma$-catcher, and especially around its corner, the vertex is too close to the PMTs: reflection on the buffer wall or on the PMTs themselves might be not negligible anymore.

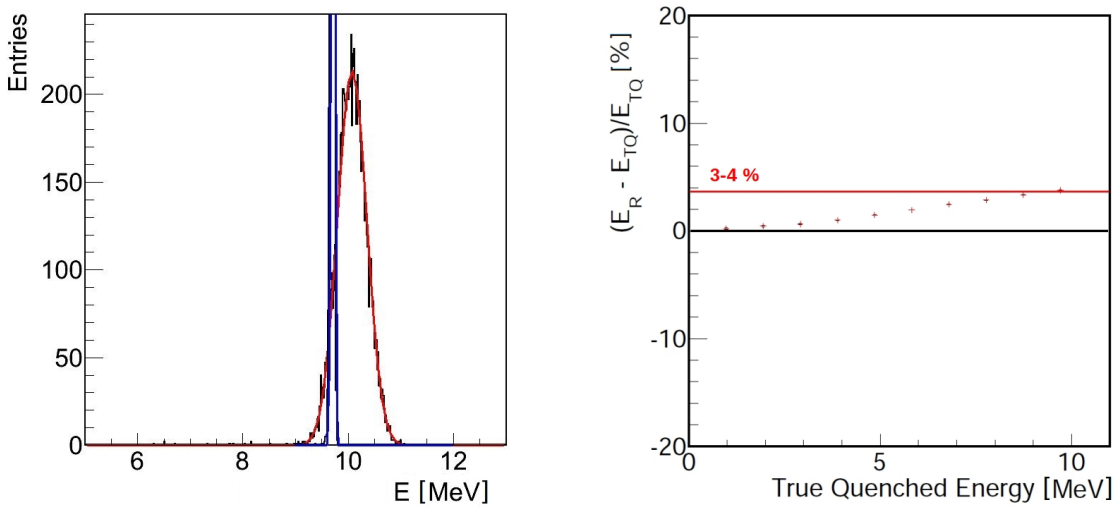


Figure 5.7: *(left) Energy distributions for 10,000 electrons simulated at 10 MeV at the center of the $\nu$-target. The blue Gaussian is the simulated true quenched energy and the red one the CocoReco reconstructed energy, in MeV. (right) Residuals for electrons simulated between 1 and 10 MeV. The red horizontal line shows the bias at 10 MeV.*

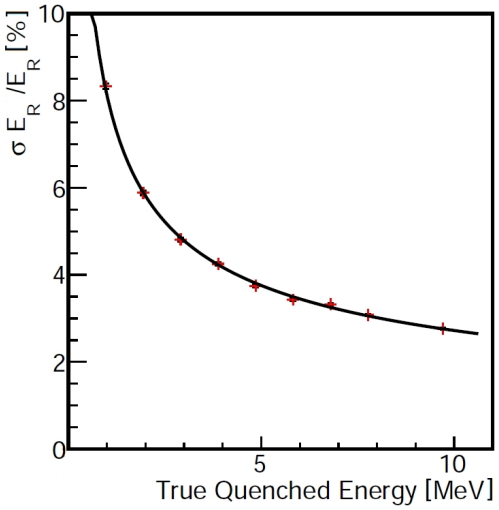


Figure 5.8: *Energy resolution, $\sigma_{E_R}/E_R$, in percent, for each simulated true quenched energy, from 1 up to 10 MeV, for electrons. The black line corresponds to the fit function $a/\sqrt{E} + b$. The $\sqrt{E}$ shape is linked to the Poisson statistics.*

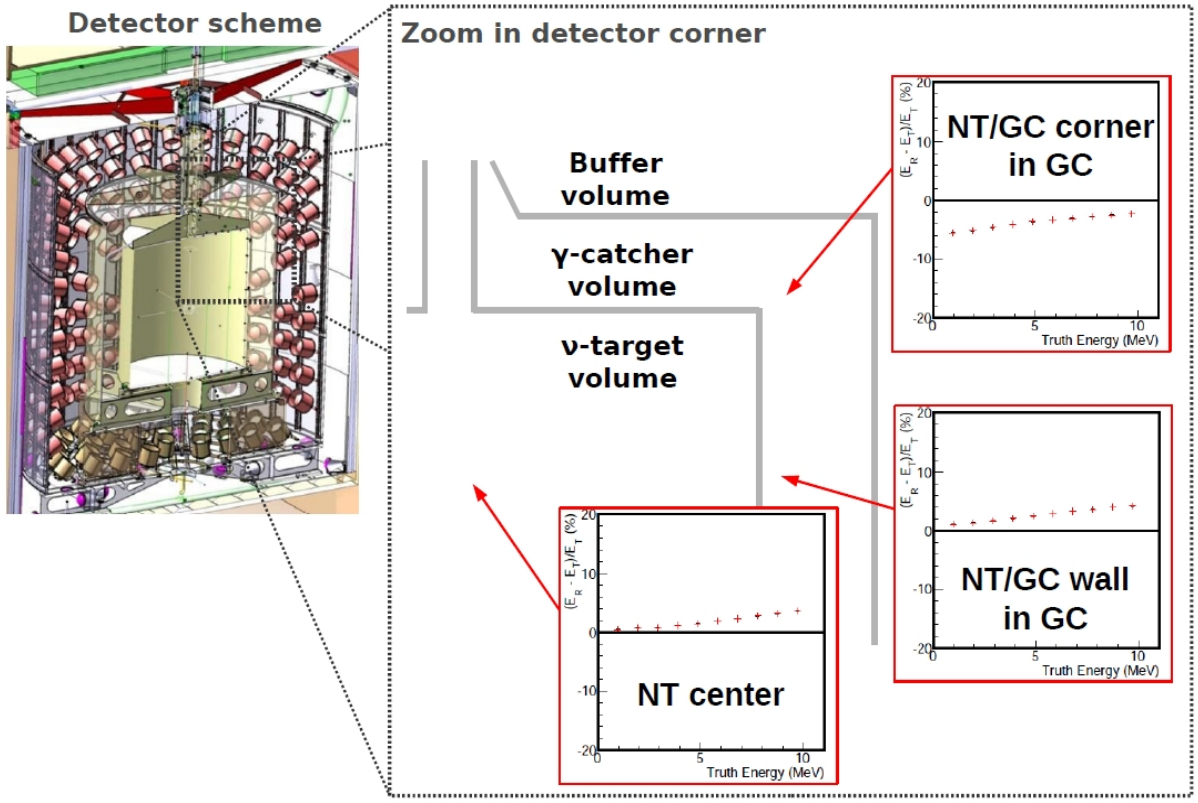


Figure 5.9: *Scheme of a corner of the Double Chooz detector. Three CocoReco energy reconstruction residuals for simulated electrons are shown: center of the $\nu$-target, near the NT/GC wall within the $\gamma$-catcher, and near the NT/GC corner within the $\gamma$-catcher as well.*

### 5.2.4 Vertex reconstruction with CocoReco

As explained at the beginning of this section, CocoReco is also a vertex reconstruction tool that provides interesting results. Since the charge pattern on the PMTs is directly related to the event position in the detector, the log-likelihood function expressed in equation (5.2) can be used to extract the vertex position. Figure 5.10 shows reconstructed vertices in the (X,Z) plane for 10,000 electrons at 1 MeV, simulated at the center of the $\nu$-target.

Although RecoBAMA is slightly better, both reconstruction algorithms show comparable performances. Their resolution is of the order of 12 to 15 cm (*cf.* Figures 4.8 and 5.10). This is also expressed in Figure 5.11, where the tridimensional distances D between the true and the reconstructed vertices is drawn for both CocoReco and RecoBAMA algorithms outputs, *i.e.*

$$\mathrm{D} = \left[ (\mathrm{x_{reco}} - \mathrm{x_{true}})^2 + (\mathrm{y_{reco}} - \mathrm{y_{true}})^2 + (\mathrm{z_{reco}} - \mathrm{z_{true}})^2 \right]^{1/2}. \tag{5.4}$$

The advantage of RecoBAMA mainly lies on its speed of processing, since it uses lookup tables of charge and time likelihoods already computed through Monte Carlo simulations, where CocoReco has to estimate each time the path lengths of photons in the three detector volumes (*cf.* Section 5.2.1).

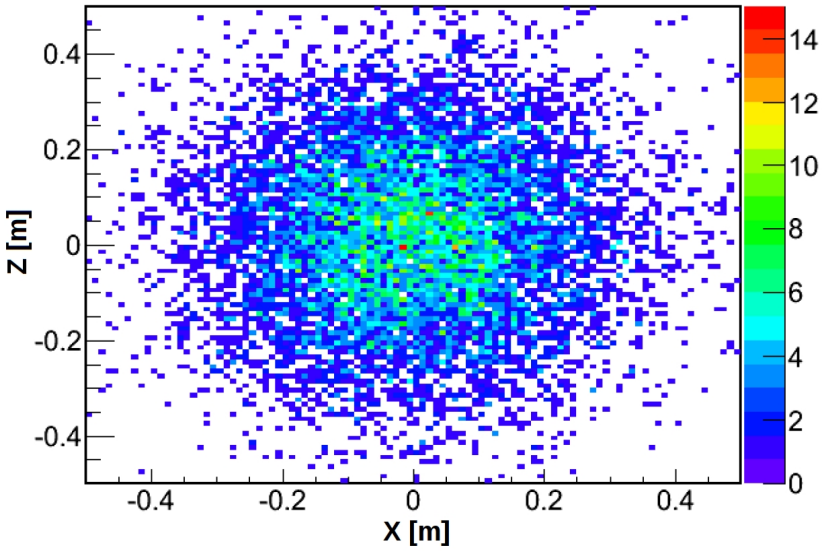


Figure 5.10: *CocoReco reconstructed vertices in the (X,Z) plan of 10,000 1 MeV electons simulated at the center of the $\nu$-target.*

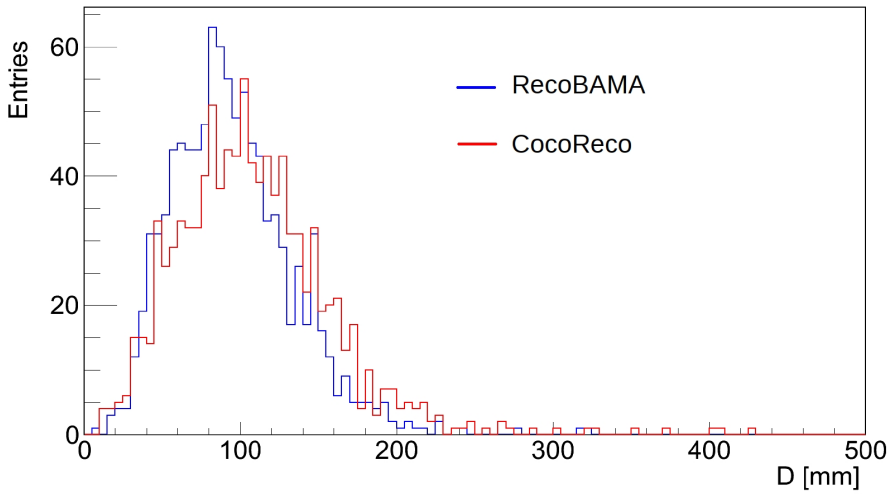


Figure 5.11: *Tridimensional distances between reconstructed and true vertices positions, for RecoBAMA (blue) and CocoReco (red).*

### 5.2.5 Perspectives

Although CocoReco has not been used on physics data so far, nor is part of the official common packages applied on data files (*cf.* Chapter 4), some improvements could be made in order to change that. Indeed, the main issue with the actual version of CocoReco is its slowness. During the minimization process, since the optical model depends on three different attenuation lengths, ray tracing from the tested vertex to the considered PMT across the three volumes have to be done. This induces complicated calculations each time a vertex position is being tried by the minimizer. Each time, the intersections positions on the cylinders ($\nu$-target and $\gamma$-catcher wall, top, and bottom) are computed. One way to improve this part of the event reconstruction could be to precalculate a tridimensional grid of the possible intersections, using Monte Carlo, and save the values in lookup tables. These would be later used through interpolation techniques for all (X,Y,Z) locations. This is the method followed for RecoBAMA, the Double Chooz official vertex reconstruction algorithm, for its charge and time likelihoods (*cf.* Section 4.3).

The precision of the outputs of CocoReco depends strongly on the attenuation lengths of each detector subvolumes. An advised choice of these values could be done, using calibration data. The pencil beam mode of the inner detector light injection system with different wavelengths could then be used [8]. Knowning the expected path of each beam within the $\nu$-target, the $\gamma$-catcher, and the buffer volumes, one should be able to estimate the actual corresponding attenuation lengths. CocoReco outputs would then be checked by deploying radioactive sources of known activities and $\gamma$ energies, at the center of the detector with the Z-axis for instance.

Concerning the position bias, mainly problematic in the GC volume, a geometrical correction term to the CocoReco optical model could also be developed. This would have to be done once the energy reconstruction algorithm is well calibrated in the $\nu$-target center. Radioactive sources could then be deployed in the guide tube, at different positions, allowing in a way a mapping of the CocoReco response to vertex position. A fine-tuning would then be possible by using the forthcoming articulated arm in order to test much more position in the $\nu$-target volume.

The use of a different Čerenkov correction functions is also possible. It was shown that these studies have been performed on Monte Carlo simulation only. Different version of CocoReco, with $\mathcal{C}^{e^-}(\mathrm{E_{vis}})$, $\mathcal{C}^{e^+}(\mathrm{E_{vis}})$, or $\mathcal{C}^{\gamma}(\mathrm{E_{vis}})$ could be tested on source calibration data, along the Z-axis system and within the guide tube and buffer tube, and soon even at every points of the $\nu$-target with an articulated arm. These new studies could allow to create an effective Čerenkov correction function, as one does not simply distinguish particle types in our detector, more suitable for every particles involved in the Double Chooz physics.

Finally, the CocoReco optical model could be improved. The bad reconstruction in some part of the $\gamma$-catcher volume could be taken care of by adding a reflection component, derived from the whole Double Chooz GEANT4. The PMTs collection efficiency shape, measured in laboratory and implement into the Monte Carlo geometry, could also be implemented in order to better and more precisely describe the physics taking place in our liquid scintillator seen by the photomultipliers.

[8] For a presentation of the Double Chooz calibration devices, see Section 3.5.4.

## 5.3 Monte Carlo tuning

During the first phase of Double Chooz, only the far detector was installed. Thus the unoscillated data which are compared to the selected data for the $\theta_{13}$ measurement entirely come from Monte Carlo simulations. Having a good and reliable Monte Carlo simulation software for the first analyses is therefore a must.

The Double Chooz Monte Carlo is first tuned from detailed laboratory measurements performed by the collaboration, but also from calibration data and MC simulation comparisons. Although most of the detector parameters, whose values were obtained during laboratory measurement campaigns, are taken into account in the Double Chooz simulation packages, data/MC discrepancies still remain. A fine-tuning allows to get rid of them. Several parameters are studied. They are linked to the optical properties of the scintillator, to the physics occurring in the detector, and even to the detector itself: the absolute and relative light yield, the quenching and Čerenkov processes, the attenuation lengths, the Gd concentration, the timing information, the buffer and PMT reflectivity, etc. Concerning the readout simulation, the PMT gain and pedestal, along with FADC related characteristics, were also tuned using calibration data during the detector commissioning. However, photocathode properties such as quantum and collection efficiencies were only measured in laboratory.

#### Light yield

The light yield of both the $\nu$-target and the $\gamma$-catcher have been required to match each other in order to guarantee an homogeneous energy response of the inner detector [31]. Fluctuations of the light yield could happen which is why dedicated IDLI calibration data are taken on a regular basis. High intensity UV light at 385 nm, in pencil beam or diffuse mode, is used to check the stability of the liquids over time.

It was first measured for both the $\nu$-target and the $\gamma$-catcher liquid scintillator in a laboratory [14]. Both values were then tuned to match the 2.2 MeV $\gamma$ ray from neutron captures on hydrogen for a $^{252}$Cf source at the center of the detector, for both calibration data and Monte Carlo simulation.

#### Attenuation

For an accurate simulation of the light propagation through the detector, measurements of the scintillator attenuation lengths were conducted in laboratory using 1 cm cells filled with $\nu$-target or $\gamma$-catcher liquids. The attenuation and reemission probabilities of each of the scintillator compounds, on the relevant wavelengths range, were implemented in the Double Chooz Monte Carlo [16]. The fine-tuning of the total attenuation was made using measurements of the complete scintillators.

#### Quenching

The ionization quenching behavior can be described effectively by the Birk's equation without considering the details of the underlying physical processes [14, 42]. This equation allows to express the amount of light produced per unit of length as a function of the energy loss per unit of length:

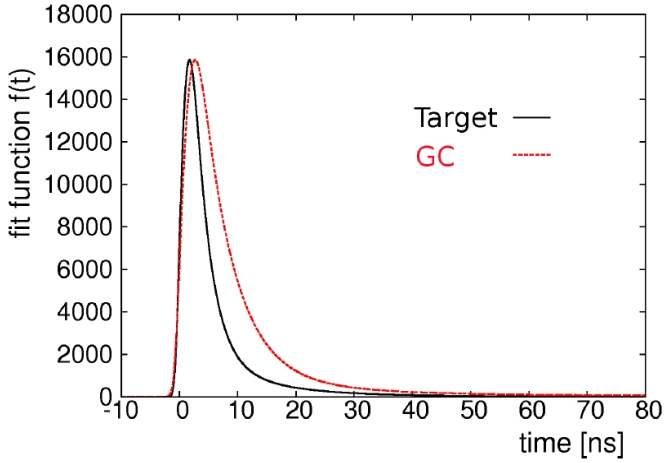


Figure 5.12: *Scintillation photon emission time distribution for $\beta$ excitation in $\nu$-target and $\gamma$-catcher [16].*

$$\frac{dL}{dx}(E) = \frac{L_0 \frac{dE}{dx}(E)}{1 + k_B \frac{dE}{dx}(E)} \tag{5.5}$$

where $L_0$ is a constant which characterizes the scintillation yield for a small dE/dx. The Birk's parameter $k_B$, also called quenching constant, is a material property which has to be determined experimentally.

Therefore, quenching constants for electrons and also $\alpha$ particles for several radioactive isotopes ($^{210}$Po, $^{222}$Rn, $^{214}$Po, etc. [9]), have been measured in laboratory [14, 15]. Delayed coincidence analyses on data between $\beta$ and $\alpha$ emissions from $^{212}$Bi and $^{214}$Bi, called Bi-Po analyses, have also been performed on data in order to check these values [194]. They were found to be in good agreement with the values measured in laboratory. The quenching constants in simulation were finally adjusted according to these measurements.

### Timing

The photon emission time probabilities used in the simulation, for the $\nu$-target and the $\gamma$-catcher, were obtained with a dedicated laboratory setup [16]. They consist of time differences betwee photon arrival on two photomultiplier tubes. Their time profiles were tuned to match these laboratory measurements, for both electron and $\alpha$ particles.

Fits of experimental measurements for electrons in both the $\nu$-target and the $\gamma$-catcher are available in Figure 5.12, where the fit function is a sum of three exponentials. The difference in term of time response in the two active volumes is due to the difference in PPO concentration in the two liquids (*cf.* Section 3.5.1) and could be used later to discriminate between events occurring in the $\nu$-target or in the $\gamma$-catcher.

[9] These nuclei are involved in the thorium and uranium chains, a natural source of accidental background for the experiment (*cf.* Section 6.3.1).

### Reflectivity

As explained in Section 3.5.1, the buffer vessel is coated and reflective. The amount of reflection of the buffer walls can affect the total light collection. For the time being, the Double Chooz simulation makes the assumption of a 40 % diffuse reflectivity. This value has been used for the first Double Chooz publications. However, in-situ measurements have been performed during the buffer integration [144]. They allowed to conclude that the buffer vessel showed a low level of non-uniformity, that could be however implemented in the simulation as random variations of the reflected light. More recent studies on $^{60}$Co or $^{137}$Cs source calibration data showed that the effective 40 % of diffuse reflectivity implemented was not enough [171].

### Monte Carlo efficiency correction

Several effects need to be also considered concerning the Monte Carlo simulation. As the selected data are compared to MC data, some discrepancies linked to the selection needs to be taken into account.

This is the case of the spill-in and spill-out effects. A typical neutrino event corresponds to the interaction between an electron antineutrino with a proton of the $\nu$-target, creating then a positron and a neutron. The positron annihilation and the neutron capture on Gd occur most of the time within the $\nu$-target boundaries. However, because of the thermalization process, it is totally possible that the neutron finally gets captured on a nucleus within the $\gamma$-catcher region. This type of event is called spill-out. Moreover, the electron antineutrino may interact within the $\gamma$-catcher close to the $\nu$-target wall, and let the neutron leak within the innermost vessel and be captured on a Gd nucleus. These events are called spill-in [145].

Both types of events have to be carefully studied, estimated, and taken into account because they directly impact the normalization of the experiment, and do not compensate for a one detector experiment (first phase of Double Chooz). Studies needed therefore to be performed [109]. Although the spill-in current was taken into account into the Double Chooz first publication Monte Carlo, the low energy neutron physics was modeled with insufficient accuracy (*cf.* Section 5.1.2) and induced that the spill-in current was overestimated. A Monte Carlo live time correction factor of 1.0072 was needed. For the second publication, the neutron physics package NeutronTH was implemented in our Monte Carlo, describing better the thermalization process. The Monte Carlo simulation indicated then that the spill-in current was about $(1.35 \pm 0.30)$ %. Since it was already included in the simulation, no correction for this effect was needed for the second Double Chooz publication. An uncertainty of 0.3 % for the final fit was however assigned to this process (*cf.* Section 7.2).

However, the difference between the gadolinium content with respect to the hydrogen content in the $\nu$-target, called gadolinium fraction, needs to be precisely tuned. This effect and its associated systematic uncertainty are described in Section 6.2.4 along with the other selection cut efficiency studies. A correction factor of 0.985 is thus applied to the Monte Carlo in order to take into account the measured discrepancy.

Finally, the multiplicity cuts described in Section 6.2.2 imply to also correct the Monte Carlo simulations with a factor amounting to 0.9945. This value comes from the rate of single events and the size of the multiplicity time windows.

# Chapter 6

# Data analysis: $\overline{\nu}_e$ selection and backgrounds studies

*What is out of the common is usually a guide rather than a hindrance.* [1]

Sherlock Holmes,
Consulting detective, London.

Prior to the oscillation fit performed to extract $\theta_{13}$, the electron antineutrino events within the data sample need to be selected. An average trigger rate of 130 Hz and two $\overline{\nu}_e$ events expected per hour in the far detector means that most of the recorded events are background. This chapter is then centered on the offline data analysis conducted in order to understand and reduce the backgrounds, hence enhancing the antineutrino signal and allowing the extraction of the antineutrino rates per day. A careful study of the efficiency of all the applied selection cuts is done. Two other analyses are presented at the end of this chapter: one in which the $^9$Li correlated background is reduced by the addition of a new cut and another one which takes advantage of both reactors being OFF in order to estimate the experiment total background and thus subtract it to the neutrino candidates selection. The strategy of the oscillation fit for the $\theta_{13}$ parameter determination, as well as its results, are presented in the next chapter.

## 6.1 Data sample

The first official physics data set of the Double Chooz phase I (far detector only) were taken on Wednesday, April 13$^{\text{th}}$ 2011. From that day, the nominal duration of a physics run is one hour. A basic data taking sequence consists of 12 physics runs followed by 8 inner detector light injection runs, where a loop is done over several wavelengths and intensities. The goal of these eight IDLI [2] runs is a frequent and precise calibration of the liquid properties, the photomultipliers gains, and the channels time offsets (*cf.* Section 4.2.1).

The data taking and the detector monitoring is done 24 hours a day, each day of the week, on site during the French working hours, and off site otherwise. The whole collaboration participates in the effort, allowing the data taking efficiency to be around 87 % for all data (daily

[1] From the "A study in scarlet" book of Sir Arthur Conan Doyle [68].

[2] See Figure 3.11 for a detector scheme and a definition of its related acronyms. Section 3.5.4 provides also information on the Double Chooz calibration devices.

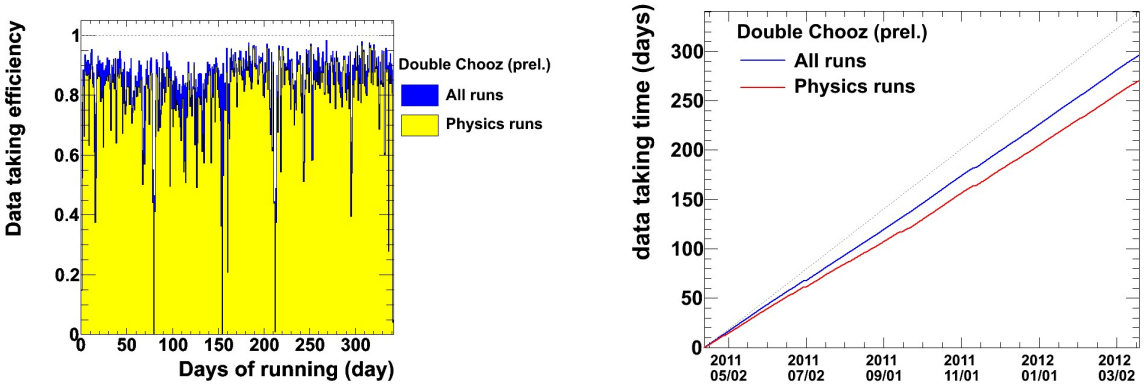


Figure 6.1: *Data taking efficiency (left) and integrated live time (right) since the first day of physics data taking, April 13$^{th}$ 2011. Even if the data are taken 24 hours a day, 7 days a week, inefficiencies can occur, mainly due to calibration data taking and instability of the DAQ.*

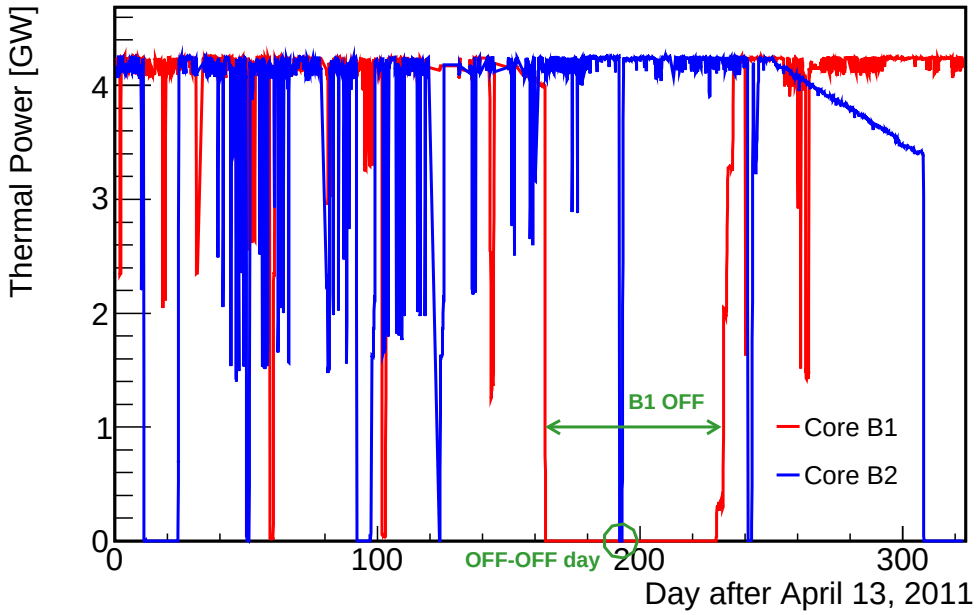


Figure 6.2: *Thermal power evolution for reactors B1 (red) and B2 (blue), per day since April 13$^{th}$ 2011, in GW. The two months period with B1 OFF and the both reactors OFF-OFF day are visible. The slow decrease of reactor B2 thermal power after day 240 up to its stop was an operating choice of the electricity company EDF.*

IDLI calibration and source calibration included), and to flirt with 80 % for the physics runs (Figure 6.1). I had myself the opportunity to be on site during four weeks, three of them as Shift Leader. This position is central for the data taking: the Shift Leader makes sure the detector and its related equipments are safely operated, that all the safety rules are observed, decides when to call the subsystems experts if a problem occurs, manage the team of shifters (five per day), and reports all the procedures, operations, and activities on and off site to the collaboration via a logbook and meetings [117].

While the first Double Chooz publication concerned 2,594 runs, for almost 102 days of physics data, from Wednesday, April 13$^{\text{th}}$ 2011 to Sunday, September 18$^{\text{th}}$ 2012 [12], the second analysis, presented below is done upon 6,321 runs and corresponds to more than 251 days of physics data [11]. During this period, the analysis could benefit from the reactor B1 shutdown for maintenance and refueling for about two months, as well as one day of two reactors OFF data taken on Saturday, October 22$^{\text{nd}}$ 2011. The end of the runs list for the second analysis, March 1$^{\text{st}}$, occurs within a core refueling phase of reactor B2. The Figure 6.2 shows the thermal power evolution as a function of time since the first day of physics data for both reactors B1 and B2.

## 6.2 Inverse $\beta$ decay candidate selection

As explained in Section 3.3, the electron antineutrinos coming from the Chooz B reactors are detected within the Double Chooz $\nu$-target by the correlated and typical signature of an inverse $\beta$ decay interaction within the scintillator liquid (*cf.* Section 3.3.2). A reactor $\overline{\nu}_e$ interacts with a proton of the medium, creating then a neutron and a positron (*cf.* Figure 3.7). The positron quickly looses its energy and annihilates with an electron. The visible energy in the detector is directly related to the positron initial energy, and thus to the neutrino one, since the neutron carries almost none. In the meantime, the neutron is thermalized in the liquid, and afterwards captured on a nucleus. Gadolinium was added in order to strongly sign the neutron capture and reject backgrounds: after a capture on Gd, the deexcitation of the nucleus typically leads to the emission of three $\gamma$ in average carrying 8 MeV in total. This is to be compared to the neutron capture on hydrogen, that leads to a 2.2 MeV peak, buried within the radioactivity lines (*cf.* Section 6.3.1). Given the concentration of Gd and the number of protons in the Double Chooz $\nu$-target liquid, about 85 % of the neutron captures happen on a Gd nucleus, leading to a characteristic capture time of roughly 30 µs (*cf.* Section 3.3.2).

The $\overline{\nu}_e$ interaction signature consists therefore of two correlated signals, in time and thus in space: one corresponding to the positron, with a visible energy going from 1.022 MeV up to roughly 8 MeV, and one corresponding to the neutron capture on Gd, typically peaking at 8 MeV. The relation between the visible energy and the antineutrino and positron ones can be found in equation (3.15).

### 6.2.1 An unexpected background: the light-noise

The Double Chooz experiment has to deal with an unexpected background, called light-noise, as briefly explained in Section 4.2.3. It consists of parasitic light emitted by some far detector PMT bases. More precisely, it is believed to be caused by discharges between high potential electrodes on the PMT base circuits [177]. This hypothesis is backed up by laboratory measurements, Monte Carlo studies, and analysis of dedicated runs [178]. It has been shown for instance that lowering the PMTs HV tends to decrease these light emissions.

Two ways are used to get rid of the light-noise: hardware and software. Indeed, 15 of the most noisy PMTs were turned off during commissioning, which induces a loss of less than 4 % of the PMTs (*cf.* Figure 4.6). The software approach is to record the remaining light-noise events in the data files anyway, and apply offline rejection cuts later. Several have been developed, with the goal of rejecting light-noise without any physics event loss. So far, two of them, MQTQ and RMS($T_{start}$) cuts, are used for the Double Chooz official analyses. These cuts applied for the first Double Chooz publications are both based on light collection isotropy considerations and are explained below.

### MQTQ cut

A photomultiplier emitting light-noise mainly sees its own parasitic light. Indeed, the emissions occur at the base of the PMTs, all of them being surrounded by a $\mu$-metal shielding [3] that tends to guide the light toward the PMT's own photocathode. However, the neutrino signal should be homogeneously spread across the PMTs. This leads to the conclusion that if a photomultiplier sees a huge amount of light with respect to the average PMT charge, this is abnormal. The maximum charge of a PMT over the total charge on an event, or MQTQ, cut is based on this idea.

This cut benefits from the fact that MQTQ calculation is easy and that it does not require any waveform nor reconstructed position information. It makes it very robust. The MQTQ variable, and actually different versions of it (whether the channels flagged, at the monitoring stage, as bad channels are used or not for the calculation), became available in the first place within the Cheetah data files (*cf.* Sections 4.5 and 4.6).

The left panel of Figure 6.3 shows the MQTQ distributions for neutrino Monte Carlo (*i.e.* no light-noise) simulated within the whole inner detector. The maximum charge over the total charge of an event is lower than 0.08 for true neutrino events, supporting the fact that this signal is homogeneously spread across the detector, illuminating all the PMTs roughly by the same amount: at most, a single PMT owns 8 % of an event charge. On the other hand, light-noise events imply sometimes that a single PMT sees 20, 50, or even 90 % of an event light (Figure 6.4). Prompt and delayed events are drawn separately and indeed show different distributions. This is expected as the energy region of the two events is different: the prompt event is peaked before 4 MeV while the delayed event corresponds to the Gd deexcitation following the neutron capture, leading to a 8 MeV $\gamma$ rays emission. This allows to consider a different cut value for selecting them. This was actually done because of a light-noise rate increase in the delayed energy region (*cf.* Section 6.3.1).

### RMS($T_{start}$) cut

The second offline cut applied on the Double Chooz data, in order to tag or suppress the light-noise, is called RMS($T_{start}$), and stands for the spread of the pulses start time on each channel, for a given event. It is also based on isotropic light collection considerations: neutrino signals are expected to have small spread in photons arrival times on PMTs. However, light-noise events produce photons that are quickly detected by the light-noise emitter and its close neighbors since these energy depositions are located close to the PMTs. The light-noise photons

[3] The $\mu$-metal shielding purpose is to disable the Earth electromagnetic field which might disturb the light collection [31].

undergo multiple reflection on the buffer wall and the PMTs themselves, then inducing a large spread between their arrival times on all the channels in a given event.

The right panel of Figure 6.3 shows the RMS($T_{start}$) distribution for $\overline{\nu}_e$ generated with the Double Chooz Monte Carlo. According to this simulation, physics events are expected to exhibit a RMS($T_{start}$) distribution bounded between 5 and 35 ns. The Figure 6.5 shows the light-noise rejection efficiency for both MQTQ and RMS($T_{start}$) variables. These are obtained by comparing physics runs and calibration data at different positions within the detector. Due to the activity of the radioactive sources, most of the events recorded during calibration runs are physics events, as opposed to light-noise ones. This allows to estimate the amount of physics events rejected by such cuts. This is found to be of the order of a few per mil, *i.e.* negligible.

Figure 6.4 shows the correlation and the complementarity of the MQTQ and the RMS($T_{start}$) variables, with a scatter plot of prompt-like events selected on physics data. The population at low MQTQ and RMS($T_{start}$) is expected to be real physics events according to our MC simulations. Also, using two cuts is a must in order to suppress as much light-noise as possible. If used separately, these cuts would need to be strongly tightened in order to provide a good light-noise rejection, therefore taking the risk of rejecting physics events. The selection is performed on physics runs and the only prescriptions are that the energy deposition does not correspond to a muon, is at least 1 ms away from one, and is between 0.7 and 12.2 MeV. Further explanations for these cuts will follow in Section 6.2.2.

#### Other light-noise cuts

Other cuts have been developed by the Double Chooz collaborators in order to cope with this unexpected background, and most of them rely on pulse shape information. Some of them may be used in future analyses under the condition that they are first studied in greater detail.

One of these variables is $T_{rise}$ and it has been studied at Saclay [57]. It corresponds to the rise time of the total pulse of an event, corrected by the time of flight of the photons. All the PMT signals with at least one pulse detected by DCRecoPulse (*cf.* Section 4.1) are corrected for the vertex-to-PMT time of flight and then summed up all together in order to create one event pulse. The rise time is the time reached at 90 % of the pulse maximum amplitude minus the time at 10 % of this maximum amplitude. Correcting for the vertex position narrows the pulse (Figure 6.6, left). Light-noise events usually have a long rise time and can present some oscillation pattern (Figure 6.6, right). This is due to the anisotropy of the primary light emission. Typical values of rise time for physics events are of the order of 10 ns. Cuts around 20 ns have been studied and have shown a good power of discrimination.

Although high MQTQ events have most of the time high $T_{rise}$, this cut was not used in the first analyses since it depends on time of flight corrections and hence on vertex reconstruction outputs, which could then induce unwanted biases. Future studies need to be carried out in order to estimate the potential impact of a systematic reconstruction effect.

Three other cuts, based on pulse shape information, are presented in detail in [89] and in Figure 6.7. Prior to their evaluation, a pulse shape distribution needs to be created. It is basically the distribution of all the pulse start times, weighted with the pulse charge, after the photon time of flight and the start time of the first hit subtractions. From this distribution, the time of the first peak $T_{peak}$, the mean time $T_{mean}$, and the ratio between the integral of the charge in the tail with respect to the total charge $T_{2tot}$, are calculated. These cuts are really promising and studies are still ongoing.

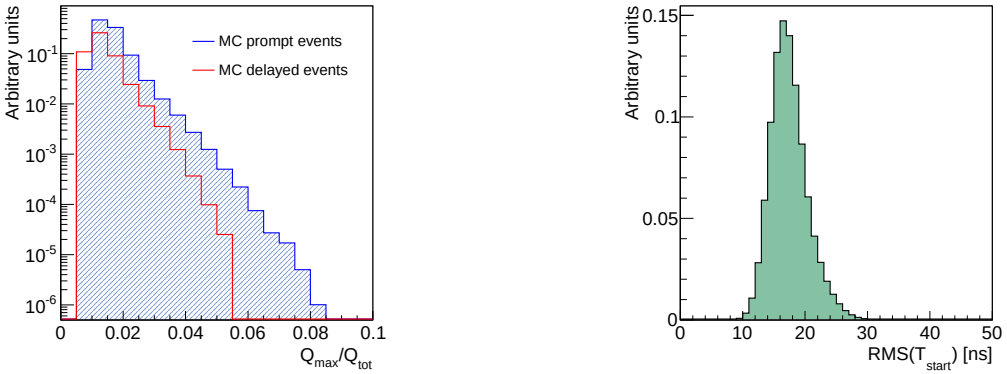


Figure 6.3: *Monte Carlo generated $\overline{\nu}_e$ light-noise variables distributions. (left) MQTQ for the prompt (dashed blue) and the delayed events (red line). (right) RMS($T_{start}$) in ns.*

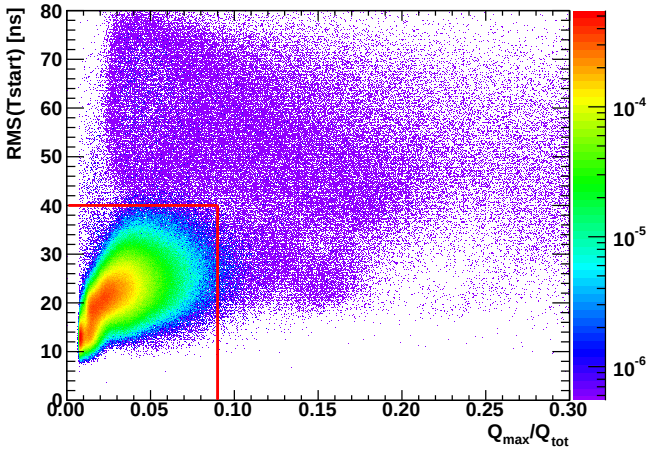


Figure 6.4: *RMS($T_{start}$) in ns versus MQTQ. The physics region is located within the red lines.*

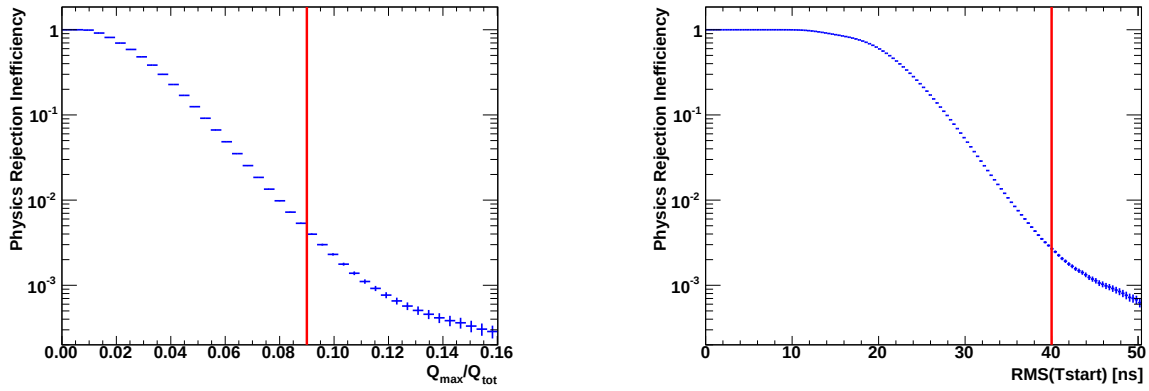


Figure 6.5: *Physics rejection inefficiency for MQTQ (left) and RMS($T_{start}$) (right) variables, estimated by comparing physics runs and calibration data, assuming calibration runs are mostly filled with physical events. They are found to be of the order of a few per mil [89].*

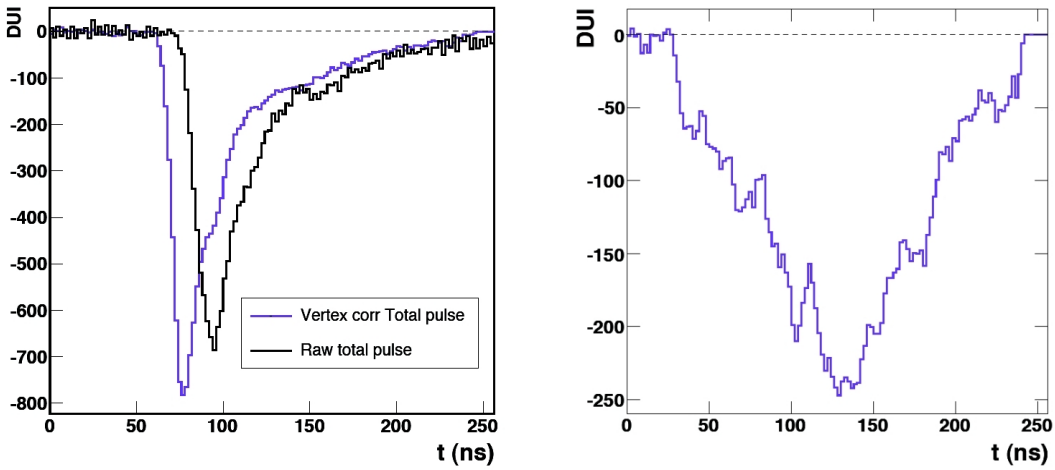


Figure 6.6: *(left) Effect of time of flight correction on a raw event total pulse. The Pulse (negative) amplitude is in DUI, an arbitrary unit of current, and the time axis is in ns. Time step is the digitization one, i.e. 2 ns (cf. Section 3.5.3). (right) Typical light-noise event pulse, with the same axes than those displayed on the left graph. $T_{rise}$ is about 90 ns, almost an order of magnitude higher than the expected rise time for physics events [57].*

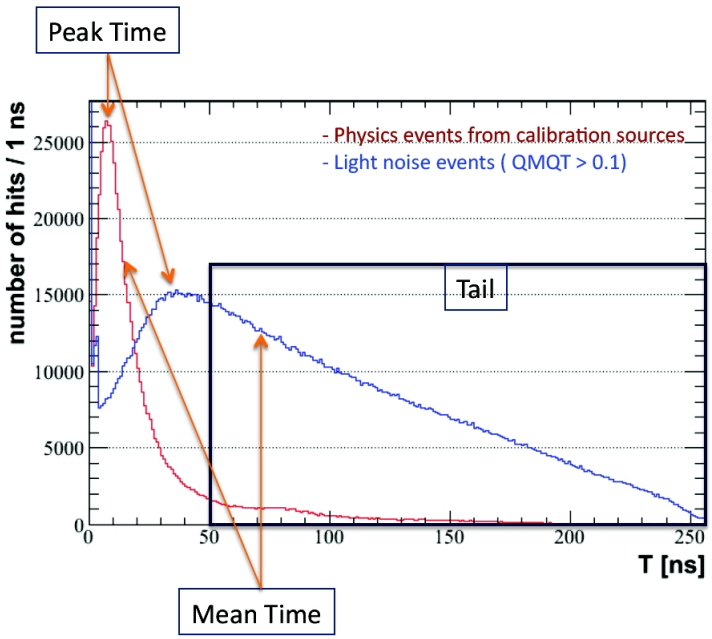


Figure 6.7: *Pulse shape distributions for calibration data (red) and for light-noise events tagged with MQTQ > 0.1 (blue), illustrating the power of discrimination of $T_{peak}$, $T_{mean}$, and $T_{2tot}$ light-noise cuts [89].*

It is important to notice that none of the light-noise cuts presented previously, such as MQTQ, RMS($T_{start}$), $T_{rise}$, nor these latter pulse shape based cuts, allow to completely get rid off this background. A combination of the MQTQ and the RMS($T_{start}$) cuts will be used in the next section for efficient light-noise tagging and inverse $\beta$ decay selection. The number of physics events rejected according to our Monte Carlo simulation is negligible while the power of light-noise rejection given by these two cuts combined together is excellent. This is checked by looking at light-noise and accidental events stability over time, since the accidental events are selected with the same criteria than electron antineutrino events (*cf.* Section 6.3.1). Indeed, while the light-noise rate increased since the first day of data taking, the accidentals rate remained flat over this period.

#### Light-noise selection results

According to the cuts described above, a light-noise event is defined as an energy deposition presenting a maximum charge over total charge higher than 0.09 or a spread of pulses start time on each channel higher than 40 ns.

Light-noise stability over time is studied by selecting, in each of the 6,321 runs, events that are not flagged as muons ($Q_{tot}^{IV} < 10{,}000$ DUQ, *cf.* Section 6.2.2), are at least 1 ms away from one, whose energy is between 0.7 and 12.2 MeV, and with MQTQ $> 0.09$ or RMS($T_{start}$) $> 40$ ns. The rates of light-noise events per day since the first day of physics data can be found in Figure 6.9. It is roughly comprised between 15 and 25 Hz over the period covered in Double Chooz second publication. Its slow increase is still not explained at the moment, but can be related to a slight temperature change, to an HV instability, or to PMT aging.

Figure 6.8 shows light-noise events distribution in the Double Chooz detector, in the (X,Y) and (Y,Z) planes, for a subset of the total runs list (here, a MQTQ $> 0.09$ cut is used). Vertices are reconstructed at various positions in the detector volume. However, most of the hot spots seems to be located in the vicinity of some of the photomultipliers. This vertex distribution is not compatible with physics events. It is important to notice that the vertex positions may be off of several centimeters with respect to their true locations. Indeed, the vertex reconstruction package RecoBAMA has been developed for physical Double Chooz events and not for this kind of unexpected background.

### 6.2.2 Electron antineutrino selection criteria

The selection of neutrino candidates consists of finding a prompt event correlated with a delayed one. All the cuts explained hereafter used to select what are called prompt and delayed events are summarized in Table 6.1.

The Double Chooz collaboration has been split up into three analysis groups, called clusters. The idea was to follow three independent analyses and compare them at different stages, for robustness. I have been strongly involved in the studies of neutrino candidates selection cuts and in the results comparison between the different cluster analysis groups [69, 72]. For that purpose, I developed my own independent analysis chain based on the Cheetah reduced files (*cf.* Section 4.6). It is able to perform the selection, check the stability, and draw histograms of relevant variables, for each kind of events occurring in the Double Chooz detector: neutrino candidates, muon events, light-noise events, singles, as well as accidental and correlated background events. Most of the plots showed hereafter have been obtained with this analysis chain, unless otherwise mentioned.

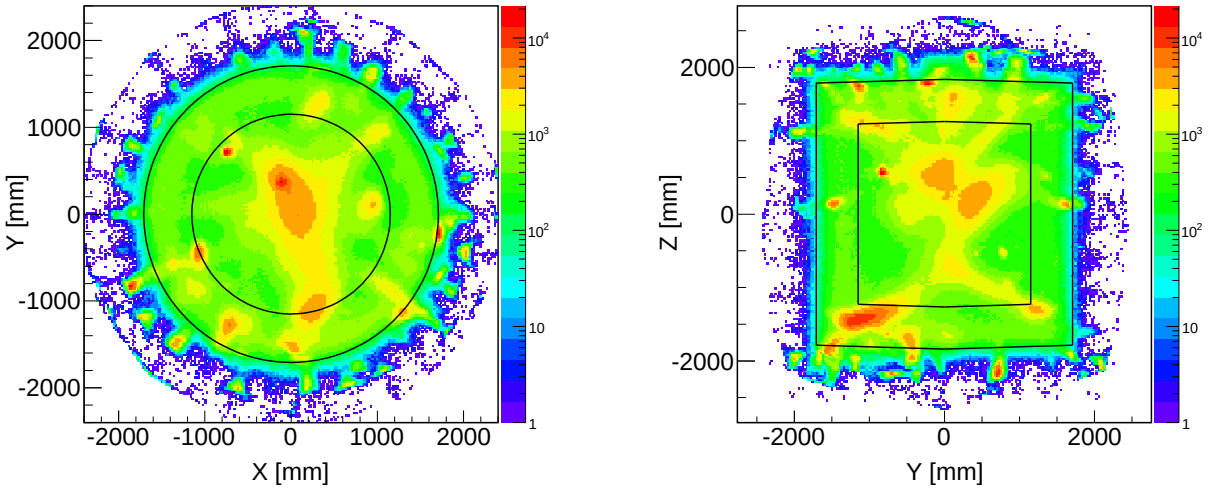


Figure 6.8: *Light-noise (events with MQTQ > 0.09 and energy between 0.7 and 12.2 MeV) vertices distribution in the (X,Y) plane (left), and the (Y,Z) plane (right), for a subset of the total runs list. The scale is logarithmic on the Z-axis. Hot spots close to noisy PMTs are visible. Solid black lines corresponds to $\nu$-target and $\gamma$-catcher walls.*

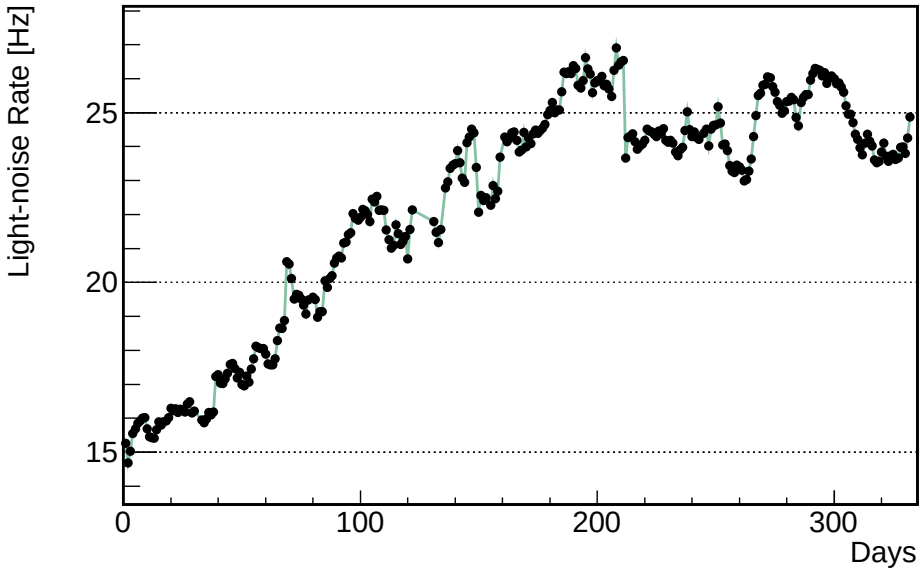


Figure 6.9: *Light-noise rate over time, in days since Wednesday, April 13$^{th}$ 2011. Energy range is [0.7 ; 12.2] MeV and light-noise prescription is MQTQ > 0.09 or RMS($T_{start}$) > 40 ns. Abrupt decreases are mostly caused by power cuts (for instance, several hours of power outage around day 211).*

### Prompt event

A prompt physical event in our detector, corresponding to the deposited energy of the positron from the inverse $\beta$ decay plus its mass at rest, is first of all asked not to be a light-noise event (*cf.* Section 6.2.1). In order to do so, the so-called light-noise cuts are applied on the maximum charge over the total charge of the event and the dispersion of the start times of the PMT signals: MQTQ $< 0.09$ and RMS($T_{start}$) $< 40$ ns. Such values are chosen according to electron antineutrino Monte Carlo simulations. Calibration data studies showed that they do not reject any real physics events (Figure 6.5).

Secondly, the prompt event is asked not to be a muon-like event. Muons in the Double Chooz detector are tagged either by the inner detector or the inner veto [4], using the following prescriptions: total charge in the IV greater than 10,000 DUQ [5] or total energy deposited in the ID greater than 30 MeV, after light-noise rejection cuts. Since the prompt energy is not expected to reach 30 MeV, the selection cut for a prompt event is then only $Q^{IV}_{tot} < 10{,}000$ DUQ. Another muon-related cut is applied when selecting an antineutrino interaction: due to channel baseline oscillations after a muon passed through the inner volume, which can artificially trigger the detector, and because events following a muon (Michel electrons for instance) need to be avoided, a 1 ms veto after each of them is applied. The prompt event is then at least 1 ms away from the closest previous muon event.

The muon veto induces a dead time which needs to be taken into account. It is of the order of 11 days, *i.e.* 4.4 % of the 251 days total run time, and implies then a small loss. The run time of each day since the first day of data taking is displayed on Figure 6.10, while the muon veto times with respect to the run times per day are available on Figure 6.11. The total amount of muon veto time is not calculated as the total number of muons times the 1 ms veto, although it would be a good estimate of its upper limit. Indeed, with 45 Hz of muons detected in the inner detector, the probability of overlapping vetos after muon events is non-negligible and has to be taken into account.

A prompt event is also neither a random nor an external trigger. As explained in Section 4.1, the data acquisition system periodically releases a trigger signal with a frequency of 1 Hz [174]. One needs to carefully check that the prompt event selected so far corresponds indeed to a real energy deposition that triggered the detector. In order to do so, cuts are applied on the 32-bit triggerword which is the result of the trigger decision saved in each data files [6]. Bits 25 and 28 of the triggerword, corresponding respectively to the random and external trigger decision, are then asked to be strictly 0.

Finally, energy selection cuts are applied. The prompt event energy has to be reconstructed between 0.7 and 12.2 MeV. The 0.7 MeV lower energy bound is set well below the inverse $\beta$ decay threshold of 1.022 MeV in the detector. It allows to record background events in the first energy bins that could help to constrain the shape of the total background at low energies. The trigger efficiency above 700 keV is 100 % (*cf.* Section 6.2.4). The upper energy bound aims also at better constraining the backgrounds, especially the correlated ones, in the 10 to 12.2 MeV region, where no neutrino signal is expected.

[4] See Figure 3.11 for a detector schematic and a definition of the related following acronyms.

[5] See Section 4.2.1 for a definition of DUQ, that is basically a unit of charge. 10,000 DUQ in the IV corresponds roughly to an energy deposition of a little less than 4 MeV [102].

[6] See Section 3.5.3 for a presentation of the Double Chooz readout and trigger system.

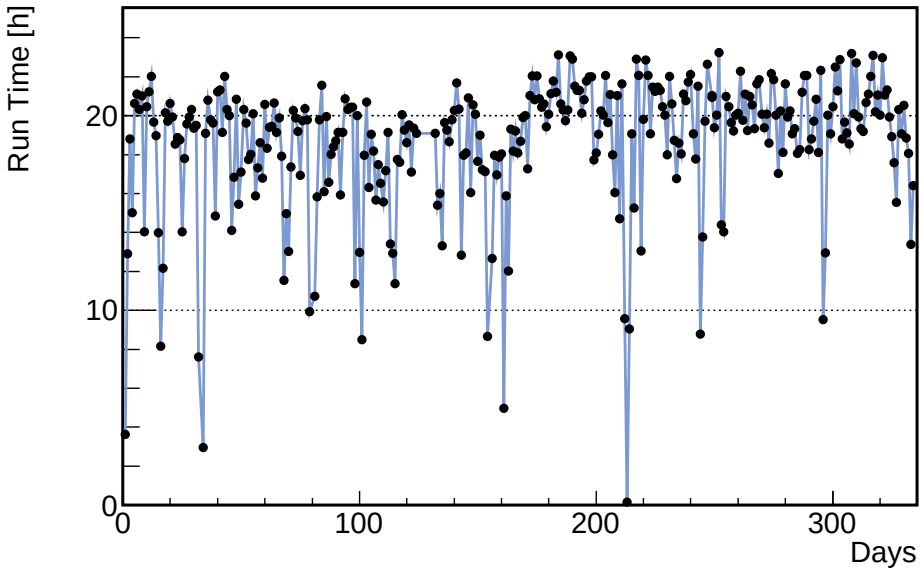


Figure 6.10: *Run time in seconds per day, since the first day on data taking, on Wednesday, April 13$^{th}$ 2011.*

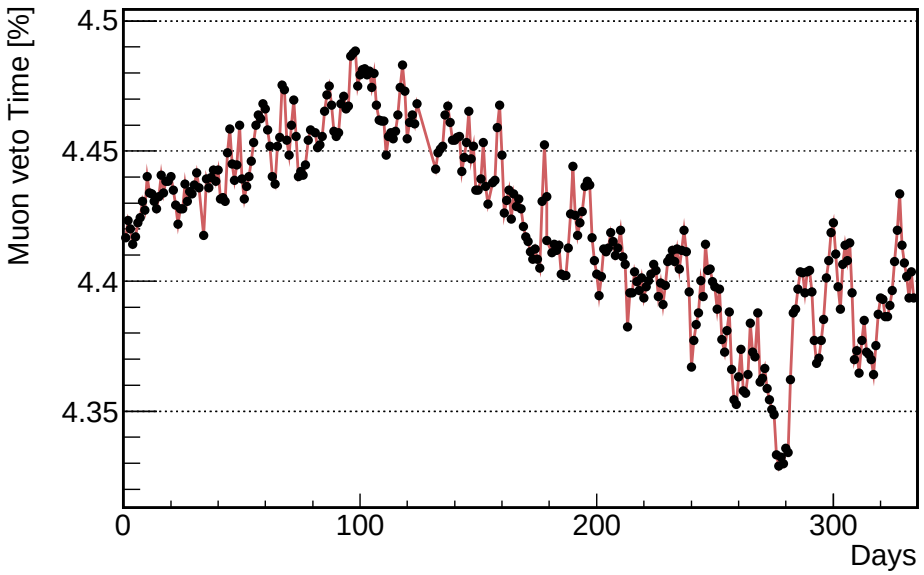


Figure 6.11: *Muon veto time in percent per day, since the first day on data taking, on Wednesday, April 13$^{th}$ 2011. The general shape follows the muon rate evolution, which is not completely understood.*

| Cuts | | Prompt | Delayed |
|---|---|---|---|
| Light-noise | MQTQ | $< 0.09$ | $< 0.055$ |
| | RMS($T_{start}$) [ns] | $< 40$ | $< 40$ |
| $\mu$-related | IV charge [DUQ] | $< 10{,}000$ | $< 10{,}000$ |
| | $\mu$-veto time [ms] | 1 | 1 |
| Triggerword | No random trigger, bit 25 | 0 | 0 |
| | No external trigger, bit 28 | 0 | 0 |
| Energy | Lower bound [MeV] | 0.7 | 6 |
| | Upper bound [MeV] | 12.2 | 12 |
| Coincidence time window [µs] | | $2 < T_d - T_p < 100$ | |
| Isolation/multiplicity [µs] | | no valid trigger in $[T_p - 100\ ;\ T_p + 400]$ but prompt and delayed | |

Table 6.1: *Summary table of the electron antineutrino candidates selection criteria. The selection cuts of both the prompt event and the delayed event, presented in the text, are reminded.*

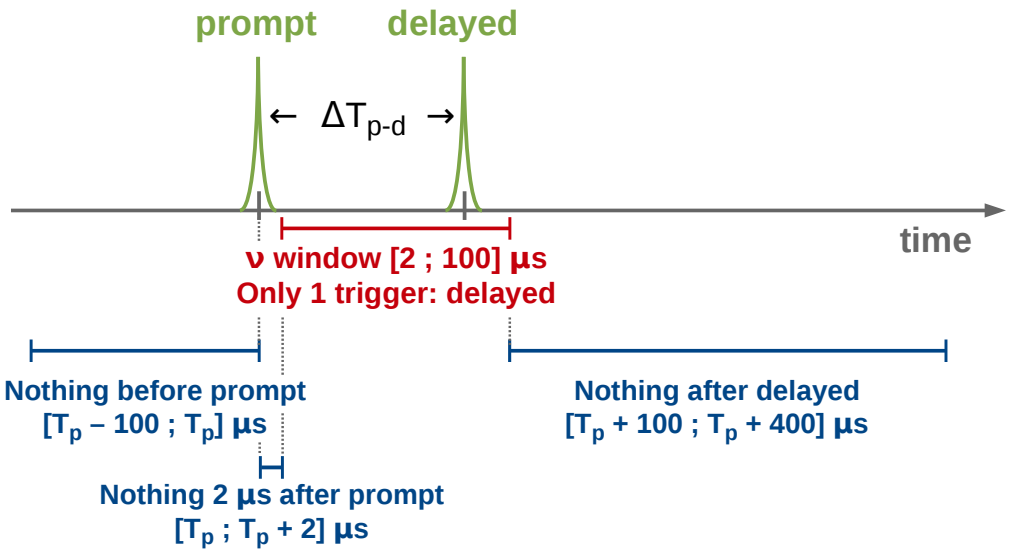


Figure 6.12: *Schematic visualization of the antineutrino selection coincidence time window and the multiplicity cuts. "Nothing" stands for "no valid trigger", whose definition can be found in the text. $T_p$ is the prompt trigger time, in µs.*

**Delayed event**

The delayed event selection follows mainly the prescriptions of the prompt one. Like the earlier energy deposition, the neutron capture is expected not to be a light-noise event, nor a random trigger, nor a muon. Thus the cut $Q_{tot}^{IV} < 10{,}000$ DUQ and the 1 ms veto after a muon event are also applied. However, the light-noise cuts are a bit different. When $RMS(T_{start}) < 40$ ns remains standard, the maximum charge over the total charge cut is more restrictive: $MQTQ < 0.055$. This cut had to be applied to overcome a sudden increase of light-noise in the energy region of the neutron capture on Gd peak. Such a rise has been spotted by looking at the accidental background stability over time (*cf.* Section 6.3.1). The Figures 6.28 and 6.29 available in the accidental background section show the single events vertex distributions within the detector: two light-noise hot spots are still present after applying the $MQTQ < 0.09$ and $RMS(T_{start}) < 40$ ns cuts. It is shown that these are not strict enough for parasitic light emissions after 6 MeV, which explains the tighter 0.055 limit for MQTQ. Further details on single events are given in Section 6.3.1.

What characterizes the delayed event, is indeed its time correlation with the prompt. A cut based on the time difference $\Delta T$ of the two events is applied: $2 < \Delta T < 100$ µs. 100 µs is chosen since it is more than three times the expected typical neutron capture time on Gd in our liquid (30 µs). If the neutron capture process was considered to simply follow a decreasing exponential law, 100 µs would corresponds to 96.4 % of the captures. This of course is a simplistic model. Indeed, the neutron capture probability is not maximal at $\Delta T = 0$, because the thermalization process takes a few microseconds (Figure 6.17).

The 2 µs low boundary is applied to avoid strange behavior following a trigger, related to electronics. Moreover, the typical distributions of prompt vertex and delayed vertex, and the $\Delta T$ and $\Delta R$ distributions of neutrino candidates selected with $\Delta T < 2$ µs do not match those obtained with $\Delta T > 2$ µs: the vertices are not homogeneously distributed within the detector volume and show hot spots around some photomultipliers. Furthermore, the delayed energy does not peak at 8 MeV. This was believed to be a correlated light-noise contribution even though the underlying physical process was not fully understood. This background was reduced by further tightening the light-noise cuts and turning off one of the PMTs.

However, this 2 µs low boundary cut is still applied as it allows to get rid of an important part of the stopping muon background (*cf.* Section 6.3.2). These low energy muons induce a correlated background for the neutrino search as they enter the detector mostly through its chimney and decay within the $\nu$-target. The muon energy lost by ionization mimics the prompt event while the Michel electrons energy deposition from the muon decay is selected as the delayed one. Figure 6.13 shows the prompt vertices distributions in the (X,Y) and ($\rho^2$,Z) planes with $\Delta T < 2$ µs. The vertices are mainly located below the chimney as expected for stopping muons. The left panel of Figure 6.14 backs it up by showing the excess of events at positive Z for prompt events selected with $\Delta T < 2$ µs along with the electron antineutrino Monte Carlo expectations. The correlated nature of this background is illustrated in the right panel of Figure 6.14: the $\Delta R$ distributions for these events and the MC generated $\overline{\nu}_e$ are both peaked at 50 cm. A comparison between correlated and accidental coincidences $\Delta R$ is diplayed in Figure 6.42 in Section 6.3.1.

No space coincidence cut is applied in the Double Chooz analysis. Indeed, the detector design has been optimized to reduce the number of cuts with respect to CHOOZ [30, 31], especially thanks to the buffer volume and the $\nu$-target/$\gamma$-catcher separation, creating then a physical fiducial volume for antineutrino interactions (*cf.* Section 3.5).

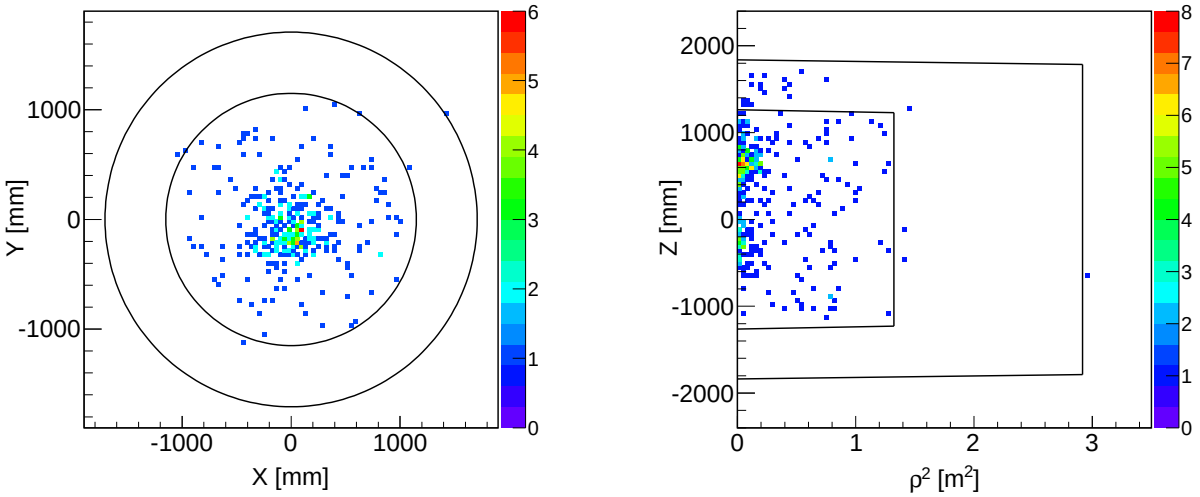


Figure 6.13: *Prompt events, from $\overline{\nu}_e$ candidates selection with $\Delta T < 2\ \mu s$, vertices distribution in the $(X,Y)$ plane (left), and the $(\rho^2, Z)$ plane (right), in mm and $m^2$. Solid black lines corresponds to $\nu$-target and $\gamma$-catcher walls.*

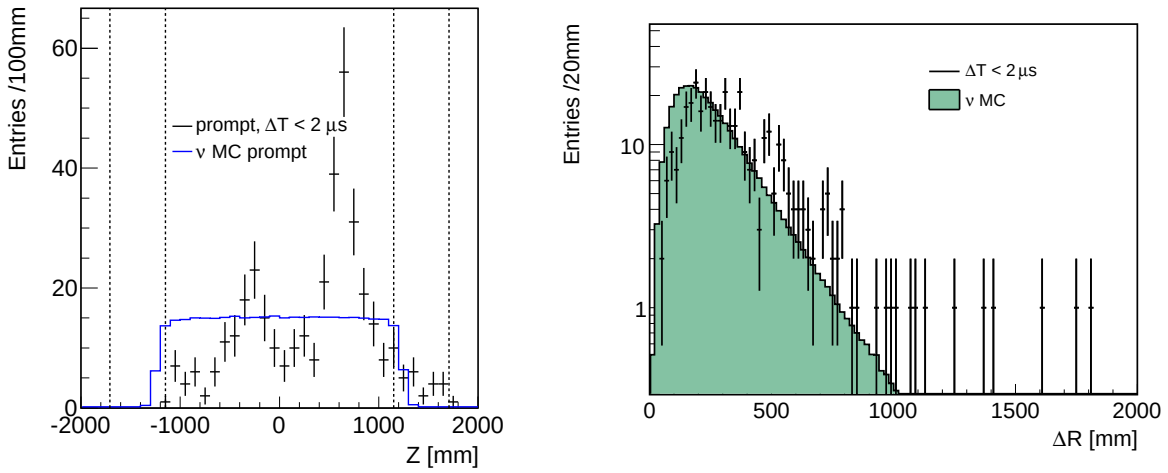


Figure 6.14: *(left) Prompt events, from $\overline{\nu}_e$ candidates selection with $\Delta T < 2\ \mu s$, Z distribution. Blue line is neutrino Monte Carlo and dashed lines corresponds to the $\nu$-target and $\gamma$-catcher wall positions. (right) Tridimensional distance distribution between delayed and prompt vertices, in mm. Green histogram is the expected distribution for neutrino Monte Carlo.*

### Multiplicity cuts

Finally, multiplicity cuts, also called isolation cuts, are applied. Their goal is to isolate the characteristic prompt-delayed pairs from other events, avoiding then the selection of multiple neutron captures as an antineutrino candidate. In order to do so, several cuts are applied: no valid triggers are allowed in the 100 µs preceding the prompt candidate, where a valid trigger is defined as a deposited energy higher than 0.5 MeV, MQTQ $< 0.09$, and RMS($T_{start}$) $< 40$ ns. The time window from 2 to 100 µs following the prompt can contain only one valid trigger which is the delayed candidate; any other valid trigger, including in the 2 µs immediately following the prompt event, causes the event to be thrown away. Furthermore, the 300 µs time window starting 100 µs after the prompt event must be completely empty of valid triggers. A schematic visualization of these cuts can be found in Figure 6.12.

Figure 6.15 shows the spectrum of the prompt events after applying the first multiplicity cut (*i.e.* no valid trigger in the 100 µs preceding the prompt event). This cut induces a reduction of an apparent 8 MeV peak in the prompt spectrum. This is understood as a neutron capture on Gd which was incorrectly selected as a prompt event of an antineutrino interaction. I have been one of the first proposing an isolation cut before the prompt event in order to reduce the neutron captures contamination in the prompt spectrum [72]. The selected prompt and delayed events may actually be multiple neutrons created after a high energy cosmic muon interaction within the detector. Figure 6.15 actually presents two spectra, with two characteristic peaks: one around 2.2 MeV and one around 8 MeV, respectively the neutron capture on hydrogen and gadolinium. The 8 MeV peak is unchanged while increasing the veto window before the prompt, supporting the fact that this peak is indeed neutron capture on Gd (100 µs is enough to select most of the neutron captures on Gd). Also, when this pre-prompt veto window is increased to 1 ms, the subtracted spectrum tends to be filled homogeneously which could be a correlated background contamination (*cf.* Section 6.3).

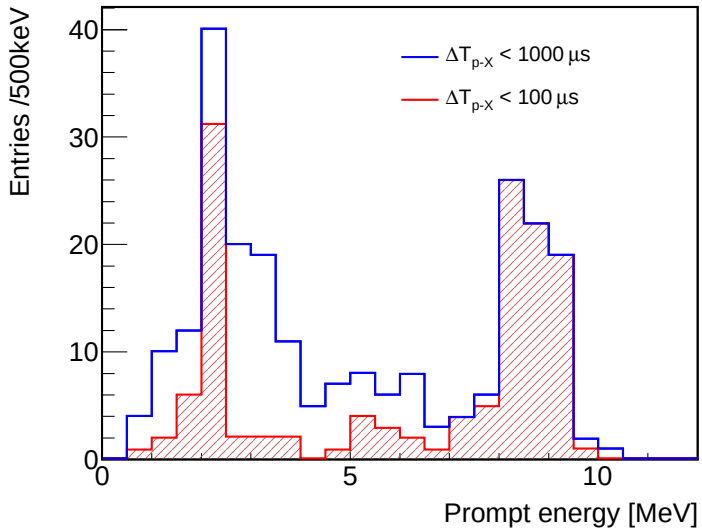


Figure 6.15: *Spectra of prompt events selected by the pre-prompt isolation cut. The blue histogram corresponds to the standard one ($\Delta T_{p\text{-}X} < 100$ µs) and the red to $\Delta T_{p\text{-}X} < 1{,}000$ µs, where X is the pre-prompt event.*

### 6.2.3 Electron antineutrino selection results

In this section, relevant distributions concerning the 9,021 antineutrino candidates selected from the 6,321 official runs are shown. The total live time amounts for 240.17 days and is calculated as the total run time minus the total muon veto time. All these results have been obtained with my own analysis chain, based on the Cheetah reduced files (*cf.* Section 4.6). So far, the official cuts presented before and summarized in Table 6.1 are applied.

The Figure 6.17 displays the $\Delta$T distributions, for the electron antineutrino candidates and the antineutrino Monte Carlo events simulated with the Double Chooz framework (*cf.* Section 5.1). $\Delta$T is the difference between the delayed and the prompt trigger times. The $\Delta$T distributions are in really good agreement, suggesting that the selected prompt and delayed events are indeed correlated via the neutron capture on Gd physics process. An exponential fit to the data distribution gives a typical capture time of $\tau = 27.61 \pm 0.43$ µs, which is compatible with the expectations in the Double Chooz detector considering the gadolinium concentration in the $\nu$-target liquid.

On the same page, the Figure 6.18 shows the $\Delta$R distributions for the neutrino candidates and a MC neutrino sample. $\Delta$R is the tridimensional distance between the delayed vertex and the prompt vertex. Both distributions are in really good agreement, especially before 1 m. Given that the typical neutron mean free path is of the order of a few tens of centimeters, the events at high $\Delta$R (higher than one meter or so), correspond to the expected accidental background contamination of the selected antineutrino sample. Indeed, the time correlation of the prompt and delayed events of a real $\overline{\nu}_e$ interaction does not allow the neutron to travel much more than 1 m, given the scintillator liquid density and Gd concentration (*cf.* Section 3.3.2). A careful study of the backgrounds is then needed, in order to take them into account within the final fit (*cf.* Chapter 7), or subtract them prior to it (*cf.* Section 6.5.6).

The distributions of the prompt and delayed vertices, in the (X,Y) and ($\rho^2$,Z) planes, are available in Figures 6.19 and 6.20, where $\rho^2$ is defined as $X^2+Y^2$. The $\nu$-target and the $\gamma$-catcher top, side, and bottom are also drawn with solid black lines. The neutrino candidates vertices are as expected located within the $\nu$-target volume. However, a background contamination is visible for positive Z, below the chimney. This background is first understood to come from accidental coincidences due to high rate of single events coming from the outside through the chimney (*cf.* Section 6.3.1), and second to come from stopping muons correlated background entering the detector (*cf.* Section 6.3.2). The plot in the ($\rho^2$,Z) plane is preferred to a (Y,Z) one because of the cylindrical geometry of the Double Chooz detector, as it allows to check the uniformity of the distribution of the selected events.

The Figures 6.21 and 6.22 show the same information but as one dimension distributions. The background contamination pointed out above is expressed as an excess around null $\rho^2$ and for positive Z. These neutrino candidates distributions are all drawn on the same canvas with the expected neutrino Monte Carlo, allowing a direct comparison between the data and the MC and making these excesses more visible. However, the shapes of the distributions are in really good agreement, even close to the acrylics where the physics seems well modeled by our simulation.

The following plots display on Figures 6.23 and 6.24 the two light-noise variables distributions for both the prompt events and the delayed events selected on data, along with the expectations. The MQTQ distribution of the $\overline{\nu}_e$ candidates is in good agreement with the Monte Carlo simulation. Regarding RMS($T_{start}$), even though the general shapes are similar, the agreement is not as good. However, these plots seem to indicate that almost no $\overline{\nu}_e$ events leak outside the

boundaries of 40 ns for RMS($T_{start}$) and 0.09 and 0.055 for MQTQ. This was expected according to calibration studies presented in Figure 6.5.

Once the selection is performed, one can extract an electron antineutrino average rate over the data taking period of 37.6 $\pm$ 0.4 $d^{-1}$. Figure 6.16 presents the neutrino candidates rate per day. This plot is completely correlated with Figure 6.2 as the number of neutrino interactions measured in the detector is directly related to the thermal power of the reactors. Figure 6.16 shows three kinds of periods. The first one when the neutrino candidate rate is around 50 per day corresponds to both reactor being ON, close to their maximum power. This is consistent with the number quoted in Table 3.2 that expresses the expected antineutrino rates at the far detector with the detector efficiency and dead time taken into account. The Figure 6.16 also shows periods with an average rate per day of roughly 25, around day 20 or between days 160 and 230, for instance. This corresponds to a period when one of the two reactors was shut down. Finally, there is also one day with almost no candidate, corresponding to 24 hours of both reactors OFF, called OFF-OFF period (*cf.* Section 6.5.6).

Finally, both prompt spectrum and delayed spectrum are available in Figures 6.25 and 6.26, respectively.

The delayed spectrum corresponds to the neutron capture peak on Gd. Both neutrino Monte Carlo and electron antineutrino candidates are drawn. The slight disagreement between the two distributions is caused by the limitation of the current energy determination, which does not completely corrects for non-linearity (*cf.* Section 4.2.4.

Regarding the prompt spectrum, there is a good agreement between the selected data and the corresponding Monte Carlo simulation. However, a slight deficit at low energy is visible and can be explained by a non-zerot $\theta_{13}$ (*cf.* Chapter 7, for the oscillation fit chapter). It is interesting to notice the low statistics in energy bins after 8 MeV. This is actually what is expected for neutrino events, since only 0.4 % of the electron antineutrino events are expected to be in this energy region. Most of the events above 8 MeV are therefore background contamination. This is why the backgrounds need to be studied and subtracted to the electron antineutrino candidates selection, or at least taken into account in the fit.

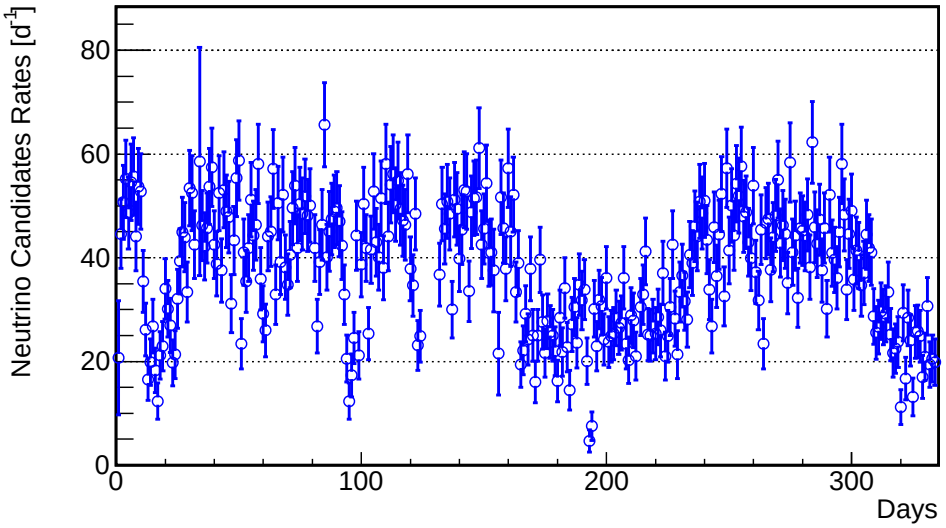


Figure 6.16: *$\overline{\nu}_e$ candidates rates evolution over the Double Chooz second publication period.*

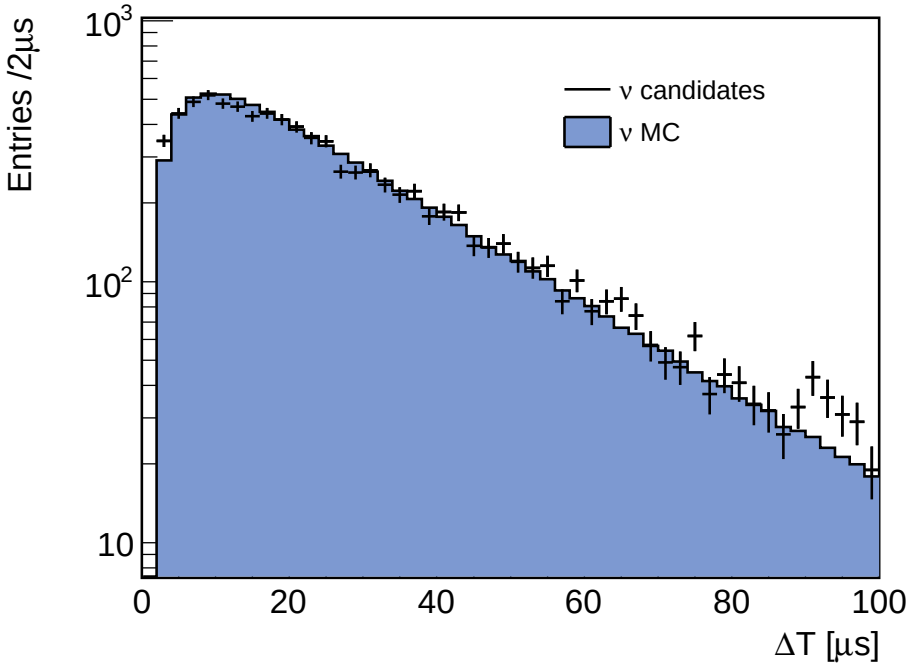


Figure 6.17: *Time difference distribution between selected antineutrino candidates delayed event and prompt event, in $\mu s$.*

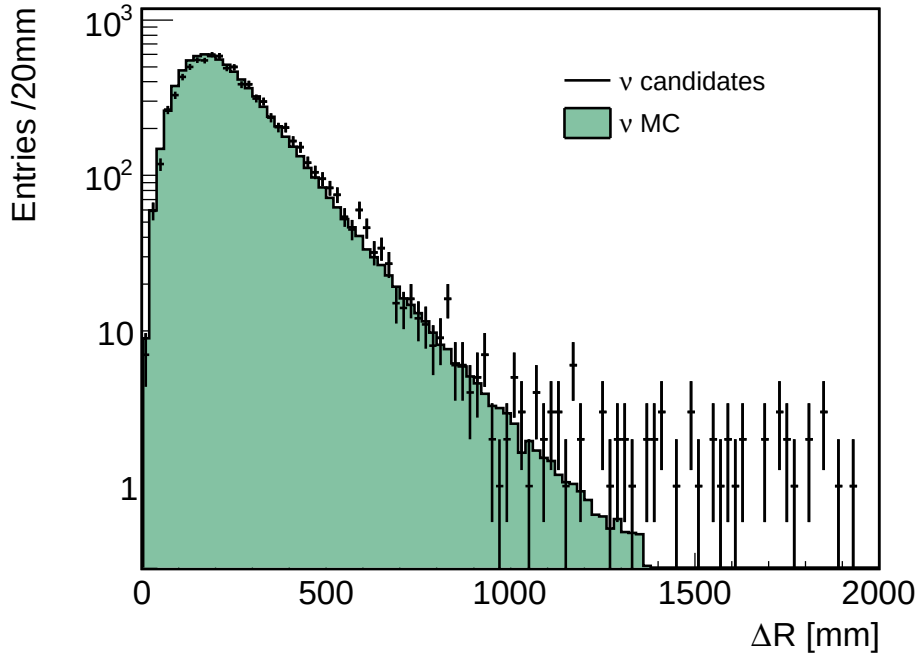


Figure 6.18: *Tridimensional distance distribution between selected antineutrino candidates delayed event and prompt event vertices, in mm. The disagreement between the data and the Monte Carlo at high $\Delta R$ is explained by accidental background contaminations.*

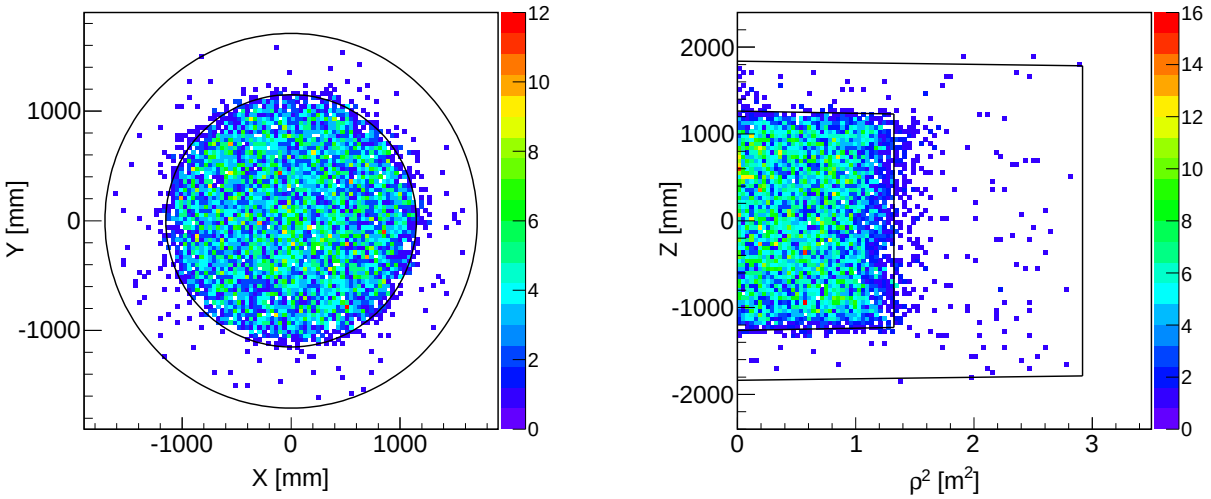


Figure 6.19: *Prompt events, from $\overline{\nu}_e$ candidates selection, vertex distributions in the (X,Y) plane (left), and in the ($\rho^2$,Z) plane (right). Solid black lines correspond to the $\nu$-target and the $\gamma$-catcher walls.*

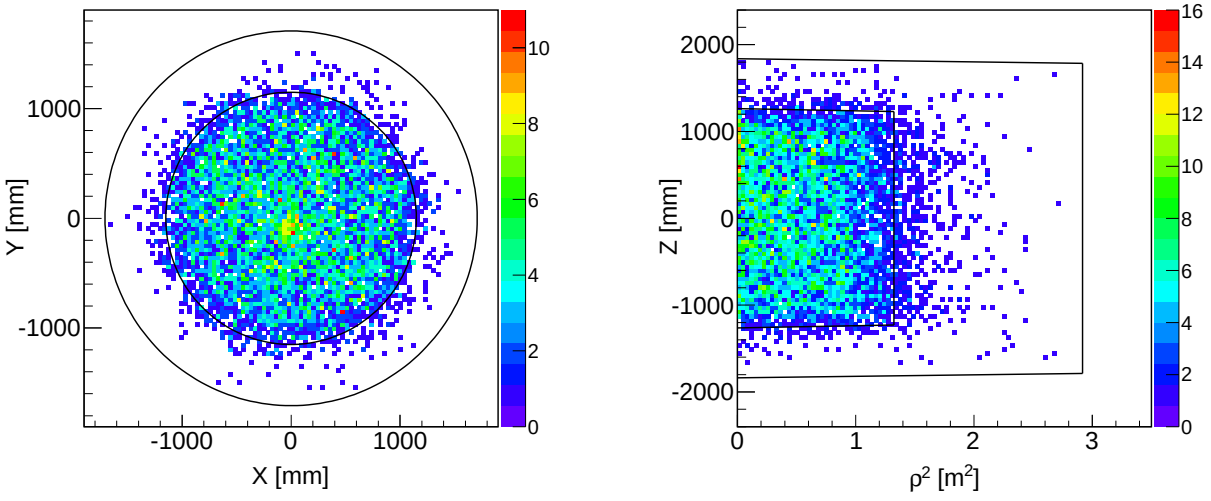


Figure 6.20: *Delayed events, from $\overline{\nu}_e$ candidates selection, vertex distributions in the (X,Y) plane (left), and in the ($\rho^2$,Z) plane (right). Solid black lines correspond to the $\nu$-target and the $\gamma$-catcher walls.*

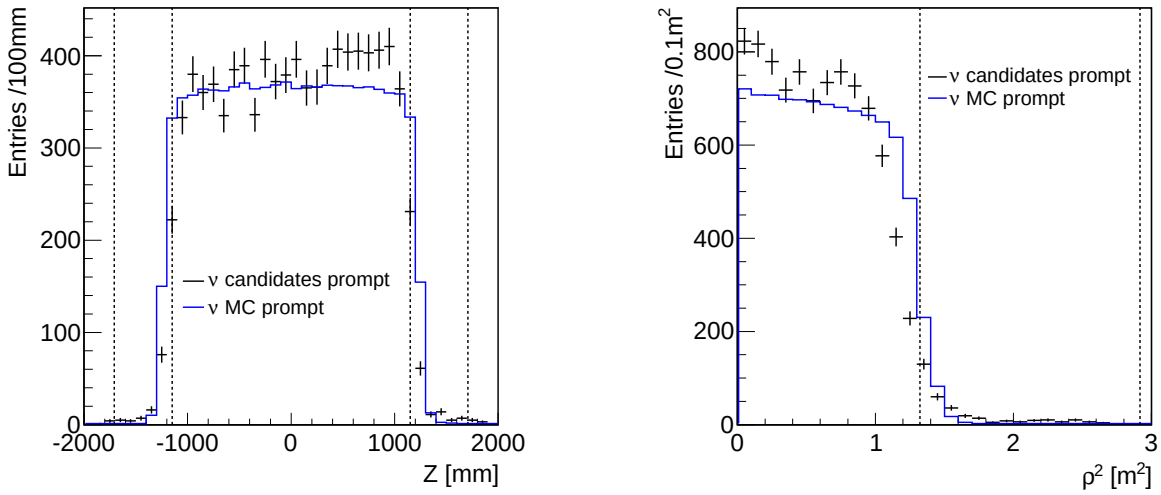


Figure 6.21: *Prompt events, from $\overline{\nu}_e$ candidates selection, Z in mm (left) and $\rho^2$ in $m^2$ (right) distributions. Black points are data, while solid blue lines are neutrino Monte Carlo. Dashed lines corresponds to the $\nu$-target and the $\gamma$-catcher walls positions.*

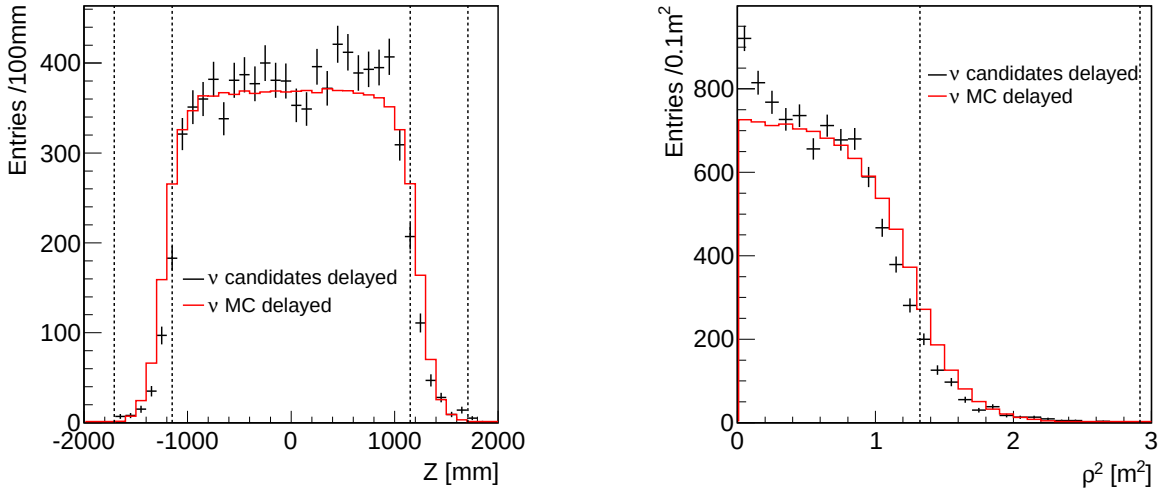


Figure 6.22: *Delayed events, from $\overline{\nu}_e$ candidates selection, Z in mm (left) and $\rho^2$ in $m^2$ (right) distributions. Black points are data, while solid red lines are neutrino Monte Carlo. Dashed lines corresponds to the $\nu$-target and the $\gamma$-catcher walls positions.*

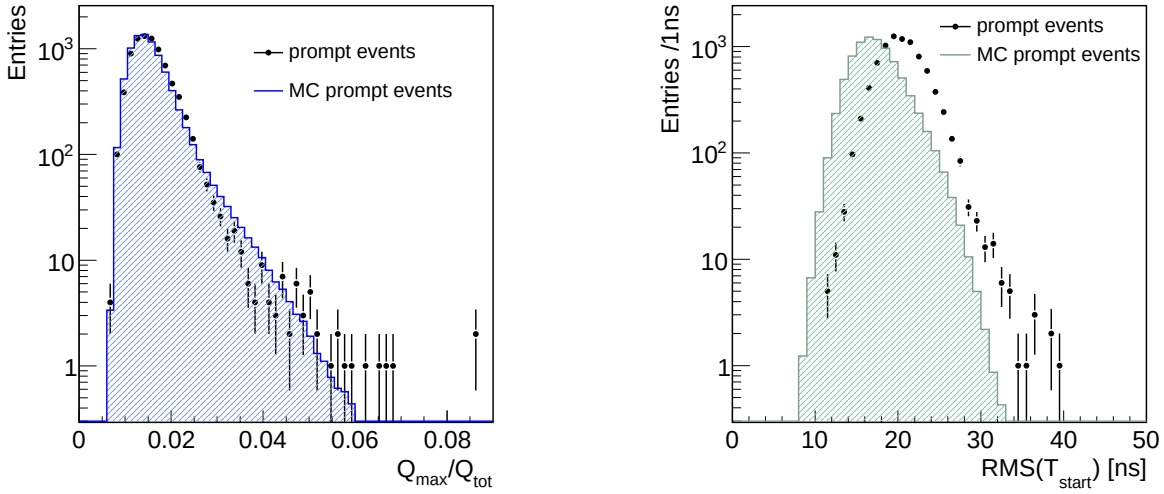


Figure 6.23: *Light-noise rejection cuts distributions for prompt events, from $\overline{\nu}_e$ candidates selection on data (black points) and on Monte Carlo. (left) Maximum charge over total charge distribution; solid blue line is MC. (right) Start time spread, in ns; solid green line is MC.*

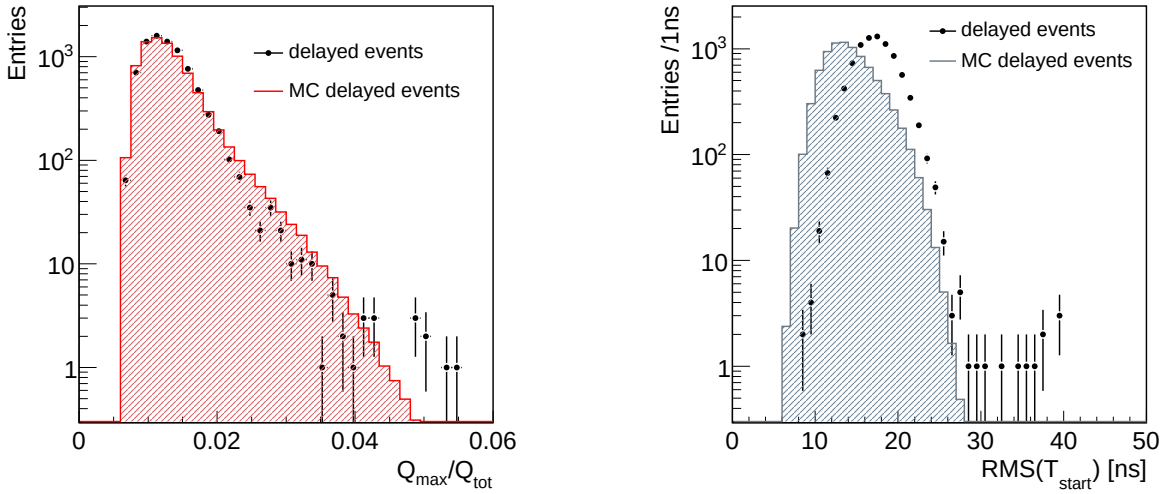


Figure 6.24: *Light-noise rejection cuts distributions for delayed events, from $\overline{\nu}_e$ candidates selection on data (black points) and on Monte Carlo. (left) Maximum charge over total charge distribution; solid red line is MC. (right) Start time spread, in ns; solid green line is MC.*

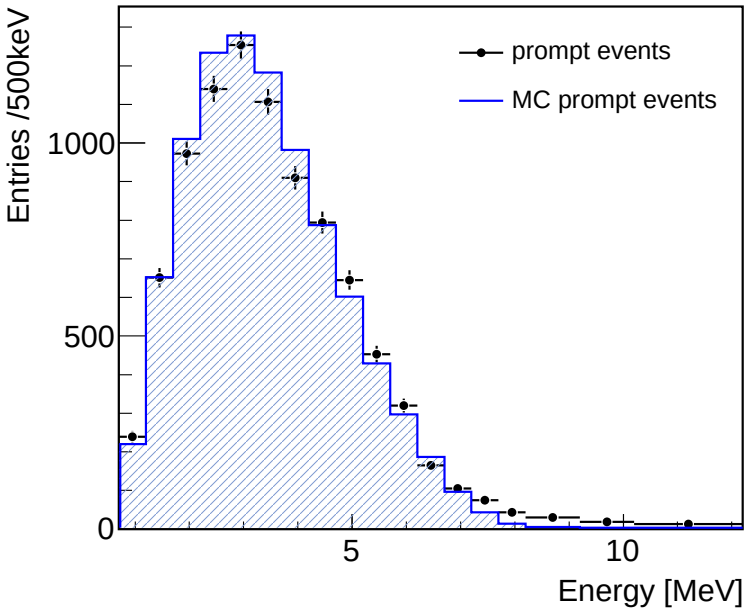


Figure 6.25: *Prompt spectra of both electron antineutrino events selected on data (black points) and Monte Carlo simulation (solid blue line).*

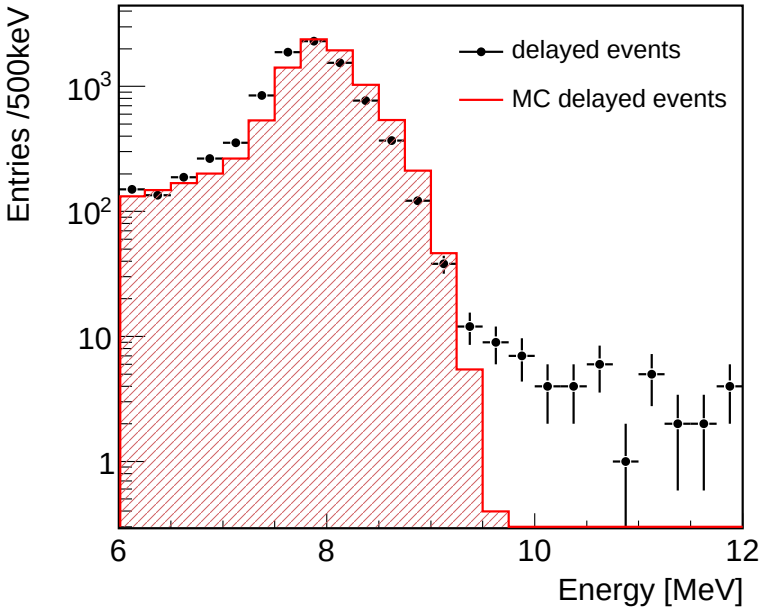


Figure 6.26: *Delayed spectra of both electron antineutrino events selected on data (black points) and Monte Carlo simulation (solid red line).*

### 6.2.4 Cuts efficiencies

Calibration data taken with a $^{252}$Cf neutron source were used to check the Monte Carlo prediction for any biases in the neutron selection criteria and estimate their contributions to the systematic uncertainty [53, 54]. The three effects studied below are the delayed window cut $\Delta$T, the fraction of neutron captures on Gd, and the fraction of neutron capture on Gd within the delayed energy window, [6 ; 12] MeV. The spontaneous fission of $^{252}$Cf leads to the emission of $\gamma$ rays and an average of 3.7 neutrons, which are captured on a nucleus.

#### Time coincidence cut

The coincidence window for neutrino selection between the prompt event and the delayed event goes from 2 to 100 µs. The $\Delta$T upper limit is chosen to be roughly three times the expected neutron capture time in the $\nu$-target liquid scintillator, due to the Gd concentration of 1 g/L. A 100 µs limit allows to select most of the neutrons (estimated to be 96.4 %, *cf.* Section 6.2.2). The $\Delta$T cut efficiency $\epsilon_{\Delta T}$ should then be carefully studied.

As defined in the top left panel of Figure 6.27, the $\Delta$T cut efficiency is calculated as the ratio of the number of selected neutrons within the official time window over the number selected in an expanded 200 µ$s$ time window for $^{252}$Cf data, averaged for several positions around the detector center along the Z-axis calibration system [7]. This $\Delta$T upper limit is chosen because it is expected to correspond to the selection of 99.9 % of the neutron capture. The efficiency is:

$$\epsilon_{\Delta T} = \frac{\mathrm{N}\left(2 < \Delta\mathrm{T} < 100\ [\mu\mathrm{s}]\right)}{\mathrm{N}\left(0 < \Delta\mathrm{T} < 200\ [\mu\mathrm{s}]\right)}. \tag{6.1}$$

On neutron captures from $^{252}$Cf data, the efficiency is estimated to be $\epsilon_{\Delta T} = 96.40 \pm 0.24$ %, while it is $\epsilon_{\Delta T} = 96.88 \pm 0.10$ % on Monte Carlo [128]. These are average values over all Z positions around the $\nu$-target center (Figure 6.27, top left). The simulation reproduces very well the 96.5 % efficiency of the data and the relative difference between data and MC simulation is $0.51 \pm 0.27$ %. However, the total systematic uncertainty assigned to the $\Delta$T cut is the sum of the Z-axis data spread and the relative difference between data and Monte Carlo, integrated in the [0 ; 1150] mm range ($\nu$-target only), from an extrapolation between the Z-axis points and the guide tube ones (Figure 6.27, top right). This allows to use the calibration points in the $\gamma$-catcher. It is found to be 0.20 %. The total systematic uncertainty is then 0.44 %, the sum of 0.20 % and 0.24 %. A conservative 0.50 % is finally considered to take into account results of other studies [52].

#### Neutron capture on Gd efficiency

The neutron capture on a Gd nucleus efficiency is estimated by studying the gadolinium fraction within the scintillator liquid, for both $^{252}$Cf Monte Carlo and calibration data [53, 54]. In order to do so, the delayed spectrum of correlated events with prompt signals between 7 and 25 MeV, 1.5 ms away from a valid trigger [8], is drawn. The $\Delta$T between the prompt and the delayed is asked to be lower than 1 ms, and the delayed MQTQ $< 0.055$. As for neutrino selection, a Gd capture is considered between 6 and 12 MeV.

Both 2.2 MeV hydrogen and 8 MeV gadolinium capture peaks are fitted, respectively by a Gaussian and a function which models the Gd $\gamma$ rays with Gaussians and error functions [9]

[7] For a presentation of the Double Chooz calibration devices, see Section 3.5.4.

[8] Valid trigger: energy above 0.5 MeV, with MQTQ $< 0.09$ and RMS($\mathrm{T_{start}}$) $< 40$ ns (*cf.* Section 6.2.2).

[9] This model takes into account two photopeaks from $^{155}$Gd and $^{157}$Gd, the main contributors to the neutron capture, along with the Compton continuum from electrons generated in Compton scatterings [62].

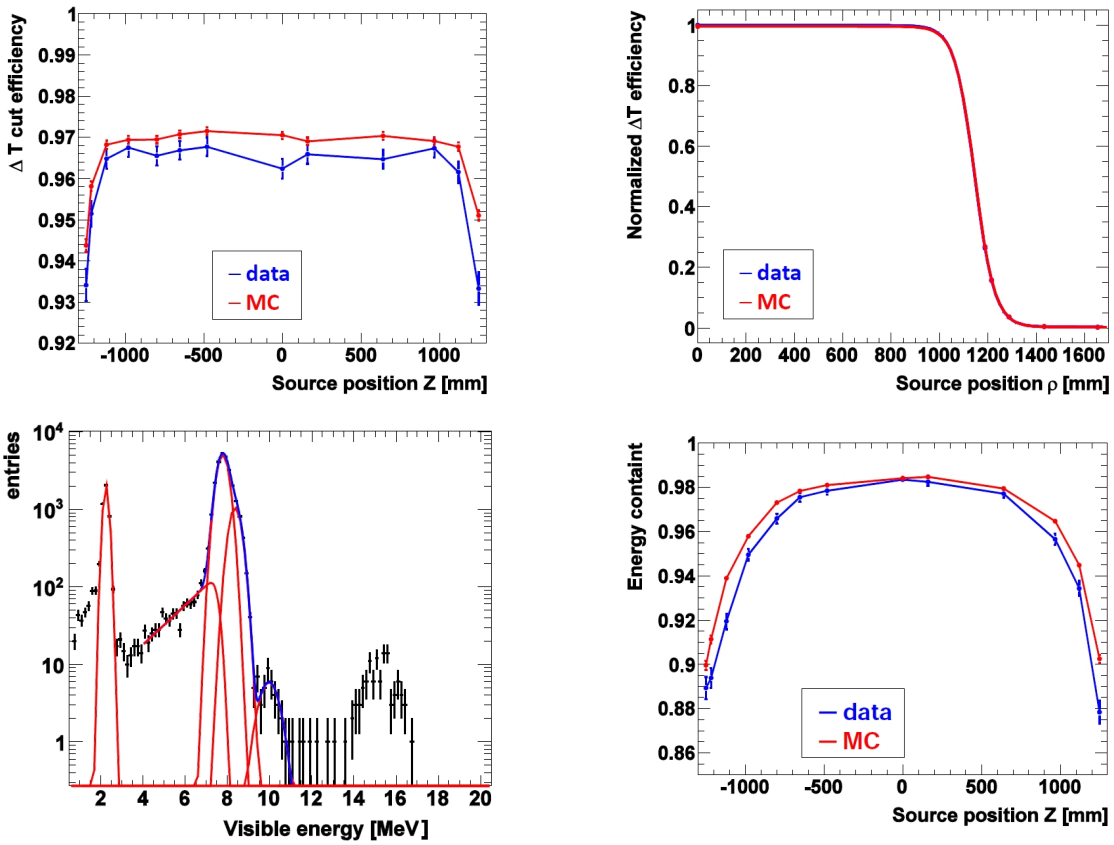


Figure 6.27: *(top left) $\Delta T$ cut efficiency versus the Z position of the $^{252}Cf$ source, for both data and MC. (top right) Extrapolation from Z-axis to guide tube calibration points. (bottom left) $^{252}Cf$ delayed energy spectrum fitted. (bottom right) Energy containment versus the Z position of the $^{252}Cf$ source, for both data and MC [52, 53, 54, 128].*

(Figure 6.27, bottom left). The Gd fraction on $^{252}$Cf calibration data is found to be $\epsilon_{\mathrm{Gd}} = 86.57 \pm 0.11$ %, and $87.85 \pm 0.07$ % on Monte Carlo. The relative difference between data and MC is then 1.5 %. The Monte Carlo is then corrected by the scale factor 0.985 (*cf.* Section 5.3).

### Delayed energy containment

The delayed event energy containment $\epsilon_{\Delta \mathrm{E}}$ is the fraction of neutron captures on Gd within the 6 to 12 MeV energy range. In order to do so, as for the two effects described above, $^{252}$Cf calibration data are used. The energy containment is defined as the number of neutron capture between 6 and 12 MeV divided by the one in the 4 to 12 MeV energy region:

$$\epsilon_{\Delta \mathrm{E}} = \frac{\mathrm{N}\left(6 < \mathrm{E}_{\mathrm{delayed}} < 12\ [\mathrm{MeV}]\right)}{\mathrm{N}\left(4 < \mathrm{E}_{\mathrm{delayed}} < 12\ [\mathrm{MeV}]\right)}. \tag{6.2}$$

On calibration events, the energy containment is estimated to be $\epsilon_{\Delta \mathrm{E}} = 96.43 \pm 0.22$ %, while it is $96.97 \pm 0.09$ % on Monte Carlo (Figure 6.27, bottom right). The method of guide tube calibration data points extrapolation explained above for the $\Delta$T efficiency is applied as well. The total systematic uncertainty of the delayed event low energy cut is therefore estimated to be 0.7 %, from calibration data and Monte Carlo simulation comparisons [52, 128].

Concerning the prompt event, the energy containment is to a very good approximation 100 %, from trigger efficiency studies [175].

## 6.3 Backgrounds studies

### 6.3.1 Accidental background

#### Singles

The single events, or sometimes simply called singles, are non-correlated events that trigger the detector. They are mainly caused by ambient radioactivity $\gamma$ but can also be all kinds of events: real electron antineutrino prompt or delayed energy deposition (*cf.* Section 6.2), fast-neutrons (*cf.* Section 6.3.2), decay of cosmogenics isotopes (*cf.* Section 6.3.3), Michel electrons, etc. As explained in the previous section, only a coincidence study allows to distinguish single events from our actual signal.

The search of single events in our detector is done by looking for 0.7 to 12.2 MeV energy depositions which are neither flagged as light-noise (prompt prescription: MQTQ $< 0.09$ and RMS($T_{start}$) $< 40$ ns), nor as muon (total charge in the inner veto lower than 10,000 DUQ), and which are at least 1 ms away from a muon event (corresponding to a total charge in the IV higher than 10,000 DUQ or a deposited energy in the inner detector above 30 MeV).

As shown on Figures 6.28 and 6.29, even if no position cut is applied, most of the singles are located in the vicinity of the detector chimney and near the photomultiplier tubes. This is expected since these events mostly come from the ambient natural radioactivity, getting in the detector from outside via the chimney (radon naturally present in the air), and also coming from the inside of the detector via the $^{40}$K decay in the PMTs glass or in the acrylics of the inner vessels. The Figure 6.31 shows indeed a singles spectrum mostly populated at low energies, basically before 3 MeV, consistent with a radioactivity spectrum. The last visible line belongs to the $^{208}$Tl $\gamma$ ray emission at 2.614 MeV, a decay product of $^{232}$Th. The decay chain of the naturally present $^{238}$U, in the rock and in the air, is also a source of single events. The 8 MeV peak corresponds to thermal neutrons being captured on the liquid scintillator gadolinium.

The singles mean rate in the detector, from 0.7 to 12.2 MeV, is $8.2025 \pm 0.0006$ Hz, while it was designed to be 10 Hz in the Double Chooz proposal [31]. Furthermore, the measured thermal neutrons capture rate in the delayed energy window (from 6 to 12 MeV) is of the order of 20 per hour, while it was expected to be higher than 80 per hour. This is explained by the tremendous work performed by the collaboration, which struggled to install the detector and operate its related equipments at low radioactivity level [158]. The careful selection of the construction material along with the detector design, with the buffer volume and its shielding, seem also to pay off. For comparison, the former CHOOZ experiment found a prompt-like singles rate of $64.8 \pm 0.1$ Hz and $45 \pm 2$ h$^{-1}$ events in the delayed energy window [30].

Looking at the light-noise variable distributions for single events in the delayed energy window allows to explain the choice of a tighter MQTQ cut for this kind of events, as stated in Section 6.2.2. The Figure 6.30 is a scatter plot representing the RMS($T_{start}$) versus the MQTQ variables for single events, from 0.7 to 12.2 MeV on the left panel, and from 0.7 to 6 MeV on the right panel. One of the two light-noise blobs, also visible in the vertex distributions on Figures 6.28 and 6.29, can be removed with a stronger cut on the MQTQ variable, lower than 0.06. MQTQ $< 0.055$ is chosen as it allows to cancel the significant increase in the accidental rate induced by the light-noise background but is still a safe choice for no physical events rejection, according to the Monte Carlo distribution of Figure 6.3.

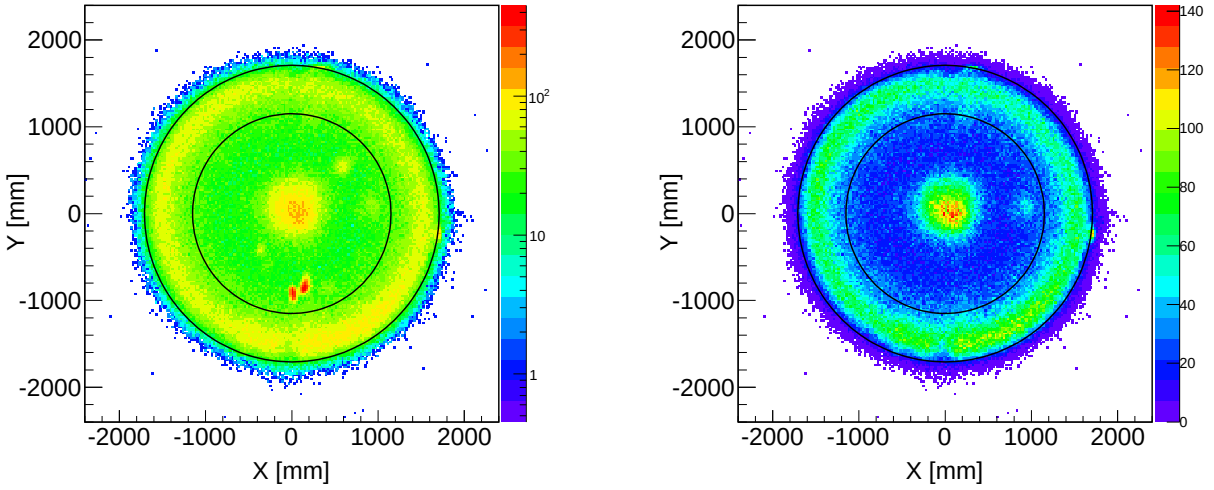


Figure 6.28: *Single events vertex distributions in the (X,Y) plane, from 0.7 to 12.2 MeV in logarithmic scale (left) and from 0.7 to 6 MeV (right), in mm. The two hot spots on the left plot are explained with Figure 6.30, the RMS($T_{start}$) and MQTQ scatter plot for singles. Solid black lines corresponds to the $\nu$-target and the $\gamma$-catcher walls.*

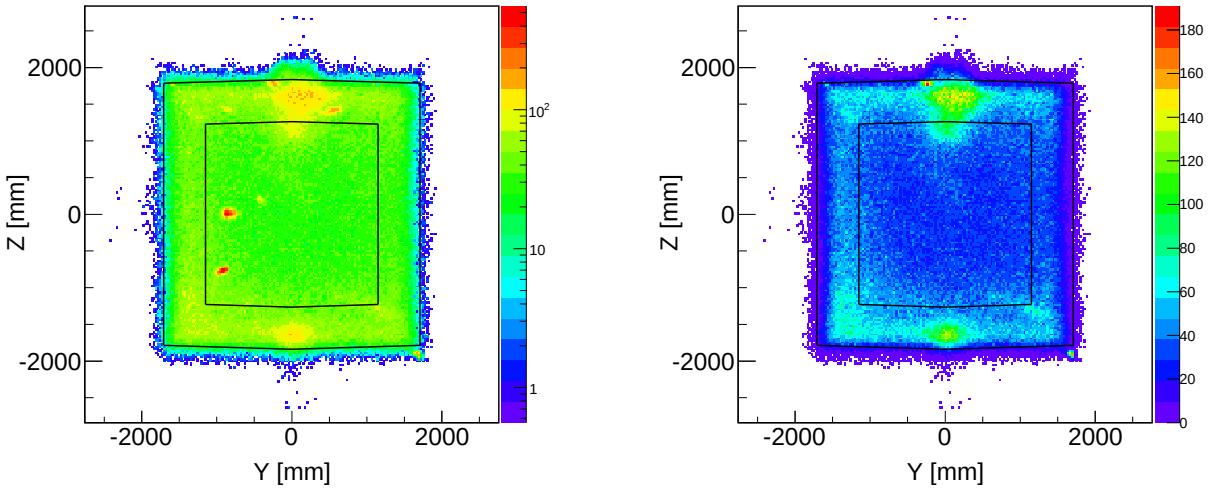


Figure 6.29: *Single events vertex distributions in the (Y,Z) plane, from 0.7 to 12.2 MeV in logarithmic scale (left) and from 0.7 to 6 MeV (right), in mm. The two hot spots on the left graph are explained with Figure 6.30, the RMS($T_{start}$) and MQTQ scatter plot for singles. Solid black lines corresponds to the $\nu$-target and the $\gamma$-catcher walls.*

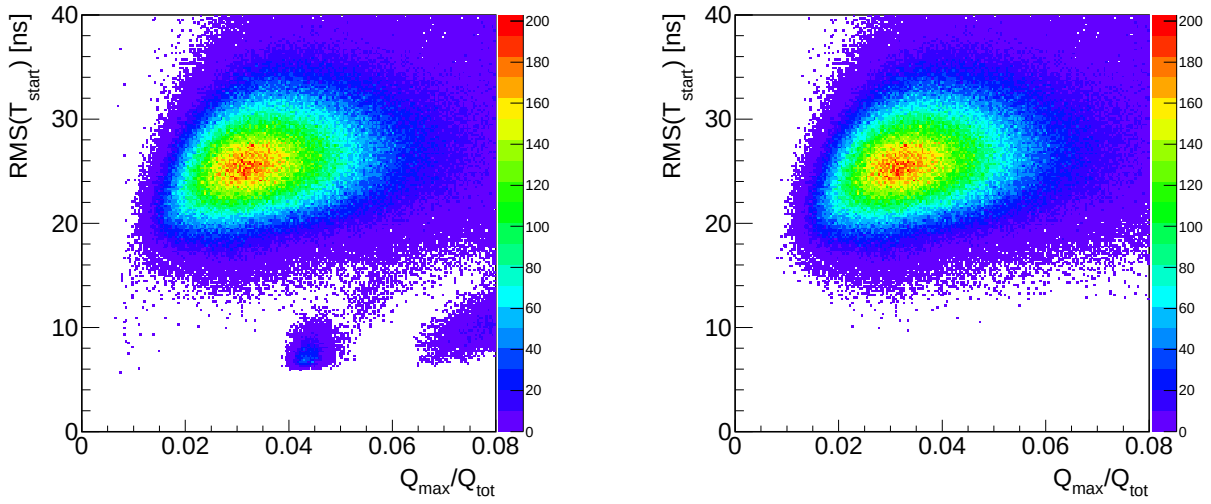


Figure 6.30: *RMS($T_{start}$) versus MQTQ variable for single events, from 0.7 to 12.2 MeV (left) and from 0.7 to 6 MeV (right). These scatter plots illustrate the need of a tighter light-noise cut for the delayed event selection, MQTQ < 0.055. However, it does not allow to get rid of the events at low RMS($T_{start}$) and MQTQ around 0.045.*

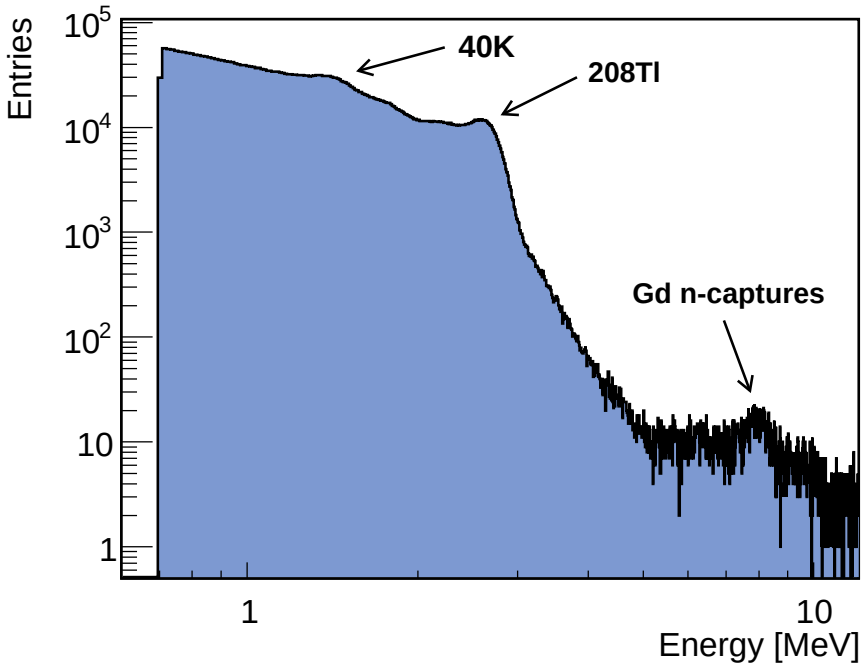


Figure 6.31: *Single events spectrum, in MeV. The $^{208}Tl$ line before 3 MeV, the $^{40}K$ one, and the 8 MeV thermal neutron capture on Gd peak are visible.*

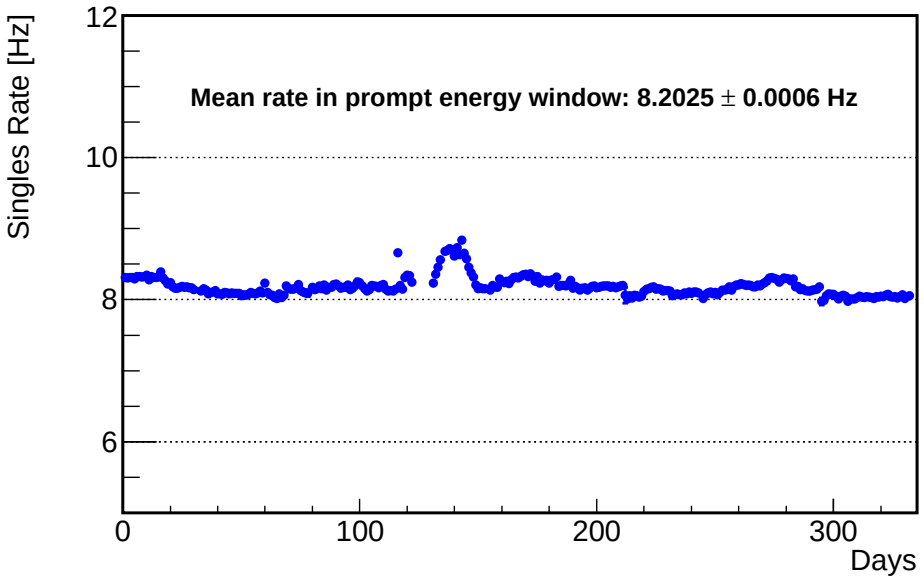


Figure 6.32: *Singles rate in the prompt energy region [0.7 ; 12.2] MeV, per day. The slight increase from day 120 corresponds to important light-noise emissions in the delayed energy region. This was taken care of by tightening the delayed MQTQ cut.*

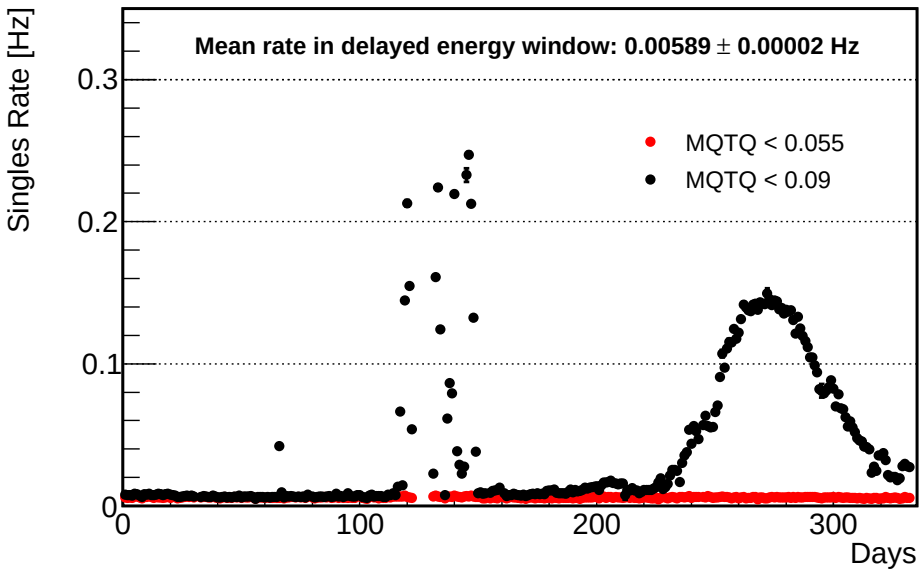


Figure 6.33: *Singles rate in the delayed energy region [6 ; 12] MeV, per day. Both light-noise prescriptions are drawn: the old one MQTQ < 0.09 (black) and the tight one MQTQ < 0.055 (red). The two large rate increases around day 120 and 230 were taken care of by applying MQTQ < 0.055 for delayed-like events. The mean rate quoted in the plot concerns MQTQ < 0.055.*

### Accidental coincidences search

The accidental background corresponds to the fortuitous coincidences of two single events, mimicking the electron antineutrino prompt event and delayed event features. The two energy depositions selected in the antineutrino 98 µs time window are therefore not related by any physical process. This background is also called "accidentals" in the following sections. Its expected rate in the detector, according to the Double Chooz proposal, is of the order of two coincidences per day [31].

The accidentals search is really similar to the electron antineutrino event search. The prompt and delayed prescriptions are the same than for signal: this allows to really estimate the accidental background contamination in the neutrino candidate selection presented before (*cf.* Section 6.2). The only difference lies in the $\Delta$T cut. Indeed, in order to select completely non-correlated events, an offtime window method is used: the delayed search is performed 1 s after the selected prompt event, making these two energy depositions non-related by any physical process. In a way, a "virtual" prompt event is considered 1 s after the selected prompt, and used as a reference for the delayed search in the classical 2 to 100 µs time window. The multiplicity cuts are similar to the ones applied on neutrinos, but specify that both the selected prompt and the virtual prompt are isolated, with no valid trigger 100 µs before each of them, and no valid trigger 400 µs after. A schematic view of this search algorithm and the related isolation cuts is proposed in Figure 6.34. The offtime window is chosen such as it is really large with respect to the coincidence window since a smaller one (of the order of the millisecond) would allow cosmogenics $^{12}$B correlated background events to be selected (half-life of 20 ms) [154]. This background tends to pollute the accidental prompt spectrum from 6 to 12 MeV with an unexpected high rate of events.

This method of accidentals selection unfortunately lacks of a high statistics. In order to increase the statistics, I was one of the firsts to use a multiple offtime window method. Instead of considering the virtual prompt only once 1 s after the selected prompt, the search is done by going forward 1 s plus 500 µs times 198. This number of consecutive offtime windows is chosen to provide enough statistics. Each time the specific accidentals isolation cuts are applied.

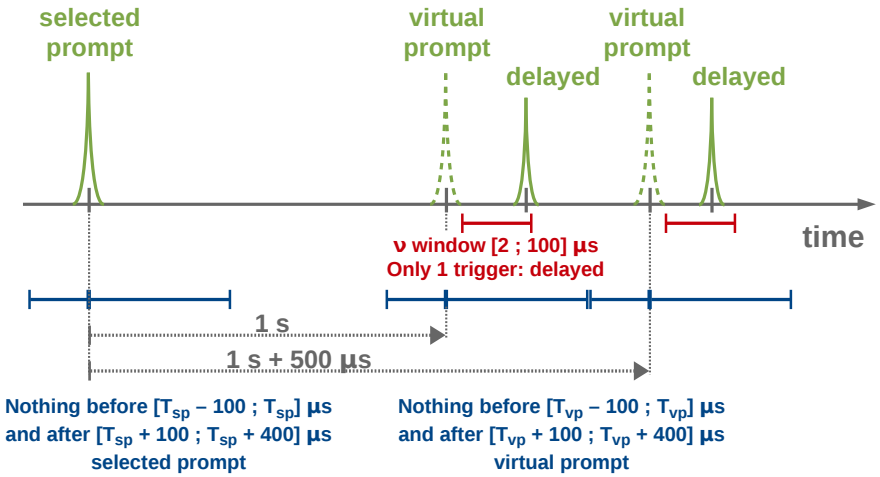


Figure 6.34: *Schematic view of the accidental background selection coincidence time window and the multiplicity cuts. As for Figure 6.12, "nothing" stands for "no valid trigger", whose definition can be found in the text. $T_{sp}$ and $T_{vp}$ are the selected prompt and the virtual prompt trigger times in µs, respectively.*

### Accidental background selection results

From this selection, the accidental background rate over the whole data period of the Double Chooz second publication is found to be 0.345 $\pm$ 0.003 $d^{-1}$, which is 6 times lower than what was quoted in the Double Chooz proposal [31].

The rate obtained with the offtime window method can be cross-checked by a simple calculation. The accidental events rate roughly corresponds to the product of the prompt-like event rate (energy deposition that is not light-noise nor muon, between 0.7 and 12.2 MeV, 1 ms away from a muon, with no valid trigger 100 µs before, or 400 µs after), the delayed-like event rate (same as prompt-like, but in a different energy window, from 6 to 12 MeV), and the 98 µs time window. These rates are not exactly the ones presented in the single events paragraph since these events are here asked to be isolated. The estimated rate with this method for the whole data period considered so far gives 0.358 $\pm$ 0.001 $d^{-1}$ in good agreement with the one coming from the multiple offtime windows method.

The rate per day of this background is drawn on Figure 6.35. It is very stable over the data taking period. Around day 120, an increase occured when the delayed MQTQ was asked to be below 0.09: this is visible in both Figures 6.32 and 6.33. It was explained by a sudden raise of light-noise in the delayed energy region. As explained in Section 6.2.2, this is taken care of by tightening the light-noise MQTQ prescription for the neutron-like event, from 0.09 to 0.055 [153].

As expected, the prompt spectrum of the accidentals search is compatible with the singles ones. The Figure 6.36 gives both singles and prompt accidentals spectra on the same canvas.

The Figures 6.37 and 6.38 show the vertex distributions for both prompt-like and delayed-like accidental events. The nature itself of this uncorrelated background implies a different behavior than the electron antineutrino candidates distributions, and thus different dispersion within the detector. The prompt distribution is really similar to the singles one: most of this background is located in the $\gamma$-catcher, close to the PMTs whose glass contains $^{40}$K and therefore contributes extensively to the accidentals. This is even more clear looking at the left panel of Figure 6.40, where one can see an excess of events in the $\gamma$-catcher volume with respect to the $\nu$-target distribution. Another excess is as expected located above the chimney. The left panel of Figure 6.39, which is the Z coordinate distribution for accidental prompt-like events, shows that even if these events occur at high $\rho^2$, they are unevenly distributed along the vertical axis of symmetry. Excesses are visible at high and low Z. The reason explaining the excess at high Z has been given before, and is related to the chimney. The one at low Z is explained by a filling tube that is more radioactive than expected. Indeed, a hot spot is visible on the left panel of Figure 6.38 at $\rho^2 = 0$ $m^2$ and Z = 1,700 mm.

The plots related to the delayed events basically show a uniform distribution of the neutron capture vertices in the $\nu$-target, supporting the fact that theses selected events mostly correspond to the 8 MeV Gd peak. However, excesses at high $\rho^2$, within the $\gamma$-catcher boundaries, are likely to be caused by incoming fast-neutrons creating recoil proton signals in the right energy range. This is backed up by drawing the energy distribution, which is roughly flat in this region, although slightly decreasing with a small 8 MeV peak visible.

Figure 6.41 is the time difference distribution between the virtual prompt and the delayed event. This distribution starts at 1 s as a consequence of the offtime window method. This $\Delta$T distribution is quite flat as expected for uncorrelated coincidences, although a fit to these points favors a soft negative slope. The $\chi^2$ per degrees of freedom $\chi^2$/NDF is 2 for a flat fit function and 1.3 for a first order polynomial, with a p-value of the order of a per mil and roughly 15 %, respectively. The negative slope is explained by calculating the Poisson probability of

one fortuitous coincidence in a $\Delta$T between two random events. This probability is expected to exponentially decrease with $\Delta$T given the mean rate of accidental coincidences.

The tridimensionnal distance between the selected virtual prompt and delayed is drawn on Figure 6.42. The $\Delta$R distribution for the selected electron antineutrino candidates is also shown. While for the neutrino candidates the distance between the two events is correlated to the neutron mean free path in the scintillator and is therefore peaked around a few tens of centimeters, the accidentals distribution is mainly populated between 2 and 3 m. The $\Delta$R distribution for accidental events goes up to 5 m. This is explained because 5 m is the maximal distance between two events in the Double Chooz detector, distance given by the $\gamma$-catcher diagonal which has a diameter and a height of 3,416 mm and 3,572 mm, respectively.

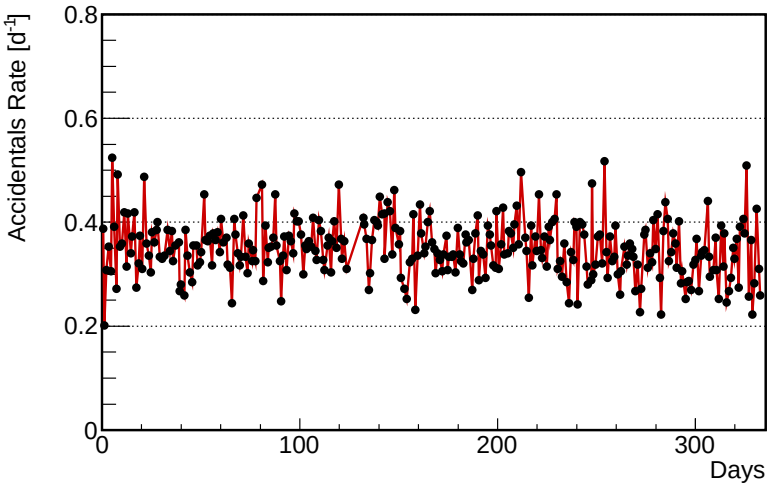


Figure 6.35: *Accidental events rate per day. The stability is very good and the mean rate over the second publication period is 0.345 ± 0.003 d$^{-1}$.*

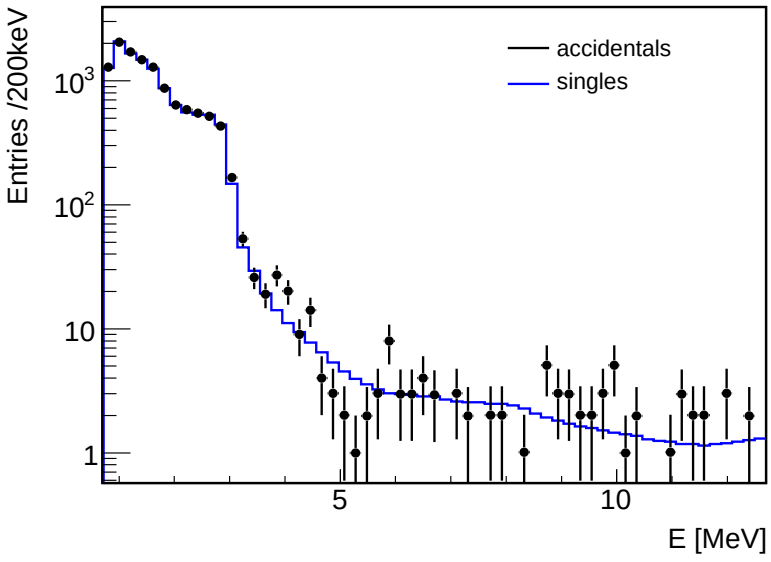


Figure 6.36: *Accidental events prompt spectrum (black points) with the single events spectrum surimposed and scaled (blue).*

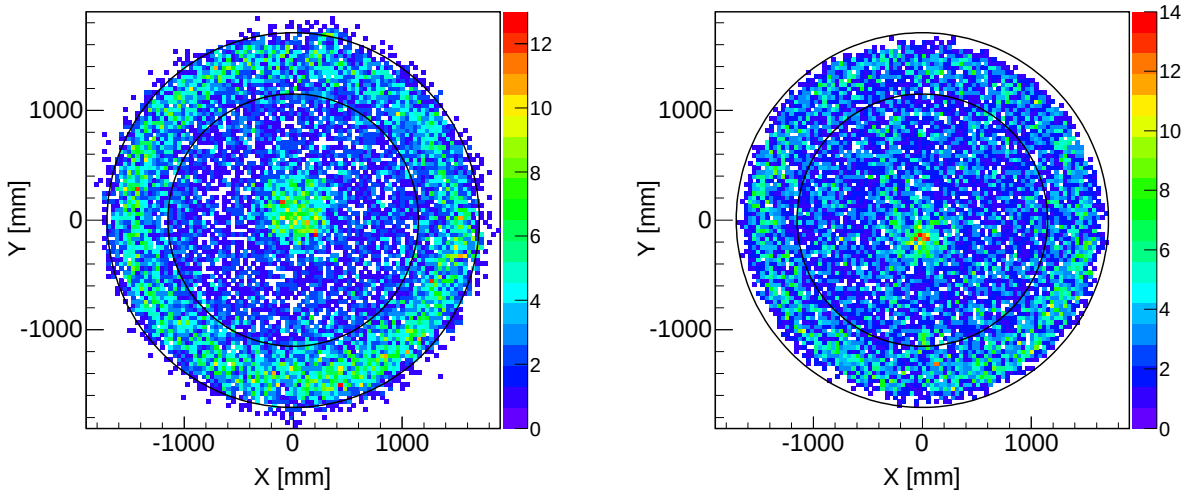


Figure 6.37: *Accidentals vertex distributions in the (X,Y) plane for prompt-like (left) and delayed-like (right) events. Solid lines correspond to the $\nu$-target and $\gamma$-catcher walls.*

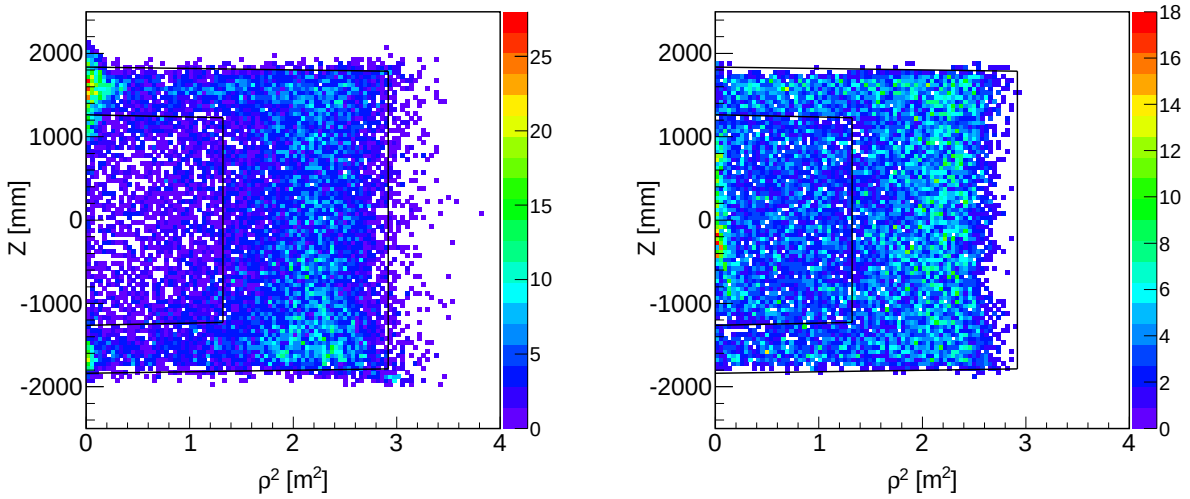


Figure 6.38: *Accidentals vertex distributions in the ($\rho^2$,Z) plane for prompt-like (left) and delayed-like (right) events. Solid lines correspond to the $\nu$-target and $\gamma$-catcher walls.*

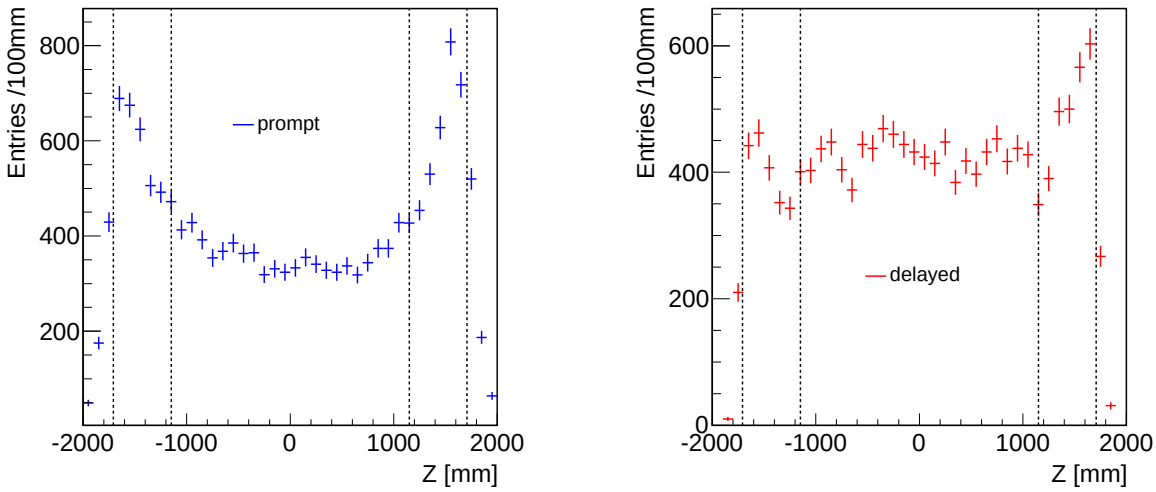


Figure 6.39: *Accidentals vertex Z coordinate distributions for prompt-like (left) and delayed-like (right) events. Dashed lines correspond to the $\nu$-target and $\gamma$-catcher walls.*

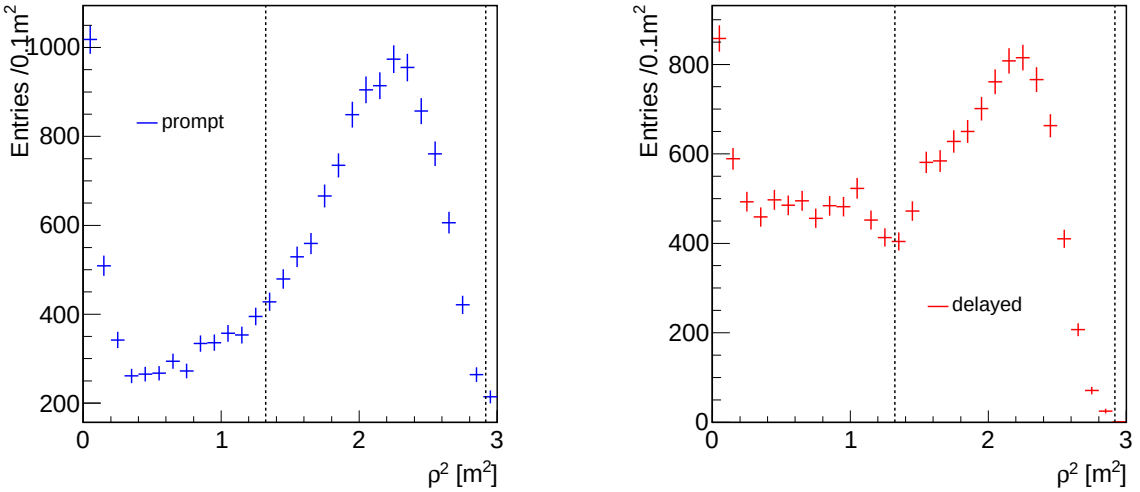


Figure 6.40: *Accidentals vertex $\rho^2$ distributions for prompt-like (left) and delayed-like (right) events. Dashed lines correspond to the $\nu$-target and $\gamma$-catcher walls.*

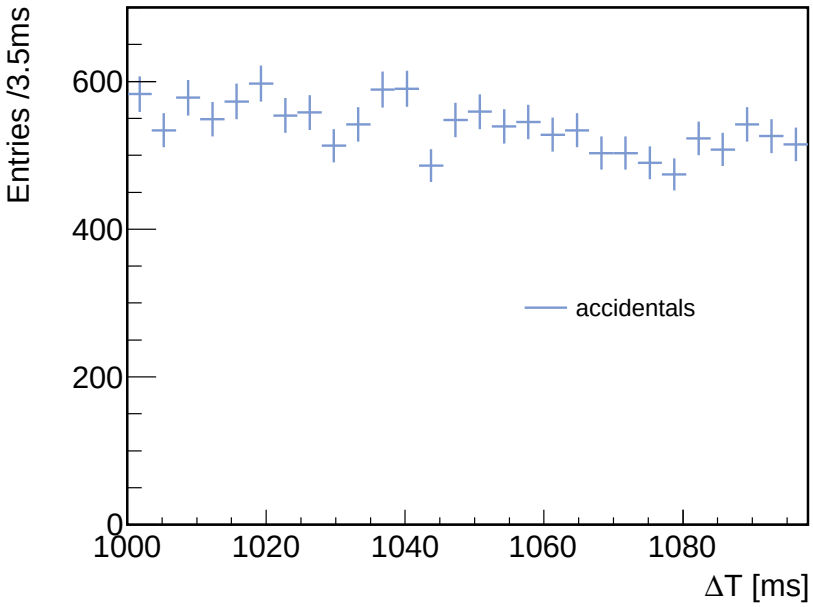


Figure 6.41: *Time difference distribution between selected accidentals delayed and prompt events, in $\mu$s. The X-axis starts at 1000 $\mu$s because of the fortuitous events search method.*

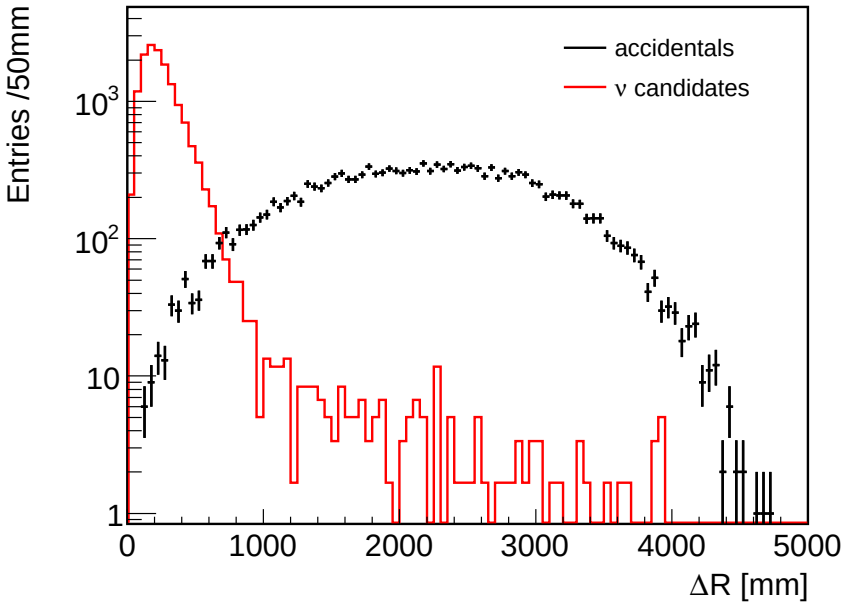


Figure 6.42: *Tridimensional distance distribution between selected accidentals delayed and prompt vertices, in mm (black points). The red line corresponds to the neutrino candidates $\Delta R$ distribution presented before, rescaled to the same amount of entries.*

### 6.3.2 Correlated background: fast-neutrons and stopping muons

Three kinds of correlated background can be selected within the electron antineutrino candidates sample. Two of them may be studied together: the fast-neutrons and the stopping muons.

The fast-neutron background is due to high energy neutrons created by cosmic muons interacting outside the detector, typically in the surrounding rocks. When the fast-neutrons enter the inner vessels, they loose their energy by collisions on proton of the medium. The recoil of these protons create then a signal in the liquid scintillator. Once the fast-neutrons are thermalized, they can be captured on a Gd nucleus. Therefore, proton recoils and neutron captures, physically related to each other, tend to mimic the antineutrino signal. The stopping muons component is created by muons entering the detector through its chimney and decaying within the inner volume. The muon energy lost by ionization mimics the prompt event and the Michel electron from the muon decay mimics the delayed event.

Although knowledge on this physics is far from being perfect, the energy spectrum of the recoil protons is expected to be roughly flat [30]. This background contribution was obtained in the first place by searching for neutrino candidates in a different prompt energy window, from 12.2 to 30 MeV, away from the prompt energy window for real neutrino candidates [12]. The number of selected events in this [12.2 ; 30] MeV window was therefore extrapolated down to the analysis window [0.7 ; 12.2] MeV, under the assumption of the flatness of this correlated background spectrum. The separation between the fast-neutrons and the stopping muons could be done by applying a time coincidence cut between the prompt event and the delayed one. This approach did not allow to obtain directly the spectral shape of the correlated background in the $\overline{\nu}_e$ energy region and relies on an assumption which, a priori, may not be true.

For the second publication, a different and more sophisticated approach has been followed. It is explained in great detail in [159]. The fast-neutrons and the stopping muons are studied separately. The main idea is to define a tagging technique to select a high purity sample of correlated background in the [0.7 ; 30] MeV energy region with a low contamination of $\overline{\nu}_e$ and accidental coincidences. The tagged sample is then used to infer the energy spectrum and define a shape model in agreement with it, without any prior assumption.

The fast-neutrons and the stopping muons background are first separated into two samples. For both backgrounds, the prompt energy is asked to be above 12.2 MeV. The $\Delta$T distribution between the selected prompt and delayed events shows two components, a fast one below 10 $\mu$s and a slower one above (Figure 6.43). While the faster component is understood to be due to the correlation between a stopping muon and the Michel electron following the muon decay, with a mean capture time linked to the muon lifetime of 2.2 $\mu$s, the slower component is understood to be caused by fast-neutrons captured on Gd, whose typical capture time is close to 30 $\mu$s.

When the fast-neutron enters the detector it is really likely to loose some energy within the inner veto (IV) [10]. Since the Double Chooz trigger system allows to record events in both inner detector (ID) and inner veto for an IV trigger, the fast-neutrons can be tagged using the IV information. Fast-neutrons are therefore tagged if an energy deposition in the inner detector occurs in coincidence with an IV event where two or more PMTs have been hit. A cut on the distance between prompt and delayed candidates, lower than 150 cm, is also applied in order to reduce accidental background contamination. Finally, to ensure the correlation between the neutrino candidate and the inner veto energy deposition, a cut is applied on the difference between the pulse start time in the IV and the ID. A linear fit of the IV-tagged spectrum, with

[10] A detector schematic is given in Figure 3.11.

the time and spatial cuts applied, shows that a first order polynomial model is favored with respect to a flat function. A total rate of fast-neutron is found to be 0.33 $\pm$ 0.16 $d^{-1}$.

Concerning the stopping muons, this background spectrum is well known and extends to 60 MeV. A pure sample is therefore obtained by doing the delayed energy search in [20 ; 60] MeV. However, an important contamination of high energy light-noise was found in this region. Such light-noise events show different features than the low energy light-noise events which contaminate the electron antineutrino selection (*cf.* Section 6.2.1). In order to suppress such events, since they show no correlation between selected prompt and delayed events, an offtime window method is applied. A linear fit with slope is used to fit the selected stopping muons background. A total rate of 0.62 $\pm$ 0.20 $d^{-1}$ is found. A combination of fast-neutron and stopping-muons gives 0.93 $\pm$ 0.26 $d^{-1}$. By applying the $^9$Li veto explained in Section 6.4 one finds a rate 0.69 $\pm$ 0.18 $d^{-1}$. The final shape and shape uncertainty are displayed in Figure 6.44.

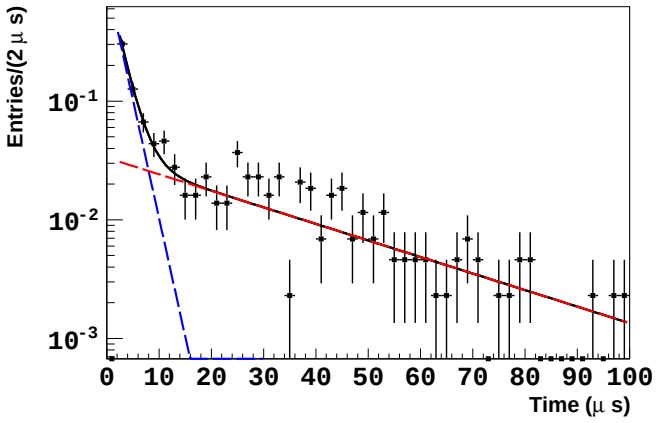


Figure 6.43: *$\Delta T$ distribution between prompt (in [12.2 ; 30] MeV) and delayed events [159]. The two exponential components are the stopping muons (blue) and the fast-neutrons (red).*

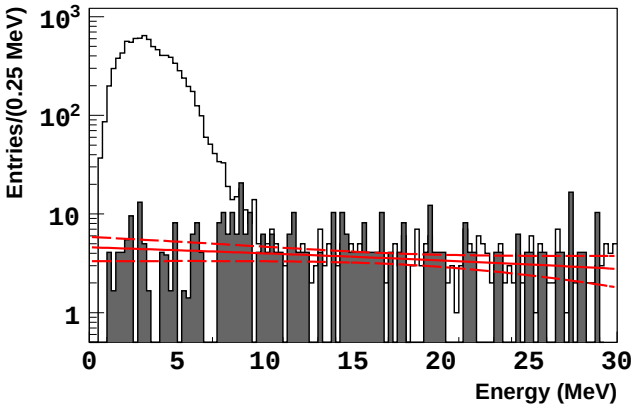


Figure 6.44: *Final shape (plain line) and shape uncertainty (dashed line) for the total stopping muon and fast-neutron correlated background [159]. White histogram is the prompt spectrum for $\overline{\nu}_e$ selection extended to high energy. Grey one is selected correlated background.*

### 6.3.3 Correlated background: cosmogenics $^9$Li and $^8$He

Cosmic muons interacting by spallation reactions with $^{12}$C atoms of the target liquid may lead to the creation of so-called cosmogenics isotopes, mostly $^9$Li and $^8$He. These elements generate an important correlated background for the Double Chooz experiment, different in the near and far detector [11]. A bad estimation, selection, or reduction of this cosmogenic background would be a serious issue for the experiment. I have therefore performed significant studies on these three key points during my thesis.

The $^9$Li isotopes $\beta$ decays into unstable excited states of $^8$Be or into a stable state of $^9$Be, and almost 51 % of the time along with a neutron emission. The $^8$Be almost instantly decays into two $\alpha$ particles (Figure 6.45). The endpoint of the $\beta^-$ decay spectrum is 13.6 MeV. Electrons and neutrons from $^9$Li may therefore mimic the characteristic $\overline{\nu}_e$ signals in the Double Chooz liquid scintillator. The corresponding energy spectrum and the time behavior of such decays are essentially undistinguishable from the electron antineutrino events [12]. The issue with this background is a relatively long half-life of the considered isotopes. With 46 Hz of muons in the detector, and a lifetime of 257 ms (and a half-life of 178 ms), it is impossible to veto the $^9$Li background, by using information of the inner veto or outer veto for instance. Indeed, a 1 s or even 600 ms veto after each muon would lead to a dramatic increase of the muon veto time, implying a huge loss of statistics. We will see however in Section 6.4 that reducing the lithium contamination with this veto method, that I studied during my thesis, can be interesting if done with caution [76, 77].

Concerning the $^8$Be, its endpoint is 10.7 MeV while its half-life is 119 ms. With only a branching ratio to $\beta$-neutron decays of 16 %, its contribution is less important than the $^9$Li one. Its production rate is also smaller according to KamLAND results [8]. Since it would be very tricky (because of the similar half-lives and spectra) and almost useless to try to distringuish between the two, no explicite separation of the $^9$Li and $^8$He contributions is done. In this section, the studies are therefore centered on the $^9$Li isotope. It is then more correct to stress that "$^9$Li background" actually refers from now on to both isotopes and even to other cosmogenic nuclei that may be created via spallation reactions on muons, but whose contributions are negligible.

#### $^9$Li background estimation using CHOOZ data

Before looking at the Double Chooz data, it is interesting to estimate the $^9$Li contamination in the Double Chooz far detector by using CHOOZ data. This is possible since the two experiments share the same site and therefore the same cosmic muon flux, but also use similar detector technologies. As explained in Sections 3.4 and 2.2.4, the CHOOZ experiment took advantage of a long both reactors shutdown period, allowing then a measurement of its total background. By fitting these data, one may estimate the $^9$Li contribution. Then, taking into account the difference in terms of target mass and volume, carbon content, and detection efficiency, the CHOOZ results can be scaled to the Double Chooz experiment. This is something I looked at

[11] The production rates of cosmogenics isotopes is highly related to the muon flux. Since the overburdens at both sites are different, the muon rate is expected to be different [31].

[12] Since the prompt energy spectrum of electron antineutrinos ends around 8 MeV (*cf.* Section 3.2.3), an excess of $^9$Li events should be particularly visible at high energy, up to the $^9$Li $\beta$ spectrum endpoint. This property is actually one of the reason the upper energy boundary for the inverse $\beta$ decay selection was chosen to be 12.2 MeV: the energy region between 8 and 12.2 MeV helps indeed to better constrain the total background shape in the final oscillation fit.

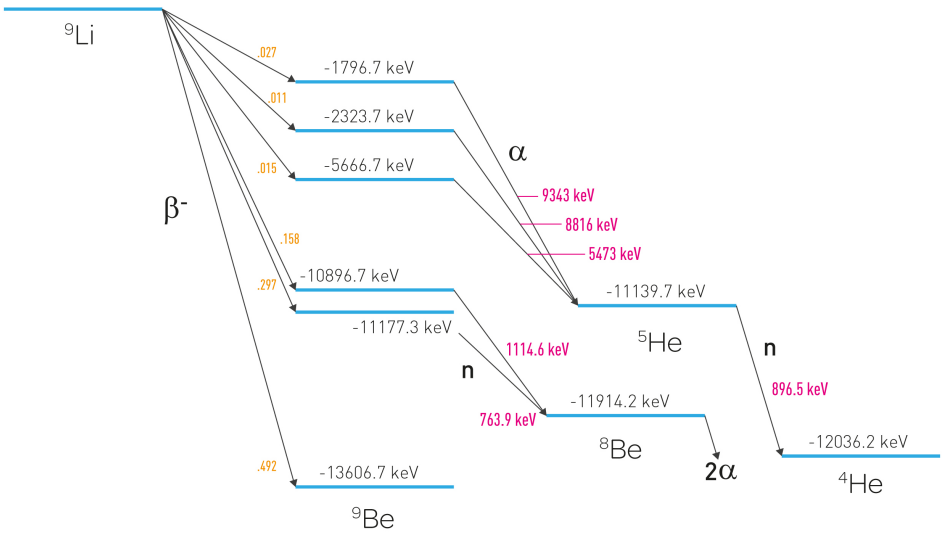


Figure 6.45: *$^9$Li decay scheme. 50.8 % of the times the $^9$Li nucleus decays into $\alpha$ particles, with $\beta^-$ and neutron emission, mimicking the characteristic antineutrino signal.*

at the beginning of my thesis [74, 73]. The CHOOZ data used in this study, with reactors ON or OFF, are taken from the last CHOOZ collaboration paper [30].

The scatter plot on Figure 6.46, obtained from CHOOZ data, represents the delayed event energy as a function of the prompt event energy, when "topological" cuts are applied. These cuts are explained in the CHOOZ paper. There are four of them: on the relative positron-neutron distance and time difference, on the neutron multiplicity, and on the distance from the $\nu$-target boundary [30]. Data were taken during a both reactors shutdown phase and therefore do not correspond to real electron antineutrino signal.

The Figure 6.47 shows two spectra of prompt signal, with reactors ON and with reactors OFF. The different shapes are explained by the fact that the one obtained with reactors OFF only corresponds to the total background of the experiment: the sum of the accidental and correlated backgrounds. The data taking period with both reactors OFF is 114.1 days; 211 neutrino candidates are selected, with the official CHOOZ cuts, *i.e.* the delayed event energy between 6 and 12 MeV and the event prompt one below 8 MeV.

In order to avoid a mixup between the correlated background that is studied and the accidental events, a cut is applied on the prompt event energy. Since the last line of the radioactivity spectrum in the detector is the $^{208}$Tl one at 2.614 MeV (*cf.* Section 6.3.1) and since CHOOZ energy resolution is about 7 % [30], a cut is set at 2.84 MeV, 2 $\sigma$ away from the thallium line mean value. Therefore the remaining energy range is fitted as cosmogenics isotopes and fast-neutrons backgrounds only. It is indeed fair to assume a really low accidental contamination beyond 2.84 MeV (*cf.* Figure 6.36). Indeed, the three energy bins between 1.2 and 2.4 MeV of the reactors OFF spectrum of Figure 6.47 are in good agreement with what is expected for accidental background.

The fast-neutrons contamination of the Double Chooz data is studied in Section 6.3.2. This background comes from recoil of protons exciting the scintillator. These are induced by collisions with fast-neutrons produced outside the detector by cosmic muons interacting on the rock sur-

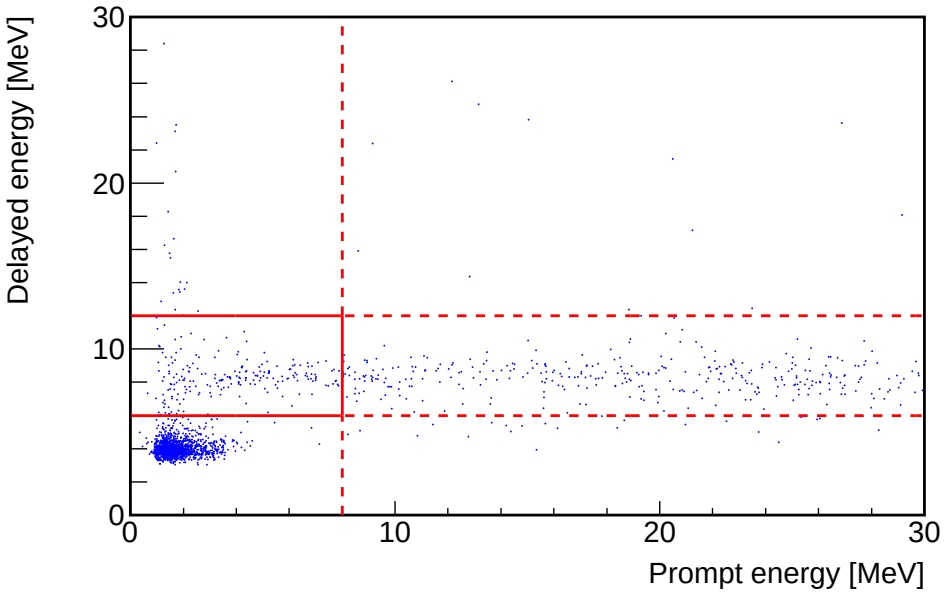


Figure 6.46: *Delayed event energy as a function of the prompt event energy for correlated events passing the "topological" cuts, from CHOOZ data with both reactors OFF [30]. Solid red lines determine the electron antineutrino candidates region. The horizontal band between the red dashed lines, with* $6 < E_{delayed} < 12$ *MeV, is expected to be fast-neutrons background only. The events in the blob at low energy are consistent with radioactivity events.*

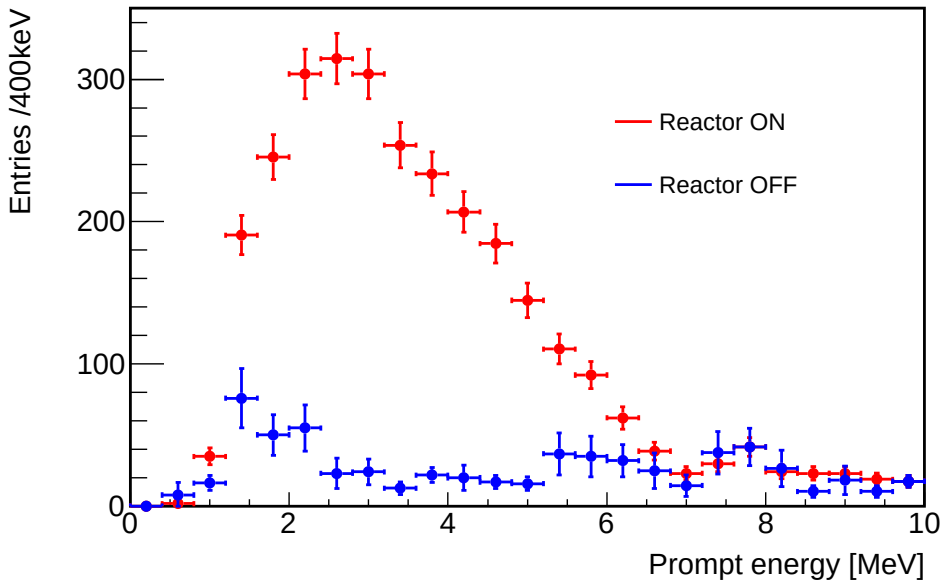


Figure 6.47: *Experimental prompt spectra in reactors ON (red) and both reactors OFF (blue) cases, from CHOOZ data [30]. Blue points are therefore background only.*

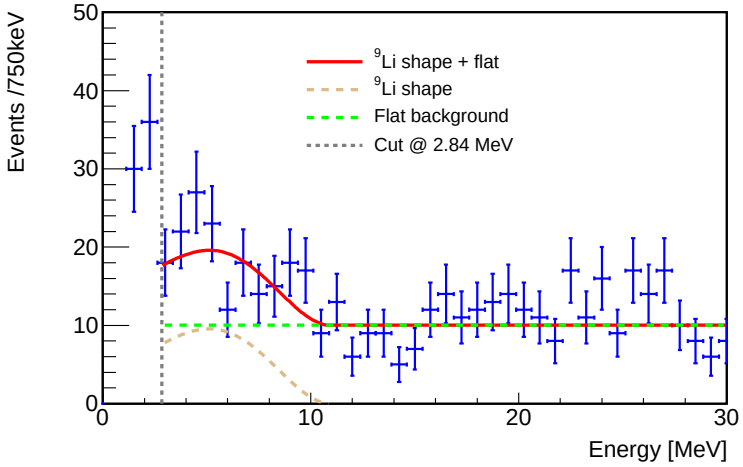


Figure 6.48: *CHOOZ background fitted with the $^9$Li shape from [131] plus a constant to account for the fast-neutrons. An energy threshold is set at 2.84 MeV to avoid accidentals contamination.*

rounding the detector. Although it is not completely understood, this background is expected to populate a rather flat spectrum for all the energy range. A flat component is then used to account for the fast-neutrons.

Regarding the $^9$Li spectrum, it corresponds to the positron energy of the isotope decay. It is then fitted by a $\beta^-$ decay spectrum. According to [167], the shape of such a spectrum is:

$$\frac{\mathrm{dn}_{(\mathrm{E_e})}}{\mathrm{dE_e}} = \mathcal{F}_{(\mathrm{Z,E_e})} \times \mathrm{E_e}(\mathrm{E_0}-\mathrm{E_e})^2 \times \sqrt{\mathrm{E_e^2}-\mathrm{m_e^2c^4}} \times \left(1-\frac{\mathrm{m_\nu^2 c^4}}{(\mathrm{E_0}-\mathrm{E_e})^2}\right)^{1/2}, \tag{6.3}$$

where $\mathrm{E_e}$ is the electron energy, $\mathrm{E_0}$ the maximum energy (the endpoint, here equal to 13.6 MeV), Z the charge of the nucleus, $\mathcal{F}_{(\mathrm{Z,E_e})}$ the Fermi function, or Coulomb correction factor, and $\mathrm{m_e}$ and $\mathrm{m}_\nu$ the respective masses of the electron and the electron antineutrino.

However, the $^9$Li spectrum finally used in the following CHOOZ data analysis is a description of the isotope decay as a two-body system, $^8$Li$^*$ + neutron, that allows to deduce the $\beta$ spectrum from nuclear data. In this case, the $^9$Li spectrum is fully constructed from known neutron spectra [131]. The spectrum shape obtained from the study presented in [131] is used in the following fits. It is called from now on $\mathcal{S}_{\mathrm{Li}}$ [13]. The corresponding shape is the light orange dashed line of Figure 6.48.

The fit is performed on the full prompt spectrum selected on reactor OFF-OFF data, up to 30 MeV, in order to strongly constrain the fast-neutron component, with a simple two parameters fit function $f = a \times \mathcal{S}_{\mathrm{Li}} + b$, where $a$ is a normalization parameter of the $^9$Li spectrum and $b$ the fast-neutrons flat parameter. The two fitted parameters $a$ and $b$ are highly anticorrelated: if the fast-neutrons background is estimated too high, the $^9$Li contribution is lowered, and vice versa. Concerning the upper energy boundary of 30 MeV, it gives an essential constraint on the flat component. Indeed, if the data are only fitted between 2.84 and 10 MeV, the results are inconclusive given that both correlated backgrounds cannot be disentangled in this range. However, the [10 ; 30] MeV energy range is expected to be recoil protons from fast-neutrons only.

[13] This spectrum is finally found to be consistent with the Monte Carlo $^9$Li spectrum used by the collaboration (red spectrum in Figure 6.58), which was not available when this CHOOZ data study was conducted.

Before performing the $^9$Li fit, it is fundamental to use an appropriate binning. Few events in some energy bins (typically less than 5) disturb the fitting procedure. They will then be given too much importance. The flat component may then be artificially low. Several criteria can be used to estimated the appropriate number of bins according to the data. The Sturges' formula allows to find the minimum number of bins $N_{bins}^{min}$ for an histogram without losing information, according to the number N of events it contains: $N_{bins}^{min} = \lfloor \log_2(N+1) \rfloor$ [176]. The number of energy bins is finally chosen to be 75, leading to a bin width of 400 keV between 0 and 30 MeV. In order not to lose too much information on the $^9$Li component itself, it was however important to consider enough energy bins below 10 MeV also.

From the fit presented in Figure 6.48 using the fit function $f = a \times \mathcal{S}_{Li} + b$, the rate of $^9$Li events estimated from CHOOZ data in the Double Chooz prompt energy range [0.7 ; 12.2] MeV, is 0.68 $\pm$ 0.14 d$^{-1}$. The $\chi^2$ per degrees of freedom $\chi^2$/NDF and the p-value are both fairly reasonable, at respectively 1.19 and 20 %. The fast-neutrons component is estimated to be 1.48 $\pm$ 0.09 d$^{-1}$ in the same energy range. This value is however not relevant for the Double Chooz experiment and will not be scaled to its geometry since its new design, with the buffer volume for instance, has been indeed thought to reduce the fast-neutrons background.

Finally, the "no $^9$Li background" hypothesis is also tested by fitting the both reactors OFF spectrum with a constant only, from 2.84 to 30 MeV. The goodness of the fit is bad according to its $\chi^2$/NDF and p-value, respectively 1.85 and 0.1 %. It may stress that the presence of $^9$Li is this data set cannot be excluded. Moreover, this assumption is backed up by the fact that the $^9$Li rate calculated above is not consistent with 0.

We can now extrapolate the $0.68 \pm 0.14$ d$^{-1}$ rate estimation to the Double Chooz experiment. If CHOOZ and Double Chooz were completely different, four effects would need to be taken into account: the different cosmic muon fluxes $\delta\phi_\mu^k$, the different number of target $^{12}$C atoms $\delta N_{^{12}C}^k$, the different detector volumes $\delta\mathcal{V}^k$, and finally the different detector efficiencies $\delta\epsilon_{det}^k$, where k is C for CHOOZ and DC for Double Chooz. The $^9$Li rate $R_{^9Li}^{DC}$ in the Double Chooz detector can be expressed as follows:

$$R_{^9Li}^{DC} = R_{^9Li}^{C} \times \frac{\phi_\mu^{DC}}{\phi_\mu^{C}} \times \frac{\mathcal{V}^{DC}}{\mathcal{V}^{C}} \times \frac{N_{^{12}C}^{DC}}{N_{^{12}C}^{C}} \times \frac{\epsilon_{det}^{DC}}{\epsilon_{det}^{C}}. \tag{6.4}$$

However, since CHOOZ and Double Chooz share the same location, the muon fluxes and the muon energy spectra are similar. The production rate of cosmogenics $^9$Li in both detectors would therefore differ because of the geometry, the composition, and the efficiency of detection.

The information concerning the CHOOZ liquids and geometry are available in their long last paper [30]. The CHOOZ $\nu$-target volume is 5.6 m$^3$ and its carbon mass proportion is 84.4 wt.%. Concerning the Double Chooz experiment, the $\nu$-target volume is 10.3 m$^3$ while the liquid carbon composition amounts for 86.3 % [16, 31]. The related correction factor is then 1.9.

Both $\epsilon_{det}^{DC}$ and $\epsilon_{det}^{C}$ factors are taken as total $\overline{\nu}_e$ detection efficiency. The CHOOZ paper gives a neutrino detection efficiency combined from all effects of 69.8 %. Concerning the Double Chooz experiment, an overall detection efficiency of 90.1 % is considered according to the estimatation performed in Section 6.2.4. This leads to an additional correction factor of 1.29.

The 0.68 $\pm$ 0.14 d$^{-1}$ rate estimation obtained from CHOOZ data finally is scaled according to equation (6.4). The cosmogenics $^9$Li events rate is therefor expected to be 1.66 $\pm$ 0.34 d$^{-1}$ in the Double Chooz detector.

### $^9$Li background estimation from Double Chooz data

Without extensive both reactors OFF data like the CHOOZ experiment, the $^9$Li events search in the Double Chooz data is tricky. The cosmogenics spectra are embedded within the $\overline{\nu}_e$ energy range which makes the $^9$Li events selection more complicated than the fast-neutrons. Indeed, it has been explained previously that the fast-neutron background can be estimated using an extended prompt energy range up to 30 MeV, for instance. Furthermore, the accidentals contribution is obtained from the offtime window method (*cf.* Sections 6.3.1 and 6.3.2).

The method used to extract the $^9$Li contamination is only statistical. The production of cosmogenic isotopes is expected to be caused by cosmic muons spallation on carbon nuclei. Therefore a study of the coincidences between the antineutrino candidates and the previous muons which deposited a large amount of energy in the detector is necessary. Indeed, the electron antineutrino candidates should be completely uncorrelated to muon events. The number of muons in time bin previous to an inverse $\beta$ decay candidate should therefore be constant.

A search for triple coincidences between a muon (with different energy prescriptions) and an electron antineutrino candidate is performed. The time difference $\Delta T_{\mu-p}$ between the muon and the prompt event is drawn (left panel of Figure 6.49). If the cosmogenics nuclei do contaminate the neutrino events selection, the shape of the $\Delta T_{\mu-p}$ distribution is expected to exponentially decrease with the $^9$Li 257 ms lifetime at low $\Delta T_{\mu-p}$. The left panel of Figure 6.49 shows the $\Delta T_{\mu-p}$ distribution between all the muons, *i.e.* all the inner detector energy depositions higher than 30 MeV, preceding all the selected antineutrino candidates in a 20 s time window. This distribution is consistent with a flat shape, which is in agreement with fortuitous coincidences. No excess whatsoever of correlated events is visible at low $\Delta T_{\mu-p}$. This can be explained by the high rate of low energy muons, which are not expected to produce $^9$Li isotopes as the probability of spallation goes up with the energy deposited by the muons. The $^9$Li contribution might then be smothered in the accidental $\mu$-neutrino candidate coincidences. The triple coincidences search is then conducted again by changing the prescription for the minimum muon energy. The Figure 6.52 and the right panel of Figure 6.49 both display the $\Delta T_{\mu-p}$ distribution between muons with $E_\mu > 600$ MeV and neutrino-like events, in two time windows. A clear exponential shaped excess at low $\Delta T_{\mu-p}$ is now visible. A fit to these data using a sum of a decreasing exponential and a constant can therefore be performed to estimate the $^9$Li contamination:

$$f(t) = \frac{N_{^9\mathrm{Li}}}{\tau} e^{-\frac{t}{\tau}} + K, \tag{6.5}$$

where $N_{^9\mathrm{Li}}$, $\tau$, and $K$ are the fitted parameters. $N_{^9\mathrm{Li}}$ is the number of $^9$Li events, $\tau$ is the $^9$Li lifetime which can be fixed at 257 ms prior to the fit, and $K$ is a constant term corresponding to the rate of fortuitous coincidences between electron antineutrino candidates and muons. This flat parameter can also be fixed, at a value coming from a previous fit of the flat part, before the number of $^9$Li events determination.

The number of $^9$Li events is therefore the number of entries in the area between the flat component and the decreasing exponential function. The flat parameter corresponds to the rate of muons above a certain energy threshold. For instance, the fit of the uncorrelated part of the $\Delta T_{\mu-p}$ (between 2 and 20 s) gives as expected roughly 13 Hz and 0.18 Hz for a minimum muon energy of 30 MeV and 600 MeV, respectively.

In order not to disturb the fit of the low $\Delta T_{\mu-p}$ region of the distribution, the uncorrelated part is first fitted using a flat function. The result of this first fit is then fed into the decreasing exponential fit performed to extract a $^9$Li estimation. The $\Delta T_{\mu-p}$ is fitted over a large range of 18 s to lower the error on the flat parameter. Results of a study on the relative uncertainty on

the flat parameter for two muon energy prescriptions can be found in both panels of Figure 6.50. It is shown that the uncertainty can be strongly reduced by increasing the fitting window: the first point corresponds to a fit between 2 and 4 s only whereas the last one shows the results of a fit between 2 and 20 s. This last option is therefore chosen.

The fitted characteristic time parameter of the exponential, which is actually expected to be the $^9$Li lifetime, can also be either fixed or left free to vary. If left free for a $\Delta T_{\mu-p}$ distribution with $E_\mu > 600$ MeV (Figure 6.52), the fit will find back a value of the $^9$Li lifetime quite close to the expected 257 ms and even in agreement within the error bars: $\tau = 215.69 \pm 41.40$ ms. The slight difference with respect to 257 ms has a marginal impact on the number of selected $^9$Li events. The fact that the lifetimes are found in good agreement is explained because of the high energy threshold applied to the muons: high energy muons are more likely to produce cosmogenics isotopes, thus the $\Delta T_{\mu-p}$ distribution is barely polluted by fortuitous $\mu$-$\overline{\nu}_e$ candidate coincidences. The fit of the time difference between muons with $E_\mu^{min} = 400$ MeV using a free decreasing exponential does not work so well and gives a lifetime compatible with 0 since the distribution is rather flat. However, fixing this parameter allows to estimate a number of $^9$Li events produced by muons with $E_\mu > 400$ MeV, even though the uncertainty on this measurement is very large (Figures 6.51 and 6.53).

By increasing the minimum muon energy, it is possible to determine more and more precisely the $^9$Li contamination. The results on the number of selected $^9$Li events from $\Delta T_{\mu-p}$ distributions fits, as a function of the minimum muon energy, are summarized in Figure 6.53. Two remarks can be made. First, the uncertainty on the fit is worsen when decreasing the muon energy threshold, because of the high rate of muons at low energy (Figure 6.55). Secondly, the number of selected $^9$Li events decreases when increasing the minimum muon energy, showing then a clear correlation between high energy muons and cosmogenic isotopes production. This idea is backed up in the Section 6.4 by looking at the neutron multiplicity following the muons.

Moreover, the same idea is displayed on the right panel of Figure 6.54. It corresponds to the number of selected $^9$Li events per muon energy bins (*i.e.* the number of selected events in the $i^{th}$ bin minus the number of events in the next bin). This plot shows that the production of $^9$Li seems to happen mostly for muons whose energies are higher than 550 MeV, while the uncertainty for bins up to 500 MeV is too high to say anything about these low energies. A production peak is visible around 650 MeV muons. The left panel of Figure 6.54 shows the relative uncertainty $\sigma_{N_{^9Li}}/N_{^9Li}$ on the measured number of $^9$Li events as a function of the minimum muon energy. The relative uncertainties are really large below 500 MeV, whereas they comprised between 15 and 35 % for $500 > E_\mu > 800$ MeV.

The official handling of the cosmogenics background makes also use of the output of a muon track reconstruction algorithm [14]. Indeed, created by a muon, a $^9$Li isotope is expected to decay close to the muon path. The addition of a distance cut with respect to the muon reconstructed track improves the selection. The number of random neutrino-like event and high energy deposition coincidences is then strongly reduced. In order to take into account the different $^9$Li rates found with different muon energy thresholds (Figure 6.53), the final $^9$Li rate is determined from separate estimations for three muon energy ranges combined together. The three ranges concern the so-called high energy muons, medium energy muons, and low energy muons [193]. The high energy muons correspond to energy depositions higher than 600 MeV and are likely to be caused by muons crossing the $\nu$-target. No spatial cut is necessary to extract the $^9$Li contribution as the excess of events in the $\Delta T_{\mu-p}$ distribution is easily fitted (Figure 6.52). The $\Delta T_{\mu-p}$ distribution is fitted with equation (6.5) and gives a rate of $0.95 \pm 0.11$ d$^{-1}$. The medium energy muons are

[14] The muon track reconstruction algorithm RecoMuHamID has been briefly presented in Section 4.4.

energy depositions between 275 and 600 MeV, and the $^9$Li is asked to be 80 cm away from the track at most. It allows to clean the selection from many muon-neutrino accidental coincidences. Because of the huge amount of muons with an energy between 275 and 600 MeV, the measured $^9$Li rate is still sizable. Indeed, $1.08 \pm 0.44$ d$^{-1}$ is found from the $\Delta T_{\mu-p}$ distribution fit. Finally, concerning the lower energy region, energy depositions between 30 and 275 MeV are considered. The same spatial cut is also applied. Fitting the resulting $\Delta T_{\mu-p}$ distribution seems to indicate that no cosmogenic isotopes are created by these muons. An upper limit of 0.3 d$^{-1}$ is used.

By combining the previous results, the overall rate of $^9$Li events is finally found to be $2.05^{+0.62}_{-0.52}$ d$^{-1}$. It can be compared to the $1.66 \pm 0.34$ d$^{-1}$ rate obtained by scaling the $^9$Li selection performed on CHOOZ data. Although the estimation from CHOOZ seems to slightly underestimate this background, the agreement is quite good within the error bars.

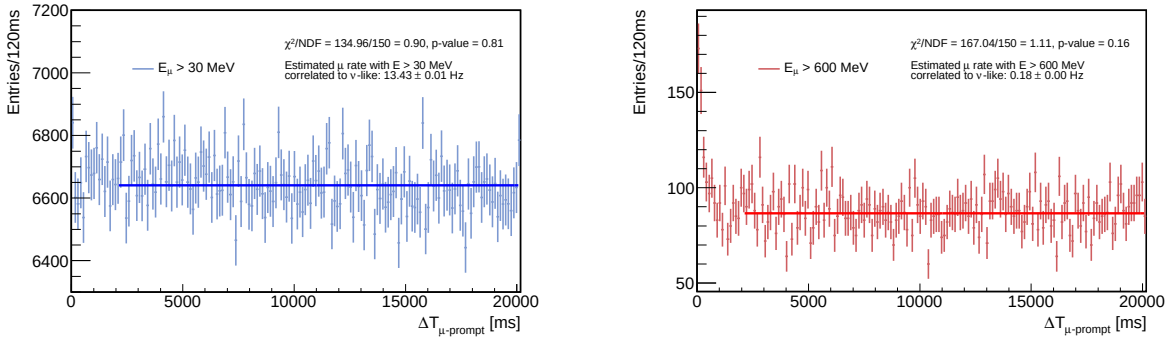


Figure 6.49: *$\Delta T_{\mu\text{-}p}$ distributions up to 20 s for $E_\mu^{min}$ = 30 MeV (left) and $E_\mu^{min}$ = 600 MeV (right). They are used to fit and fix the flat part of the $\Delta T$ distributions prior the $^9$Li fit. The flat parameters give the muon rates with $E_\mu^{min}$ at 30 MeV and 600 MeV.*

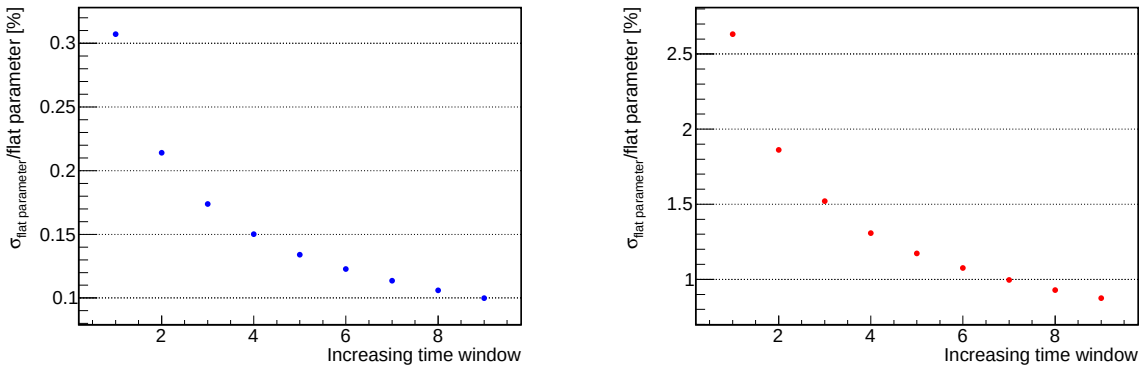


Figure 6.50: *Evolution of the relative uncertainty on the flat parameter while increasing the fit time window, for both $E_\mu^{min}$ = 30 MeV (left) and $E_\mu^{min}$ = 600 MeV (right). The time window width goes from 2 s (between 2 and 4 s) up to 18 s (between 2 and 20 s). This last value is used to fix the flat parameter of the $\Delta T_{\mu\text{-}p}$ $^9$Li.*

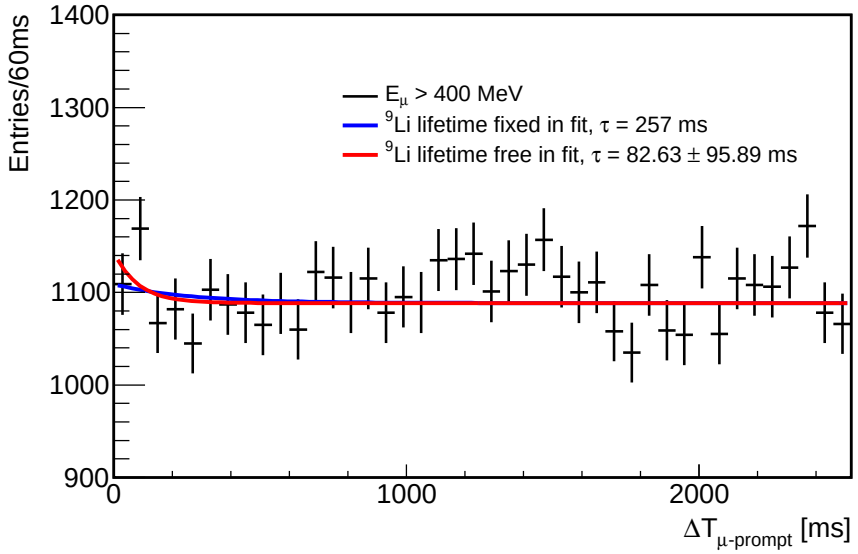


Figure 6.51: $\Delta T_{\mu\text{-}p}$ *distribution for* $E_{\mu}^{min} = 400$ *MeV. No excess at low* $\Delta T_{\mu\text{-}p}$ *is visible. Two fits are displayed: with the lifetime as a free fitted parameter or fixed at 257 ms.*

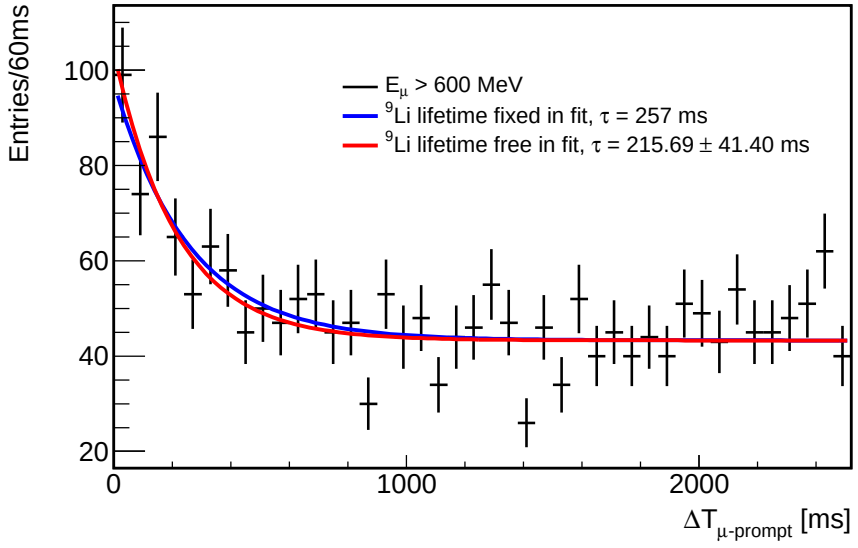


Figure 6.52: $\Delta T_{\mu\text{-}p}$ *distribution for* $E_{\mu}^{min} = 600$ *MeV. An excess is visible at low* $\Delta T_{\mu\text{-}p}$*. Two fits are displayed: with the half-life as a free fitted parameter or fixed at 257 ms.*

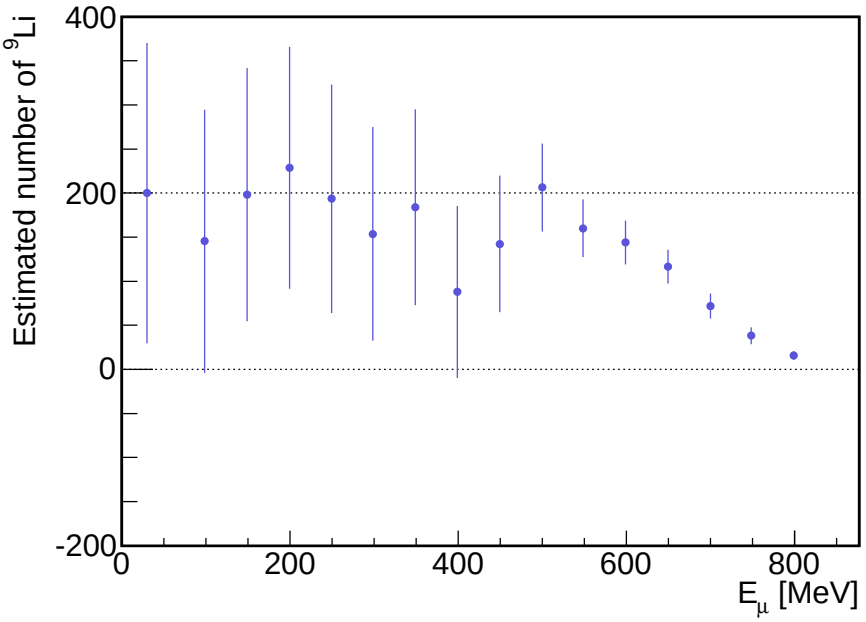


Figure 6.53: *Number of measured $^9$Li events obtained from fits of $\Delta T_{\mu\text{-}p}$ distributions as a function the minimum muon energy.*

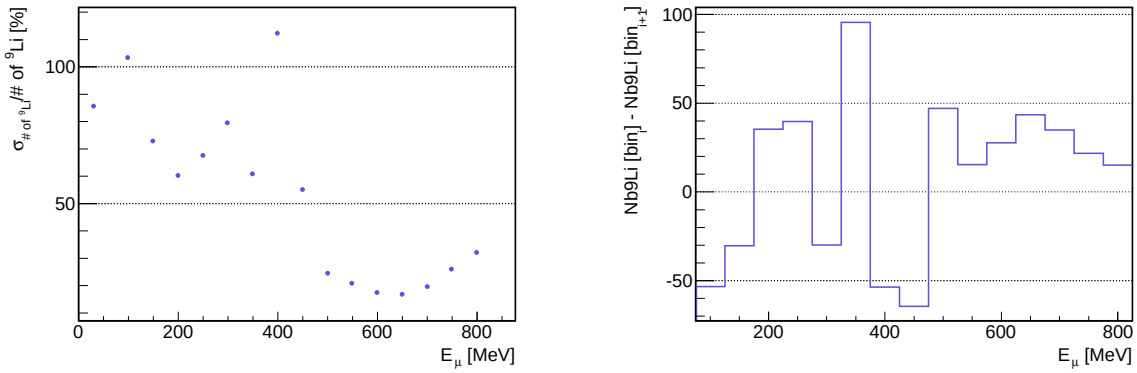


Figure 6.54: *(left) Relative uncertainty $\sigma_{N_{^9Li}}/N_{^9Li}$ on the measured number of $^9$Li events obtained from fits of $\Delta T_{\mu\text{-}p}$ distributions as a function of the minimum muon energy. (right) Contribution to $^9$Li production per muon energy bin.*

## 6.4 Lithium-free analysis

In the previous section, the contamination of cosmogenic events within the electron antineutrino selection has been studied. We found a rate of $2.05^{+0.62}_{-0.52}$ $^9$Li events per day. The so-called "Lithium-free analysis" presented hereafter aims at reducing the cosmogenics background.

The Figures 6.49, 6.51, and 6.52 show an energy dependance of the $^9$Li isotopes creation by cosmic muons, even though the recorded energy in the detector do not correspond to the true initial energy of the muons. The $^9$Li production is then associated with high energy muons or high energy depositions. Due to the dimensions of the Double Chooz detector, the average track length of muons is about 1.5 m in the $\nu$-target (from Double Chooz simulation studies) and the deposition energy goes up to 800 MeV (Figure 6.55).

The hypothesis that $^9$Li are mainly produced by high energy muons is backed up by looking at the neutron multiplicity following events recorded as muons. Indeed, the creation of $^9$Li isotopes by spallation reaction of a cosmic muon on a $^{12}$C atom is followed by three neutrons. Moreover, these high energy muons tend to really create a shower of particles in the detector when they deposit several hundreds of megaelectronvolts. They are indeed sometimes called showering muons. However, using this name implies a clear selection of this type of events, which is not possible in the Double Chooz detector. The appelation "high energy depositions", or just muons, is then prefered.

I selected neutron captures on gadolinium after high energy depositions in the inner volume with the analysis chain I developed. The neutrons follow the delayed events prescriptions presented in Section 6.2.2: not light-noise events (MQTQ $< 0.055$ and RMS($T_{start}$) $< 40$ ns), not muons ($Q^{IV}_{tot} < 10{,}000$ DUQ), and with an energy between 6 and 12 MeV. Once an energy deposition above 300 MeV is detected, the neutron captures on Gd are recorded in the following 10 ms. The neutron multiplicity as a function of the energy deposition higher than 300 MeV is available on the top panel of Figure 6.56. This plot shows that the higher the muon energy is, the more important the neutron multiplicity. However, the region around 400 MeV seems to show an important number of neutron captures. The issue is that the muon rate is not constant per energy bins. Indeed, according to Figure 6.55, the muon spectrum in the inner detector is peaked around 400-450 MeV and decreases from that value. The bottom panel of Figure 6.56 displays the neutron multiplicity per number of muons per energy bin, as a function of the deposited energy. This plot thus displays the correlation between high neutron multiplicity and high deposited energy. The high neutron multiplicity, and therefore the $^9$Li isotopes production, seem to be related to muons whose energies are above 550-600 MeV. This backs up what was already stated in the previous section using the results of the $\Delta T_{\mu-p}$ fits.

A new selection cut based on the neutron multiplicity immediately following high energy muons is then tested [77]. The Figure 6.57 displays the time difference $\Delta T_{\mu-p}$ between energy deposition higher than 600 MeV and electron antineutrino candidates. Three cases are shown: when no multiplicity cut is applied, when the neutron multiplicity following a muon in coincidence with an $\overline{\nu}_e$ candidate is strictly below 3, when the neutron multiplicity is less than 2. The excess of events at low $\Delta T_{\mu-p}$, correlated to high energy depositions, is strongly reduced. The measured number of $^9$Li events is also reduced, basically by a factor of 3 in the case of a neutron multiplicity strictly lower than 2.

Instead of suppressing the events with a high neutron multiplicity, the inverse can be done. In order to select a sample of $^9$Li events and compute their spectrum, the neutron multiplicity is asked to be stricly above 2. The Figure 6.58 displays this spectrum along with a simulated prompt $^9$Li spectrum. Even though this study was performed on a subset of the total run list of the second publication, these spectra show a fairly good agreement. The official prompt

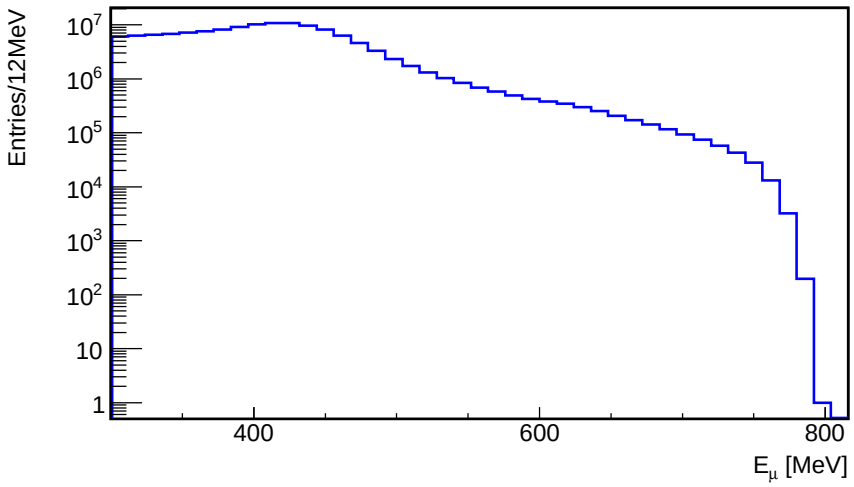


Figure 6.55: *Muon spectrum in the inner detector, with $E_\mu > 300$ MeV.*

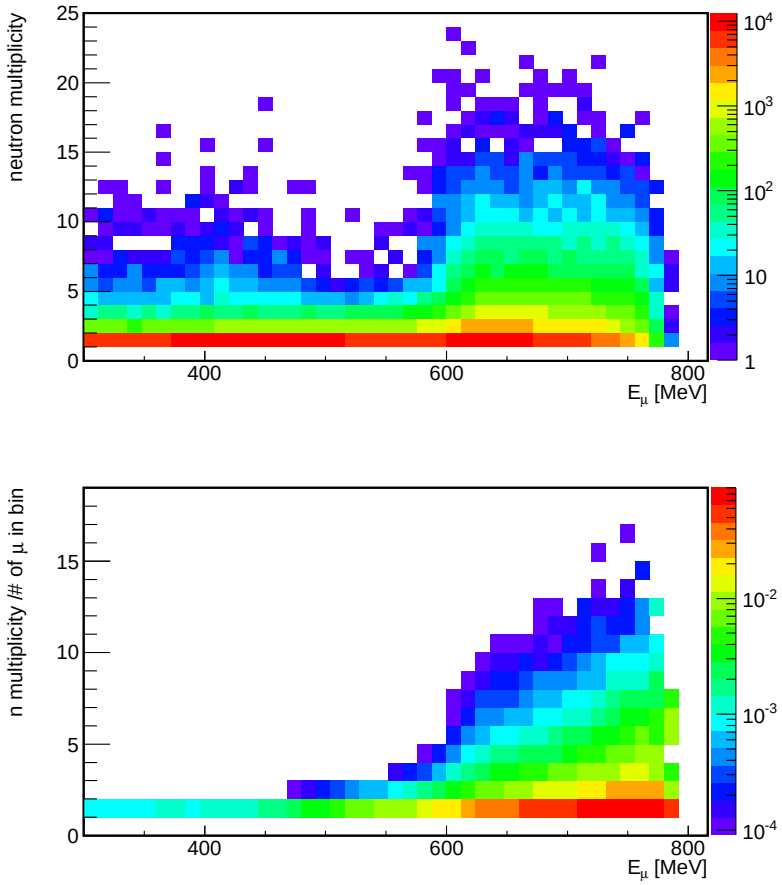


Figure 6.56: *(top) Neutron multiplicity as a function of the deposited energy in the inner detector. (bottom) Neutron multiplicity scaled to the number of $\mu$ per energy bin (cf. Figure 6.55).*

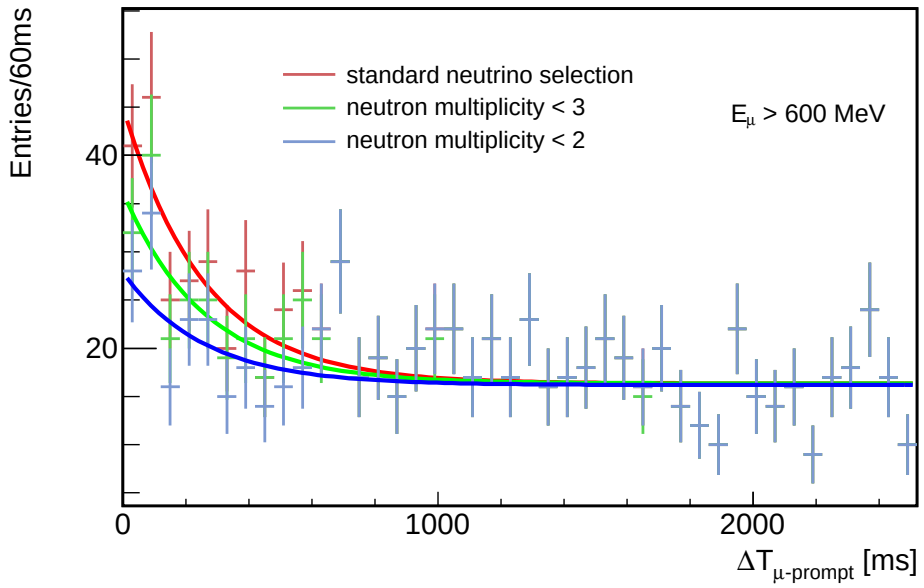


Figure 6.57: $\Delta T_{\mu\text{-}p}$ *distributions, for* $E_\mu > 600$ *MeV, with and without neutron multiplicity cut. This cut seems to suppress events correlated to high energy deposition.*

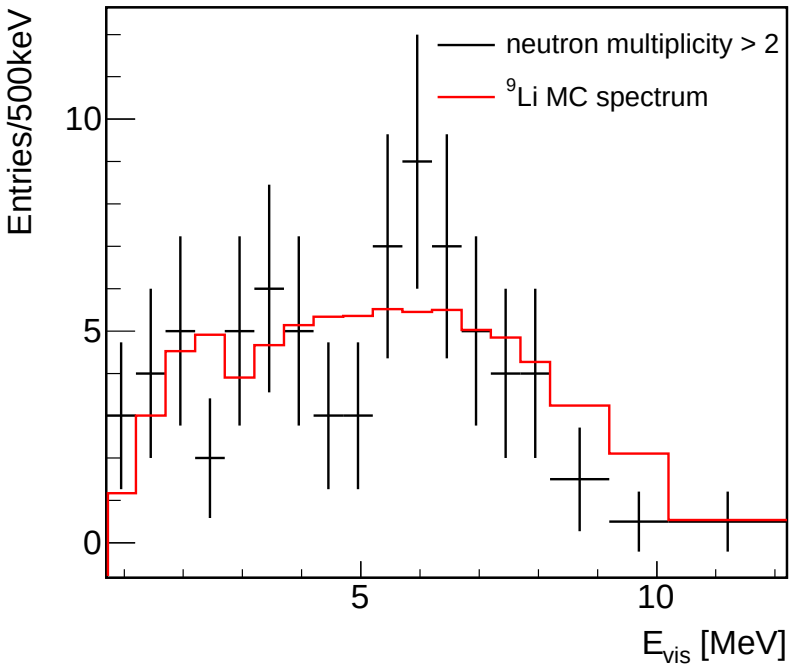


Figure 6.58: *Prompt spectrum subtracted using the neutron multiplicity cut* ($n < 2$). *The* $^9Li$ *Monte Carlo spectrum is drawn in red.*

$^9$Li spectrum used in the final fit (*cf.* Chapter 7) is finally obtained from a fit of the $\Delta T_{\mu-p}$ distribution, with $E_\mu > 620$ MeV and a distance between the muon and the electron antineutrino candidate lower than 0.7 m. The selection is even more cleaned by asking the prompt event and the delayed event to be at most 0.9 m apart. The contamination of accidental coincidences is then statistically subtracted.

The method followed by the Double Chooz collaboration to reduce the cosmogenics background is to apply a veto after some muons. I have been the first to present such analyses to collaborators [76, 77]. At that time, these studies were performed on the first publication run list and aimed at proposing a better estimation of the cosmogenics background for the second publication. The main idea was to improve the signal over noise ratio by reducing the most problematic background, but keeping the statistics as high as possible. Indeed, vetoing for several lifetimes after each muon would lead to an unacceptable large loss of statistics. For the first publication, 4,121 electron antineutrino candidates were found. This lead to a 1.55 % statistical error. The detector and reactor systematic uncertainties amounted for 2.1 % and 1.8 %, respectively. This meant that the Double Chooz experiment was not limited by statistics. An increase of the dead time due to the muon veto and a fewer electron antineutrino candidates were thus affordable, provided that the statistical error was kept below roughly 2 %.

I studied several configurations for a new high energy muons related cut. Vetos of 600 ms (more than $2\tau_{\mathrm{Li}}$) and 1000 ms (almost $4\tau_{\mathrm{Li}}$) after energy depositions between 400 and 700 MeV were considered. For instance, a 600 ms veto after 700 MeV muons would suppress 4.2 % of the electron antineutrino candidates and therefore increase the statistical error to 1.59 %, while a 600 ms veto after 400 MeV muons would increase dramatically the statistical error up to 5.78 %. Using a $\theta_{13}$ fitting package developed at Saclay [138], the remaining number of $^9$Li events was each time fitted following a pull term approach [15]. It consisted on fitting $\theta_{13}$ along with the remaining $^9$Li rate for different vetos. For the first publication, the $^9$Li rate was estimated to be $2.3 \pm 1.2$ d$^{-1}$. The pull term approach gave for instance a remaining $^9$Li rate of $0.90 \pm 0.44$ d$^{-1}$ for a 600 ms veto after 500 MeV muons and $1.14 \pm 0.42$ d$^{-1}$ for the same veto after 700 MeV. These number are in good agreement with estimations from $\Delta T_{\mu-p}$ fits. The Figure 6.59 displays the statistical error as a function of the minimum muon energy, for 600 ms veto.

For the second Double Chooz analysis, 9,021 electron antineutrino candidates are found. This implies a statistical uncertainty of roughly 1.05 %. Again, since the reactor systematic uncertainty still amounts for almost 1.8 %, this means that the Double Chooz experiment is not yet limited by statistics.

Vetoing all electron antineutrino candidates within 500 ms following a muon which deposited at least 600 MeV implies a reduction of the $^9$Li rate by more than a factor of two: $0.89 \pm 0.10$ events per day are removed from the data sample, while the $^9$Li estimation presented before is $2.05^{+0.62}_{-0.52}$ d$^{-1}$. The residual cosmogenic isotope background rate becomes therefore $1.25^{+0.59}_{-0.48}$ d$^{-1}$. This new cut rejects a little more than 5 % of the $\overline{\nu}_e$ candidates. The candidate selection amounts now for 8,347. It implies a statistical error of 1.09 %.

The $^9$Li background could even further be reduced, by lowering the minimum muon energy or by increasing the veto time window. Indeed, the 500 ms veto is expected not to suppress all the cosmogenic isotopes created by muons, since the $^9$Li lifetime is 257 ms. A 600 ms veto after 400 MeV energy deposition along with a distance cut candidate to muon track $d < 800$ mm if $E_\mu < 550$ MeV, would imply a loss of half the statistics, which is unacceptable. A compromise has to be found. The idea was to maximize the reduction of the cosmogenics background while assuring at the same time that the corresponding loss in neutrino statistics was low, *i.e.* of the order of 5 %.

[15] The oscillation fit is presented in Chapter 7, along with the pull term method.

The regular analysis performed on 251.27 days implies a live time of 240.17 days because of more than 11 days of muon veto (1 ms veto after all muons). This new analysis adds 12 days to the muon veto time and corresponds therefore to a live time of 228.25 days. An extra background reduction cut was also added to the official Double Chooz second analysis: the electron antineutrino candidates are asked not to be in coincidence with an outer veto trigger [16]. This provides a further reduction of backgrounds related to muons. The accidental coincidences are also reduced.

The final electron antineutrino candidates sample amounts for 8,249, selected over a run time of 251.27 days and live time of 227.93 days.

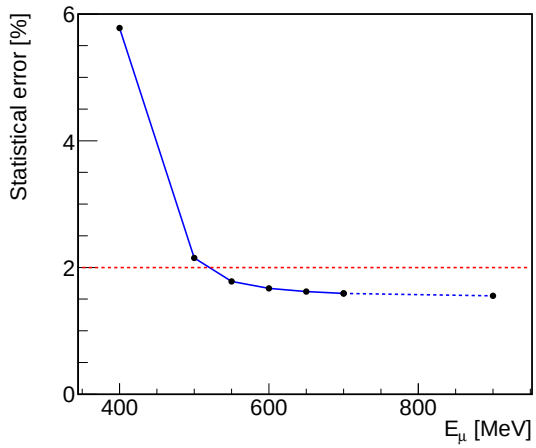


Figure 6.59: *Statistical error for the first Double Chooz analysis (4,121 candidates) as a function of the minimum muon energy, for 600 ms veto. The red line represents a 2 % statistical error. The last point, here shown at 900 MeV, actually corresponds to no veto [76, 77].*

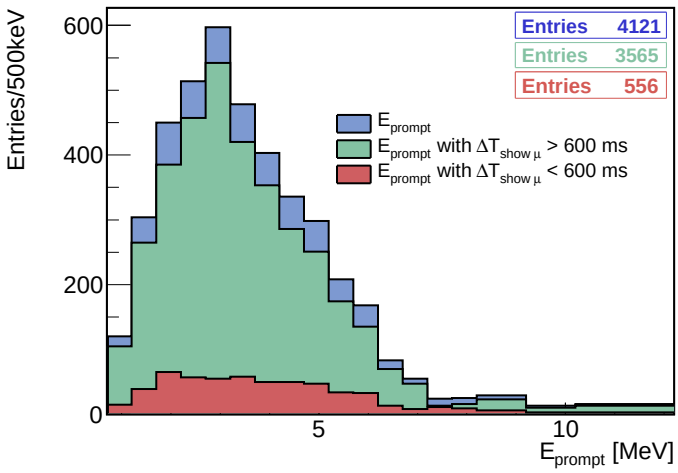


Figure 6.60: *Prompt event spectrum from $\overline{\nu}_e$ candidates selection of the first publication run list: standard selection (blue), selection when a 600 ms veto after 600 MeV muons is applied (green), and rejected events by the veto (red) [76, 77].*

[16] See Figure 3.11 for a detector scheme and Section 3.5.2 for a brief description of the outer veto.

## 6.5 Both reactors OFF and background subtraction

This section presents an analysis performed on both reactors OFF data, called in the following paragraphs reactor OFF-OFF. This kind of data, although unlikely to happen, is truly a godsend for the Double Chooz physicists. Indeed, background estimation, and especially $^9$Li one, provides one of the dominant systematic error for the Double Chooz result [12]. By shutting down the source of electron antineutrinos, one can study the experiment total background in great detail. The previous CHOOZ experiment could benefit from the stop of both Chooz B reactors for a long period and could therefore strongly constrain the sum of theirs backgrounds to the measured value in OFF-OFF data [30].

The neutrino candidates selection performed on one day of reactors shutdown, which happened in the middle of the Double Chooz second publication run list, and on seven additional days which are not part of this run list, is presented. A simple method to subtract correlated backgrounds using the information taken from this selection is also introduced. I did these studies with the Saclay group when only one day of both reactors OFF data was available [70, 75].

### 6.5.1 Reactor OFF-OFF data

From September 2011, the Chooz B nuclear power station was subjected to the maintenance and refueling of the reactor B1, thus leading to several weeks with one reactor (*cf.* Section 6.1). On Saturday, 22$^{\text{nd}}$ October 2011, at 3:00 a.m., the second reactor was stopped for servicing. The nuclear core started ramping up on Sunday the 23$^{\text{rd}}$ at 4:30 a.m. (Figure 6.61). The estimated OFF-OFF period is about 24 hours.

During the refueling of reactor B2, which began on Wednesday, 15$^{\text{th}}$ February 2012, a technical issue was found on one of the four pumps of the primary circuits, leading to the impossibility to restart normally this reactor during the summer. One additional week of both reactors OFF data could therefore be recorded by the Double Chooz far detector, from Sunday, 27$^{\text{th}}$ May 2012 to Monday, 4$^{\text{th}}$ June 2012.

### 6.5.2 Expected neutrino spectrum at residual power

In order to stop a nuclear reactor, neutron absorbers are introduced into the core: either rods are inserted in the assemblies or boron concentration in the water of the primary circuit is increased [17]. When enough absorber is present to capture all emitted neutrons, the reactor is stopped and no fission occurs anymore in the core. However, a residual antineutrino flux is still emitted from $\beta$ decays of fission products. This effect has to be evaluated for a short reactor OFF-OFF period, and especially if this period is contiguous to a full power operation period.

The time evolution of the residual neutrino spectrum is estimated using the FISPACT code [58, 88]. FISPACT is a nuclear core evolution code predicting the inventory of nuclei after irradiating material in a neutron flux. The complete history of the Chooz cores has been roughly simulated over the previous three cycles to take into account the refueling of one third of the core at the end of each cycle. This provides an estimate of the core composition just

[17] For a brief overview of a Pressurized Water Reactor see Section 3.2.1. For a more detailed explanation of a PWR functioning see [188].

| Time skipped | Expected $N_{\nu,resid}$ | $E_{threshold}$ at $N_{\nu,resid} < 0.1$ [MeV] |
|---|---|---|
| 0h | 1.03 | 5.25 |
| 1h | 0.42 | 3.375 |
| 2h | 0.33 | 3 |
| 3h | 0.29 | 2.875 |
| 4h | 0.27 | 2.875 |
| 5h | 0.24 | 2.75 |
| 6h | 0.22 | 2.75 |

Table 6.2: *Number of expected $\overline{\nu}_e$ according to the time skipped after the power shutdown (Figure 6.61). The energy threshold above which less than 0.1 neutrino event is expected during the considered time period is also showed [70, 75].*

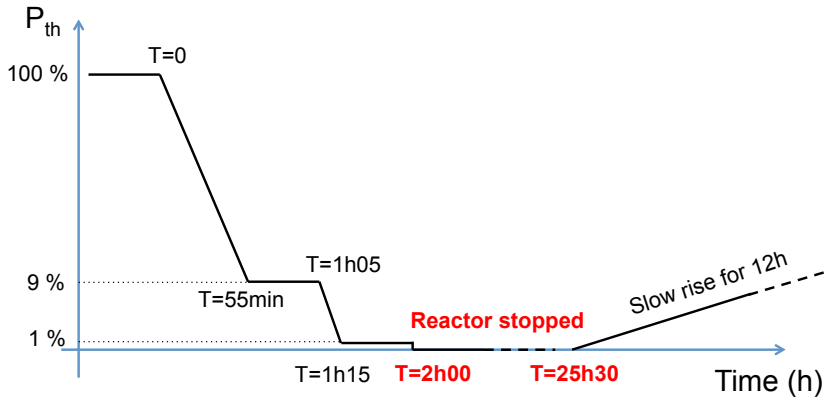


Figure 6.61: *Strip chart of the reactor power during reactor stop measurement for the first one day of OFF-OFF data [70, 75].*

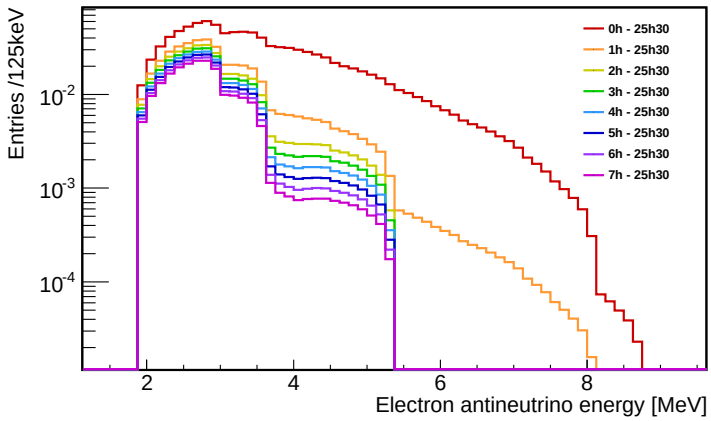


Figure 6.62: *Expected detected electron antineutrino spectra from FISPACT code, for different analysis time window [70, 75]. The spectra all begin at 1.8 MeV, the detection threshold for an inverse $\beta$ decay in the Double Chooz detector (cf. Section 3.3.1).*

before the reactor stops. The correct normalization of the detected neutrino flux at this time is forced to match the Double Chooz expectation at full power. Then the relative deviation of the detected neutrino spectrum with respect to this reference is computed following the power history of the reactor stop with five minutes steps. For each time step, FISPACT predicts how many $\beta$ decays of a given fission product occurred and the corresponding neutrino spectrum is computed using the BESTIOLE database [18]. The Figure 6.61 shows the power profile of the first one day reactor stop.

The Figure 6.62 illustrates the exponential decrease of the detected antineutrino spectrum after the reactor stop and its concomitant shrinking to the low energy region. Since the expected correlated background during one day of OFF-OFF is of the order of few events, waiting few hours after the reactor stop allows to get rid of most of the residual neutrinos, with no significant contribution above a certain energy threshold. The Table 6.2 gives the number of expected $\overline{\nu}_e$ according to the time skipped after the power shutdown. The energy threshold above which less than 0.1 neutrino event is expected during the considered time period is also showed. From the numbers in this table, starting our background measurement for the one day of OFF-OFF two hours after the shutdown seems to be a good compromise between reduction of the systematic error associated to the residual neutrinos and small statistical loss of background measurement. The expected $\overline{\nu}_e$ event amounts therefore for 0.33 events.

Concerning the second period of OFF-OFF data, the same method is applied. The FISPACT code is run again and 1.49 $\overline{\nu}_e$ events are expected during this one week period. During the total both reactors OFF period, 1.82 electron antineutrino events are expected for a total run time of 7.53 days.

### 6.5.3 Electron antineutrino candidates in reactor OFF-OFF data

The official electron antineutrino candidates selection is first performed on the one day of reactor OFF-OFF data, and then on the week recently acquired. I was the first to perform a OFF-OFF selection and a background subtraction using one day of both reactors OFF [70]. The results showed below are obtained by applying the selection cuts presented in Section 6.2 using the analysis software I developed.

#### One day of reactor OFF-OFF

Three electron antineutrino candidates are selected on the first 24 hours of both reactors OFF. Another candidate is found when extending the prompt energy upper boundary to 30 MeV. The time difference $\Delta$T distribution is displayed on the left panel of Figure 6.64, while the tridimensional distance between the prompt vertex and the delayed vertex $\Delta$R is drawn on the right panel. The vertices position are displayed on both panels of the Figure 6.63. Two visualizations are proposed: in the (X,Y) plane and in the ($\rho^2$,Z) plane. The prompt events and the delayed events are on the same canvas, in different colors. A dashed line links each couple and the distance in millimeters between the two events is written close to the prompt vertex.

The event found when extending the prompt energy range is consistent with a stopping-muon event. Indeed, the prompt event is in coincidence with an outer veto trigger. Furthermore, the

[18] The BESTIOLE database is a build up database of roughly 800 nuclei and 10,000 $\beta$ branches [144]. It was created by the Saclay group, for the new reactor electron antineutrino spectrum determination presented in Section 3.2.3.

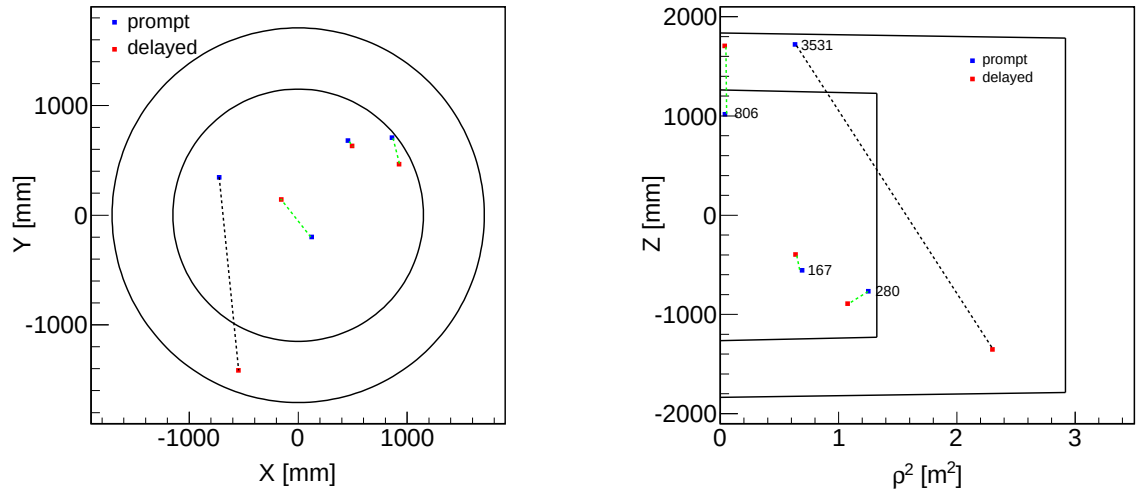


Figure 6.63: *$\overline{\nu}_e$ candidates vertex distributions selected on the first period with both reactors OFF (one day), in the (X,Y) plane (left), and in the ($\rho^2$,Z) plane (right). Solid black lines correspond to the $\nu$-target and the $\gamma$-catcher walls. Both prompt event (blue) and delayed event (red) are drawn. Each couple is linked by a dashed line, which is green if the events are less than 1 m apart. The distance between the prompt and the delayed event is displayed, close to the prompt vertex, in millimeters.*

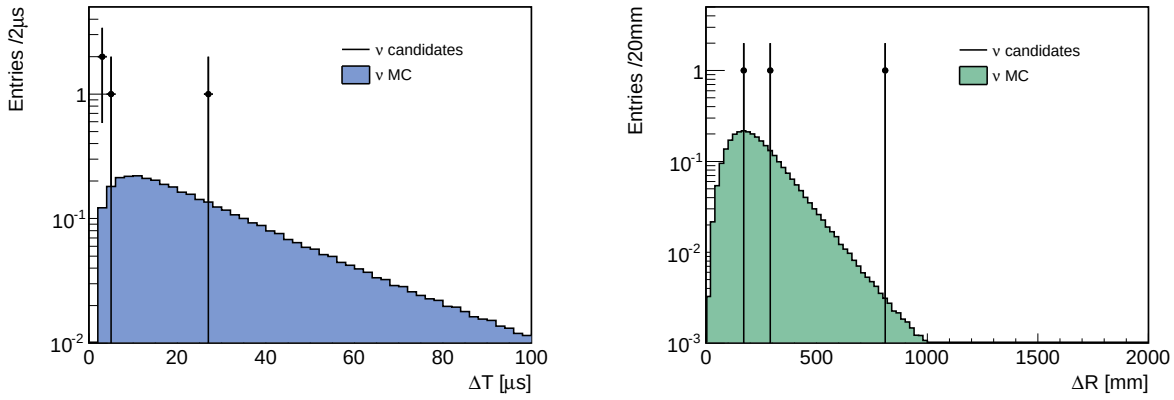


Figure 6.64: *For the first day of OFF-OFF data. (left) Time difference distribution between the delayed events and the prompt events, in $\mu$s. (right) Tridimensional distance distribution between the delayed event and the prompt event vertices, in mm. The $\overline{\nu}_e$ Monte Carlo is also drawn.*

time difference between the prompt event and the delayed event is 2.16 µs, when the muon lifetime is 2.2 µs. This event is moreover not in coincidence with a high energy deposition, since the previous one is recorded several seconds before, and therefore seems to not be a $^9$Li event.

Another event can be understood as an accidental coincidence. Indeed, the prompt and the delayed are several meters from each other. This pair corresponds to the two vertices linked by the black dashed line on Figure 6.63. Given the time correlation between them (around 2 µs), they seem to be fortuitous coincidences. Moreover, the prompt energy is found to be 0.75 MeV, which is a propable value for a radioactivity $\gamma$ (*cf.* Figure 6.36 and Section 6.3.1).

The last two events are consistent with cosmogenic events. Indeed, their prompt energy are 4.8 MeV and 9.4 MeV and their $\Delta$T reasonable for a neutron capture on gadolinium. The vertices are moreover located within the $\nu$-target. One of these two events is even rejected when is applied the $^9$Li veto of 600 ms after 600 MeV energy depositions presented in the previous section.

A standard analysis on the one day of reactor OFF-OFF data provides therefore a total background rate of $3.38 \pm 1.95$ d$^{-1}$. This rate is reduced by applying the $^9$Li veto and becomes $2.37 \pm 1.67$ d$^{-1}$.

**All reactor OFF-OFF data**

A further selection of electron antineutrino candidates can be performed on the additional one week of reactor OFF-OFF data. If the first day is also used, the total run time amounts for 7.53 days, in which 21 candidates are selected. This data set correponds finally to a total live time of 6.83 days once the muon veto dead time taken into account.

Both prompt events and delayed events spectra are showed on Figures 6.69 and 6.70, respectively. The vertices distributions in the (X,Y) and the ($\rho^2$,Z) planes are available in Figure 6.65. Nine events are located above the chimney and could be stopping-muons. Ten other events are mostly found in the the $\nu$-target volume, while two others are situated in the $\gamma$-catcher. The time difference and tridimensional distance distributions are displayed in both panels of Figures 6.66. One event with $\Delta$R = 3.5 m is not visible on the $\Delta$R distribution. The $\Delta$T distribution seems to show two kind of populations: one at low $\Delta$T before 10 µs and another after. This was used in Section 6.3.2 for the fast-neutron background and stopping muon background separation.

Among the 21 candidates, 5 are removed by the 600 ms $^9$Li veto applied after each 600 MeV energy depositions. The events rejected by this cut are evenly spread within the $\nu$-target.

The outer veto coincidence cut allows to reject 8 other events. They all present a $\Delta$T value below 10 µs and are therefore consistent with stopping muon events. An exponential fit to the $\Delta$T distribution before 10 µs can be performed. It gives a characteristic time parameter of $1.96 \pm 0.86$ µs, with a fairly good p-value at 57 %. This fitted value is in agreement with the expected 2.2 µs from the muon lifetime, even though the error bars are large and the statistics really low. All the events rejected by the outer veto coincidence cut are located under the chimney, backing up even more the assumption that these events are mostly stopping muons.

Finally, only 8 events remain in the total reactor OFF-OFF data selection. The total background rate is found to be $1.2 \pm 0.4$ d$^{-1}$. From selection on physics data, presented in Section 6.3, $2.0 \pm 0.6$ d$^{-1}$ was estimated. If neither the $^9$Li veto nor the outer veto tagging are used, the total measured background rate on OFF-OFF data is $2.9 \pm 0.6$ d$^{-1}$, while it is $3.4 \pm 0.6$ d$^{-1}$ from selection on regular data. A slight tension between these two results is therefore visible. However, it disappears if the outer veto cut is the only one not applied: $2.3 \pm 0.6$ d$^{-1}$ on OFF-OFF data and $2.4 \pm 0.6$ d$^{-1}$ from regular background selections. The background reduction by the outer veto cut on the OFF-OFF selection is three times higher than on regular data.

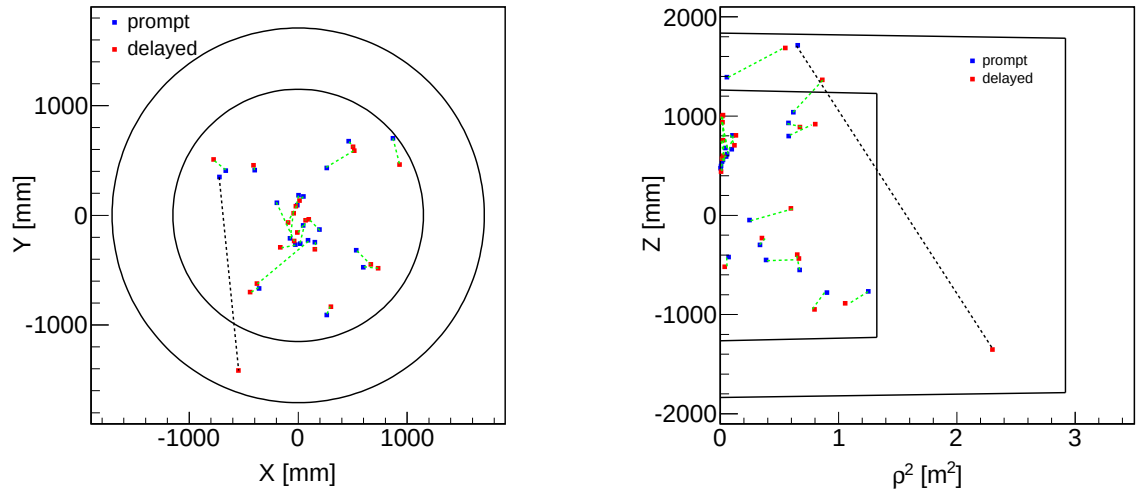


Figure 6.65: *$\overline{\nu}_e$ candidates vertex distributions selected on all both reactors OFF periods (7.53 days), in the (X,Y) plane (left), and in the ($\rho^2$,Z) plane (right). Solid black lines correspond to the $\nu$-target and the $\gamma$-catcher walls. Both prompt event (blue) and delayed event (red) are drawn. Each couple is linked by a dashed line, which is green if the events are less than 1 m apart.*

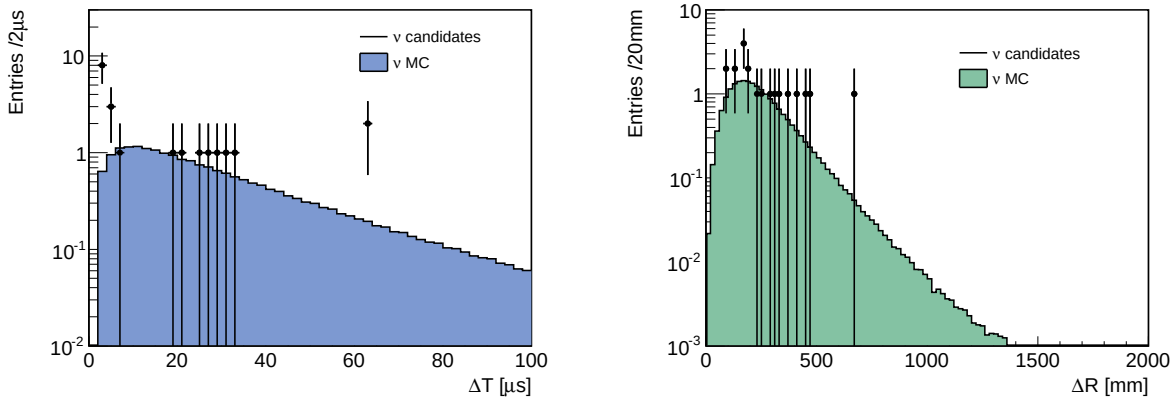


Figure 6.66: *For all the reactor OFF-OFF data (7.53 days). (left) Time difference distribution between the delayed events and the prompt events, in $\mu$s. (right) Tridimensional distance distribution between the delayed event and the prompt event vertices, in mm. The $\overline{\nu}_e$ Monte Carlo is also drawn.*

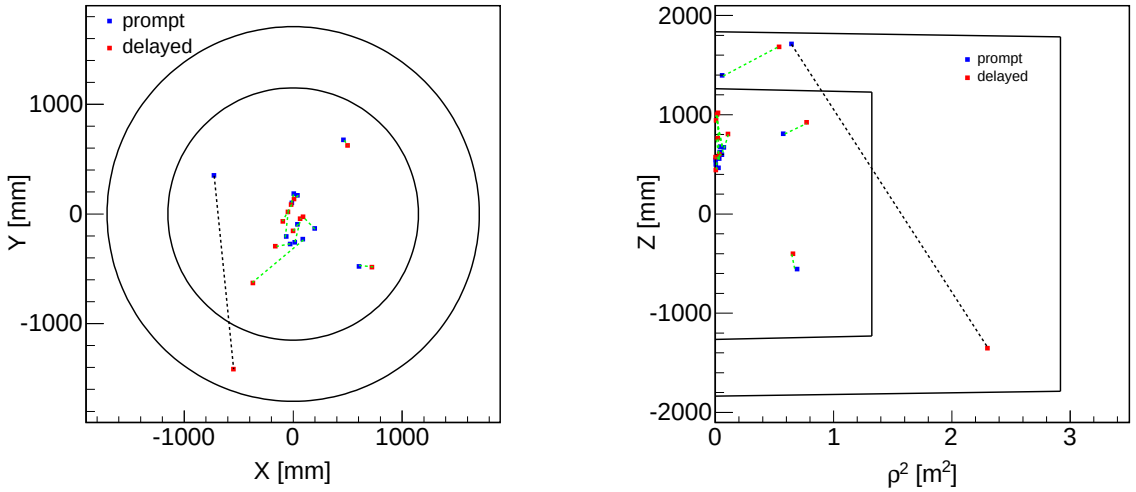


Figure 6.67: *$\overline{\nu}_e$ candidates vertex distributions selected on all both reactors OFF periods (7.53 days), for $\Delta T < 10\ \mu s$, in the (X,Y) plane (left), and in the ($\rho^2$,Z) plane (right). Solid black lines correspond to the $\nu$-target and the $\gamma$-catcher walls. Both prompt event (blue) and delayed event (red) are drawn. Each couple is linked by a dashed line, which is green if the events are less than 1 m apart.*

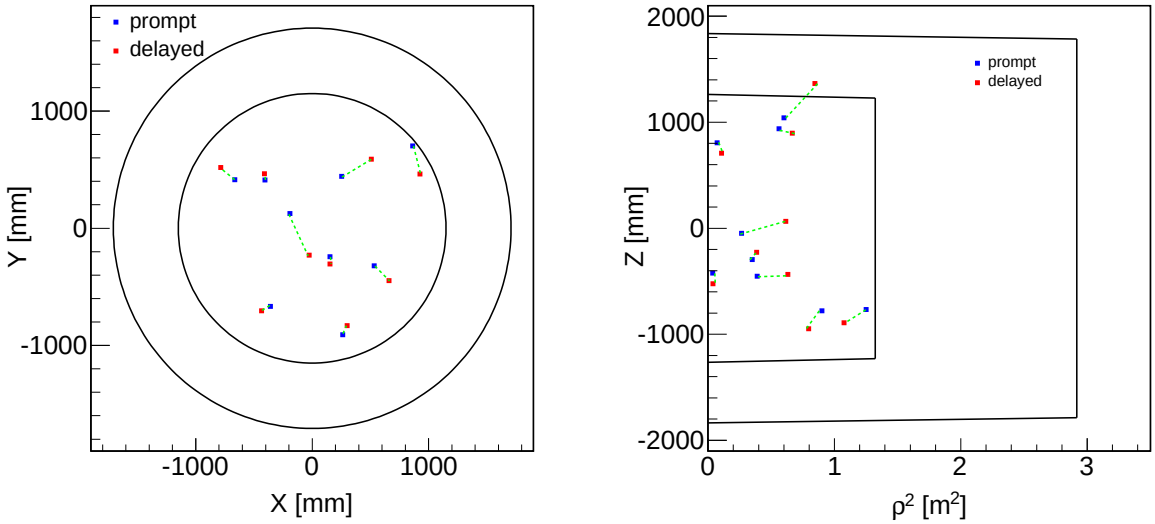


Figure 6.68: *$\overline{\nu}_e$ candidates vertex distributions selected on all both reactors OFF periods (7.53 days), for $\Delta T > 10\ \mu s$, in the (X,Y) plane (left), and in the ($\rho^2$,Z) plane (right). Solid black lines correspond to the $\nu$-target and the $\gamma$-catcher walls. Both prompt event (blue) and delayed event (red) are drawn. Each couple is linked by a dashed line, which is green if the events are less than 1 m apart.*

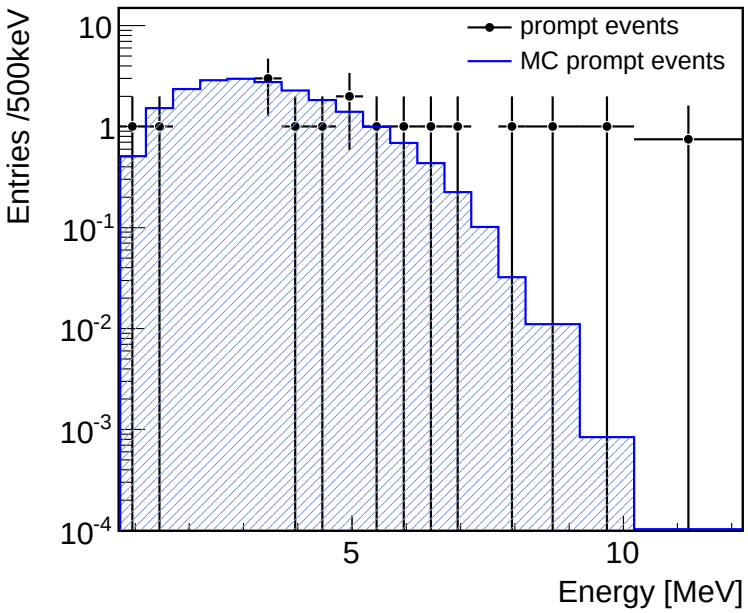


Figure 6.69: *Prompt spectra of both background selection on the whole reactor OFF-OFF data (black points) and $\overline{\nu}_e$ Monte Carlo simulation (solid blue line). The $^9$Li veto and the outer veto cut are not applied.*

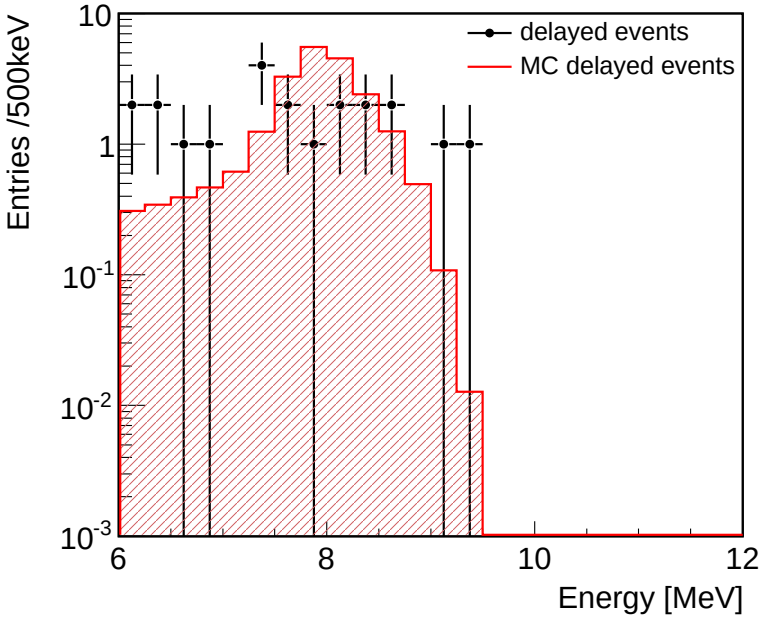


Figure 6.70: *Delayed spectra of both background selection on the whole reactor OFF-OFF data (black points) and $\overline{\nu}_e$ Monte Carlo simulation (solid red line). The $^9$Li veto and the outer veto cut are not applied.*

### 6.5.4 Background subtraction principles: rate only

In this section a background subtraction method is presented. It has been developed for the first day of OFF-OFF data by the Saclay group and myself [70, 75]. Part of the results presented above were obtained for the first Double Chooz analysis, where 4,121 antineutrino candidates were found on 102 days of data. They give an indication to what can be expected for the second publication analysis. First, a rate only analysis is performed, where the antineutrino signal over the whole energy spectrum is integrated.

#### Subtraction uncertainty

First, the gross signal measured during the reactor ON data taking period ($\mathrm{T_{on}}$) is considered. It consists in $\mathrm{N_{on}} = \mathcal{S} + \mathcal{B}_{\mathrm{on}}$ events, where $\mathcal{S}$ is the neutrino signal and $\mathcal{B}_{\mathrm{on}}$ the background signal during the reactor ON period. This background is assumed to be both accidental and correlated backgrounds.

During a reactor OFF-OFF period of duration $\mathrm{T_{off}}$, the total experiment background is measured. In this case, $\mathrm{N_{off}} = \mathcal{B}_{\mathrm{off}}$ events are selected. The question of the subtraction of the backgrounds to the number of selected events during the reactor ON period, based on the measurement made during the OFF-OFF period, is now addressed. The net signal can be expressed as:

$$\mathcal{S} \;=\; \mathrm{N_{on}} - \frac{\mathrm{T_{on}}}{\mathrm{T_{off}}} \times \mathrm{N_{off}} \;=\; (\mathcal{S} + \mathcal{B}_{\mathrm{on}}) - \frac{\mathrm{T_{on}}}{\mathrm{T_{off}}} \times \mathcal{B}_{\mathrm{off}}, \tag{6.6}$$

where the background rates during ON and OFF periods are assumed to be equal [19]. Under this hypothesis, the background rate is now called $b = \mathcal{B}_{\mathrm{off}}/\mathrm{T_{off}}$. The net signal rate itself is written $s = \mathcal{S}/\mathrm{T_{on}}$. It is important to notice that, statistically, $\mathcal{S}$ and $\mathcal{B}_{\mathrm{off}}$ are independent.

For a rate only analysis the relative uncertainty on the net signal obtained by subtracting the reactor OFF period is finally:

$$\sigma \;=\; \frac{\sqrt{\mathrm{var}(\mathcal{S})}}{\mathcal{S}} \;=\; \frac{\sqrt{\mathrm{N_{on}} + \left(\frac{\mathrm{T_{on}}}{\mathrm{T_{off}}}\right)^2 \times \mathcal{B}_{\mathrm{off}}}}{\mathrm{N_{on}} - \frac{\mathrm{T_{on}}}{\mathrm{T_{off}}} \times \mathcal{B}_{\mathrm{off}}}. \tag{6.7}$$

#### Cross-check with CHOOZ data

It is possible to estimate the relative uncertainty on the net signal $\sigma$ for the CHOOZ experiment in order to compare to what is expected for Double Chooz. Based on information collected in the CHOOZ experiment last publication [30], we assume 2,704 neutrino candidates detected during a period of 181 days of both reactors ON, and 287 events detected during 138 days of reactor OFF-OFF. The Figure 6.71 displays the evolution of $\sigma$ as a function of the reactor OFF-OFF period, in days. The horizontal dashed line represents the statistical uncertainty only, assuming no background. For CHOOZ the signal statistical uncertainty was $\sigma = 1/\sqrt{2704} = 1.9$ %. From equation (6.7), the statistical error corrected for the background subtraction error of reactor OFF-OFF periods is expected to be $\sigma = 2.45$ %. This value is less than their published

[19] The background of the experiment is expected not to fluctuate during the data taking, which is confirmed by backgrounds stability studies over time (*cf.* Section 6.3).

2.8 % [30]. The discrepancy is not yet understood. The Figure 6.71 shows that the long both reactors OFF period allowed CHOOZ to measure precisely their backgrounds. In 24 hours of both reactors shutdown, CHOOZ measured a background of 2.1 events on average, for a signal of 22.4 events, leading to a signal over background ratio of $s/b = 10.6$ and $s/\sqrt{b} = 15.5$. The corresponding statistical error corrected for a 24 hours background subtraction measurement would have been about 11 %.

### Application to 24 hours of Double Chooz data

Using the same method as for CHOOZ data, one can estimate the background subtraction systematic uncertainty for a rate only analysis of the first 4,000 antineutrino candidates of Double Chooz. The signal statistical uncertainty is expected to be $\sigma = 1/\sqrt{4000} = 1.6$ %. After 24 hours of reactor OFF-OFF data, the statistical error corrected for the background subtraction measurement is going to depends on the number of events detected. Assuming 2 events in 24 hours, one expects an uncertainty of 4 % for the first Double Chooz result (both panels of Figure 6.71). For a correlated background of 2 events per day and a signal of 50 events per day (estimate without oscillation), $s/b = 25$ and $s/\sqrt{b} = 36$. This is a great improvement with respect to CHOOZ. As a consequence, the reactor OFF-OFF time period needed to reach $\sigma = 2$ % (similar to the error associated to the reactor neutrino flux uncertainty) will be less than 10 days, even for a correlated background rate of a few events per day. The Figure 6.71 indeed displays the evolution of $\sigma$ as a function of the reactor OFF-OFF period, in days. One needs to remember that the present evaluation, rate only, does not depend on any model of the backgrounds. However, the method proposed in the next section uses the energy spectra information.

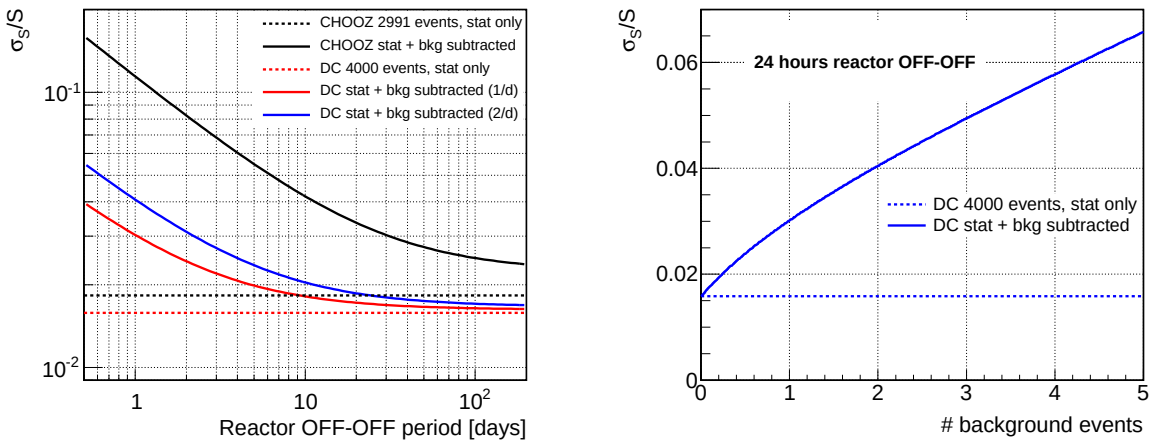


Figure 6.71: *(left) Relative uncertainty on the signal* $\sigma = \sqrt{var(S)}/S$ *for CHOOZ and Double Chooz with far detector only, as a function of reactor OFF-OFF period duration, in days. 4,000 neutrinos candidates is used for Double Chooz signal. The red and blue solid lines represent two hypotheses for the number of correlated background events detected per day. The horizontal dashed lines are the statistical uncertainties only. (right)* $\sigma = \sqrt{var(S)}/S$ *as a function of the number of background events detected in Double Chooz during 24 hours of reactor OFF-OFF, and 4,000 neutrino candidates detected in 100 days.*

### 6.5.5 Background subtraction principles: rate and shape

In this section is evaluated the systematic uncertainty associated to the subtraction of the backgrounds measured during the short reactor OFF-OFF period (one day), including the signal and background energy spectrum information, according to the Double Chooz best guess.

#### Toy Monte Carlo

First of all, in order to test the subtraction method, we performed a toy Monte Carlo simulation of 10,000 Double Chooz experiments with far detector only running for 100 days and detecting 4,000 events on average ($s = 40/d$). Uncorrelated bin-to-bin statistical errors on the positron energy spectrum were considered, for its $\mathrm{N_{bins}}$. It was assumed to be already subtracted from the accidental background component. Therefore, a background component with a rate of $b$ events per day distributed according to a flat energy spectrum between 0 and 10 MeV was considered.

For one realization of the Double Chooz experiment, the Figure 6.72 displays: the true $\nu$-induced positron spectrum ($\mathcal{S}_{\mathrm{true}}$), the measured candidates spectrum (N), the true background spectrum ($\mathcal{B}_{\mathrm{true}}$), the background spectrum extrapolated to 100 days ($\mathcal{B}_{\mathrm{est}}$), and the reconstructed $\nu$-induced positron spectrum ($\mathcal{S}_{\mathrm{est}}$).

The first step of the background subtraction is to assume a correlated background rate of $b_{\mathrm{off,true}} = 0.5,\ 1,\ 2,\ 3,\ 4,\ 5$ events per day. Therefore, $\mathcal{B}_{\mathrm{off}}$ is the number of events detected taken as a Poisson random number with a mean value $b_{\mathrm{off,true}}$, scales to $\mathrm{T_{off}} = 24$ hours of reactor OFF-OFF. In what follows we assume that this number corresponds to the correlated background only, considering here only the fast-neutron component. The same exercise could be repeated by changing the background shape to account for the cosmognenics background. We assumed that the accidental background had already been correctly subtracted. The measured background rate is then taken as $b_{\mathrm{off,est}} = \mathcal{B}_{\mathrm{off}}/\mathrm{T_{off}}$. It is extrapolated to the reactor ON period: $\mathcal{B}_{\mathrm{on}} = \mathrm{T_{on}}\, b_{\mathrm{off,est}}$. The background contribution in each energy bin is then taken as a Poisson random number with a mean value $\mathcal{B}_{\mathrm{on,i}} = \mathcal{B}_{\mathrm{on}}/\mathrm{N_{bins}}$.

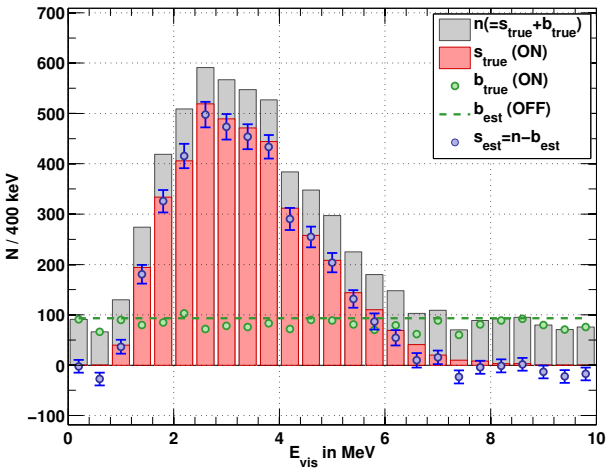


Figure 6.72: *One of the 10,000 toy Monte Carlo experiments, where the flat fast-neutron background component has been exagerated to improve the visibility of the plot [70, 75].*

### Background subtraction uncertainty

The left panel of Figure 6.73 is the relative difference between the estimated and the true positron spectra, $(\mathcal{S}_{\text{est}} - \mathcal{S}_{\text{true}})/\mathcal{S}_{\text{true}}$, where $\mathcal{S}$ are integrated over the entire energy spectra. This is done for 10,000 toy Monte Carlo Double Chooz experiments, with a true background rate varying between 0.5 to 4 events per day measured during a 24 hours of reactor OFF-OFF. It is assumed to be fast-neutrons with a flat energy spectrum. The bias tends to be Gaussian for a high number of detected background events during the OFF-OFF period. This figure shows that a short reactor OFF-OFF time period is suitable to measure the total background without bias, regardless the number of events measured per day. This information is also available in the Table 6.3, where the total relative biases due to the background subtraction of different values of measured background rates are given.

The right panel of Figure 6.73 concerns also 10,000 toy Monte Carlo Double Chooz experiments. It displays a stack of the statistical uncertainties per energy bin together with the background subtraction uncertainties, with a true background rate varying between 0.5 to 4 events per day measured during one day of both reactors OFF. The total relative uncertainty of the low energy region of the spectrum is particularly small. This region is actually the one concerned by the electron antineutrino deficit at 1 km linked to $\theta_{13}$ (*cf.* Sections 3.4 and 7.4).

| Measured background rate [$\text{d}^{-1}$] | 0.5 | 1 | 2 | 3 |
|---|---|---|---|---|
| Added uncertainty due to background subtraction [%] | 1.8 | 2.5 | 3.6 | 4.4 |
| Total relative uncertainty due to background subtraction [%] | 2.4 | 3.0 | 3.9 | 4.7 |
| Total relative bias due to background subtraction [%] | 0.04 | 0.01 | -0.04 | -0.04 |

Table 6.3: *Summary of the impact of subtracting a short reactor OFF-OFF time period for Double Chooz first phase with one far detector.*

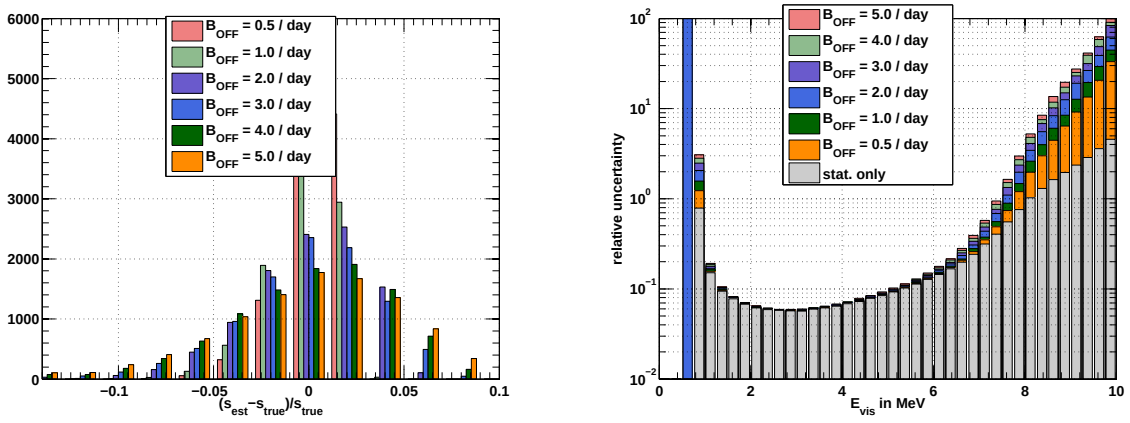


Figure 6.73: *(left) Relative distribution $(\mathcal{S}_{est} - \mathcal{S}_{true})/\mathcal{S}_{true}$ for a background rate varying between 0.5 and 5 events per day. (right) Stack of the statistical uncertainties together with the background subtraction uncertainties for 10,000 toy Monte Carlo experiments, with a true background rate varying between 0.5 and 5 events per day (assumed to be fast-neutrons with a flat energy spectrum) measured during a 24 h reactor OFF-OFF time period [70, 75].*

### 6.5.6 Application to the Double Chooz data

The previous methods aimed to quantify the systematic uncertainty associated with an in-situ measurement of 24 hours of reactor OFF-OFF data. First, the uncertainty on a rate-only measurement was quantified, on the back of the envelop. However, the knowledge of the spectral shape of the backgrounds is a useful information too. The background rate measurement performed during the reactor OFF-OFF data can be used to subtract, bin per bin, the backgrounds from the selected electron antineutrino candidates sample, using the accidental and the correlated backgrounds expected energy distributions. The accidental background can be subtracted using in-situ reactor ON measurements (*cf.* Section 6.3.1). The correlated backgrounds, whose spectra would be renormalized with the rate information extracted from the reactor OFF-OFF data, would then be also subtracted [70, 75].

The background subtraction uncertainty is finally obtained using the method in the previous section. The study should however be conducted again using the $^{9}$Li shape.

# Chapter 7

# Neutrino oscillation analysis

*People can come up with statistics to prove anything.*
*14 % of people know that.* [1]

Homer Simpson,
Nuclear Safety Inspector of the Sprinfield Nuclear Power Plant.

In order to measure the leptonic parameter $\theta_{13}$, the oscillation fit is performed on the $\overline{\nu}_e$ candidates selected on data, following the prescriptions presented in the previous section, compared to the expected signal. The estimations of the backgrounds are subtracted to the neutrino candidates or used as prior knowledge of the selection contamination in pull terms. All the uncertainties that either affect the expected rate of $\overline{\nu}_e$ events, or the shape of the selected prompt spectrum, or both, are taken into account in covariance matrices or in pull terms within a $\chi^2$ function. Both rate only (whether the deficit in the far detector is studied on the total number of events only), and rate and shape analyses (whether additional information from the spectral shape are used) are presented below along with their respective results on $\sin^2 2\theta_{13}$. First of all, the method followed by the Double Chooz collaboration in order to lower the systematic uncertainties on the $\overline{\nu}_e$ flux prediction is presented. This "anchor point" technique is necessary since the experiment is still missing its near detector and thus a direct comparison between non-oscillated data and potentially oscillated data is so far impossible.

## 7.1 Flux prediction and Bugey 4 anchor point

### Electron antineutrino flux prediction

For the time being, since the near detector is still under construction, a far/near detector comparison for the $\theta_{13}$ effect extraction is impossible. The first phase of Double Chooz, with far detector only, needs therefore a non-oscillated flux prediction. The packages DCRxtrTools and the core simulation codes MURE and DRAGON are used for this prediction [90, 119, 152].

The expected rate of electron antineutrino in the far detector can be written as follows:

$$\mathrm{R}_{\nu}^{\mathrm{exp}}(\mathrm{E}) = \sum_{\mathrm{R}=1,2}^{\mathrm{rxt}} \frac{1}{4\pi \mathrm{L}_{\mathrm{R}}^2} \times \mathrm{N_p}\, \epsilon_{\mathrm{det}} \times \frac{\mathcal{P}_{\mathrm{th}}^{\mathrm{R}}(\mathrm{t})}{< \mathrm{E}_f >_{\mathrm{R}}} \times < \sigma_f >_{\mathrm{R}}, \tag{7.1}$$

[1] From the Fox "The Simpsons" animated sitcom created by Matt Groening. Season 5, episode 11.

where $L_R$ is the distance from the reactor R to the far detector, $N_p$ is the number of protons in the $\nu$-target measured to be $6.785 \times 10^{29}$ [46, 146], $\epsilon_{det}$ is the detector efficiency, $\mathcal{P}_{th}^{R}(t)$ is the thermal power for reactor R, $< E_f >_R$ is the mean energy released per fission in the reactor R, and $< \sigma_f >_R$ is the mean cross-section per fission for $\overline{\nu}_e$ from reactor R.

The instantaneous thermal power of each reactor core is provided by the French Electricity Company EDF (*Électricité de France*) as a fraction of the total power. The uncertainty on the maximal thermal power 4.25 GW is 0.4 %. Since the EDF measurements are performed when the reactor is running at full power, the uncertainty at lower power is slightly larger.

The mean cross-section per fission is effectively a spectrum averaged cross-section:

$$< \sigma_f >_R = \sum_k \alpha_k^R(t) < \sigma_f >_k = \sum_k \alpha_k^R(t) \int_0^\infty S_k(E)\, \sigma_{IBD}(E)\, dE, \tag{7.2}$$

where k corresponds to the four main isotopes composing the nuclear core, $^{235}U$, $^{238}U$, $^{239}Pu$, and $^{241}Pu$. $S_k(E)$ is the reactor $\overline{\nu}_e$ reference spectrum of the $k^{th}$ isotope from [112, 147] (*cf.* Section 3.2.3), $\sigma_{IBD}(E)$ is the inverse $\beta$ decay cross-section from [185], and the $\alpha_k^R(t)$ are the fractional fission rates defined from the fission rates $f_k$ as $\alpha_k^R = f_k^R / \sum_k f_k^R$.

The determination of the fission rates depends on the fuel composition of the core and requires therefore the simulation of the reactor core [119, 152].

The $\alpha_k^R(t)$ of each isotope are needed to calculate the mean cross-section per fission of equation (7.2), but also to compute the mean energy released per fission for the reactor R:

$$< E_f >_R = \sum_k \alpha_k^R(t) < E_f >_k, \tag{7.3}$$

where the sum is again done over k, the four main isotopes in a PWR. The mean energies released per fission per isotope $< E_f >_k$ are given in Table 3.1.

### Bugey 4 anchor point

For the first Double Chooz phase with a far detector only, in order to limit the effect of the large uncertainty on the reference spectra described above, and also to avoid being affected by possible very short baseline $\overline{\nu}_e$ oscillations due to heavy sterile neutrinos or a bias in the $\overline{\nu}_e$ prediction (*cf.* Section 3.2.3), the global normalization is fixed to the Bugey 4 rate measurement, with its associated 1.4 % uncertainty [2]. This measurement is therefore considered as an "anchor point" for Double Chooz. This technique was previously used by the CHOOZ experiment [30]. In a certain sense, Bugey 4 is the near detector of Double Chooz:

$$< \sigma_f >_R \;=\; < \sigma_f >^{Bugey4} + \sum_k \left[ \alpha_k^R(t) - \alpha_k^{Bugey4}(t) \right] < \sigma_f >_k . \tag{7.4}$$

Since both measurements did not occur at the same reactors, the Bugey 4 mean cross-section per fission has to be corrected for the differences in core composition between the Chooz reactor and the Bugey reactor. This is the role of the second term of the previous formula: the differences are calculated for each isotopes in terms of fractional fission rates. This method allows to lower the electron antineutrino flux uncertainty from 2.7 % to 1.8 % (Table 7.1).

[2] Bugey 4 was a very short baseline reactor antineutrino experiment, located 15 m away from the Bugey reactor, whose rate measurement is the most precise among the other reactor antineutrino experiments [67, 141].

## 7.2 Uncertainties

All the detector and reactor systematic uncertainties affect the observed rate of electron antineutrino events. Indeed, a systematic underestimation of, say, the energy scale of the detector, would lead to a different number of selected events since energy-based selection cuts are applied on data (*cf.* Section 6.2.2). There are also other systematics which affect the shape of the selected spectrum: the background shape uncertainties, the reactor spectrum uncertainties, but also the energy scale uncertainty. All the systematic uncertainties, which need to be taken into account for the oscillation fit, are summarized in Table 7.1. Both first publication and second publication uncertainties are shown.

For the first Double Chooz publication, the larger errors came from the correlated backgrounds estimations (0.9 % for the fast-neutrons and 2.8 % for the cosmogenic isotopes) and the energy scale (1.7 %). The discrepancies between the data and the Monte Carlo simulations in terms of energy scale used to be handled by applying two empirical correction functions to the Monte Carlo. One function used to correct for a charge non-linearity and another one for a Z position bias [12]. Concerning the backgrounds, a huge work has been done between the two publications in order to better understand and even reduce them. I have actually been involved in the $^{9}$Li analysis, determination, and reduction (*cf.* Sections 6.3.3 and 6.4).

| Error description | DC 1$^{st}$ pub [%] | DC 2$^{nd}$ pub [%] |
|---|---|---|
| **Total Reactor** | 1.8 | **1.8** |
| Bugey 4 measurement | 1.4 | 1.4 |
| Fuel composition | 0.9 | 0.9 |
| Thermal power | 0.5 | 0.5 |
| Reference spectra | 0.5 | 0.5 |
| Energy per fission | 0.2 | 0.2 |
| IBD cross-section | 0.2 | 0.2 |
| Baseline | 0.2 | 0.1 |
| **Total Detector** | 2.1 | **1.7** |
| Energy scale | 1.7 | 0.3 |
| Delayed energy containment | 0.6 | 0.7 |
| Gd fraction | 0.6 | 0.3 |
| $\Delta$T | 0.5 | 0.5 |
| Spill-in/out | 0.4 | 0.3 |
| Trigger efficiency | 0.4 | $< 0.1$ |
| Number of target H | 0.3 | 0.3 |
| **Total Backgrounds** | 3.0 | **1.6** |
| Fast-neutrons | 0.9 | 0.5 |
| Cosmogenics | 2.8 | 1.4 |

Table 7.1: *Table with the systematic uncertainties on the detected $\overline{\nu}_e$ rate related to the detector, the reactor, and the backgrounds with respect to signal, in percent [11, 12]. IBD stands for inverse $\beta$ decay.*

## 7.3 $\chi^2$ definition

The large amount of statistics in the Double Chooz experiment allowed the collaboration to chose a $\chi^2$ approach to perform the final fit for the $\theta_{13}$ measurement. In that case, it is equivalent to a binned likelihood ratio. Also, compared to an event by event likelihood, this method needs less care on the development at current stage.

The $\chi^2$ function depends on $\theta_{13}$. The fit strategy consists therefore on minimizing the $\chi^2$ with respect to $\theta_{13}$ in order to find the best estimate of a single physical parameter, $\sin^2 2\theta_{13}$, according to the selected and expected electron antineutrino and background events rates, and the systematic effects. In order to do so, two approaches can be followed: all the uncertainties can be included in the $\chi^2$ through the use of covariance matrices, or the systematic effects can be modeled as nuisance parameters, also called pull terms, which basically are additional terms in the $\chi^2$. However, the covariance matrix and the nuisance parameter approaches are totally equivalent. The covariance $\chi^2$ is the same as the nuisance parameter $\chi^2$ already minimized on the nuisance parameters. The covariance $\chi^2$ uses therefore the best estimates for each nuisance parameter. Moreover, it is possible to mix both approaches and fit $\theta_{13}$ along with few other parameters. The mixed approach is the one followed by Double Chooz collaboration for the $\theta_{13}$ parameter determination [11, 139].

### 7.3.1 Covariance matrix approach

The first approach is based on covariance matrices. All the uncertainties presented in Section 7.2 are thus taken into account in these matrices. Since there are correlations between the energy bins, some of the covariance matrices are not simply diagonal ($\mathcal{M}_{cov}(\epsilon_\mathrm{i}, \epsilon_\mathrm{j}) \neq \delta_\mathrm{ij}\sigma_\mathrm{i}^2$). The $\chi^2$ function is minimized with respect to $\theta_{13}$, the only fitted parameter. It is defined as follows:

$$\begin{aligned}\chi^2(\theta_{13}) &= \left(\mathrm{N_i} - \left(\sum_{\mathrm{R}=1,2}^{\mathrm{rxt}} \mathrm{N_i}^{\nu,\mathrm{R}}(\theta_{13}) + \sum_{b}^{\mathrm{bkg}} \mathrm{N_i}^{b}\right)\right) \\ &\times \left(\mathcal{M}_\mathrm{ij}^\mathrm{rxt}(\theta_{13}) + \mathcal{M}_\mathrm{ij}^\mathrm{det}(\theta_{13}) + \mathcal{M}_\mathrm{ij}^\mathrm{stat}(\theta_{13}) + \mathcal{M}_\mathrm{ij}^\mathrm{eff}(\theta_{13}) + \sum_{b}^{\mathrm{bkg}} \mathcal{M}_\mathrm{ij}^{b}\right)^{-1} \\ &\times \left(\mathrm{N_j} - \left(\sum_{\mathrm{R}=1,2}^{\mathrm{rxt}} \mathrm{N_j}^{\nu,\mathrm{R}}(\theta_{13}) + \sum_{b}^{\mathrm{bkg}} \mathrm{N_j}^{b}\right)\right)^{\mathrm{T}},\end{aligned} \tag{7.5}$$

where $\mathrm{N_i}$, $\mathrm{N_i}^{\nu,\mathrm{R}}$, and $\mathrm{N_i}^{b}$ are the total number of events (signal and background), the predicted number of detected electron antineutrino events, and the predicted number of background events, in the $\mathrm{i}^{\mathrm{th}}$ energy bin, respectively. The index $b$ runs over the accidental background, the correlated fast-neutron and stopping muons events, and the $^9$Li cosmogenics background (*cf.* Section 6.3). $\mathrm{N_i}^{\nu,\mathrm{R}}$ is considered separately for the two nuclear reactors.

The seven matrices $\mathcal{M}$ of equation (7.5) are covariance matrices. Each matrix represents the covariance of the prediction of signal and backgrounds between the $\mathrm{i}^{\mathrm{th}}$ and the $\mathrm{j}^{\mathrm{th}}$ energy bins, due to a given uncertainty source. These matrices are presented below.

### Signal covariance matrix

$\mathcal{M}^{\text{rxt}}$ is the signal, or reactor, covariance matrix. It represents the uncertainties on the electron antineutrino signal output of the Double Chooz generator DCRxtrTools, converted to reconstructed positron energy. The MultiSim approach is used to convert the simulated true $\overline{\nu}_e$ spectrum into reconstructed positron spectrum [90]. The method used to derive the predicted number of electron antineutrino events is presented in Section 7.1.

The uncertainties accounted for in this matrix are then mostly reactor related, or at least linked to the detection of the $\overline{\nu}_e$. It represents our knowledge on the predicted neutrino spectra: the reactors thermal power, the Bugey 4 anchor point, the number of target protons, the detector efficiency, the mean energy and the mean cross-section per fission, the reactor-detector baselines, and the fuel composition.

### Detector covariance matrix

The detector covariance matrix $\mathcal{M}^{\text{det}}$ takes into account the detector energy response uncertainties. The systematic uncertainty associated to the Double Chooz energy scale determination amounts for 1.13 % (*cf.* Section 4.2.4). It corresponds to three uncertainties: the relative non-linearity, the non-uniformity, and the time instability. Therefore, a linear 1.13 % shift, of the form $\text{E} \rightarrow \text{E}(1 + 1.13\ \%)$ is applied to properly normalize the signal, and the correlated backgrounds (cosmogenics $^9$Li, fast-neutrons, and stopping-muons) predictions. Since the accidental background is estimated from the data, the linear energy scale shift is not applied to this component.

In the next section, we will see that this detector response uncertainty can be implemented as a nuisance parameter with a 1.13 % uncertainty pull term. In that case, the detector matrix is omitted from the total covariance matrix.

The matrix itself is obtained by testing on Monte Carlo simulations the effect of the 1.13 % linear shift and the matrix elements $\mathcal{M}^{\text{det}}_{\text{ij}}$ correspond therefore to the relative difference caused by the energy scale uncertainty. Basically, for an electron antineutrino generated spectrum $\mathcal{S}$, $\mathcal{M}^{\text{det}}_{\text{ij}} = \delta\mathcal{S}_{\text{i}} \times \delta\mathcal{S}_{\text{j}}$, where $\delta\mathcal{S}$ is $\mathcal{S}(\text{E}(1 + 1.13\%)) - \mathcal{S}(\text{E})$.

### Statistical covariance matrix

$\mathcal{M}^{\text{stat}}$ is the statistical covariance matrix and is filled with the signal and backgrounds selection. This is a diagonal matrix with no bin-to-bin correlation: $\mathcal{M}^{\text{stat}}_{\text{ii}} = \text{N}_{\text{i}}$, where $\text{N}_{\text{i}}$ is the total number of events (signal and backgrounds) in the energy $\text{i}^{\text{th}}$ bin.

### Efficiency covariance matrix

Uncertainties of the efficiencies linked to the detector and the selection cuts are included in the fit through the efficiency covariance matrix $\mathcal{M}^{\text{eff}}$.

This matrix is therefore composed by the $\nu$-target proton measurement uncertainty, dominated by the uncertainty of the weight measurement used to estimate it [46]. It is of the order of 0.3 %. The Gd fraction efficiency uncertainty is also part of this matrix. It is estimated by looking at the fraction of neutrons which are captured on Gd in the $\nu$-target, from a combined fit of the relative heights of the Gd and H capture peaks (*cf.* Section 6.2.4). This systematic uncertainty is found to be 0.3 %. The $\Delta$T cut efficiency uncertainty is also part of this matrix and account for 0.5 %. Finally, the delayed energy containment efficiency implies a 0.7 % uncertainty. As explained in Section 5.3, the spill-in and spill-out effects have to be taken into account as well. An uncertainty of 0.3% is assigned to this process.

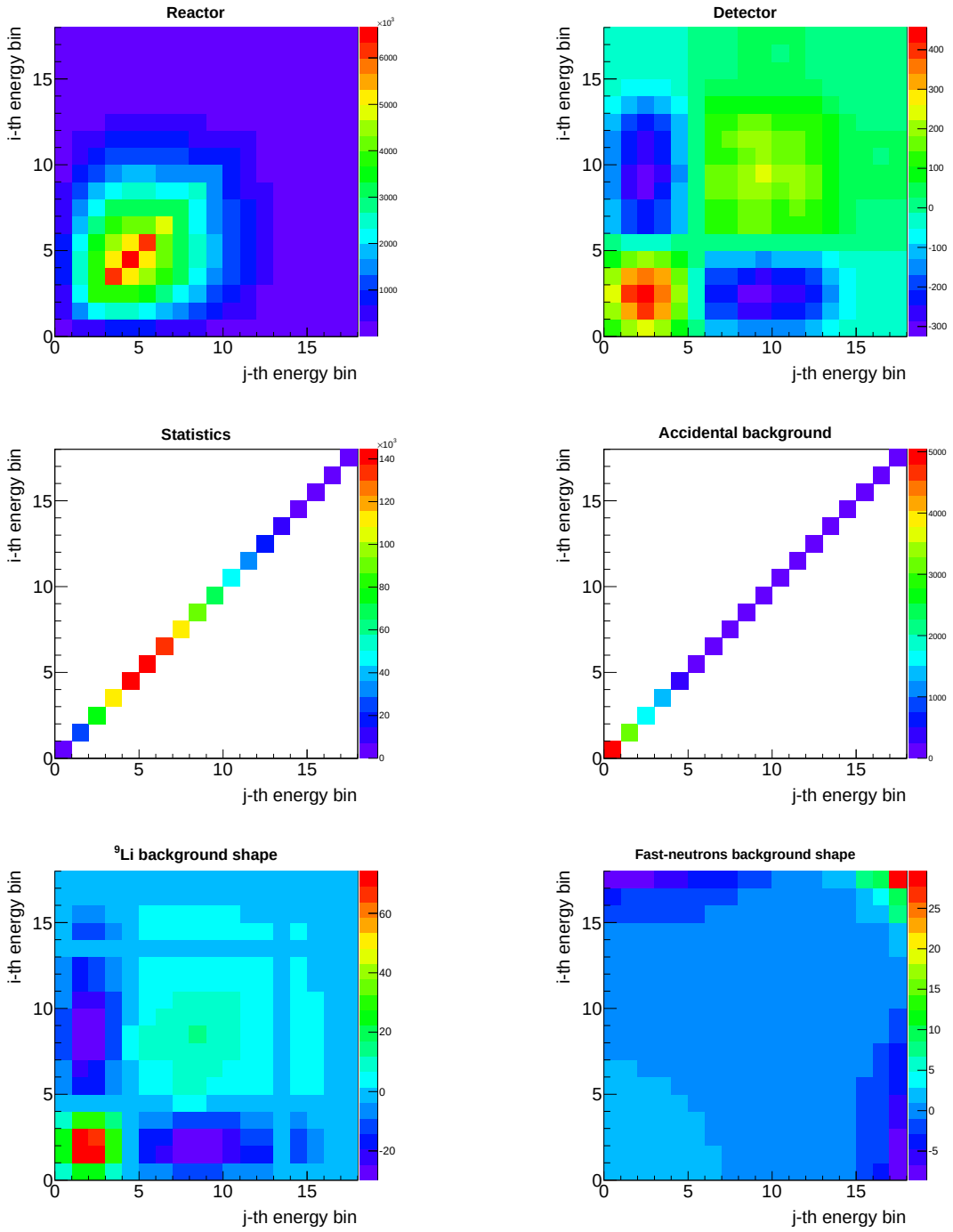


Figure 7.1: *Covariance matrices: (top left) signal or reactor, (top right) detector, (middle left) statistics, (middle right) accidental background, (bottom left) shape of the $^9$Li background, and (bottom right) shape of the fast-neutrons and stopping muons background.*

**Backgrounds covariance matrix**

Finally, each $\mathcal{M}^b$ covariance matrix corresponds to a background $b$, where $b$ can be the accidental events, the fast-neutron and stopping muons correlated background, or the $^9$Li background. It represents both the rate and shape uncertainties.

The $^9$Li matrix contribution contains spectral shape uncertainties estimated using different Monte Carlo event generation parameters (*cf.* Section 6.3.3). The slope of the fast-neutrons and stopping muons spectrum is allowed to vary from a nearly-flat spectrum following the measurements described in Section 6.3.2.

Since the accidental background is measured to a high precision from many offtime windows (*cf.* Section 6.3.1), its uncertainties are included as a diagonal covariance matrix, with no bin-to-bin correlation.

In a covariance matrix approach, these background matrices also include information on the rate of the correlated $^9$Li and fast-neutrons backgrounds, whereas they are treated as nuisance parameters in the official Double Chooz oscillation fit, as explained in the following section.

### 7.3.2 Pull terms approach

The pull terms approach provides additional information compared to the covariance approach. The minimization process implies now several parameters: the physical parameter $\theta_{13}$ and the nuisance parameters [3]. The best fit value of nuisance parameters and their deviation from the a priori information give an interesting diagnostic on the model. It can point out tension in the fit results, which cannot be done with a covariance matrix. Indeed, the information on the best fit values of the nuisance parameters is lost in the covariance matrix approach. For instance, the use of pull terms showed that the background estimates performed on data were slightly underestimated (Section 7.4.2).

The current Double Chooz final fit is a mixed covariance matrices-nuisance parameters approach. The covariance matrices concern most of the uncertainties: the normalization, the reactor simulation (fuel and burnup, Bugey 4 anchor point, and thermal power uncertainties), the cross-section uncertainty, and all the efficiences. However, pull terms take into account the correlated backgrounds, the energy scale, and the $\Delta m^2_{31}$ uncertainties, which are parameters we would like to know the best fit values and uncertainties. The $\chi^2$ function is then:

$$\begin{aligned}
\chi^2(\theta_{13}) \;=\; & \left( \mathrm{N_i} - \left( \sum_{\mathrm{R}=1,2}^{\mathrm{rxt}} \mathrm{N_i}^{\nu,\mathrm{R}}(\theta_{13}) + \sum_{b}^{\mathrm{bkg}} \mathrm{N_i}^{b} \right) \right) \\
& \times \left( \mathcal{M}^{\mathrm{rxt}}_{\mathrm{ij}}(\theta_{13}) + \mathcal{M}^{\mathrm{det}}_{\mathrm{ij}}(\theta_{13}) + \mathcal{M}^{\mathrm{stat}}_{\mathrm{ij}}(\theta_{13}) + \mathcal{M}^{\mathrm{eff}}_{\mathrm{ij}}(\theta_{13}) + \sum_{b}^{\mathrm{bkg}} \mathcal{M}^{b}_{\mathrm{ij}} \right)^{-1} \\
& \times \left( \mathrm{N_j} - \left( \sum_{\mathrm{R}}^{\mathrm{rxt}} \mathrm{N_j}^{\nu,\mathrm{R}}(\theta_{13}) + \sum_{b}^{\mathrm{bkg}} \mathrm{N_j}^{b} \right) \right)^{\mathrm{T}} \\
& + \frac{(\epsilon_{\mathrm{FN}} - 1)^2}{\sigma^2_{\mathrm{FN}}} + \frac{(\epsilon_{^9\mathrm{Li}} - 1)^2}{\sigma^2_{^9\mathrm{Li}}} + \frac{(\alpha_{\mathrm{ES}} - 1)^2}{\sigma^2_{\mathrm{ES}}} + \frac{(\Delta m^2_{31} - (\Delta m^2_{31})^{\mathrm{MINOS}})^2}{\sigma^2_{\mathrm{MINOS}}}.
\end{aligned} \tag{7.6}$$

[3] There is no loss of degrees of freedom when the nuisance parameters approach is used, despite what can be thought, since each pull term implies another parameter to fit. Each extra pull term in the $\chi^2$ of equation (7.6) can be actually considered as an extra bin compared to the data points.

The two parameters $\epsilon_{\mathrm{FN}}$ and $\epsilon_{^9\mathrm{Li}}$ are allowed to vary as part of the fit. They scale the rate of the two correlated backgrounds: fast-neutron and stopping muon for $\epsilon_{\mathrm{FN}}$ and cosmogenic isotopes for $\epsilon_{^9\mathrm{Li}}$. The rate of accidental events is not allowed to vary since its initial uncertainty is precisely determined on data (*cf.* Section 6.3.1). The energy scale for the predicted signal and the $^9$Li events is allowed to vary linearly according to the $\alpha_{\mathrm{ES}}$ parameter with an uncertainty $\sigma_{\alpha_{\mathrm{ES}}} = 1.13$ % (*cf.* Section 4.2.4). A final parameter constraints the mass splitting $\Delta m^2_{31}$ using the MINOS measurement of $\Delta m^2_{31} = (2.32 \pm 0.12) \times 10^{-3}$ eV$^2$ as an a priori value, but increasing its uncertainty to account for different interpretations of the neutrino mass hierarchy [19].

## 7.4 Final fit results

Three final fit packages, one for each analysis cluster, have been developed and their outputs showed to be in good agreement, pointing out the robustness of the Double Chooz analysis. One of them is linked to CATS, a statistical framework developed at Saclay to lead systematical uncertainty analyses which provides powerful diagnosis tools [138].

As explained in Section 3.4, the effect of a non-zero $\theta_{13}$ in the Double Chooz far detector is a deficit from expectations of electron antineutrino events. The Figure 3.10 displays the expected far to near spectrum ratio for a non-zero $\theta_{13}$. This plot shows also that the near spectrum and far spectrum would have a different shape and that the deficit mostly concerns the low energy bins of the spectrum. This means that the signature of $\theta_{13}$ can be extracted using two types of information: the rate and the shape. A rate only analysis just uses the total number of expected and observed numbers of $\overline{\nu}_e$ events. It means that the whole spectrum is integrated. A shape only analysis consists in studying the distortion of the observed spectrum shape with respect to the expected spectrum one, especially at low energies.

The Double Chooz official analysis is based on a combined fit to antineutrino rate and spectral shape [11, 12]. The electron antineutrino candidates are selected from detector data as described in Section 6.2.2. The data are compared to Monte Carlo signal and background events from high statistics samples. The same selections are done on both signal and background, with corrections applied to Monte Carlo only when necessary in order to match the detector performances.

The selected signal and backgrounds events are binned in 18 energy intervals. This binning was fixed prior to the data release to ensure a non-biased analysis. Due to low number of events in the highest energy bins, a non-constant binning was chosen to provide sufficient statistics per bin. From 0.7 to 8.2 MeV a 500 keV binning was chosen, while the next two bins up to 10.2 MeV were 1 MeV wide, and the last one 2 MeV.

Two integration periods are used in the fit to help separate background and signal flux. One set contains data periods where one reactor is operating at less than 20 % of its nominal thermal power, according to power data provided by EDF, while the other set contains data from all other times, typically when both reactors are running (*cf.* Figures 7.2 and 7.3). All data end up in one of the two integration periods. The use of multiple periods of data integration, a novelty of the Double Chooz second publication with respect to its first one, takes advantage of the different signal/background ratios in each period, as the signal rate varies with reactor power while the backgrounds remain constant in time. This technique adds information about background behavior to the fit.

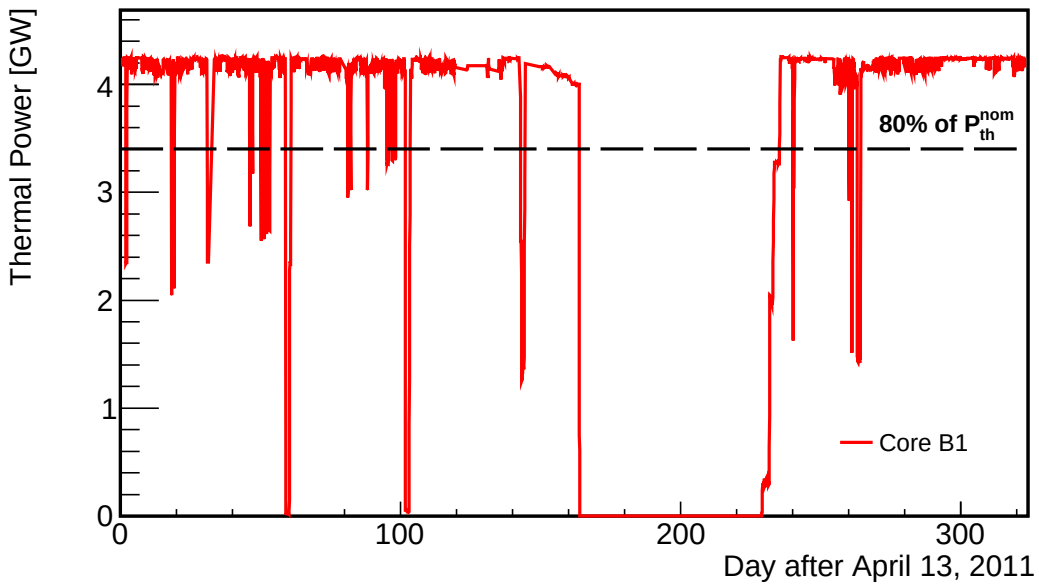


Figure 7.2: *Thermal power evolution for reactor B1, per day since April 13$^{th}$ 2011, in GW. The black dashed line represents 80 % of the nominal thermal power.*

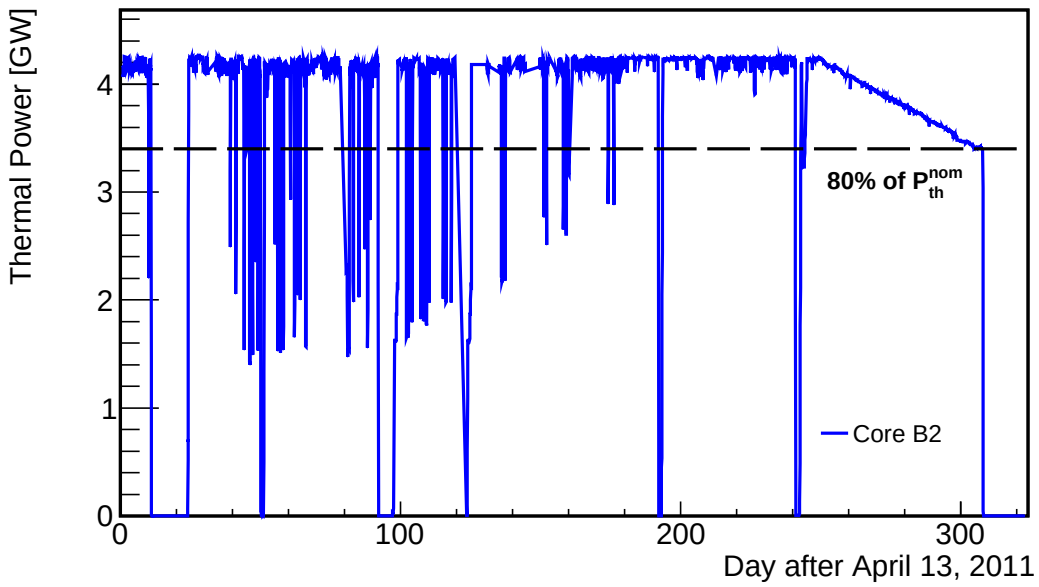


Figure 7.3: *Thermal power evolution for reactors B2, per day since April 13$^{th}$ 2011, in GW. The black dashed line represents 80 % of the nominal thermal power.*

### 7.4.1 Rate only analysis

A rate only analysis is a simple analysis based on a comparison between the observed and the expected electron antineutrino rates. It is used to compare the results of the different fitting softwares developed within the Double Chooz collaboration.

An analysis comparing only the total observed number of electron antineutrino candidates in each integration period to the expectations, thus ignoring the spectral information, gives a best-fit of $\sin^2 2\theta_{13} = 0.170 \pm 0.052$, with a $\chi^2$ per degrees of freedom at $\chi^2/\text{NDF} = 0.50/1$.

### 7.4.2 Rate and shape analysis with pull terms

For the rate and shape Double Chooz official analysis, the $\chi^2$ function of equation (7.6) is minimized. The use of energy spectra information in the oscillation fit allows additional knowledge on background rates to be gained from the pull terms, in particular because of the small number of electron antineutrino candidates between 8 and 12 MeV. The rate and shape analysis is the standard fit for the Double Chooz collaboration because it is more powerful than a rate only analysis, which cannot constrain the backgrounds using their shape at high energy. As explained in Section 7.3.2, the two parameters linked to the rate of the two correlated backgrounds, $\epsilon_{\text{FN}}$ and $\epsilon_{^9\text{Li}}$, are allowed to vary and are minimized during the fitting procedure, while the accidental events rate is fixed to its precise measured value determined on data.

#### Results on $\theta_{13}$

The rate and shape oscillation fit gives $\sin^2 2\theta_{13} = 0.109 \pm 0.030\,(\text{stat}) \pm 0.025\,(\text{syst})$, with $\Delta m^2_{31} = 2.32 \times 10^{-3}\,\text{eV}^2$. The $\chi^2$ per degrees of freedom is $\chi^2/\text{NDF} = 42.1/35 = 1.20$. The results obtained on all data are available in Figure 7.4. The no-oscillation hypothesis is drawn along with the best fit value and the data points on the upper panel. All the backgrounds are also shown on the same plot. The ratio of the selection over the prediction without oscillation per energy bin is given in Figure 7.4 as well. This ratio is not compatible with one, as expected for a non-zero $\theta_{13}$. The last information given in this figure is the relative difference between the selection performed on data and the prediction without oscillation per energy bin. It shows a clear deficit at low energy, before 6 MeV, as expected from a disappearence caused by $\theta_{13}$ (*cf.* Figures 3.10 and 5.1). The Figure 7.5 displays the neutrino spectra for both integration periods, obtained from CATS, the final fit package developped at Saclay.

#### Pull terms evolution

The pull term linked to the mass splitting $\Delta m^2_{31}$ keeps its initial value obtained from the MINOS measurement [19]. The energy scale was allowed to vary linearly according to the pull term $\alpha_{\text{ES}}$ with an uncertainty $\sigma_{\text{ES}} = 1.13\,\%$. The fitted value deviates for 1.4 % from the initial value, favouring a $\alpha_{\text{ES}} = 0.986 \pm 0.007$, anyway really close to the a priori.

Concerning the correlated backgrounds rates, the fast-neutrons and stopping muons component mostly stays the same. The fitted pull term gives $0.64 \pm 0.13\ \text{d}^{-1}$, while the initial value was $0.67 \pm 0.20\ \text{d}^{-1}$ (*cf.* Section 6.3.2). The cosmogenics $^9$Li rate seems however a little bit overestimated since its associated pull term favours $1.00 \pm 0.29\ \text{d}^{-1}$, while its estimation from data gave $1.25 \pm 0.54\ \text{d}^{-1}$ (*cf.* Sections 6.3.3 and 6.4).

The background rates and uncertainties, as well as the energy scale, are therefore further constrained in the oscillation fit following the mixed approach covariance matrices-pull terms. The estimations on data show that they are however very good.

### Confidence intervals

Confidence intervals for the rate and shape analysis were determined using a frequentist technique [85]. This approach is used to calculate the probability of excluding the no-oscillation hypothesis. This study compares the data to 10,000 simulations generated at each of 21 test points in the range $0 \leq \sin^2 2\theta_{13} \leq 0.25$. A $\Delta\chi^2$ statistic, equal to the difference between the $\chi^2$ at the test point and the $\chi^2$ at the best fit, is used to determine the region in $\sin^2 2\theta_{13}$ where the $\Delta\chi^2$ of the data is within the given confidence probability. The allowed region at 68 % (90 %) confidence level is $0.060\,(0.044) < \sin^2 2\theta_{13} < 0.15\,(0.17)$. An analogous technique shows that the data excludes the no-oscillation hypothesis at 99.8% (2.9 $\sigma$).

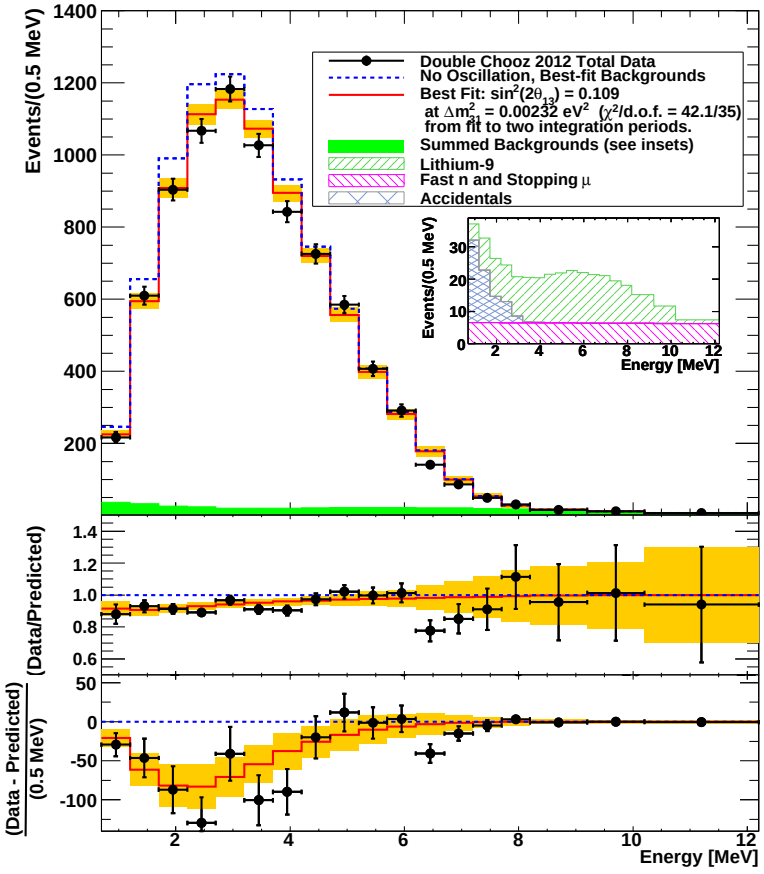


Figure 7.4: *(top) Measured prompt energy spectrum of the sum of both integration periods (black points) compared to the expected prompt energy spectrum with no-oscillation (dashed blue line). The backgrounds are also drawn (inset is a stacked backgrounds spectra), along with best fit (red line), for $\sin^2 2\theta_{13} = 0.109$ and $\Delta m^2_{31} = 2.32 \times 10^{-3}$ eV$^2$. (middle) Ratio of data over no-oscillation prediction and best fit over no-oscillation prediction. (bottom) Differences between data and no-oscillation prediction, and between best fit and no-oscillation prediction. The orange band represents the systematic uncertainties on the best fit prediction [11].*

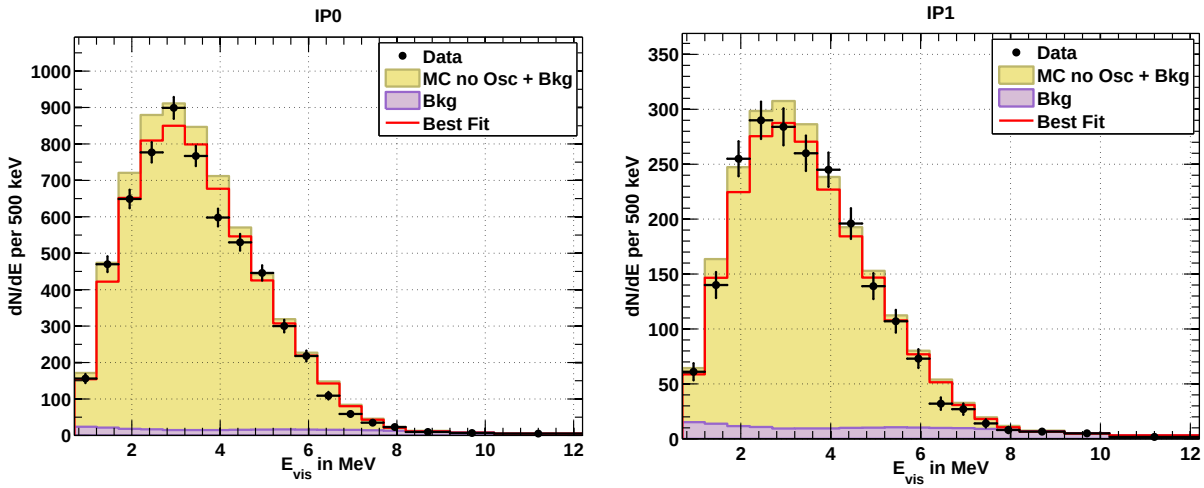


Figure 7.5: *Measured prompt energy spectrum for each integration period (black points) superimposed on the expected prompt energy spectrum (yellow) including the backgrounds (purple). The best fit is also drawn (red line).*

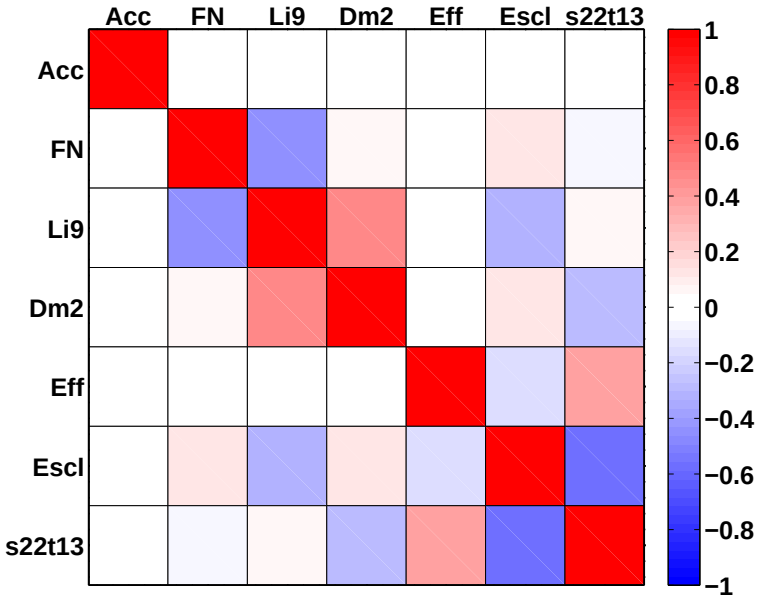


Figure 7.6: *Fit parameters correlation matrix. It displays the correlation or the anticorrelation among all the fitted parameters: $sin^2 2\theta_{13}$ and the nuisance parameters.*

### Fit diagnostics

An interesting feature of the CATS software is that it provides many fit diagnostics plots. It is important to inspect them to check the validity of the model and the fit results, and not only the $\chi^2$/NDF for instance.

The correlations between the fitted parameters are displayed on Figure 7.6. A look at this matrix allows to check whether the parameters are correlated or anticorrelated as expected. For instance, the fast-neutron background (called FN) and the cosmogenics background (called Li9) are anticorrelated: indeed, if the normalization of the fast-neutrons is increased, the fitted $^9$Li background will be decreased, and vice versa. Concerning the accidental background, it is not correlated to any other parameters. That is explained in the following paragraphs using the Cook's distance. However, the energy scale has a strong impact on the other fitted parameters, and is especially anticorrelated with the $^9$Li background and $\theta_{13}$.

The first thing to look at to check the validity of the fit is the residuals. The left panel of Figure 7.7 shows the standardized residuals of the $\theta_{13}$ fit performed by CATS. They are the differences between the observed data and the best fit model value, divided by its standard deviation. Each energy bin of each integration period is considered, along with the pull terms. The right panel of Figure 7.7 displays the standardized residuals distribution, showing that the degrees of freedom are basically all consistent with the best fit model within 1 $\sigma$ and that this distribution is in very good agreement with a standard normal distribution. This is an indication that the hypothesis that the error distribution is normal is correct.

The Figure 7.8 displays the leverages of each degrees of freedom. This quantity checks the influence of each information on the fit. The vertical dashed lines correspond to $p/n$ and $2p/n$, where $p$ is the total number of parameters (all fitted parameters, *i.e.* $\sin^2 2\theta_{13}$ and the nuisance parameters) and $n$ is the total number of bins (in a general sense, *i.e.* the number of energy bins plus the pull terms). This plot shows that all the systematics (the backgrounds, the $\Delta m^2_{31}$, the efficiencies, and the energy scale) contribute to the results of the fit. They are all influencial. This means that a precise determination of them is of the utmost importance.

Another interesting diagnostic is given in Figure 7.9. The standardized residuals are plotted as a function of the leverages and the Cook's distances for each energy bins of each integration period and all the pull terms are also shown. This represents in a way the distance of a data point with respect to the cloud of all the other data points, taking into account all the available information provided. A data point with a low residual and a low leverage, or even with a high residual (called outlier point) but a low leverage, will not influence the global fit. However, if both the residual and the leverage are high, this data point will be highly influent and strongly pull the fit result towards a certain direction. Even though the residual is low, a data point can also have an important Cook's distance if its leverage is high.

Concerning the results of the fit performed with the CATS software, most of points in the fit are OK, either bins (round point) or pull terms (stars). Indeed, every points in the white area do not have a strong impact on the fit and have a Cook's distance lower than 0.5. The two farthest points are the efficiency pull term and the accidental pull term. This means that they are influent parameters on the final fit, *i.e.* on the determination of $\theta_{13}$ and the nuisance parameters best fit. However, even though they are located in the red zone, it does not mean that they are problematic. First, they are really close to the white area. Secondly, the pull term on the accidental is determinant to fix the accidental rate, and this indicates that the a priori information is so accurate that the other data points do not bring any further information. This is why the residual with respect to a priori value is so low. Concerning the efficiency, the pull

term is also quite influential and this diagram indicates also that there is a small tension in the fit between the data and the pull term, but this tension is small anyway since the residual of the efficiency nuisance parameter with respect to the a priori value is below 1 $\sigma$. This effect comes from the slight difference of best fit on $\theta_{13}$ between rate only analysis and shape only analysis. In a rate and shape analysis, in order to get a coherent $\theta_{13}$, the fit has to change a little bit the efficiency nuisance parameters, and therefore changes a little bit the normalization of the spectrum. A rate only analysis completely depends on the normalization, which explains the high leverage of the efficiency pull term. The fit presented earlier uses the $\chi^2$ of equation (7.6), which does not include any efficient pull term nor accidentalpull term. These diagnostics were therefore performed with a modified version of equation (7.6).

The plot of Figure 7.9 also displays that the energy bins which are around 2 $\sigma$ away from the best fit (Figure 7.7) are actually non-influencial for the fit, since their leverage values are really low, and therefore own a small Cook's distance.

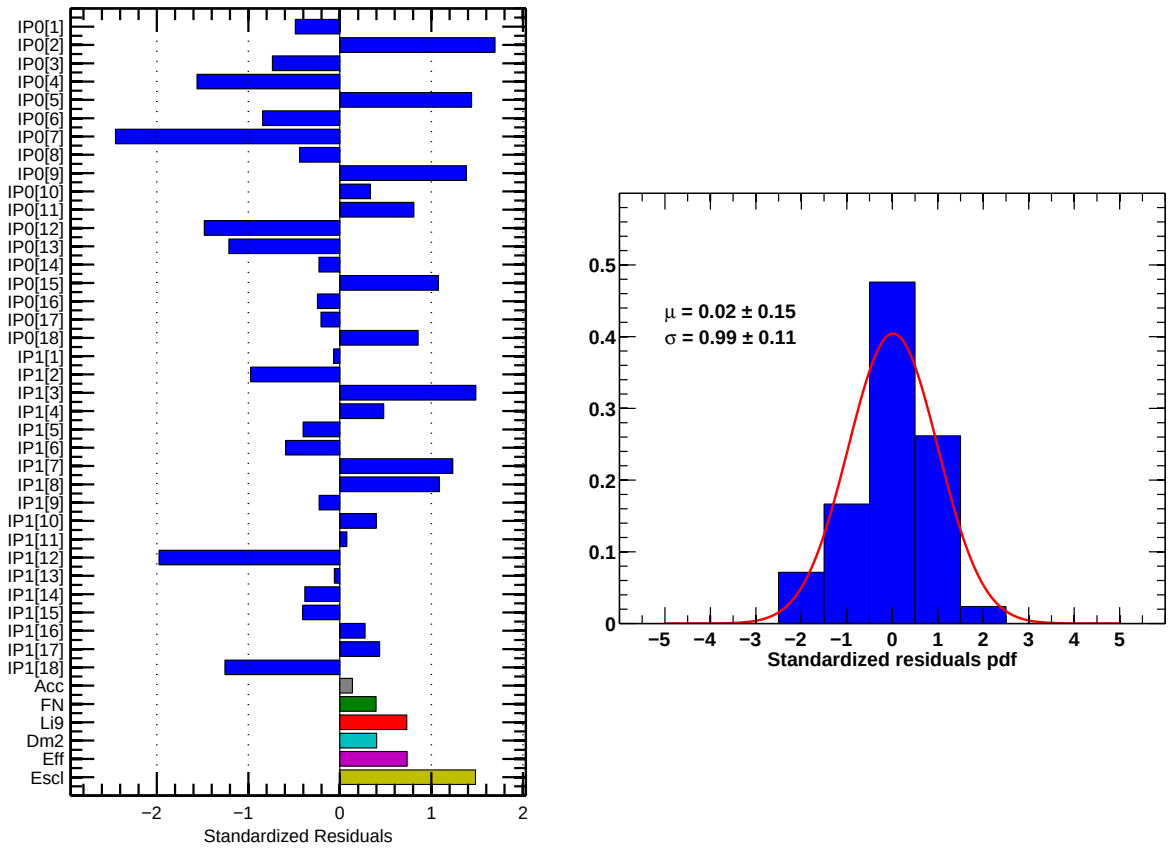


Figure 7.7: *(left) Standardized residuals of the fit defined as the difference between data and the best fitted model divided by the standard deviation of the latter. (right) Distribution of the standardized residuals with a normal distribution fit.*

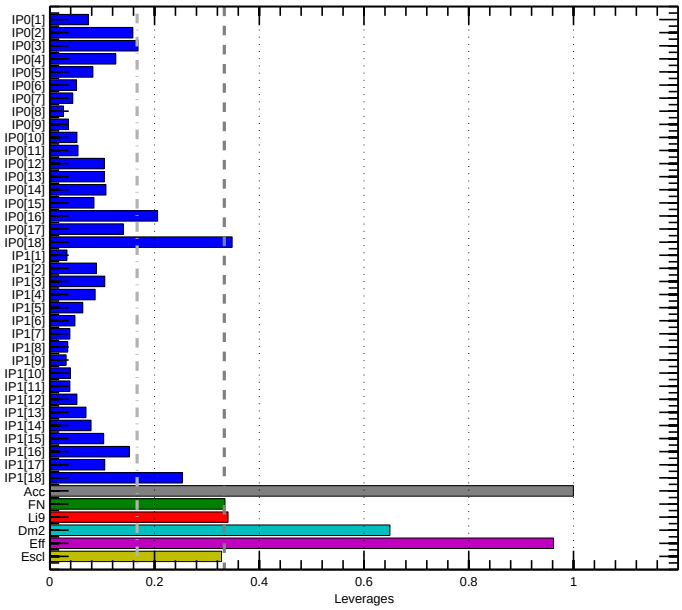


Figure 7.8: *Leverages of all the energy bins of both integration periods and of all the pull terms. The vertical grey dashed lines correspond to $p/n$ and $2p/n$, where $p$ is the total number of parameters and $n$ the total number of bins.*

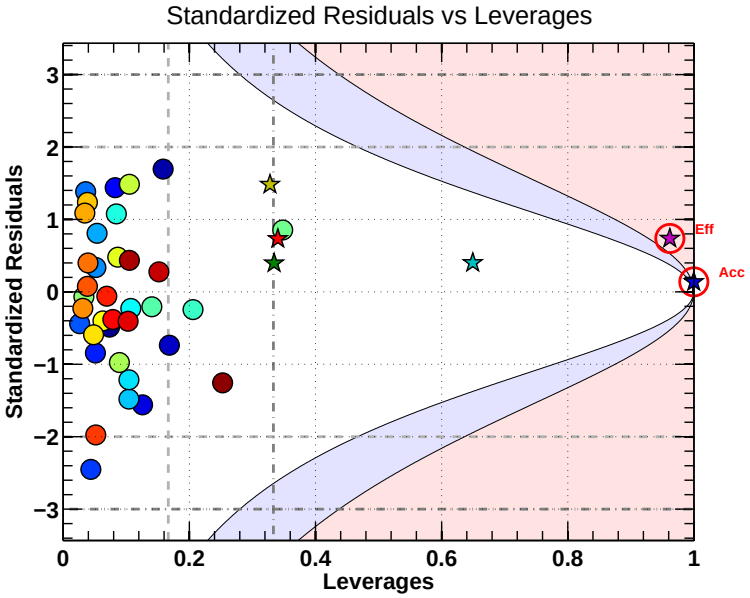


Figure 7.9: *Standardized residuals of the fit as a function of the leverages. The round points are the energy bins of both integration periods, while the stars are the pull terms. The color of the round points goes from blue to red, from the lower energy bins to the higher ones. The white area corresponds to low Cook's distances and the red area to large Cook's distances. The vertical grey dashed lines correspond to $p/n$ and $2p/n$, where $p$ is the total number of parameters and $n$ the total number of bins. The horizontal grey dashed lines correpond to $\pm$ 2 $\sigma$ and $\pm$ 3 $\sigma$.*

# Conclusion

*Sometimes I'll start a sentence and I don't even know where it's going. I just hope I find it along the way...* [4]

Michael Scott,
Regional Manager of Dunder Mifflin Inc., Paper Company, Scranton, PA.

The neutrino oscillations are nowadays understood as resulting from a three flavors mixing that can be parametrized with three angles, a possible CP-violating phase, and two differences of squarred masses (*cf.* Section 1.4). Many convincing evidences have been acquired over the past decades (*cf.* Chapter 2). If few anomalies are put aside, all of these experimental results, either coming from natural sources like the Sun and the cosmic rays, or from man-made sources like the accelerators and the nuclear reactors, are in excellent agreement. This clear picture presents however few grey areas as the CP-violating phase and the sign of one of the differences of squarred masses are unknown. The measurement of these parameters depends on the knowledge of all three mixing angles. Until really recently, $\theta_{13}$ was the last unknown leptonic mixing parameter (*cf.* Section 2.2.4).

The Double Chooz experiment has been built in order to measure $\theta_{13}$ from electron antineutrinos emitted by a nuclear power plant (*cf.* Chapter 3). The particularities of Double Chooz are an increased target mass with respect to the previous experiments and a new detector design with the addition of a buffer volume to strongly lower the backgrounds. A tremendous work has been performed to create a scintillator which ensures a long-term stability, and a huge effort was put into material compatibility checks. Another important specificity is a two identical detectors concept, one near the cores for a measurement before oscillation, and one far close to the maximum of oscillation, allowing a signal comparison between them and the extraction of the $\theta_{13}$ parameter. The detector is so far working really well, with a lower radioactivity contamination than expected and no sign of liquid degradation. The first year of exploitation showed the new design to be a success. Also, using the Bugey 4 anchor point method for the normalization since the near detector is not yet built (*cf.* Section 7.1), the first Double Chooz results are in good agreement with the other experiments Daya Bay and RENO, proving the strongness of our analysis method and final results (*cf.* Sections 2.2.4.3 and 7.4).

With only a far detector, Double Chooz gave the first indication for the disappearance of reactor electron antineutrinos one kilometer away from nuclear cores. This first measurement was later updated with twice the statistics and a precise determination of $\theta_{13}$ could be given: $\sin^2 2\theta_{13} = 0.109 \pm 0.030\,(\text{stat}) \pm 0.025\,(\text{syst})$, with $\Delta m^2_{31} = 2.32 \times 10^{-3}\,\text{eV}^2$. The no-oscillation hypothesis was even excluded at 2.9 $\sigma$.

[4] From the NBC "The Office" television series created by Ricky Gervais. Season 3, episode 18.

During this thesis, I had the opportunity to work on many aspects of the Double Chooz analysis. Before the electron antineutrino candidates selection and the determination of the background contamination, the data need to be reconstructed and calibrated. With a task on the channel time offsets determination at the beginning of my thesis, I was able to start looking at the data and contribute to the calibration effort (*cf.* Section 4.2.2).

Concerning the reconstruction, I developed an energy and vertex reconstruction algorithm called "CocoReco" (*cf.* Section 5.2). Studied and improved on Monte Carlo simulations, it is based on the understanding of the physics occurring within a liquid scintillator. It allowed me to use the whole Double Chooz Monte Carlo chain, from the generation of events to their reconstruction. This algorithm showed great performances for both vertex and energy reconstruction on simulated data. The maximal bias between the true simulated energy and the reconstructed energy could be reduced from 13 % to 3 % by adding a Čerenkov radiation correction term obtained from GEANT4 studies. This reconstruction package gives a fairly homogenous response throughout the $\nu$-target volume, but tends to underestimate the energy deposition in the $\gamma$-catcher. "CocoReco" could be improved by reducing its processing speed using lookup tables and could be tuned with calibration data in order to reduce the position dependence in the $\gamma$-catcher.

More at a software level, I was also involved in the Common Trunk, a package which groups all the reconstruction algorithms. This implied processing the RAW data files and monitoring them, as well as checking the sanity of the reconstructed outputs. In order to improve the speed of the data processing, we created at Saclay the "Cheetah" software, which could create really quickly light outputs allowing fast data analyses (*cf.* Section 4.6). The typical size of such files is now few tens of megabytes whereas it originally was several gigabytes for the official Common Trunk files. I was in charge of the reduced data files production at a critical time for the collaboration, and dealt with the production and monitoring of these files. I provided the whole collaboration with reduced data files during the whole first paper analysis period. The "Cheetah" software is now embedded in the official Common Trunk package and reduced files based on its architecture are processed along with heavy ones.

The neutrino analysis is the core of my thesis work (*cf.* Chapter 6). The $\theta_{13}$ determination depends on the selected electron antineutrino candidates and the estimation of the background contamination. I have been strongly involved from the beginning in these studies. Over 240.17 days of live time from April 13$^{\text{th}}$ 2011, 9,021 $\overline{\nu}_e$ candidates were selected. My work on the selection cuts allowed to get rid of a contamination in the prompt spectrum, coming mainly from neutron captures on gadolinium, by adding a multiplicity cut around the prompt-delayed events coincidence pairs (*cf.* Section 6.2.2).

The backgrounds studies, and especially the cosmogenics $^9$Li one, have also been one of the main subjects of my thesis (*cf.* Section 6.3). By using the data of the former experiment CHOOZ and scaling them to Double Chooz, I estimated the $^9$Li contamination in our detector to be $1.66 \pm 0.34$ d$^{-1}$. I continued studying this background by working on understanding and reducing it from Double Chooz data themselves. The $^9$Li events were selected by fitting the time differences between high energy depositions and neutrino candidates, with a model following the expected $^9$Li livetime (*cf.* Section 6.3.3). By separating the energy depositions in three ranges, the total cosmogenic isotopes contamination has been estimated to be $2.05^{+0.62}_{-0.52}$ d$^{-1}$. Although the estimation from CHOOZ seems to slightly underestimate this background, the agreement is quite good within the error bars. Moreover, the pull terms fit tends to show that the $^9$Li selection on Double Chooz data may be overestimated by 25 % (*cf.* Section 7.4.2). The neutron multiplicity after high energy depositions was also studied and brought additionnal information on the cosmogenics production.

Furthermore, I proposed an analysis called lithium-free based on applying a 600 ms veto after high energy depositions (typically E $>$ 600 MeV) likely to be caused by high energy muons, and thus expected to produce cosmogenics isotopes (*cf.* Section 6.4). This veto method became

official for the second Double Chooz collaboration analysis. It directly affects the experiment live time, reducing it by 4 % to 228.25 days. The number of selected $\overline{\nu}_e$ candidates became 8,249 and the remaining $^9$Li rate was estimated to be $1.25\,^{+0.59}_{-0.48}$ d$^{-1}$.

The particularity of the Double Chooz experiment is that, located near only two reactors, both reactors being OFF at the same time is likely to occur. This kind of data is really a godsend as it allows to measure the experiment total background, since the source of electron antineutrino is basically shut down. I performed an event selection on the first day of OFF-OFF data, and on the second period amounting for roughly a week, and developed for the first day a background subtraction method, using the rate information or both the rate and the shape (*cf.* Section 6.5). An estimation of the additional systematic error such a subtraction would imply was then done and found to amount for 3 % for two background events selected in 24 hours of both reactors OFF data. A total background rate of $1.20 \pm 0.4$ d$^{-1}$ was finally found, while $2.0 \pm 0.6$ d$^{-1}$ was measured on regular data. The slight tension between these results disappears once one of the cuts, the outer veto tag, is not applied, highlighting the fact that this detector is not yet totally understood.

Although the $^9$Li background is now better understood thanks notably to the analyses I performed, it still is the main contributor to the overall systematic uncertainty. It therefore needs more detailed studies, especially using the information both reactors OFF data could provide.

Finally, in order to determine the $\theta_{13}$ parameter, I used the fitting package developed at Saclay called CATS. After a presentation of the electron neutrino flux prediction procedure and the Bugey 4 anchor point method, needed since only the far detector is running, I presented the results for a $\theta_{13}$ fit using only the deficit of number of events in the far detector (rate only analysis) and using it along with the spectral shape distortion information (rate and shape analysis) (*cf.* Section 7.4). These results were discussed and diagnostics plots from CATS were presented.

The systematic uncertainties will be soon strongly lowered once the near detector acquires data. The Double Chooz near laboratory is already under construction and its detector is expected to be delivered in 2013. By comparing the far detector data to the near detector one instead of flux predictions, the Bugey 4 anchor point method will not be needed anymore, therefore considerably lowering the systematics, since it amounts now for 1.4 % (one of the dominant systematics). This will allow the Double Chooz experiment to reach an even better precision for the $\theta_{13}$ measurement. The 5 $\sigma$ exclusion of the no-oscillation hypothesis would be possible to reach in less than three years of data taking with two detectors. Moreover, the Double Chooz near detector will provide an additionnal test of the Bugey 4 anchor point method and even allow to further study the reactor antineutrino anomaly.

Precise measurements of the leptonic mixing parameters are necessary to allow a determination of the sign of $\left|\Delta m^2_{31}\right|$ and a study of a potential CP symmetry violation for the neutrinos, which could be performed by the T2K experiment or by the forthcoming NO$\nu$A one. Before that, the three reactor electron antineutrino experiments, Double Chooz, Daya Bay, and RENO will have to come to an agreement on the $\theta_{13}$ value once their respective spectrum and neutrino rate are perfectly understood.

# Bibliography


[1] K. N. Abazajian et al., *Cosmological and Astrophysical Neutrino Mass Measurements*, Astropart. Phys., 35 (2011), pp. 177–184.

[2] K. N. Abazajian et al., *Light Sterile Neutrinos: A White Paper*, (2012).

[3] J. Abdurashitov et al., *Measurement of the solar neutrino capture rate with gallium metal*, Phys. Rev., C60 (1999), p. 055801.

[4] K. Abe et al., *Indication of Electron Neutrino Appearance from an Accelerator-produced Off-axis Muon Neutrino Beam*, Phys. Rev. Lett., 107 (2011), p. 041801.

[5] K. Abe et al., *Search for Differences in Oscillation Parameters for Atmospheric Neutrinos and Antineutrinos at Super-Kamiokande*, Phys. Rev. Lett., 107 (2011), p. 241801.

[6] K. Abe et al., *The T2K Experiment*, Nucl. Instrum. Meth., A659 (2011), pp. 106–135.

[7] S. Abe et al., *Precision Measurement of Neutrino Oscillation Parameters with KamLAND*, Phys. Rev. Lett., 100 (2008), p. 221803.

[8] S. Abe et al., *Production of Radioactive Isotopes through Cosmic Muon Spallation in KamLAND*, Phys. Rev., C81 (2010), p. 025807.

[9] Y. Abe, *ID calibration constants by IDLI*, Double Chooz internal talk (2012).

[10] Y. Abe et al., *Linearized-PE calibration technical note*, Double Chooz internal note (2012).

[11] Y. Abe et al., *Reactor $\overline{\nu}_e$ disappearance in the Double Chooz experiment*, Phys. Rev. D, (2012), accepted/to be published.

[12] Y. Abe et al., *Indication for the disappearance of reactor $\overline{\nu}_e$ in the Double Chooz experiment*, Phys. Rev. Lett., 108 (2012), p. 131801.

[13] C. Aberle, *Double Chooz GEANT4 Summary Talk*, Double Chooz internal talk (2012).

[14] C. Aberle, *Optimization, simulation and analysis of the scintillation signals in the Double Chooz experiment*, PhD thesis, Combined Faculties for the Natural Sciences and for Mathematics of the Ruperto-Carola University of Heidelberg (2011).

[15] C. Aberle et al., *Light output of double chooz scintillators for low energy electrons*, Journal of Instrumentation, 6 (2011), p. 11006.

[16] C. Aberle et al., *Large scale Gd-beta-diketonate based organic liquid scintillator production for antineutrino detection*, JINST, 7 (2012), p. P06008.

[17] B. Achkar et al., *Comparison of anti-neutrino reactor spectrum models with the Bugey-3 measurements*, Phys. Lett., B374 (1996), pp. 243–248.

[18] T. Adam et al., *Measurement of the neutrino velocity with the OPERA detector in the CNGS beam*, (2011).

[19] P. Adamson et al., *An improved measurement of muon antineutrino disappearance in MINOS*, Phys. Rev. Lett., 108 (2012), p. 191801.

[20] N. Agafonova et al., *Observation of a first $\nu_\tau$ candidate in the OPERA experiment in the CNGS beam*, Phys. Lett., B691 (2010), pp. 138–145.

[21] A. Aguilar-Arevalo et al., *Evidence for neutrino oscillations from the observation of anti-neutrino(electron) appearance in a anti-neutrino(muon) beam*, Phys. Rev., D64 (2001), p. 112007.

[22] A. Aguilar-Arevalo et al., *Event Excess in the MiniBooNE Search for $\bar{\nu}_\mu \to \bar{\nu}_e$ Oscillations*, Phys. Rev. Lett., 105 (2010), p. 181801.

[23] A. Aguilar-Arevalo et al., *A Combined $\nu_\mu \to \nu_e$ and $\bar{\nu}_\mu \to \bar{\nu}_e$ Oscillation Analysis of the MiniBooNE Excesses*, (2012).

[24] B. Aharmim et al., *Electron energy spectra, fluxes, and day-night asymmetries of B-8 solar neutrinos from the 391-day salt phase SNO data set*, Phys. Rev., C72 (2005).

[25] J. Ahn et al., *Observation of Reactor Electron Antineutrino Disappearance in the RENO Experiment*, Phys. Rev. Lett., 108 (2012), p. 191802.

[26] T. Akiri, *Test des Flash-ADCs, optimisation de la conception du détecteur et développement d'un nouveau concept de reconstruction spatiale dans l'expérience d'oscillation de neutrinos Double Chooz*, PhD thesis, Université Paris Diderot - Paris 7 (2010).

[27] G. Alimonti et al., *Science and technology of BOREXINO: A Real time detector for low-energy solar neutrinos*, Astropart. Phys., 16 (2002), pp. 205–234.

[28] E. Aliu et al., *Evidence for muon neutrino oscillation in an accelerator-based experiment*, Phys. Rev. Lett., 94 (2005).

[29] F. An et al., *Observation of electron-antineutrino disappearance at Daya Bay*, Phys. Rev. Lett., 108 (2012), p. 171803.

[30] M. Apollonio et al., *Search for neutrino oscillations on a long baseline at the CHOOZ nuclear power station*, Eur. Phys. J., C27 (2003), pp. 331–374.

[31] F. Ardellier et al., *Double Chooz: A Search for the Neutrino Mixing Angle $\theta_{13}$*, (2006).

[32] R. Arnold et al., *Technical design and performance of the NEMO 3 detector*, Nucl. Instrum. Meth., A536 (2005), pp. 79–122.

[33] R. Arnold et al., *Probing New Physics Models of Neutrinoless Double Beta Decay with SuperNEMO*, Eur. Phys. J., C70 (2010), pp. 927–943.

[34] K. Assamagan et al., *Upper limit of the muon-neutrino mass and charged pion mass from momentum analysis of a surface muon beam*, Phys. Rev., D53 (1996), pp. 6065–6077.

[35] ATLAS Collaboration, *Combined search for the Standard Model Higgs boson using up to 4.9 $fb^{-1}$ of pp collision data at $\sqrt{s} = 7$ TeV with the ATLAS detector at the LHC*, Phys. Lett. B, 710 (2012), pp. 49–66. Submitted to Physics Letters B.

[36] ATLAS Collaboration, *Observation of a New Particle in the Search for the Standard Model Higgs Boson with the ATLAS Detector at the LHC*, Phys. Lett. B, (2012). Submitted to Physics Letters B.

[37] D. Ayres et al., *Letter of Intent to build an Off-axis Detector to study numu to nue oscillations with the NuMI Neutrino Beam*, (2002).

[38] J. N. Bahcall et al., *Solar Models: current epoch and time dependences, neutrinos, and helioseismological properties*, Astrophys. J., 555 (2001), pp. 990–1012.

[39] R. Barate et al., *An Upper limit on the tau-neutrino mass from three-prong and five-prong tau decays*, Eur. Phys. J., C2 (1998), pp. 395–406.

[40] R. Becker-Szendy et al., *The Electron-neutrino and muon-neutrino content of the atmospheric flux*, Phys. Rev., D46 (1992), pp. 3720–3724.

[41] A. H. Becquerel, *Sur les radiations émises par phosphorescence*, 122 (1896), pp. 420–421.

[42] J. Birks, *The theory and practice of scintillation counting*, International series of monographs on electronics and instrumentation, Pergamon Press (1964).

[43] F. Boehm et al., *Final results from the Palo Verde neutrino oscillation experiment*, Phys. Rev., D64 (2001), p. 112001.

[44] N. Bohr, H. A. Kramers, and J. C. Slater, *The Quantum Theory of Radiation*, Phil. Mag., 47 (1924), pp. 785–802.

[45] L. Broglie, *Physique et microphysique*, Sciences d'aujourd'hui, A. Michel (1947).

[46] C. Buck, *Number of protons in Target and GC*, Double Chooz internal talk (2011).

[47] J. Busenitz et al., *Plan for deployment of radioactive sources*, Double Chooz internal note (2010).

[48] A. Cabrera et al., *DCRoSS*, Double Chooz internal note (2007).

[49] A. Cabrera et al., *Second Publication Energy Scale*, Double Chooz internal talk (2012).

[50] S. Capelli, *Cuoricino latest results and background analysis*, Nucl. Phys. - Proceedings Supplements, B221 (2011), p. 334.

[51] J. Chadwick, *The intensity distribution in the magnetic spectrum of $\beta$ particles from radium (B + C)*, Verh. Phys. Gesell., 16 (1914), pp. 383–391.

[52] P.-J. Chang, *Neutron efficiencies update*, Double Chooz internal note (2012).

[53] P.-J. Chang et al., *Neutrino Efficiency Analysis Results*, Double Chooz internal note (2012).

[54] P.-J. Chang et al., *Neutron Efficiency Systematics for 2nd Publication*, Double Chooz internal note (2012).

[55] CMS Collaboration, *Combined results of searches for the standard model Higgs boson in pp collisions at $\sqrt{s} = 7$ TeV.*, (2012).

[56] C. Cohen-Tannoudji et al., *Mécanique quantique*, no. vol. 1 in Collection Enseignement des sciences, Hermann (1973).

[57] A. Collin et al., *Pulse Shape*, Double Chooz internal talk (2011).

[58] A. Collin et al., *Reactors off-off, expected neutrino spectrum*, Double Chooz internal talk (2011).

[59] C. L. Cowan Jr. et al., *Detection of the free neutrino: a confirmation*, Science, 124 (1956), pp. 103–104.

[60] J. I. Crespo Anadón, *Improving The SPE Reconstruction Efficiency*, Double Chooz internal talk (2012).

[61] M. Cribier, *CeLAND Testing the fourth neutrino hypothesis with an antineutrinos generator*, GDR Neutrino talk (2012).

[62] A. S. Cucoanes, *A Toy Model for the Gamma Spectrum Generated in n-Captures on Gd*, Double Chooz internal note (2011).

[63] A. S. Cucoanes, *Status of the Nucifer Experiment*, TAUP talk (2011).

[64] G. Danby et al., *Observation of High-Energy Neutrino Reactions and the Existence of Two Kinds of Neutrinos*, Phys. Rev. Lett., 9 (1962), pp. 36–44.

[65] R. Davis Jr. et al., *Search for neutrinos from the sun*, Phys. Rev. Lett., 20 (1968), pp. 1205–1209.

[66] J. V. Dawson, *Gain Estimation Technique with Light Injection System*, Double Chooz internal note (2011).

[67] Y. Declais et al., *Study of reactor antineutrino interaction with proton at bugey nuclear power plant*, Phys. Lett., B338 (1994), pp. 383–389.

[68] A. C. Doyle, *A study in scarlet*, Penguin books, Penguin (1982).

[69] V. Durand, *Antineutrino candidates selection*, Double Chooz internal talk (2011).

[70] V. Durand, *Backgrounds subtraction with a short reactor OFF-OFF period*, Double Chooz internal talk (2011).

[71] V. Durand, *Energy Reconstruction at Saclay: CocoReco*, Double Chooz internal talk (2010).

[72] V. Durand, *Neutrino selection and the bump at 8 MeV*, Double Chooz internal talk (2011).

[73] V. Durand, *(re)-Analysis of Reactors OFF Data from CHOOZ. Studies on Cosmogenics Nuclei and Fast-Neutrons Backgrounds*, Double Chooz internal note (2010).

[74] V. Durand, *(re)-Analysis of reactors OFF data from CHOOZ. $^9$Li and fast-neutrons backgrounds*, Double Chooz internal talk (2010).

[75] V. Durand, *Subtraction of a Short Period of Reactor OFF-OFF Period*, Double Chooz internal note (2011).

[76] V. Durand, *$^9$Li-free analysis and backgrounds subtraction*, Double Chooz internal talk (2011).

[77] V. Durand, *$^9$Li-free analysis using neutron multiplicity*, Double Chooz internal talk (2012).

[78] V. Durand, *Time Offsets Studies*, Double Chooz internal talk (2010).

[79] V. Durand et al., *CocoReco, Energy Reconstruction Tool from Saclay*, Double Chooz internal note (2010).

[80] V. Durand et al., *Fast data processing for Double Chooz*, Double Chooz internal talk (2011).

[81] F. Englert and R. Brout, *Broken symmetry and the mass of gauge vector mesons*, Phys. Rev. Lett., 13 (1964), pp. 321–323.

[82] A. Etenko, *Slow Neutrons Modelling NeutronTH*, Double Chooz internal talk (2010).

[83] Evaluated Nuclear Structure Data File. `http://www.nndc.bnl.gov/ensdf/`.

[84] M. Fechner et al., *The Cheetah program*, Double Chooz internal note (2011).

[85] G. Feldman and R. Cousins, *Unified approach to the classical statistical analysis of small signals*, Phys. Rev. D, 57(7) (1998), pp. 3873–3889.

[86] E. Fermi, *An attempt of a theory of beta radiation.*, Z. Phys., 88 (1934), pp. 161–177.

[87] R. P. Feynman and M. Gell-Mann, *Theory of the fermi interaction*, Phys. Rev., 109 (1958), pp. 193–198.

[88] R. A. Forrest and M. R. Gilbert, *FISPACT-2005: User manual*, EURATOM /UKAEA Fusion Association (2005).

[89] D. Franco, *Light-noise cut test with calibration data*, Double Chooz internal talk (2011).

[90] A. J. Franke et al., *Event Generation and Uncertainty Propagation in DCRxtrTools using the Bugey4 Anchor Point*, Double Chooz internal note (2011).

[91] S. Fukuda et al., *Determination of Solar Neutrino Oscillation Parameters using 1496 Days of Super-Kamiokande-I Data*, Phys. Lett., B539 (2002), pp. 179–187.

[92] Y. Fukuda et al., *Atmospheric muon-neutrino/electron-neutrino ratio in the multiGeV energy range*, Phys. Lett., B335 (1994), pp. 237–245.

[93] Y. Fukuda et al., *Evidence for oscillation of atmospheric neutrinos*, Phys. Rev. Lett., 81 (1998), pp. 1562–1567.

[94] M. Fukugita and T. Yanagida, *Baryogenesis without grand unification*, Phys. Lett., B174 (1986), pp. 45 – 47.

[95] A. Gando et al., *Constraints on $\theta_{13}$ from A Three-Flavor Oscillation Analysis of Reactor Antineutrinos at KamLAND*, Phys. Rev., D83 (2011), p. 052002.

[96] X. Garrido, *Search for Neutrinoless Double Beta Decay: NEMO3 Results and Plans for SuperNEMO*, 23rd Rencontres de Blois, (2011).

[97] GEANT4. `http://www.geant4.org/`.

[98] C. Giunti, *Theory of neutrino oscillations*, (2004).

[99] C. Giunti and C. W. Kim, *Fundamentals of Neutrino Physics and Astrophysics*, Oxford University Press (2007).

[100] C. Giunti and M. Laveder, *Short-Baseline Electron Neutrino Disappearance, Tritium Beta Decay and Neutrinoless Double-Beta Decay*, Phys. Rev., D82 (2010), p. 053005.

[101] S. L. Glashow, *Partial Symmetries of Weak Interactions*, Nucl. Phys., 22 (1961), pp. 579–588.

[102] L. F. G. Gonzalez, *Hunting for stopping muons*, Double Chooz internal talk (2011).

[103] M. C. Gonzalez-Garcia, *Neutrinos: theory udpate/review*, ICHEP talk (2012).

[104] M. C. Gonzalez-Garcia et al., *Robust Cosmological Bounds on Neutrinos and their Combination with Oscillation Results*, JHEP, 1008 (2010), p. 117.

[105] J. Goon, *Integration Readiness Review - Laser Deployment system*, Double Chooz internal note (2011).

[106] J. Goon, *Isotropy Study of the Double Chooz Diffuser*, Double Chooz internal note (2011).

[107] A. A. Hahn et al., *Antineutrino spectra from Pu-241 and Pu-239 thermal neutron fission products*, Phys. Lett., B218 (1989), pp. 365–368.

[108] W. Hampel et al., *GALLEX solar neutrino observations: Results for GALLEX IV*, Phys. Lett., B447 (1999), pp. 127–133.

[109] J. Haser, *Spill-in/out systematics technical note*, Double Chooz internal note (2012).

[110] P. W. Higgs, *Broken symmetries and the masses of gauge bosons*, Phys. Rev. Lett., 13 (1964), pp. 508–509.

[111] A. Hourlier et al., *Neutron thermalization in the Neutrino Target*, Double Chooz internal talk (2012).

[112] P. Huber, *On the determination of anti-neutrino spectra from nuclear reactors*, Phys. Rev., C84 (2011), p. 024617.

[113] P. Huber and T. Schwetz, *Precision spectroscopy with reactor antineutrinos*, Phys. Rev. D, 70 (2004), p. 053011.

[114] IAEA International Atomic Energy Agency. `http://www-pub.iaea.org/MTCD/publications/PDF/CNPP2010_CD/pages/AnnexII/tables/table2.htm`.

[115] C. Ignarra, *MicroBooNE*, (2011).

[116] M. Ishitsuka, *Toward initial calibration using IDLI system*, Double Chooz internal talk (2010).

[117] M. Ishitsuka et al., *The Double Chooz Shifter Manual*, Double Chooz internal document (2012).

[118] J. V. Jelley, *Cerenkov radiation and its applications*, Pergamon Press London (1958).

[119] C. Jones, *Method of Obtaining Fission Rates With DRAGON*, Double Chooz internal note (2011).

[120] D. M. Kaplan, *Double Chooz LED Flasher Prototype Tests*, Double Chooz internal note (2010).

[121] I. Kirpichnikov, *Klapdor's claim for the observation of the neutrinoless double beta-decay of Ge-76. Analysis and corrections*, (2010).

[122] H. V. Klapdor-Kleingrothaus et al., *The evidence for the observation of 0nu beta beta decay: The identification of 0nu beta beta events from the full spectra*, Mod. Phys. Lett., A21 (2006), pp. 1547–1566.

[123] KLG4sim, KamLAND Experiment GEANT4. `http://general.krl.caltech.edu/KamLAND/montecarlo/KLG4sim/`.

[124] G. Knoll, *Radiation detection and measurement*, Wiley (2000).

[125] M. Kobayashi and T. Maskawa, *CP Violation in the Renormalizable Theory of Weak Interaction*, Progr. Theoret. Phys., 49 (1973), pp. 652–657.

[126] K. Kodama et al., *Observation of tau-neutrino interactions*, Phys. Lett., B504 (2001), pp. 218–224.

[127] T. Konno, *Measurement of $\theta_{13}$ by neutrino oscillation experiments*, Moriond Cosmology talk (2012).

[128] T. Konno, *Updates on neutron efficiencies*, Double Chooz internal note (2012).

[129] C. Kraus et al., *Final results from phase II of the Mainz neutrino mass search in Tritium $\beta$ decay*, Eur. Phys. J., 40 (2005), p. 447.

[130] T. Lasserre, *Testing the Reactor and Gallium Anomalies with intense $\nu_e/\overline{\nu}_e$ emitters*, Neutrino talk (2012).

[131] R. Lazauskas, *Description of cosmogenic $\beta$-n background (case of $^8$He and $^9$Li)*, Double Chooz internal talk (2008).

[132] T. D. Lee and C. N. Yang, *Question of parity conservation in weak interactions*, Phys. Rev., 104 (1956), pp. 254–258.

[133] V. M. Lobashev et al., *Direct search for mass of neutrino and anomaly in the tritium $\beta$-spectrum*, Phys. Lett., B460 (1999), pp. 227 – 235.

[134] M. Macaire, *Étude des oscillations $\nu_\mu \rightarrow \nu_e$ auprès de l'expérience T2K*, PhD thesis, Université Paris Diderot - Paris 7 (2012), to be published.

[135] Z. Maki, M. Nakagawa, and S. Sakata, *Remarks on the unified model of elementary particles*, Progr. Theoret. Phys., 28 (1962), pp. 870–880.

[136] V. Martemyanov et al., *The Kr2Det project: Search for mass 3 state contribution /U(e3)/**2 to the electron neutrino using a one reactor - two detector oscillation experiment at Krasnoyarsk underground site*, Phys. Atom. Nucl., 66 (2003), pp. 1934–1939.

[137] T. Matsubara et al., *Evaluation of 400 low background 10-in. photo-multiplier tubes for the Double Chooz experiment*, Nuclear Instruments and Methods in Physics Research A, 661 (2012), pp. 16–25.

[138] G. Mention, *CATS, Linear and locally linearized $\chi^2$ with systematics and regression diagnostics*, Double Chooz internal note (2011).

[139] G. Mention, *Double Chooz Final Fit*, GDR Neutrinos talk (2012).

[140] G. Mention, *Étude des sensibilités et bruits de fond de l'expérience Double Chooz pour la recherche du paramètre de mélange leptonique $\theta_{13}$*, PhD thesis, Université Claude Bernard - Lyon I (2005).

[141] G. Mention et al., *The Reactor Antineutrino Anomaly*, Phys. Rev., D83 (2011), p. 073006.

[142] MINOS Collaboration. `http://www-numi.fnal.gov/minwork/info/`.

[143] MINUIT. `http://lcgapp.cern.ch/project/cls/work-packages/mathlibs/minuit`.

[144] T. Mueller, *Expérience Double Chooz : simulation des spectres antineutrinos issus de réacteurs*, PhD thesis, Université Paris-Sud 11 - Orsay (2010).

[145] T. Mueller, *Spill-in/out studies and other interesting stuff about neutron physics*, Double Chooz internal note (2011).

[146] T. Mueller et al., *Détermination du nombre de proton cible de l'expérience Double Chooz au moyen d'une mesure de pesée*, Double Chooz internal note (2010).

[147] T. Mueller et al., *Improved Predictions of Reactor Antineutrino Spectra*, Phys. Rev., C83 (2011), p. 054615.

[148] H. Murayama, *Supersymmetry phenomenology*, (2000), pp. 296–335.

[149] K. Nakamura et al., *Review of particle physics*, J. Phys. G, G37 (2010), p. 075021.

[150] P. Novella, *Optimization and performance of the DC pulse reconstruction algorithm*, Double Chooz internal note (2011).

[151] P. Novella et al., *DCRecoPulse, Software and algorithms for pulse reconstruction*, Double Chooz internal note (2009).

[152] A. Onillon, *MURE strategie for Double Chooz cores simulations*, Double Chooz internal note (2011).

[153] C. Palomares, *New rates cutting on delayed energy deposition QMQT $<$ 0.055*, Double Chooz internal talk (2012).

[154] C. Palomares, *$^{12}B$ correlated background*, Double Chooz internal talk (2012).

[155] W. Pauli, *Dear radioactive ladies and gentlemen.*, Phys. Today, 31N9 (1978), p. 27.

[156] B. Pontecorvo, *Mesonium and anti-mesonium*, Sov. Phys. JETP, 6 (1957), p. 429.

[157] B. Pontecorvo, *Inverse beta processes and nonconservation of lepton charge*, Sov. Phys. JETP, 7 (1958), pp. 172–173.

[158] R. Quéval, *Characterization, Modelization and Optimization of the Double Chooz acrylic vessels: Physics Impact*, PhD thesis, Université Paris Diderot - Paris 7 (2010).

[159] A. Remoto et al., *Correlated background analysis for Double Chooz second publication*, Double Chooz internal talk (2012).

[160] M. Roehling, *Inner Veto Trigger Studies*, Double Chooz internal talk (2012).

[161] ROOT. `http://root.cern.ch/drupal/`.

[162] K. Sakashita, *Results from T2K*, ICHEP talk (2012).

[163] P. Sala, *Status of the ICARUS experiment*, Nucl. Phys. - Proceedings Supplements, B217 (2011), pp. 186 – 188.

[164] A. Salam, *Weak and electromagnetic interactions*, Almquist and Wiksell (1968).

[165] K. Schreckenbach et al., *Determination of the antineutrino spectrum from U-235 thermal neutron fission products up to 9.5 MeV*, Phys. Lett., B160 (1985), pp. 325–330.

[166] T. Schwetz et al., *Three-flavour neutrino oscillation update*, New J. Phys., 10 (2008), p. 113011.

[167] R. E. Shrock, *General theory of weak processes involving neutrinos. II. Pure leptonic decays*, Phys. Rev. D, 24 (1981), pp. 1275–1309.

[168] I. Stancu, *RecoBAMA with and without T-offsets: MC and Data Studies*, Double Chooz internal talk (2011).

[169] I. Stancu, *Revised Analysis of the LED Flasher Data and the First Set of Time Offsets*, Double Chooz internal note (2011).

[170] I. Stancu, *The Double Chooz Optical Model*, Double Chooz internal note (2011).

[171] I. Stancu, *The Energy Response Function and Reflections in Double Chooz*, Double Chooz internal talk (2012).

[172] I. Stancu, *The Ge-68 Calibration Data and the SPE Inefficiency*, Double Chooz internal talk (2011).

[173] M. Strait, *Fido Mutt: The Fused Inner Detector Outer veto MUon Track reconsTruction*, Double Chooz internal note (2012).

[174] A. Stueken, *Overview of the NuDAQ trigger system*, Double Chooz internal note (2011).

[175] A. Stueken, *Trigger Efficiency Study for Second Publication including new energy scale*, Double Chooz internal note (2012).

[176] H. A. Sturges, *The choice of a class interval*, Journal of the American Statistical Association, JSTOR 2965501 (1926), pp. 65–66.

[177] F. Suekane et al., *A proposal to make the MQTQ cut as a standard prescription for the light noise rejection*, Double Chooz internal note (2011).

[178] F. Suekane et al., *Off-site glow studies*, Double Chooz internal talk (2011).

[179] SVN Apache Subversion. `http://subversion.apache.org/`.

[180] S. Tamura, *Muon reconstruction using Inner Detector*, Double Chooz internal talk (2011).

[181] The ALEPH, DELPHI, L3, OPAL, and SLD Collaborations, *Precision electroweak measurements on the Z resonance*, Physics Reports, 427 (2006), pp. 257–454.

[182] D. Tilley et al., *Energy levels of light nuclei*, Nucl. Phys., A745 (2004), pp. 155 – 362.

[183] T. Valentine and J. Mihalczo, *MCNP-DSP: A neutron and gamma ray Monte carlo calculation of source-driven noise-measured parameters*, Annals of Nuclear Energy, 23 (1996), pp. 1271 – 1287.

[184] P. Vogel, *Analysis of the antineutrino capture on protons*, Phys. Rev. D, 29 (1984), pp. 1918–1922.

[185] P. Vogel and J. F. Beacom, *Angular distribution of neutron inverse beta decay*, Phys. Rev. D, 60 (1999), p. 053003.

[186] S. Weinberg, *A model of leptons*, Phys. Rev. Lett., 19 (1967), pp. 1264–1266.

[187] C. Weinheimer, *KATRIN, a next generation tritium $\beta$ decay experiment in search for the absolute neutrino mass scale*, Prog. Part. Nucl. Phys., 48 (2002), pp. 141 – 150.

[188] P. D. Wilson, *The Nuclear Fuel Cycle: From Ore to Waste*, Oxford University Press (1996).

[189] L. Winslow, *Decay Spectra of $^9$Li for DC1stPub*, Double Chooz internal note (2011).

[190] L. Winslow, *First Solar Neutrinos from KamLAND: A Measurement of the $^8$B Solar Neutrino Flux*, PhD thesis, University of California, Berkeley (2008).

[191] L. Wolfenstein, *Neutrino oscillations in matter*, Phys. Rev., D17 (1978), pp. 2369–2374.

[192] C. S. Wu et al., *Experimental test of parity conservation in beta decay*, Phys. Rev., 105 (1957), pp. 1413–1415.

[193] M. Wurm, *$^9$Li rate from inner detector data*, Double Chooz internal note (2012).

[194] S. Yokoyama, *Study for energy calibration. MC tuning by U/Th analysis*, Double Chooz internal talk (2012).

**Résumé :**

L'expérience Double Chooz a pour but la mesure de l'angle de mélange $\theta_{13}$ via l'étude des oscillations de $\overline{\nu}_e$ produits par les réacteurs nucléaires de Chooz, à l'aide de deux détecteurs identiques de 10,3 $m^3$, permettant ainsi de s'affranchir de la plupart des incertitudes systématiques. Le détecteur proche, dont le but est la normalisation du flux émis, sera opérationnel en 2013, alors que le lointain, qui prend des données depuis avril 2011, est quant à lui sensible à $\theta_{13}$, c'est-à-dire à un déficit et une déformation spectral des $\overline{\nu}_e$ détectés.

Au sein de cette thèse l'expérience Double Chooz est présentée, avec sa source en $\overline{\nu}_e$, sa méthode de détection, et les signal et bruits de fond attendus. Afin de sélectionner ces évènements, de nombreuses quantités doivent être reconstruites, étalonnées et sauvegardées dans des fichiers de données. Un soin spécial est donc apporté à la présentation de la détermination des retards en temps des canaux d'acquisition, de l'algorithme de reconstruction d'énergie et de vertex CocoReco, du logiciel compilant les outils de reconstruction Common Trunk et du réducteur de données Cheetah. En ce qui concerne l'analyse, toutes les coupures de sélection et leurs résultats sont présentés. En particulier, la coupure de multiplicité, la méthode des multiples fenêtres en temps décalée, le véto lithium, et les études relatives au bruit de fond $^9$Li sont discutés.

Pour 227,93 jours de données du détecteur lointain, 8249 candidats $\overline{\nu}_e$ ont été observés. La prédiction du flux émis utilise la mesure de l'expérience Bugey 4 en corrigeant des différences de composition des cœurs. En l'absence d'oscillation, 8937 évènements étaient attendus. Ce déficit est interprété comme une disparition de $\overline{\nu}_e$. Une analyse utilisant cette information et la déformation spectral des $\overline{\nu}_e$ donne $\sin^2 2\theta_{13} = 0,109 \pm 0,030$ (stat) $\pm$ 0,025 (syst) pour $\Delta m^2_{31} = 2,32 \times 10^{-3}$ eV$^2$. L'hypothèse de non-oscillation est exclue à 2,9 $\sigma$.

---

**Abstract:**

The Double Chooz experiment aims at measuring the neutrino mixing parameter $\theta_{13}$ by studying the oscillations of $\overline{\nu}_e$ produced by the Chooz nuclear reactors located in France. The experimental concept consists in comparing the signal of two identical 10.3 $m^3$ detectors, allowing to cancel most of the experimental systematic uncertainties. The near detector, whose goal is the flux normalization and a measurement without oscillation, is expected to be delivered in 2013. The farthest detector from the source is taking data since April 2011 and is sensitive to $\theta_{13}$, which is expected to affect both the rate and the shape of the measured $\overline{\nu}_e$.

In this thesis, are first presented the Double Chooz experiment, with its $\overline{\nu}_e$ source, its detection method, and the expected signal and backgrounds. In order to perform a selection, important quantities have to be reconstructed, calibrated, and saved in data files. The channel time offsets determination, the energy and vertex reconstruction algorithm CocoReco, the reconstruction packages of the Common Trunk, and the light trees maker Cheetah are especially presented. Concerning the data analysis, all the selection cuts and results for signal and backgrounds are discussed, particularly the multiplicity cut, the multiple offtime window method, the lithium veto cut, and the cosmogenic $^9$Li background studies.

The Double Chooz experiment observed 8,249 $\overline{\nu}_e$ candidates in 227.93 days in its far detector only. The reactor antineutrino flux prediction used the Bugey 4 flux measurement after correction for differences in core composition. The expectation in case of no-oscillation is 8,937 events and this deficit is interpreted as evidence for $\overline{\nu}_e$ disappearance. From a rate and shape analysis, is found $\sin^2 2\theta_{13} = 0.109 \pm 0.030$ (stat) $\pm$ 0.025 (syst), with $\Delta m^2_{31} = 2.32 \times 10^{-3}$ eV$^2$, while the no-oscillation hypothesis is even excluded at 2.9 $\sigma$.

---

**Mots clés :**

Double Chooz, oscillations de neutrinos, angle de mélange $\theta_{13}$, saveur leptonique, réacteur nucléaire, bruits de fond corrélés, isotopes cosmogéniques $^9$Li.